Chapter 2

Fundamentals of Iron and Steelmaking

E.T. Turkdogan, Consultant: Pyrometallurgy & Thermochemistry
R.J. Fruehan, Professor, Carnegie Mellon University

There have been tremendous improvements in iron and steelmaking processes in the past twenty years. Productivity and coke rates in the blast furnace and the ability to refine steel to demanding specifications have been improved significantly. Much of this improvement is based on the application of fundamental principles and thermodynamic and kinetic parameters which have been determined. Whereas, many future improvements will be forthcoming in steelmaking equipment, process improvements resulting from the application of fundamental principles and data will likewise continue.

In this chapter the basic principles of thermodynamics and kinetics are reviewed and the relevant thermodynamic data and properties of gases, metals and slags relevant to iron and steelmaking are presented. These principles and data are then applied to ironmaking, steelmaking and secondary refining processes. These principles and data are also used in subsequent chapters in this volume.

In writing this chapter, an attempt has been made to limit the discussion to an average level suitable for the students of metallurgy pursuing graduate or post-graduate education as well as for those with some scientific background engaged in the iron and steel industry. It is assumed that the reader has some basic knowledge of chemistry, physics and mathematics, so that the chapter can be devoted solely to the discussion of the chemistry of the processes.

2.1 Thermodynamics

2.1.1 Ideal Gas

A gas which obeys the simple gas laws is called an ideal gas satisfying the following relation:

$$PV = nRT \qquad (2.1.1)$$

where n is the number of mols and R the universal molar gas constant.

For one mol of an ideal gas at 273.16K and l atm pressure, the value of the molar gas constant is:

$$R = \frac{1 \times 22.414}{273.16} = 0.08205 \text{ l atm mol}^{-1} \text{ K}^{-1}$$

For pressure in Pa ($\equiv Nm^{-2} \equiv Jm^{-3}$) and volume in m³,

$$R = \frac{1.01325 \times 10^5 \times 22.414 \times 10^{-3}}{273.16} = 8.314 \text{ J mol}^{-1} \text{ K}^{-1}$$

In a gas mixture containing n_1, n_2, n_3... number of mols of gases occupying a volume V at a total pressure P, the partial pressures of the constituent gaseous species are as given below.

$$p_1 = \frac{n_1}{n_1 + n_2 + n_3 + \ldots} \times P \qquad (2.1.2)$$

$$P = p_1 + p_2 + p_3 + \ldots \qquad (2.1.3)$$

The following equations are for a given mass of gas at constant pressure, volume and temperature:

Constant pressure (isobaric) $\dfrac{V_1}{T_1} = \dfrac{V_2}{T_2} = \dfrac{V_3}{T_3} \ldots$ (2.1.4)

Constant volume (isochoric) $\dfrac{P_1}{T_1} = \dfrac{P_2}{T_2} = \dfrac{P_3}{T_3} \ldots$ (2.1.5)

Constant temperature (isothermal) $P_1 V_1 = P_2 V_2 = P_3 V_3 \ldots$ (2.1.6)

Generally speaking, deviation from the ideal gas equation becomes noticeable with easily liquefiable gases and at low temperatures and high pressures. The behavior of gases becomes more ideal with decreasing pressure and increasing temperature. The nonideality of gases, the extent of which depends on the nature of the gas, temperature and pressure, is attributed to two major causes: (1) van der Waals' forces and (2) chemical interaction between the different species of gas molecules or atoms.

2.1.2 Thermodynamic Laws

2.1.2.1 The First Law

The first law of thermodynamics is based on the concept of conservation of energy. When there is interaction between systems, the gain of energy of one of the systems is equal to the loss of the other system. For example, the quantity of heat required to decompose a compound into its elements is equal to the heat generated when that compound is formed from its elements.

2.1.2.1.1 Enthalpy (heat content)   The internal energy of a system includes all forms of energy other than the kinetic energy. Any exchange of energy between a system and its surroundings, resulting from a change of state, is manifested as heat and work.

When a system expands against a constant external pressure P, resulting in an increase of volume ΔV, the work done by the system is

$$w = P\Delta V = P(V_B - V_A)$$

Since this work is done by the system against the surroundings, the system absorbs a quantity of heat q and the energy E of the system increases in passing from state A to state B.

$$\Delta E = E_B - E_A = q - P\Delta V = q - P(V_B - V_A)$$

Upon re-arranging this equation, we have

$$(E_B + PV_B) - (E_A + PV_A) = q$$

The quantity $E + PV$ is represented by a single symbol H, thus

$$\Delta H = q = (E_B + PV_B) - (E_A + PV_A) \qquad (2.1.7)$$

The function H is known as enthalpy or heat content.

There are two fundamental thermochemical laws which express the first law specifically in terms of enthalpy. The first principle derived by Lavoisier and Laplace (1780) states that "the quantity of heat required to decompose a compound into its elements is equal to the heat evolved when that compound is formed from its elements"; i.e. the heat of decomposition of a compound is numerically

equal to its heat of formation, but of opposite sign. The second principle is that discovered by Hess (1840); it states that "the heat of reaction depends only on the initial and final states, and not on the intermediate states through which the system may pass."

2.1.2.1.2 Heat Capacity   The heat capacity of a substance is defined as the quantity of heat required to raise the temperature by one degree. The heat capacity of 1 g of a substance is called the specific heat. The heat capacity of 1 g-molecule (abbreviated as mol) is called the molar heat capacity.

The variation of energy, at constant volume, and of enthalpy, at constant pressure, with temperature gives the heat capacity of the system, thus

$$C_V = \left(\frac{\partial E}{\partial T} \right)_V \tag{2.1.8}$$

$$C_p = \left(\frac{\partial H}{\partial T} \right)_p \tag{2.1.9}$$

For an ideal gas the difference between the molar heat capacities at constant pressure, C_p, and constant volume, C_V, is equal to the molar gas constant.

$$C_p - C_V = R \tag{2.1.10}$$

Because of experimental convenience, the heat capacity is determined under conditions of constant pressure (usually atmospheric).

From the temperature dependence of heat capacity at constant pressure, the enthalpy change is obtained by integrating equation 2.1.9.

$$H_{T_2}^\circ - H_{T_1}^\circ = \int_{T_1}^{T_2} C_p dT \tag{2.1.11}$$

Above 298 K, the temperature dependence of C_p is represented by:

$$C_p = a + bT - cT^{-2} \tag{2.1.12}$$

$$\Delta H = \int_{298}^{T} \left(a + bT - cT^{-2} \right) dT \tag{2.1.13}$$

where the coefficients, a, b and c are derived from C_p calorimetric measurements at different temperatures.

In recent compilations of thermochemical data, the H values are tabulated at 100 K intervals for the convenience of users.

2.1.2.1.3 Standard State   The enthalpy is an extensive property of the system, and only the change in heat content with change of state can be measured. A standard reference state is chosen for each element so that any change in the heat content of the element is referred to its standard state, and this change is denoted by ΔH°.

The natural state of elements at 25°C and 1 atm pressure is by convention taken to be the reference state. On this definition, the elements in their standard states have zero heat contents.

The heat of formation of a compound is the heat absorbed or evolved in the formation of 1 g-mol of the compound from its constituent elements in their standard states, denoted by ΔH_{298}°.

2.1.2.1.4 Enthalpy of Reaction   The change of enthalpy accompanying a reaction is given by the difference between the enthalpies of the products and those of the reactants.

For an isobaric and isothermal reaction,

$$A + B = C + D \tag{2.1.14}$$

the enthalpy change is given by:

$$\Delta H = (\Delta H°C + \Delta H°D) - (\Delta H°A + \Delta H°B) \tag{2.1.15}$$

By convention, H is positive (+) for endothermic reactions, i.e. heat absorption, and H is negative (−) for exothermic reactions, i.e. heat evolution.

Temperature effect:

$$\Delta H_T° = \sum \Delta H_{298}° (\text{products}) - \sum \Delta H_{298}° (\text{reactants}) + \int_{298}^{T} \left[\sum C_p (\text{products}) - \sum C_p (\text{reactants}) \right] dT \tag{2.1.16}$$

$$\Delta H_T° = \Delta H_{298}° + \int_{298}^{T} \left(\Delta C_p \right) dT \tag{2.1.17}$$

The following are some examples of the special terms of the heat of reaction.

Enthalpy or heat of formation	$Fe + \frac{1}{2}O_2$	→	FeO
Heat of combustion	$C + O_2$	→	CO_2
Heat of decomposition	$2CO$	→	$C + CO_2$
Heat of calcination	$CaCO_3$	→	$CaO + CO_2$
Heat of fusion (melting)	Solid	→	Liquid
Heat of sublimation	Solid	→	Vapor
Heat of vaporization	Liquid	→	Vapor
Heat of solution	Si(l)	→	[Si] (dissolved in Fe)

2.1.2.1.5 Adiabatic Reactions   When a reaction occurs in a thermally insulated system, i.e. no heat exchange between the system and its surroundings, the temperature of the system will change in accordance with the heat of reaction.

As an example, let us consider the internal oxidation of unpassivated direct reduced iron (DRI) in a stockpile, initially at 25°C. The enthalpy of reaction at 298K is

$$Fe + \frac{1}{2}O_2 \rightarrow FeO, \quad \Delta H_{298}° = -267 \text{ kJ mol}^{-1} \tag{2.1.18}$$
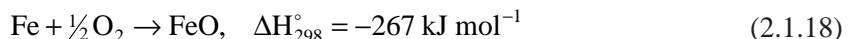
The heat balance calculation is made for 1000 kg Fe in the stockpile with 150 kg FeO formed in oxidation. The heat absorbed by the stockpile is $150 \times 10^3/72 \times 267$ kJ and the temperature rise is calculated as follows:

$$
\begin{aligned}
Q &= [n_{Fe}(C_p)_{Fe} + n_{FeO}(C_p)_{FeO}](T - 298) \\
n_{Fe} &= 17{,}905 \text{ g-mol for 1000 kg Fe} \\
n_{FeO} &= 2087.7 \text{ g-mol for 150 kg FeO} \\
C_p(Fe) &= 0.042 \text{ kJ mol}^{-1}K^{-1} \\
C_p(FeO) &= 0.059 \text{ kJ mol}^{-1}K^{-1} \\
&\therefore Q = 557{,}416 = (752 + 123)(T - 298)
\end{aligned}
$$

With this adiabatic reaction, the stockpile temperature increases to T = 935K (662°C).

The moisture in the stockpile will react with iron and generate H_2 which will ignite at the elevated stockpile temperature. This has been known to happen when DRI briquettes were not adequately passivated against oxidation.

2.1.2.2 The Second Law

The law of dissipation of energy states that all natural processes occurring without external interference are spontaneous (irreversible processes). For example, heat conduction from a hot to a cold

part of the system. The spontaneous processes cannot be reversed without some change in the system brought about by external interference.

2.1.2.2.1 Entropy   The degree of degradation of energy accompanying spontaneous, hence irreversible, processes depends on the magnitude of heat generation at temperature T and temperatures between which there is heat flow.

The quantity q/T is a measure of degree of irreversibility of the process, the higher the quantity q/T, the greater the irreversibility of the process. The quantity q/T is called the increase in entropy. In a complete cycle of all reversible processes the sum of the quantities Σq/T is zero.

The thermodynamic quantity, entropy S, is defined such that for any reversible process taking place isothermally at constant pressure, the change in entropy is given by

$$dS = \frac{dH}{T} = \frac{C_p}{T} dT = C_p \, d(\ln T) \tag{2.1.19}$$

2.1.2.3 The Third Law

The heat theorem put forward by Nernst (1906) constitutes the third law of thermodynamics: 'the entropy of any homogeneous and ordered crystalline substance, which is in complete internal equilibrium, is zero at the absolute zero temperature.' Therefore, the integral of equation given above has a finite value at temperature T as shown below.

$$S_T = \int_0^T C_p d(\ln T) \tag{2.1.20}$$

The entropy of reaction is

$$\Delta S = \Sigma S(\text{products}) - \Sigma S(\text{reactants}) \tag{2.1.21}$$

and the entropy of fusion at the melting point T_m is

$$\Delta S_m = \frac{\Delta H_m}{T_m} \tag{2.1.22}$$

2.1.2.4 Gibbs Free Energy

From a combined form of the first and second laws of thermodynamics, Gibbs derived the free energy equation for a reversible process at constant pressure and temperature.

$$G = H - TS \tag{2.1.23}$$

The Gibbs free energy is also known as the chemical potential.

When a system changes isobarically and isothermally from state A to state B, the change in the free energy is

$$G_B - G_A = \Delta G = \Delta H - T\Delta S \tag{2.1.24}$$

During any process which proceeds spontaneously at constant pressure and temperature, the free energy of the system decreases. That is, the reaction is thermodynamically possible when $\Delta G < 0$. However, the reaction may not proceed at a perceptible rate at lower tempertures, if the activation energy required to overcome the resistance to reaction is too high. If $\Delta G > 0$, the reaction will not take place spontaneously.

As in the case of enthalpy, the free energy is a relative thermodynamic property with respect to the standard state, denoted by $\Delta G°$.

The variation of the standard free energy change with temperature is given by:

$$\Delta G_T° = \Delta H_{298}° + \int_{298}^T \Delta C_p dT - T\Delta S_{298}° - T \int_{298}^T \frac{\Delta C_p}{T} dT \tag{2.1.25}$$

#### 2.1.2.4.1 Generalization of Entropy Change of Reaction

1. When there is volume expansion accompanying a reaction, i.e. gas evolution, at constant pressure and temperature the entropy change is positive, hence, ΔG decreases with an increasing temperature.

$$C + CO_2 = 2CO$$
$$\Delta G° = 166,560 - 171.0TJ \tag{2.1.26}$$

2. When there is volume contraction, i.e. gas consumed in the reaction, at constant pressure and temperature the entropy change is negative, hence ΔG increases with an increasing temperature.

$$H_2 + \tfrac{1}{2}S_2 = H_2S$$
$$\Delta G° = -91,600 + 50.6TJ \tag{2.1.27}$$

3. When there is little or no volume change the entropy change is close to zero, hence temperature has little effect on ΔG.

$$C + O_2 = CO_2$$
$$\Delta G° = 395,300 - 0.5TJ \tag{2.1.28}$$
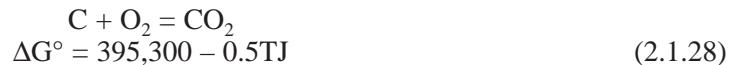
2.1.2.4.2 Selected Free Energy Data
For many reactions, the temperature dependence of $\Delta H°$ and $\Delta S°$ are similar and tend to cancel each other, thus the nonlinearity of the variation of $\Delta G°$ with the temperature is minimized. Using the average values of $\Delta H°$ and $\Delta S°$, the free energy equation is simplified to

$$\Delta G° = \Delta H° - \Delta S°T \tag{2.1.29}$$

The standard free energies of reactions encountered in ferrous metallurgical processes can be computed using the free energy data listed in Table 2.1.

2.1.3 Thermodynamic Activity

The combined statement of the first and second laws for a system doing work only against pressure gives the following thermodynamic relation.

$$dG = VdP - SdT \tag{2.1.30}$$

At constant temperature $G = VdP$ and for 1 mol of an ideal gas $V = RT/P$; with these substituted in equation (2.1.30) we obtain

$$dG = RT \frac{dP}{P} = RT \, d(\ln P) \tag{2.1.31}$$

Similarly, for a gas mixture

$$dG_i = RT \, d(\ln p_i) \tag{2.1.32}$$

where p_i is the partial pressure of the ith species in the gas mixture, and G_i partial molar free energy.

In a homogeneous liquid or solid solution, the thermodynamic activity of the dissolved element is defined by the ratio

$$a_i = \left(\frac{\text{vapor pressure of component (i) in solution}}{\text{vapor pressure of pure component}} \right)_T \tag{2.1.33}$$

In terms of solute activity, the partial molar free energy equation is

$$dG_i = RT \, d(\ln a_i) \tag{2.1.34}$$

Integration at constant temperature gives the relative partial molar free energy in solution

$$G_i = RT \ln a_i \tag{2.1.35}$$

In terms of the relative partial molar enthalpy and entropy of solution

$$\overline{G}_i = \overline{H}_i - \overline{S}_i T \qquad (2.1.36)$$

which gives

$$\ln a_i = \frac{\overline{H}_i}{RT} - \frac{\overline{S}_i}{R} \qquad (2.1.37)$$

or

$$\log a_i = \frac{\overline{H}_i}{2.303\,RT} - \frac{\overline{S}_i}{2.303\,R} \qquad (2.1.38)$$

2.1.3.1 Solutions

A solution is a homogeneous gas, liquid or solid mixture, any portion of which has the same state properties. The composition of gas solution is usually given in terms of partial pressures of species in equilibrium with one another under given conditions. For liquid solutions, as liquid metal and slag, the composition is given in terms of the molar concentrations of components of the solution.

The atom or mol fraction of the component i in solution is given by the ratio

$$N_i = \frac{n_i}{\sum n}$$

where n_i is the number of g-atoms or mols of component i per unit mass of solution, and n the total number of g-atoms or mols. Since the metal and slag compositions are reported in mass percent, n_i per 100g of the substance is given by the ratio

$$n_i = \frac{\%i}{M_i}$$

where M_i is the atomic or molecular mass of the component i.

Noting that the atomic mass of iron is 55.85g, the atom fraction of solute i in low alloy steels is given by a simplified equation

$$N_i = \frac{\%i}{M_i} \times 0.5585 \qquad (2.1.39)$$

In low alloy steelmaking, the composition of slag varies within a relatively narrow range, and the total number of g-mol of oxides per 100g of slag is within the range $\sum n = 1.6 \pm 0.1$. With this simplification, the mol fraction of the oxide in the slag is given by

$$N_i = \frac{\%i}{1.6\,M_i} \qquad (2.1.40)$$

2.1.3.1.1 Ideal Solutions – Raoult's Law:

The solutions are said to be ideal, if the activity is equal to the mol or atom fraction of the component i in solution,

$$a_i = N_i \qquad (2.1.41)$$

A thermodynamic consequence of Raoult's law is that the enthalpy of mixing for an ideal solution, $H^{M,id}$, is zero. Substituting $a_i = N_i$ and $H^{M,id} = 0$ in the free energy equation gives for the entropy of formation of an ideal solution.

$$S^{M,id} = R(N_1 \ln N_1 + N_2 \ln N_2 + N_3 \ln N_3 + ...) \qquad (2.1.42)$$

Table 2.1   The Standard Free Energies of Formation of Selected Compounds from Compiled Thermochemical Data

Notations: < > solid,   { } liquid,   ( ) gas, d decomposition, m melting, b boiling.

	$\Delta G° = \Delta H° - \Delta S°T$			
	$-\Delta H°$	$-\Delta S°$	$\Delta G°$	Temp.Range
	kJ mol^{-1}	J mol^{-1}K^{-1}	±kJ	°C
<Al> = {Al}	−10.8	11.5	0.2	660m
2{Al} + $^3/_2$(O$_2$) = <Al$_2$O$_3$>	1683.2	325.6	8	660–1700
{Al} + $^1/_2$(N$_2$) = <AlN>	328.3	115.5	4	660–1700
<C> + 2(H$_2$) = (CH$_4$)	91.0	110.7	2	25–2000
<C> + $^1/_2$(O$_2$) = (CO)	114.4	−85.8	2	25–2000
<C> + (O$_2$) = (CO$_2$)	395.3	−0.5	2	25–2000
<Ca> = {Ca}	−8.5	7.7	0.5	842m
{Ca} = (Ca)	153.6	87.4	0.5	842–1500b
{Ca} + $^1/_2$(O$_2$) = <CaO>	900.3	275.1	6	842–1500b
{Ca} + $^1/_2$(S$_2$) = <CaS>	548.1	103.8	4	842–1500b
<CaO> + <Al$_2$O$_3$> = <CaAl$_2$O$_4$>	19.1	− 17.2	8	25–1605m
<CaO> + (CO$_2$) = <CaCO$_3$>	161.3	137.2	4	25–880d
2<CaO> + <SiO$_2$> = <Ca$_2$SiO$_4$>	118.8	− 11.3	10	25–1700
<CaO> + <SiO$_2$> = <CaSiO$_3$>	92.5	2.5	12	25–1540m
<Cr> = {Cr}	−16.9	7.9	–	1857m
2<Cr> + $^3/_2$(O$_2$) = <Cr$_2$O$_3$>	1110.3	247.3	2	900–1650
<Fe> = {Fe}	−13.8	7.6	1	1537m
0.947<Fe> + $^1/_2$(O$_2$) = <Fe$_{0.947}$O>	263.7	64.3	4	25–1371m
{Fe} + $^1/_2$(O$_2$) = {FeO}	225.5	41.3	4	1537–1700
3<Fe> + 2(O$_2$) = <Fe$_3$O$_4$>	1102.2	307.4	4	25–1597m
2<Fe> + $^3/_2$(O$_2$) = <Fe$_2$O$_3$)	814.1	250.7	4	25–1500
<Fe> + $^1/_2$(S$_2$) = <FeS>	154.9	56.9	4	25–988m
{Fe} + $^1/_2$(O$_2$) + <Cr$_2$O$_3$>=<FeCr$_2$O$_4$>	330.5	80.3	2	1537–1700
2<FeO> + <SiO$_2$> = <Fe$_2$SiO$_4$>	36.2	21.1	4	25–1220m
(H$_2$) + $^1/_2$(O$_2$) = (H$_2$O)	247.3	55.9	1	25–2000
(H$_2$) + $^1/_2$(S$_2$) = (H$_2$S)	91.6	50.6	1	25–2000
$^3/_2$(H$_2$) + $^1/_2$(N$_2$) = (NH$_3$)	53.7	32.8	0.5	25–2000
{K} = (K)	−84.5	82.0	0.5	63–759b
(K) + <C> + $^1/_2$(N$_2$) = {KCN}	171.5	93.5	16	622–1132b
{KCN} = $^1/_2$(KCN)$_2$	109.2	76.7	4	622–1132b
<Mg> = {Mg}	−9.0	9.7	0.5	649m
{Mg} = (Mg)	129.6	95.1	2	649–1090b
(Mg) + $^1/_2$(O$_2$) = <MgO>	759.4	202.6	10	1090–2000
(Mg) + $^1/_2$(S$_2$) = <MgS>	539.7	193.0	8	1090–2000
2<MgO> + <SiO$_2$> = <Mg$_2$SiO$_4$>	67.2	4.3	8	25–1898m
<MgO> + <SiO$_2$> = <MgSiO$_3$>	41.1	6.1	8	25–1577m
<MgO> + (CO$_2$) = MgCO$_3$)	116.3	173.4	8	25–402d
<Mn> = {Mn}	−14.6	9.6	1	1244m
<Mn> + $^1/_2$(O$_2$) = <MnO>	391.9	78.3	4	25–1244m
{Mn} + $^1/_2$(O$_2$) = <MnO>	406.5	87.9	4	1244–1700
{Mn} + $^1/_2$(O2) = {MnO}**	352.2	61.5	4	1500–1700
** supercooled liquid below the melting point 1785°C				
<Mn> + $^1/_2$(S$_2$) = <MnS>	277.9	64.0	4	25–1244m
{Mn} + $^1/_2$(S$_2$) = <MnS>	292.5	73.6	4	1244–1530m
{Mn} + $^1/_2$(S$_2$) = {MnS}	265.0	66.1	4	1530–1700
<MnO> + <SiO$_2$) = <MnSiO$_3$)	28.0	2.8	12	25–1291m
<Mo> = {Mo}	−27.8	9.6	6	2620m
<Mo> + (O$_2$) = <MoO$_2$>	578.2	166.5	12	25–2000
<Mo> + $^3/_2$(O$_2$) = (MoO$_3$)	359.8	59.4	20	25–2000

Table 2.1 *(continued)*

	$\Delta G° = \Delta H° - \Delta S°T$			
	$-\Delta H°$ kJ mol^{-1}	$-\Delta S°$ J mol^{-1}K^{-1}	$\Delta G°$ ±kJ	Temp.Range °C
$1/2(N_2) + 3/2(H_2) = (NH_3)$	53.7	116.5	0.5	25–2000
$1/2(N_2) + 1/2(O_2) + (NO)$	−90.4	−12.7	0.5	25–2000
$1/2(N_2) + (O_2) + (NO_2)$	−32.3	63.3	1	25–2000
$\{Na\} = (Na)$	−101.3	87.9	1	98–883b
$(Na) + <C> + 1/2(N_2) = \{NaCN\}$	152.3	83.7	16	833–1530b
$2(Na) + 1/2(O_2) = \{Na_2O\}$	518.8	234.7	12	1132–1950d
$<Nb> = \{Nb\}$	−26.9	9.8	–	2477m
$2<Nb> + 1/2(N_2) = <Nb_2N>$	251.0	83.3	16	25–2400m
$<Nb> + 1/2(N_2) = <NbN>$	230.1	77.8	16	25–2050m
$2<Nb> + 5/2(N_2) = <Nb_2O_5>$	1888.2	419.7	12	25–1512m
$<Ni> = \{Ni\}$	−17.5	10.1	2	1453m
$<Ni> + 1/2(O_2) = <NiO>$	235.6	86.1	2	25–1984m
$<Ni> + 1/2(S_2) = <NiS>$	146.4	72.0	6	25–600
$3<Ni> + (S_2) = <Ni_3S_2>$	331.5	163.2	8	25–790m
$1/2(S_2) + (O_2) = (SO_2)$	361.7	72.7	0.5	25–1700
$<Si> = \{Si\}$	−49.3	30.0	2	1412m
$\{Si\} + 1/2(O_2) = (SiO)$	154.7	−52.5	12	1412–1700
$<Si> + (O_2) = <SiO_2>$	902.3	172.9	12	400–1412m
$\{Si\} + (O_2) = <SiO_2>$	952.5	202.8	12	1412–1723m
$<Ti> = \{Ti\}$	−18.6	9.6	–	1660m
$<Ti> + 1/2(N_2) = <TiN>$	336.3	93.3	6	25–1660m
$<Ti> + (O_2) = <TiO_2>$	941.0	177.6	2	25–1660m
$<V> + \{V\}$	−22.8	10.4	–	1920m
$<V> + 1/2(N_2) = <VN>$	214.6	82.4	16	25–2346d
$2<V> + 3/2(O_2) = <V_2O_3>$	1202.9	237.5	8	25–2070m
$\{Zn\} = (Zn)$	−118.1	100.2	1	420–907b
$(Zn) + 1/2(O_2) = <ZnO>$	460.2	198.3	10	907–1700
$\{Zn\} + 1/2(S_2) = <ZnS>$	277.8	107.9	10	420–907b
$(Zn) + 1/2(S_2) = (ZnS)$	−5.0	30.5	10	1182–1700
$<Zr> = \{Zr\}$	−20.9	9.8	–	1850m
$<Zr> + 1/2(N_2) = <ZnN>$	363.6	92.0	16	25–1850m
$<Zr> + (O_2) = <ZrO_2>$	1092.0	183.7	16	25–1850m
$<Zr> + (S_2) = <ZrS_2>$	698.7	178.2	20	25–1550m
$<ZrO_2> + <SiO_2> = <ZrSiO_4>$	26.8	12.6	20	25–1707m

* References to the compiled thermochemical data used in deriving $\Delta H°$ and $\Delta S°$ values are given in Ref. 27 cited in Section 2.2.2.4
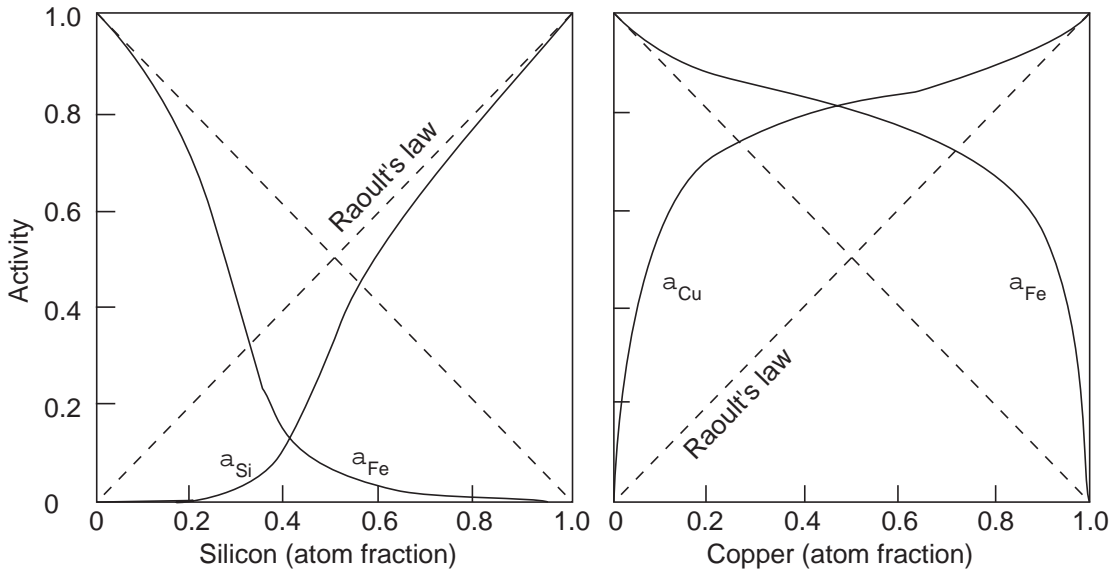
Fig. 2.1 Activities in liquid Fe–Si and Fe–Cu alloys at 1600°C showing strong negative and positive departures from Raoult's law.

2.1.3.1.2 Nonideal Solutions Almost all metallic solutions and slags exhibit nonideal behavior. Depending on the chemical nature of the elements constituting a solution, the activity vs composition relation deviates from Raoult's law to varying degrees, as demonstrated in Fig. 2.1 for liquid Fe–Si and Fe–Cu systems at 1600°C.

2.1.3.2 Activity Coefficient

The activity coefficient of solute i is defined by the ratio

$$\gamma_i = \frac{a_i}{N_i} \tag{2.1.43}$$

If the activity is relative to the pure component i, it follows from Raoult's law that as $N_i \rightarrow 1$, $\gamma \rightarrow 1$.

2.1.3.2.1 Henry's Law for Dilute Solutions In infinitely dilute solutions, the activity is proportional to the concentration

$$\boldsymbol{a}_i = \gamma_i^\circ N_i \tag{2.1.44}$$

The approach to Henry's law at dilute solutions is demonstrated in Fig. 2.2 for the activity of carbon (relative to graphite) in austenite at 1000°C. The austenite containing 1.65%C ($N_C = 0.072$) is saturated with graphite at 1000°C for which the carbon activity is one relative to graphite.

Since Henry's Law is valid at infinite dilution only, the ration γ_i/γ_i° is used as a measure of departure from Henry's Law for finite solute contents in dilute solutions. For solute concentration in terms of mass percent, Henry's activity coefficient is defined by the ratio
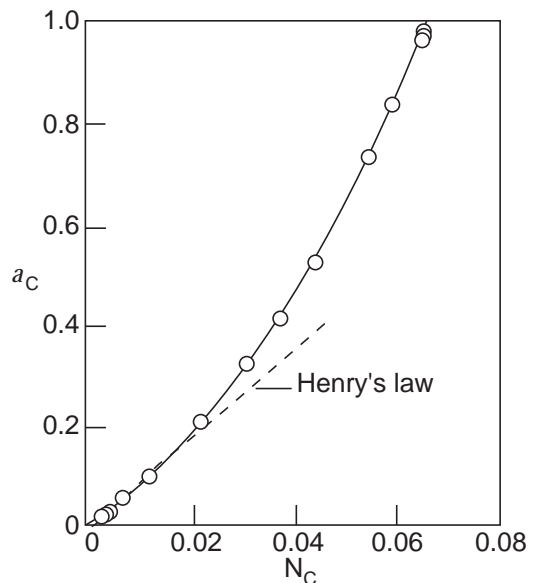
Fig. 2.2 Activity of carbon in austenite (relative to graphite) at 1000°C, demonstrating deviation from Henry's law.

$$f_i = \frac{\gamma_i}{\gamma_i^\circ} \tag{2.1.45}$$

such that $f_i \to 1$ when $\%i \to 0$.

2.1.3.2.2 Interaction Coefficients   Over several mass percentages of the solute, the composition dependence of activity coefficient f_i of solute i in binary systems is represented by the following relation in terms of mass $\%i$.

$$\log f_i = e_i^i[\%i] \tag{2.1.46}$$

where e is called the solute interaction coefficient. For multi-component solutions, the following summation is used

$$\log f_i = e_i^i[\%i] + \Sigma e_i^j[\%j] \tag{2.1.47}$$

where e_i^j is the effect of the alloying element j on the activity coefficient of solute i.

2.1.3.3 Conversion from One Standard State to Another

In steelmaking processes we are concerned with reactions involving dissolved elements at low concentrations in liquid steel. Therefore, it is convenient to express the solute activity relative to Henry's law. The free energy change accompanying the isothermal transfer of solute from state A to state B is

$$\Delta G = RT \ln\left(\frac{a_B}{a_A}\right) \tag{2.1.48}$$

Taking a pure component for state A, i.e. $a_A = 1$ and Henry's law for state B, i.e. $a_B = \gamma_i^\circ N_i$

$$\Delta G = RT \ln(\gamma_i^\circ N_i) \tag{2.1.49}$$

For one mass percent solute in iron,

$$N_i \approx \frac{0.5585}{M_i} \tag{2.1.50}$$

where M_i is the atomic mass (g) of the solute. Assuming that Henry's law holds at 1 mass %, the standard free energy of solution of pure component i in iron at 1 mass % is

$$\Delta G_s = RT \ln\left(\frac{0.5585}{M_i}\gamma_i^\circ\right) \tag{2.1.51}$$

Since Henry's law is valid at infinite dilution only, appropriate correction must be made for non-ideal behavior when using the above equation.

2.1.4 Reaction Equilibrium Constant

Let us consider the following reaction equilibrium occurring at constant temperature and pressure.

$$mM + nN = uU + vV \tag{2.1.52}$$

The state of equilibrium is defined by the following thermodynamic relation involving the activities of reactants M and N and the activities of the products U and V.

$$K = \frac{(a_U)^u (a_V)^v}{(a_M)^m (a_N)^n} \tag{2.1.53}$$

where the equilibrium constant K can be derived from the standard free energy change accompanying the reaction thus,

$$\Delta G^\circ = -RT \ln K \tag{2.1.54}$$

Since $\Delta G°$ is a function of temperature only, the equilibrium constant is also a function of temperature only.

$$\ln K = -\frac{\Delta G°}{RT} \qquad (2.1.55)$$

In terms of enthalpy and entropy changes

$$\ln K = -\frac{\Delta H°}{RT} + \frac{\Delta S°}{R} \qquad (2.1.56)$$

In exothermic reactions ΔH is negative, therefore the equilibrium constant K decreases with an increasing temperature. The temperature effect on K is the opposite in endothermic reactions.

For $\Delta G°$ in J, R = 8.314 J mol⁻¹K⁻¹ and substituting log for ln,

$$\log K = -\frac{\Delta G°}{19.144\,T} \qquad (2.1.57)$$

As an example, let us consider the following reaction equilibrium between liquid slag and low alloy steel.

$$(MnO) + [C] = [Mn] + CO(g) \qquad (2.1.58)$$

where the parenthesis ( ) and [ ] represent respectively the oxides dissolved in slag and elements dissolved in iron. From the free energy data in Table 2.1 and those in Table 2.8 in section 2.4 for the dissolution of graphite and liquid manganese in liquid iron, the standard free energy change accompanying reaction 2.1.58 is

$$\Delta G° = 230,560 - 147.32T\,J \qquad (2.1.59)$$

which gives for the equilibrium constant K

$$\log K = -\frac{12,043}{T} + 7.695 \qquad (2.1.60)$$

$$K = \frac{[\%Mn]\,p_{CO}}{(a_{MnO})[\%C]} \qquad (2.1.61)$$

where p_{CO} is in atm, the oxide activity is with respect to pure molten MnO and at low concentrations, the mass percentages of Mn and C in the steel are essentially equivalent to their activities, i.e. f_{Mn} and f_C are close to unity.

For a steelmaking slag of basicity 3.0 containing 5% MnO, $a_{MnO} = 0.088$; at 1600°C the equilibrium constant is K = 18.42 for which equation 2.1.61 gives for the slag-metal equilibrium [%Mn]/[%C] = 1.62 at 1 atm pressure of CO.

2.2 Rate Phenomena

There are many different facets of rate phenomena involving homogeneous or heterogeneous chemical reactions, mass transfer via atomic or molecular diffusional processes, viscous flow, thermal and electrical conduction and so on. The concepts of diffusion, mass transfer and chemical kinetics presented briefly in this section of Chapter 2, are confined to cases which are relevant to the study of the rates of reactions in the iron and steelmaking processes.

2.2.1 Diffusion

2.2.1.1 Fick's Diffusion Laws

The first law is for the steady state diffusion.

The quantity of diffusing substance which passes per unit time through unit area of a plane perpendicular to the direction of diffusion, known as the flux J, is proportional to the concentration gradient of the diffusing substance

$$J = -D \frac{dC}{dx} \tag{2.2.1}$$

The coefficient D is the diffusivity of the substance in the medium; C is the concentration of the substance per unit volume and x the distance in the direction of diffusion.

The second law is for the nonsteady state diffusion.

The rate of accumulation of diffusing substance in a given volume element is the difference between the inward and outward flux. In other words, what goes in and does not come out, stays there.

The rate of concentration change −dC/dt resulting from flux over a distance dx is

$$J = -\frac{dC}{dt} dx \tag{2.2.2}$$

Hence, the change in flux with distance is

$$\frac{dJ}{dx} = -\frac{dC}{dt} \tag{2.2.3}$$

Invoking the first law and re-arranging gives the second law.

$$\frac{dJ}{dx} = -\frac{d}{dx}\left(D\frac{dC}{dx}\right)$$
$$\frac{dC}{dt} = D\frac{d^2C}{dx^2} \tag{2.2.4}$$

The solution of this equation depends on the geometry and on the boundary conditions of the medium in which the dissolved substance is diffusing.

2.2.1.2 Chemical and Self-Diffusivities

There are two kinds of diffusivities:

(i) The chemical diffusivity is the coefficient of diffusion defined by Fick's law $D_i = -J_i(\partial C/\partial x)$ for the single diffusing species i.

(ii) The self-diffusivity is the coefficient of diffusion measured in a homogeneous medium with the radioactive or stable isotope (tracer) of the diffusing species. The self-diffusion is a consequence of random movements of atoms or molecules.

For an ideal solution, or an infinitely dilute solution, we have the equality

$$D_i = D_i^* \tag{2.2.5}$$

For nonideal solutions in general (ionic or metallic), Onsager and Fuoss[1] derived the following relation for the chemical diffusivity corrected for departure from ideal behavior.

$$D_i = D_i^*\left(\frac{\partial \ln a_i}{\partial \ln C_i}\right) = D_i^*\left(1 + \frac{\partial \ln \gamma_i}{\partial \ln C_i}\right) \tag{2.2.6}$$

where a_i is the activity and γ_i the activity coefficient of the single diffusing species i.

2.2.1.3 Types of Diffusional Processes

There are various types of diffusional processes, depending on the medium in which the diffusion occurs.

2.2.1.3.1 Diffusion in Molten Slags and Glasses   Because of the ionic nature of the medium, the diffusion in molten slags and glasses is by the ions. The ionic conduction is a purely random jump

process. For the limiting case of purely free and random movements of ions, the self-diffusivity of the ionic species i is related to the electrical conductivity λ_i by the Nernst-Einstein[2] equation

$$D_i^* = \frac{RT}{F^2 Z_i^2 C_i} \lambda_i \qquad (2.2.7)$$

where Z_i is the valence and C_i the concentration (mol cm^{-3}) of the species i and F = 96,489 C mol^{-1} the Faraday constant.

Reference may be made to a previous publication by Turkdogan[3] on the review of interrelations between ionic diffusion and conduction in molten slags.

2.2.1.3.2 Diffusion in Porous Media   The rate of a heterogeneous reaction between a gas and a porous medium is much affected by the counter-diffusive flow of gaseous reactants and products through the pores of the medium. There are two types of effective gas diffusivities, depending on the pore structure of the medium:

   (i) Molecular diffusivity in large pores and at ordinary to high pressures.

   (ii) Knudsen diffusivity in small pores and at low pressures.

The pore diffusion is discussed in more detail in Section 2.3.

2.2.1.3.3 Eddy Diffusivity   The mass transfer occurring within a turbulent fluid flow is characterized by the diffusion coefficient called eddy diffusivity which is a function of the time-averaged and fluctuating velocity components in turbulent flow. This subject is covered in detail in a text book on fluid phenomena by Szekely[4].

2.2.2 Mass Transfer

In high temperature processes as in pyrometallurgy, the rates of interfacial chemical reactions are in general much faster than the rates of transfer of the reactants and reaction products to and from the reaction site. The formulations of rate equations for transport controlled reactions vary considerably with the physical properties and type of fluid flow over the surface of the reacting condensed phase. Then, there are formulations of rate equations for different regimes of gas bubbles in liquid metal and slag. For a comprehensive discussion of the transport controlled rate phenomena in metallurgical processes, reference may be made to textbooks by Szekely and Themelis[5] and by Geiger.[6]

There are numerous computer software packages, as for example PHOENICS, FLUENT, CFDS-FLOWS3D, GENMIX, TEACH(2D, 3D), 2E/FIX, SOLA/VOF, METADEX(R) and FID, which are used in the steel industry in the process and design engineering of plant facilities and in the control of steelmaking processes. References may also be made to the publications by Szekely *et al.*[7-9] on the mathematical and physical modelling of metallurgical processes involving fluid flow, heat transfer, mass transfer and gas-slag-metal reactions.

There are of course many other publications on this subject which cannot all be cited here as the subject matter is well outside the scope of this book.

The rate phenomena discussed in this chapter are on chosen subjects which are pertinent to various aspects of ferrous-pyrometallurgical processes, in addition to oxygen steelmaking, ladle refining and degassing.

2.2.2.1 Parabolic Rate of Oxidation of Iron

The scale forming in the oxidation of iron, or low alloy steels, consists of three layers of oxides: wustite on the iron surface followed by magnetite then hematite on the outer surface of the scale. From several experimental studies it was found that the average wustite:magnetite:hematite thickness ratios were about 95:4:1. In iron oxides, the diffusivity of iron is greater than the oxygen

diffusivity. The rate of oxidation is controlled primarily by diffusion of iron through the wustite layer from the iron-wustite interface to the wustite-gas or wustite-magnetite interface, then through the thin layers of magnetite and hematite.

$$X^2 = \lambda t \qquad (2.2.8)$$

where λ is the parabolic rate constant, cm^2 (scale) s^{-1}

If the measurement of the rate of oxidation is made by the thermogravimetric method, then the parabolic rate constant k_p would be in units of $(gO)^2 cm^{-4} s^{-1}$. From the compositions and densitites of the oxides, with the relative thickness ratios of wustite:magnetite:hematite = 95:4:1, the values of k_p and λ are related as follows.

$$k_p \ (gO)^2 \ cm^{-4} \ s^{-1} = 1.877\lambda, \ cm^2 \ (scale) \ s^{-1} \qquad (2.2.9)$$

Many experimental studies have been made of the rate of oxidation of iron in air and oxygen at temperatures 600 to 1300°C. The temperature dependence of the parabolic rate constant is shown in Fig. 2.3; the references to previous studies denoted by different symbols are given in a paper by Sheasby *et al.*[10]

From theoretical considerations, Wagner[11] derived the following equation for the parabolic rate constant in terms of the activity of oxygen and self-diffusivities of the mobile species in the scale. For the case of wustite with $D^*_{Fe} \gg D^*_O$ Wagner's equation is simplified to

$$\lambda = 2 \int_{a'_O}^{a''_O} \frac{N_O}{N_{Fe}} D^*_{Fe} \, d(\ln a_O) \qquad (2.2.10)$$
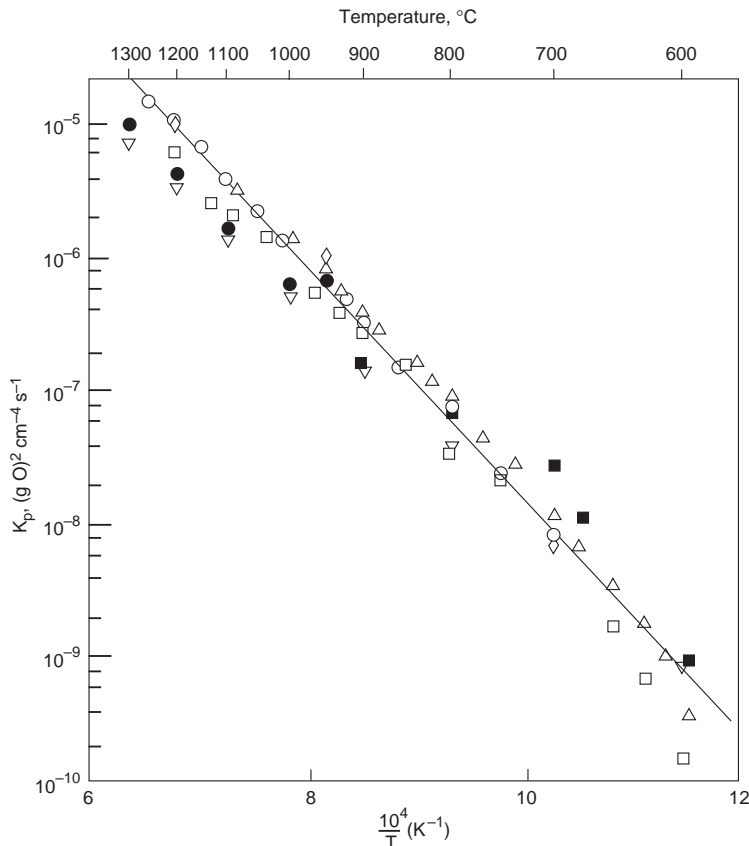
Fig. 2.3 Temperature dependence of the parabolic rate constant for oxidation of iron in air or oxygen with or without H_2O. *From Ref. 10.*
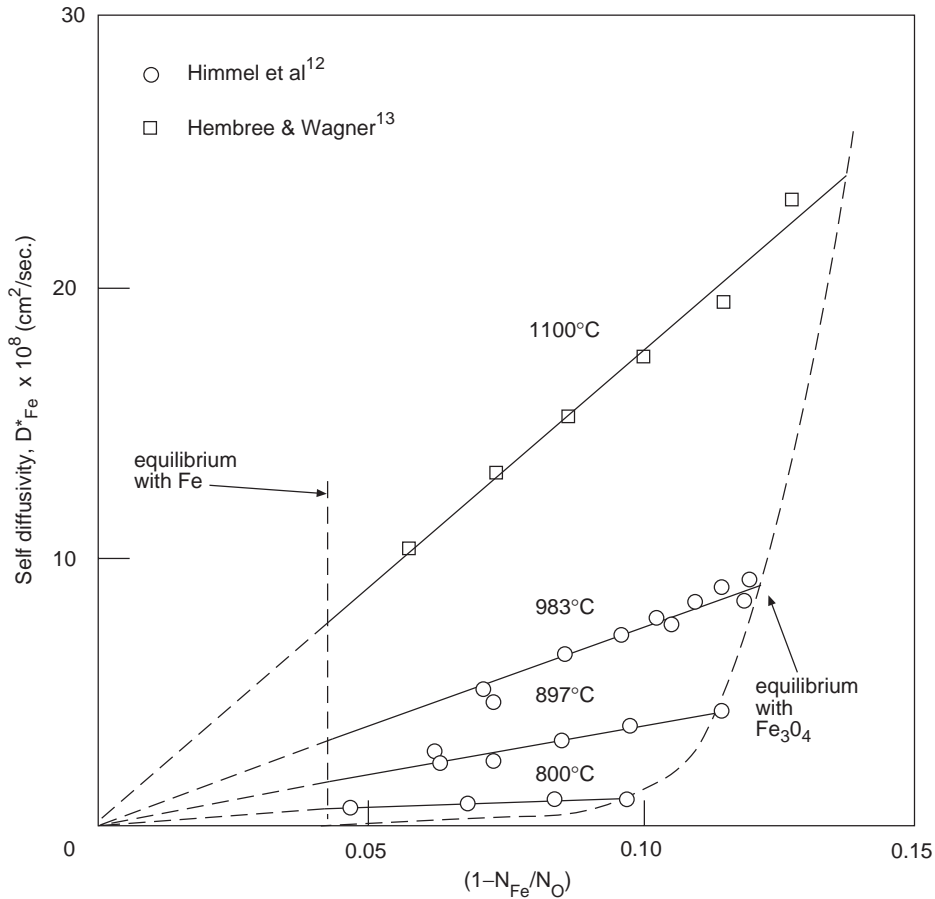
Fig. 2.4 Self-diffusivity of iron as a function of $(1 - N_{Fe}/N_O)$ fraction of iron deficiency.

where a_O and a'_O are oxygen activities at the iron-wustite and wustite-magnetite interfaces, respectively. The diffusion of iron ions in the nonstoichiometric phase wustite Fe_XO, is via the cation vacant sites in the wustite lattice. It is for this reason that the self-diffusivity of iron increases with an increasing O/Fe atom ratio in wustite, i.e. with increasing iron deficiency, as shown in Fig. 2.4

The values of $k_p = 1.877\lambda$ calculated from the measured tracer diffusivity of iron using Wagner's equation, are consistent with the average experimental values in Fig. 2.3 which is represented by the following equation.

$$\text{Log}\, k_p = -\frac{8868}{T} + 0.9777 \qquad (2.2.11)$$

2.2.2.2 Oxidation of Carbon in CO_2–CO Mixtures

Most forms of carbon are porous, therefore the rate of oxidation, i.e. gasification of carbon, is decisively affected by the pore structure, internal pore surface area, effective gas diffusivity in the pores and particle size.

In a critical review of the oxidation of carbon, Walker *et al.*[14] gave a detailed and a comprehensive account of (up to 1959) experimental and theoretical studies on this subject. In the late 1960s, Turkdogan and co-workers[15–17] pursued further experimental work on the oxidation of several types of carbon in CO_2–CO mixtures at temperatures up to 1300°C and at pressures of 0.01 to 10 atm. A few salient features of their findings are briefly given here.

Depending on the particle size, pore structure, temperature and gas pressure, there is either complete internal burning or external burning of carbon. The rate equations are of the following forms for these two limiting cases:

(i) For small porous carbon particles and at low temperatures and pressures, there is rapid counter current pore diffusion of CO_2 and CO, and the rate of oxidation is controlled by the chemical kinetics on the pore walls of the carbon. For this limiting case of complete internal burning, the rate equation is

$$\ln(1 - F) = -\phi SC_i t \tag{2.2.12}$$

where

$$
\begin{aligned}
F &= \text{the mass fraction of carbon oxidized,} \\
\phi &= \text{specific isothermal rate constant of chemical reaction per unit area of the pore wall,} \\
S &= \text{connected internal pore surface area per unit mass } cm^2 mol^{-1}, \\
C_i &= \text{molar concentration of } CO_2 \text{ per } cm^3 \text{ in the gas stream,} \\
t &= \text{oxidation time}
\end{aligned}
$$

(ii) For large carbon particles and at high temperatures and pressures, the gas diffusion is confined to the pore mouths on the surface of the carbon particle. For this limiting case of external burning the rate equation is

$$1 - (1 - F)^{\frac{1}{3}} = \frac{(\phi \rho SD_e)^{\frac{1}{2}}}{\rho r_o} C_i t \tag{2.2.13}$$

where

$$
\begin{aligned}
D_e &= \text{effective } CO_2\text{–CO pore diffusivity,} \\
\rho &= \text{molar bulk density of the carbon,} \\
r_o &= \text{initial radius of carbon particle.}
\end{aligned}
$$

The effects of the particle size and gas pressure on the rate of oxidation of electrode graphite is shown in Fig. 2.5

A mathematical analysis was made by Tien and Turkdogan[18] to formulate the pore diffusion effect on partial internal burning of relatively large carbon particles. The experimentally determined initial rates of oxidation of coke and graphite spheres ($\approx$ 2 cm dia.) in 1:1 CO_2:CO mixture at 1 atm pressure are compared in Fig. 2.6 with the
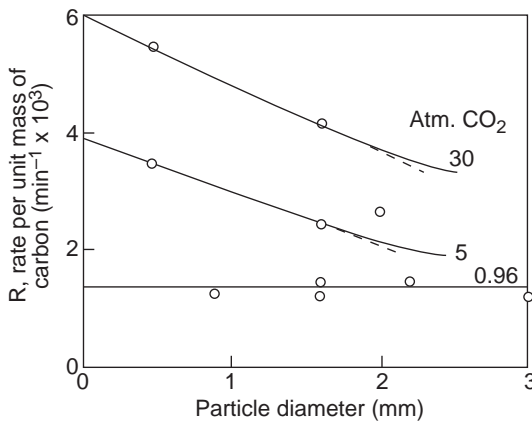
Fig. 2.5 Effect of particle size on the rate of oxidation of electrode graphite in pure carbon dioxide at 1000°C. *From Ref. 16.*
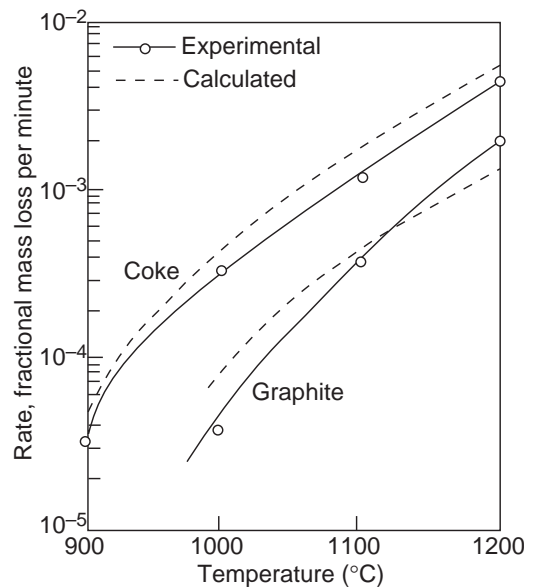
Fig. 2.6 Effect of temperature on rate of oxidation of coke and graphite (1.9 and 2.2 cm dia. spheres, respectively) in 50:50 CO_2:CO at 1 atm. *From Ref. 18.*
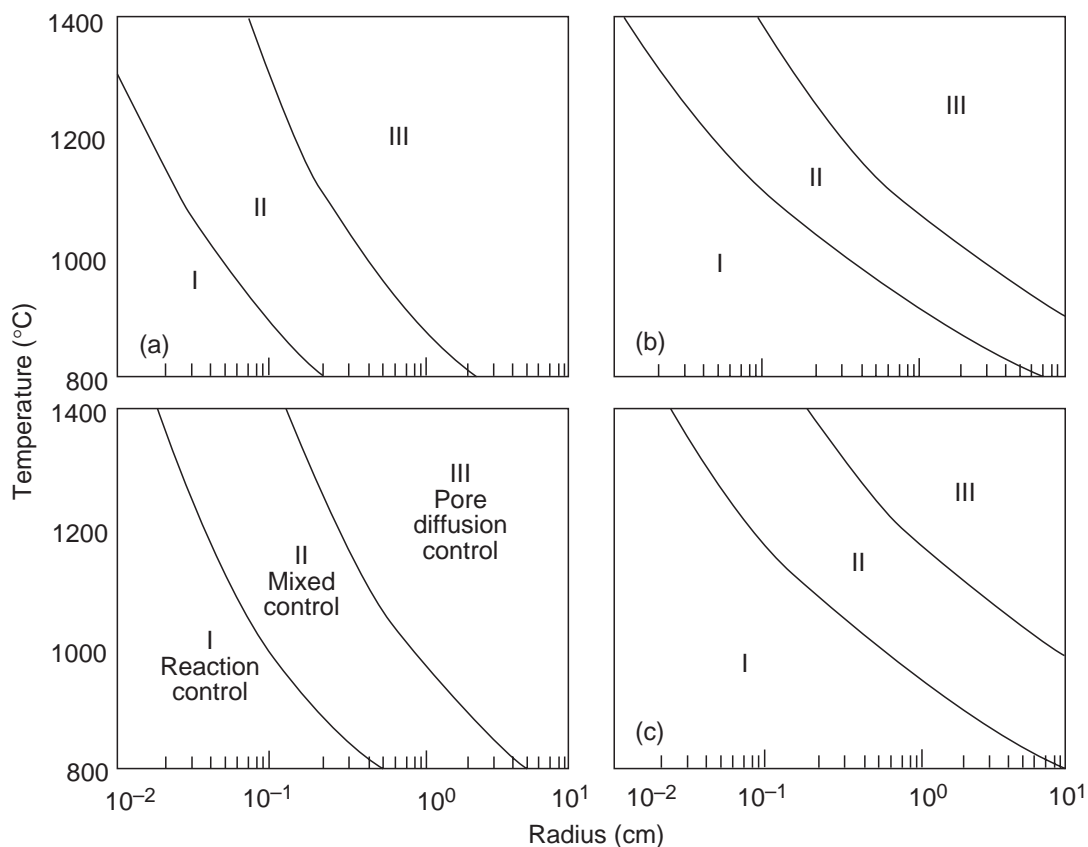
Fig. 2.7 Critical radius and temperature for the limiting rate controlling processes at 1 atm pressure. (a) Coke, 100% CO_2; (b) Coke, 1:1 $CO:CO_2$; (c) Graphite, 100% CO_2; (d) Graphite, 1:1 $CO:CO_2$. *From Ref. 18.*

values calculated from the mathematical analysis, which is summarized in Fig. 2.7. In each diagram, the lower curve is for 80% internal burning; therefore, in the region below this curve there is almost complete pore diffusion. The upper curve is for 20% internal burning; therefore, in the region above this curve, the pore diffusion control predominates.

Reference should also be made to a paper by Aderibigbe and Szekely[19] for a more detailed mathematical formulation of the rate of pore-diffusion and reaction controlled gasification of metallurgical coke in CO_2–CO mixtures.

2.2.2.3 Reduction of Iron Oxides

In view of its practical importance to the understanding and control of ironmaking processes, a great deal of research has been done on the gaseous reduction of iron oxides and iron ores. Because of the porous nature of iron oxides and the reduction products, the interpretation of the reduction rate data is inherently complex.

The formation of product layers during the gaseous reduction of dense sintered hematite and magnetite pellets or natural dense iron ore particles is a well-known phenomenon, as shown in Fig. 2.8.

In several studies made in the early 1960s[20–22] it was found that the thickness of the reduced iron layer, encasing the iron oxide core of the pellet, increased linearly with the reduction time. The measured rates were interpreted in terms of the rate-controlling chemical reaction at the iron wustite interface; the diffusive fluxes of gases through the porous layers were assumed to be relatively fast. On the other hand, Warner[23] and Spitzer *et al.*[24] have expressed the view that the rate of gaseous reduction is much affected by the gaseous diffusional processes, e.g. the gas-film resistance at the
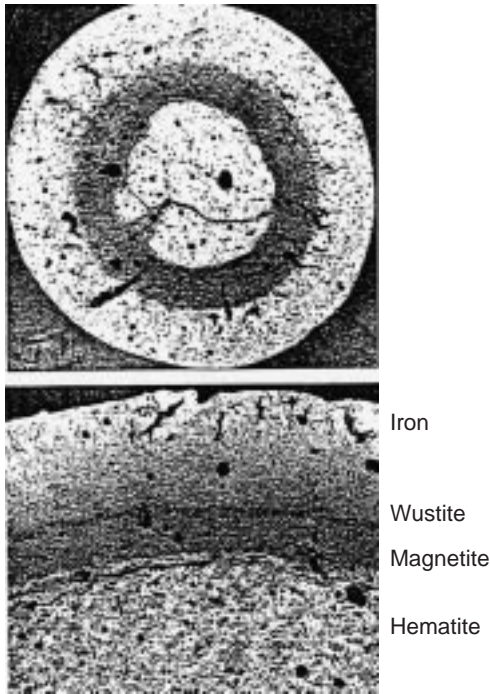
Fig. 2.8 Formation of reaction product layers in the gaseous reduction of hematite pellets.

pellet surface and particularly the resistance to diffusion in the porous product layers. The rate measurements made by Turkdogan and Vinters[25] on the reduction of hematite pellets in H_2–H_2O and CO–CO_2 mixtures have clearly demonstrated that the rate-controlling effects of gas diffusion into the pores of the oxide granules or pellets and through the porous iron layer dominate the reaction kinetics.

The sketch in Fig. 2.9 demonstrates three limiting rate controlling processes as outlined below.

(a) With fine granules there is internal reduction producing rosettes or platelets of metallic iron within the oxide particle; the rate in terms of mass fraction reduced, F, is independent of particle size.

(b) With large and dense oxide particles and at high temperatures, the gas diffusion is slow and the reaction is confined essentially to pore mouths on the outer surface of the particle, bringing about the development of a porous iron layer around the pellet. Because of the layer formation, this mode of reduction is often called topochemical reduction. In the early stages of reduction, the porous iron layer is sufficiently thin for rapid gas diffusion, therefore the initial rate of reduction is controlled jointly by (i) gas diffusion into the pore mouths of the oxide and (ii) reaction on the pore walls of the wustite.

$$\frac{dF}{dt} \propto \frac{\sqrt{\phi S D_e}}{r} \qquad (2.2.14)$$

(c) When the porous iron layer becomes sufficiently thick, the rate of reduction will be controlled essentially by the counter current gas diffusion (H_2–H_2O and CO–CO_2) for which the limiting rate equation, for a given temperature is as follows.

$$\left[3 - 2F - 3(1-F)^{2/3}\right] = Y = \frac{D_e}{\rho r^2}\left(\frac{p_i - (p_i)_{eq}}{RT}\right)t + C \qquad (2.2.15)$$
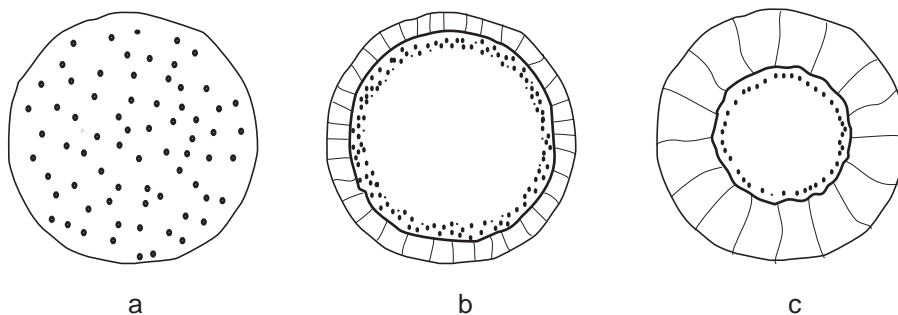
Fig. 2.9 Schematic representation of (a) uniform internal reduction of wustite to iron, (b) limiting mixed control (partial internal reduction) and (c) diffusion in porous iron as the rate-controlling step.

where p_i is the H_2 or CO partial pressure in the gas stream and $(p_i)_{eq}$ that for the iron-wustite equilibrium and C a constant (a negative number) that takes account of all early time departures from the assumed boundary conditions for this limiting case.

(d) At high reduction temperatures, with large oxide pellets and low velocity gas flows, the rate of reduction is controlled primarily by mass transfer in the gas-film layer at the pellet surface. In this limiting case the rate is inversely proportional to the square of the particle diameter.

The experimental data are given Fig. 2.10 showing the particle size effect on the initial rate of reduction of hematite granules or pellets in hydrogen.

When the thickness of the reduced porous iron layer exceeds 1 mm, the subsequent rate of reduction is controlled primarily by gas diffusion through the porous iron layer. The reduction data plotted in accord with equation 2.2.15 usually give elongated S-shaped curves as in Fig. 2.11 for 15 mm diameter spheroidal hematite ore reduced in H_2 at 1 atm. From about 50% to 95% or 99% reduction, data are well represented by straight lines. The effective H_2–H_2O diffusivities in the pores of the iron layer are derived from the slopes of the lines; details are given in Section 2.3.3.

The effect of reaction temperature on the pore surface area of iron and wustite formed by the reduction of hematite is shown in Fig. 2.12. The higher the reduction temperature, the smaller the internal pore surface area, i.e. the coarser the pore structure. The iron oxides reduced at temperatures below 800°C are known to be pyrophoric, which is a consequence of a fine pore structure with a large pore surface area as noted from the data in Fig. 2.12.
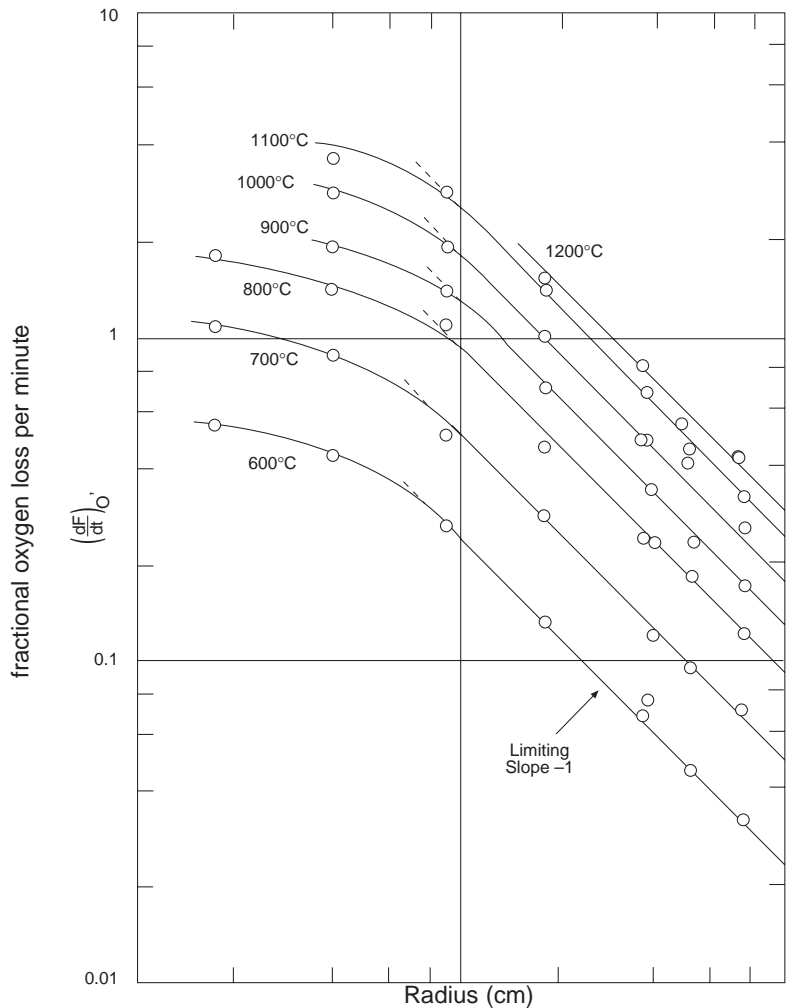
Fig. 2.10 Initial rate in hydrogen at 0.96 atm. as a function of particle radius at indicated temperatures. *From Ref. 25.*
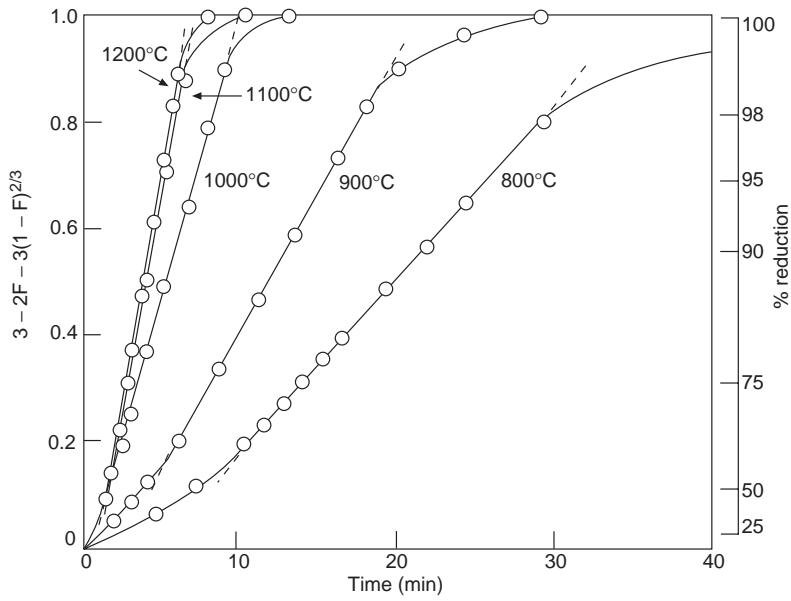
Fig. 2.11 Diffusion plot of reduction data for 15 mm diameter spheroidal hematite ore. *From Ref. 25.*
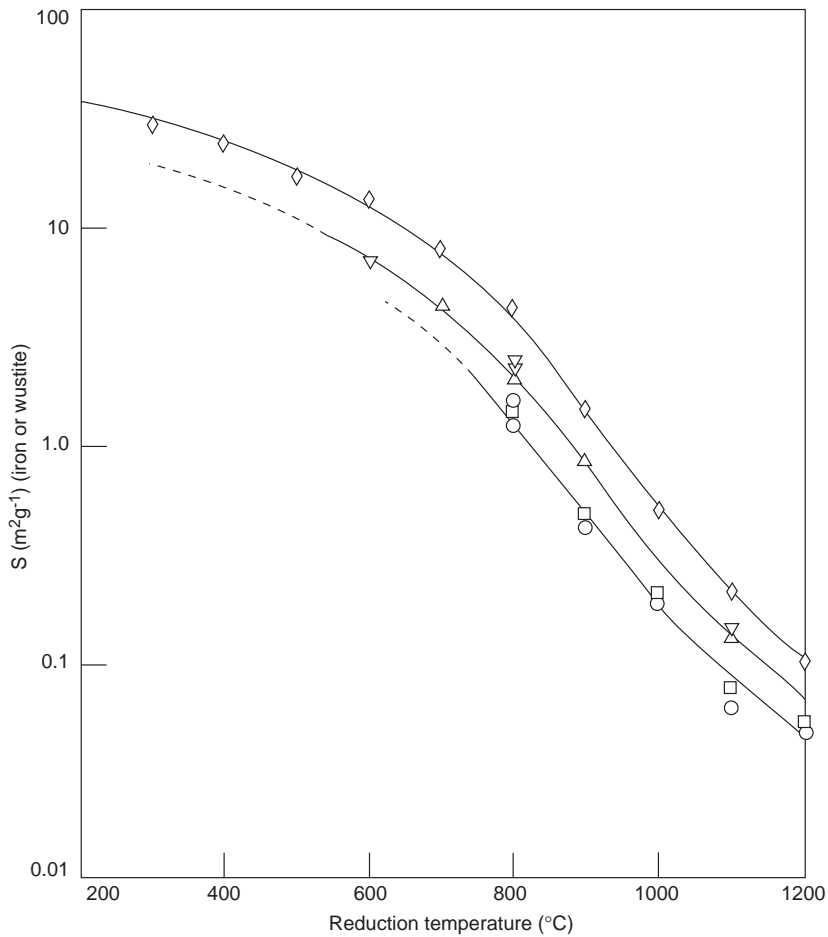
Fig. 2.12 Connected internal pore surface area of iron and wustite formed by reduction of hematite ores' A and B; (a) ore A reduced to iron in H_2 (◊); (b) ore B reduced to iron in H_2(▽) and reduced to wustite in an H_2–H_2O mixture (△); (c) ore B reduced to iron in a CO–CO_2 mixture (❑) and reduced to wustite in another CO–CO_2 mixture (○). *From Ref. 25.*

2.2.2.4 Mass Transfer with Gas Bubbles in Oxygen Steelmaking

In most practical applications of gas injection into liquids, we are concerned mainly with rates of reactions in the swarm of bubbles. Mass-transfer phenomena in the swarm of bubbles have been studied extensively with aqueous solutions; accumulated knowledge is well documented in a review paper by Calderbank.[26] Also, several studies have been made of the bubble size and velocity of rise of single bubbles in liquid metals. Szekely presented a comprehensive review of these studies in his book on *Fluid Flow Phenomena in Metals Processing*.[4]

In his recent book *Fundamentals of Steelmaking*, Turkdogan[27] made an assessment of the size range of dispersed gas bubbles and the corresponding mass transfer in liquid steel for the conditions prevailing in the BOF and Q-BOP steelmaking processes. In this assessment, the bubbles are assumed to be generated from a multitude of points across the bottom of the vessel, as though the entire vessel bottom were in fact one big porous plug.

2.2.2.4.1 Gas Holdup and Superficial Gas Velocity
The volume fraction of gas holdup (ε) is given by the following ratio:

$$\varepsilon = \frac{V_b}{V_b + V_s} = 1 - \frac{V_s}{HA} \tag{2.2.16}$$

where

$$
\begin{aligned}
V_b &= \text{transitory bubble volume in the bath at any time,} \\
V_s &= \text{steel volume in the vessel,} \\
H &= \text{average bath depth,} \\
A &= \text{average bath cross sectional area.}
\end{aligned}
$$

The velocity of bubble rise, U_b, in a swarm of bubbles is given by the ratio

$$U_b = \frac{U_s}{\varepsilon} = \frac{\dot{V}}{\varepsilon A} \tag{2.2.17}$$

where

$$
\begin{aligned}
\dot{V} &= \text{gas flow rate,} \\
U_s &= \text{superficial gas velocity.}
\end{aligned}
$$

In the studies of Calderbank and co-workers[26] with the air-water system, the gas was injected into the column of water through a sieve plate on the bottom of the column. The fractional holdup of gas was reported as shown in Fig. 2.13. The units in F factor are U_s, m s^{-1} and ρ_g (the gas density), kg m^{-3}.

The dot-dash curve is taken to represent the average values. It appears that at $F \geq 1$, the gas holdup reaches an essentially constant value of $\varepsilon = 0.6$.

In the estimation of fractional gas holdup in the steel bath, during decarburization or argon stirring, the gas flow rates taken are for the melt temperature and average gas bubble pressure. The values used are for 1600°C and 1.5 atm so that $\dot{V}_T(\text{m}^3\text{s}^{-1}) = 4.57 \times \dot{V}_o(\text{Nm}^3\text{s}^{-1})$; for these conditions the gas densities are 0.27 kg m^{-3} for N_2 and CO and 0.39 kg m^{-3} for Ar; an average value is used, $\rho_g = 0.33$ kg m^{-3}.

The average bath cross sectional area A in BOF or Q-BOP vessel increases with an increasing gas flow rate. Keeping in mind the inner dimensions of the BOF or Q-BOP vessel for 200-240 ton heats, the area values used are: A = 22 m^2 at $\dot{V}_T = 60$ m^{3}s^{-1} decreasing to A = 16 m^2 at $\dot{V}_T = 1$ m^{3}s^{-1}. On this basis, the following equation is obtained for the superficial gas velocity U_s as a function of $\dot{V}_T$.

$$U_s\left(\text{m s}^{-1}\right) = \frac{\dot{V}_T}{14.55 + 0.089\,\dot{V}_T} \tag{2.2.18}$$

The volume fraction gas holdup and bubble velocity of rise calculated using equation 2.2.18 and Fig. 2.13 are plotted in Fig. 2.14 as a function of the gas flow rate. The gas holdup in the slag layer is a more complex phenomenon, because of slag foaming and injection of large amounts of steel droplets into the slag layer during decarburisation with oxygen blowing.

2.2.2.4.2 Estimation of Bubble Size for Uniformly Dispersed Bubbles in the Steel Bath

Many estimates were made in the past of gas bubble diameters in steelmaking processes, the estimates varying over a wide range from 1 to 8 cm or more. Bubbles with diameters >1cm acquire a spherical cap shape as they rise in liquids. The apparent diameter is that of a sphere which has a volume equivalent to that of the spherical cap shaped bubble.

Calderbank and co-workers[26] and Leibson *et al.*[28] have found that in aqueous solutions the bubble size becomes smaller with an increasing gas flow rate, ultimately reaching a minimum size of about 0.45 cm diameter at large gas flow rates. Relatively large gas bubbles in motion are subject to deformation and ultimately to fragmentation into smaller bubbles. The drag force exerted by the liquid on a moving bubble induces rotational and probably a turbulent motion of the gas within the bubble.

This motion creates a dynamic pressure on the bubble surface; when this force exceeds the surface tension, bubble breakup occurs. Because of the large difference between the densitites of the gas and liquid, the energy associated with the drag force is much greater than the kinetic energy of the gas bubble. Therefore, the gas velocity in the bubble will be similar to the bubble velocity. On the basis of this theoretical reasoning, Levich[29] derived the following equation for the critical bubble size as a function of bubble velocity.
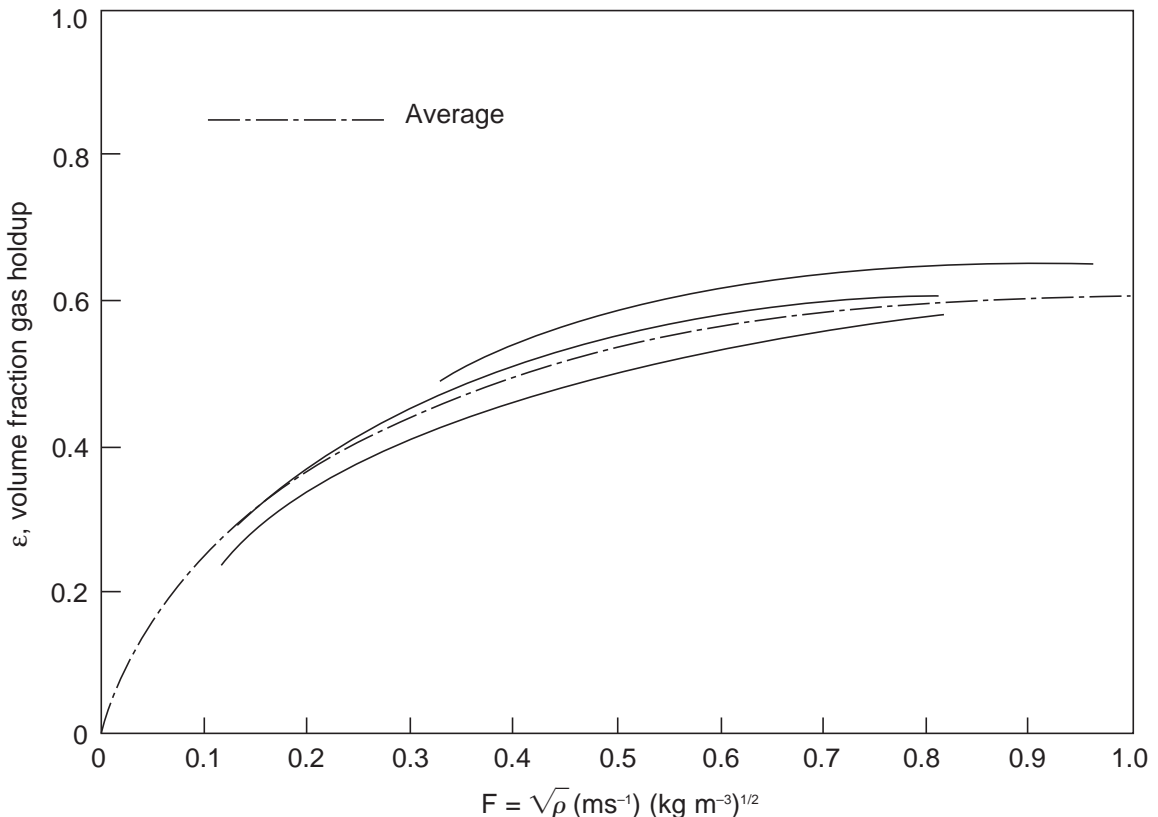
Fig. 2.13 Experimental data of Calderbank[26] on gas holdup in sieve plate columns for the air-water system.
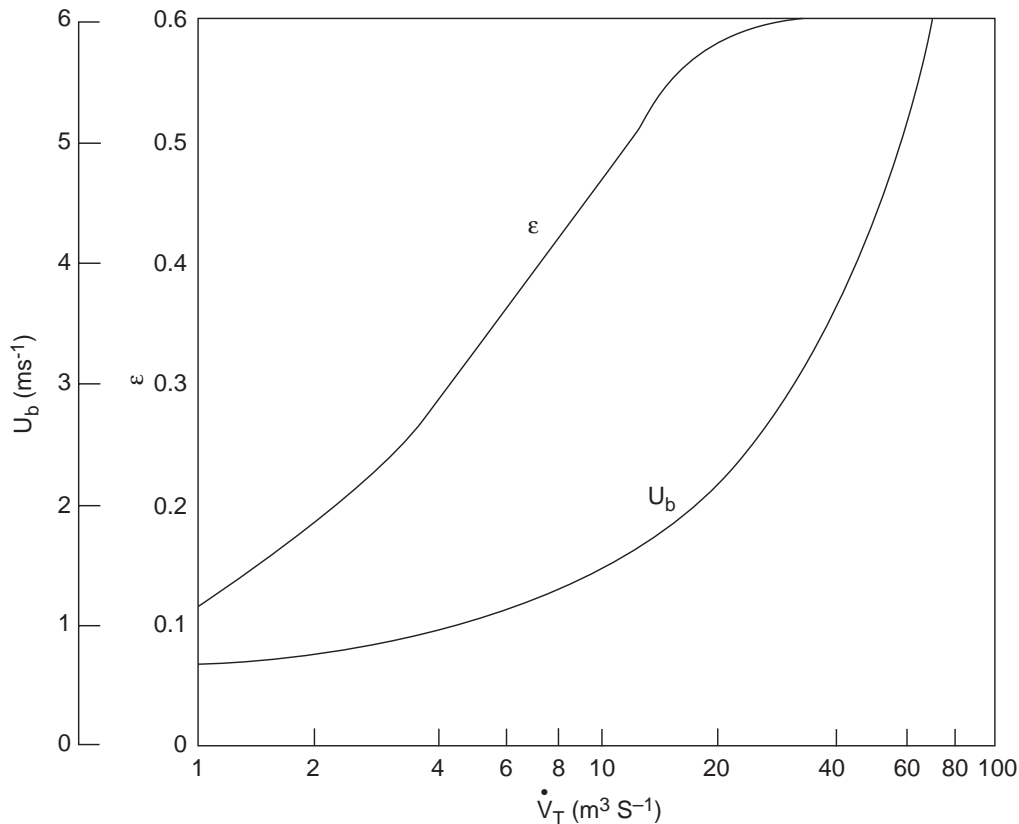
Fig. 2.14 Gas holdup and bubble velocity as a function of gas flow rate. *From Ref. 27.*

$$d_c = \left(\frac{3}{C_d\, \rho_g\, \rho_\ell^2}\right)^{\!\frac{1}{3}} \frac{2\sigma}{U_b^2} \qquad (2.2.19)$$

where σ is the surface tension and C_d the drag coefficient, which is close to unity. As the bubble size decreases with increasing bubble velocity, the gas circulation within the bubble diminishes, thus becoming less effective in bubble fragmentation. Another view to be considered is that, as the gas holdup increases with increasing gas flow rate, the liquid layer separating the bubbles becomes thinner. Consequently, the dynamic gas pressure exerted on the bubble surface becomes nullified by similar forces exerted in the neighboring bubbles, hence the cessation of bubble fragmentation at high values of ε.

The bubble fragmentation with increasing ε, hence increasing U_b, is calculated for bubbles in water with $\sigma = 0.072$ Nm^{-1} and in liquid steel with (a) $\sigma = 1.7$ Nm^{-1} in the presence of $O < 4$ ppm and 40 ppm S, and (b) $\sigma = 1.3$ Nm^{-1} in the presence of 600 ppm O and 120 ppm S. The results are shown in Fig. 2.15. As noted earlier, the limiting bubble size in air-water system is $d = 0.45$ cm which intersects the fragmentation curve at $\varepsilon = 0.41$, depicting the cessation of bubble fragmentation.

In an attempt to estimate the minimum bubble size in the swarm of bubbles in liquid steel, Turkdogan proposed the following hypothesis: 'the surface energy of bubbles per unit mass of liquid which the bubbles displace, are equal for all liquids.' Thus, surface energy E_b of dispersed bubbles of uniform size per unit mass of liquid which they displace is given by:

$$E_b = \frac{6\varepsilon}{1-\varepsilon}\left(\frac{\sigma}{\rho\, d}\right) \text{J kg}^{-1} \text{ liquid} \qquad (2.2.20)$$
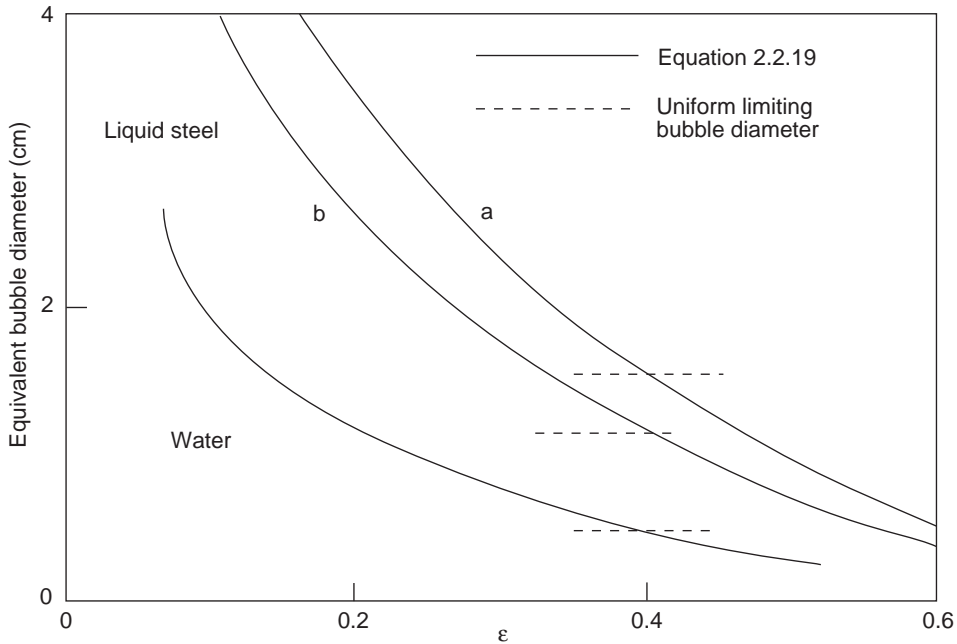
Fig. 2.15 Calculated bubble diameter for bubble fragmentation mechanism equation 2.2.19, compared with uniform limited diameter at high values for water and liquid steel: (a) for O < 4 ppm and 40 ppm S (b) for 600 ppm O and 120 ppm S. *From Ref. 27.*

This conjectured statement leads to the following similarity relation for non-foaming inviscid liquids.

$$\frac{\sigma_1}{\rho_1 d_1} = \frac{\sigma_2}{\rho_2 d_2} = \cdots \text{J kg}^{-1} \text{ liquid} \qquad (2.2.21)$$

With $\sigma_1 = 0.072$ Jm^{-2} and $d_1 = 0.45$ cm for gas-water system and $\sigma_2 = 1.3$ Jm^{-2} and $\rho_2 = 6940$ kg m^{-3}, we obtain $d_2 = 1.16$ cm for the limiting bubble diameter in liquid steel containing $\approx$ 600 ppm O and 120 ppm S. For the melt containing O < 4 ppm and 40 ppm S, $d_2 = 1.52$ cm. These limiting values intersect the fragmentation curves for liquid steel at about $\varepsilon = 0.40$, similar to that for water.

A uniform constant bubble size and essentially constant $\varepsilon = 0.6$ at high gas flow-rates, means a constant number of bubbles per unit volume of the emulsion. Noting that for the close-packed (fcc) arrangement of bubbles, the packing fraction (gas holdup) is $\varepsilon = 0.74$, the thickness of the liquid film at the nearest approach of the bubbles is derived from the following equality of the bubble number.

$$\frac{0.6}{d^3} = \frac{0.74}{(d + \delta/2)^3} \qquad (2.2.22)$$

Noting that for water the experimental data give $d = 0.45$ cm and that estimated for liquid steel $d = 1.16$ cm, equation 2.2.22 gives $\delta = 0.65$ mm for bubbles in aqueous solutions and $\delta = 1.68$ for bubbles in liquid steel at the limiting value of $\varepsilon = 0.6$ for non-foaming inviscid liquids.

2.2.2.4.3 Rate Equation for Transport Controlled Gas Bubble Reactions in Liquid Steel   For mass-transfer controlled reactions of gas bubbles in liquid steel, the rate equation has the following form:

$$\ln \frac{\%X - \%X_e}{\%X_o - \%X_e} = -S_o k_m t \qquad (2.2.23)$$

where X_o and X_e are the initial and gas-metal equilibrium concentrations of the diffusing reactant in the melt, k_m the mass-transfer coefficient and S_o the bubble surface area which is in terms of ε.

$$S_\circ = \frac{6\varepsilon}{d}, m^2/m^3 \text{ gas - melt emulsion} \tag{2.2.24}$$

Bubble surface area with respect to unit mass of liquid is:

$$S_m = \frac{6\varepsilon}{1-\varepsilon}\left(\frac{1}{\rho d}\right), m^2 / kg \text{ liquid} \tag{2.2.24a}$$

From many studies of gas bubble reactions in nonfoaming aqueous solutions, the following formulation have been derived for the liquid-phase mass-transfer coefficient for the regime of surface-renewal at the gas-liquid interface.[26]

$$k_m = 1.28\left(\frac{D U_b}{d}\right)^{\frac{1}{2}} \tag{2.2.25}$$

where D is the diffusivity of the reactant in the liquid-film boundary layer.

In the presence of surface active solutes such as oxygen and sulphur in liquid steel, the bubble surface will be less mobile hence the rate constant k_m will be somewhat less than that given by equation 2.2.25 for the mobile surface, which is a necessary condition for surface-renewal. On the other hand, the surface active solutes decrease the bubble diameter, hence increase the bubble surface area for a given gas holdup. It appears that the product $S_o k_m$ may not be too sensitive to the presence of surface active solutes in the liquid.

The rate constant $S_o k_m$ for the transport controlled reaction is obtained from the combination of equations 2.2.17, 2.2.24 and 2.2.25 as given below for an average solute diffusivity $D = 5 \times 10^{-9}$ m²s⁻¹.

$$S_\circ k_m = \frac{5.43 \times 10^{-4}(\varepsilon U_s)^{\frac{1}{2}}}{d^{\frac{3}{2}}} \tag{2.2.26}$$

Fig. 2.16 Calculated rate constant for mass-transfer controlled reaction of gas bubbles in 220 $\pm$ 20 ton steel bath in the BOF or OBM (Q-BOP) vessel. *From Ref. 27.*

The rate constant thus calculated is plotted in Fig. 2.16 against the gas flow rate $\dot{V}_T$ at 1600°C and for an average gas pressure of 1.5 atm in the steel bath for 220 $\pm$ 20 ton heats.

2.2.2.4.4 Maximum Rate of Degassing of Liquid Steel with Argon Purging   If the rates of diffusional processes and chemical reactions are sufficiently fast, the argon bubbles traversing the melt will be saturated with N_2 or H_2 to the corresponding equilibrium values for the concentrations present in the melt. It is for this limiting case that the following rate equation is applicable.

Denoting N and H by X, and using molar contents in the gas bubbles,

$$\dot{n}_{X_2} = \frac{d(ppm X)}{dt} \frac{10^{-6}}{M} \times 10^6 \text{ g - mol } X_2/\text{min ton} \tag{2.2.27}$$

$$\dot{n}_{Ar} = \frac{\dot{V}}{22.414 \times 10^{-3}} \text{ g - mol Ar/min ton} \tag{2.2.28}$$

where M is the molecular mass of X_2 and $\dot{V}$ the argon blowing rate in Nm³ min⁻¹t⁻¹ In the X_2-saturated argon bubbles for $\dot{n}_{Ar} \gg \dot{n}_{X_2}$

$$p_{X_2} = \frac{\dot{n}_{X_2}}{\dot{n}_{Ar}} \overline{P} = \frac{d(ppm\ X)}{dt} \frac{22.414 \times 10^{-3}}{M\dot{V}} \overline{P} \tag{2.2.29}$$

where $\overline{P}$ is the average bubble pressure in the melt.

Since the gas bubbles are in equilibrium with the melt

$$p_{X_2} = \frac{[ppm\ X]^2}{K^2} = \frac{d(ppm\ X)}{dt} \frac{22.414 \times 10^{-3}}{M\dot{V}} \overline{P} \tag{2.2.30}$$

where K is the equilibrium constant. The integration of the above rate equation gives with X_o being the initial concentration,

$$\frac{1}{ppm\ X} - \frac{1}{ppm\ X_o} = \frac{M\dot{V}}{22.414 \times 10^{-3}\ K^2\ \overline{P}}\ t \tag{2.2.31}$$

For the average liquid steel temperature of 1650°C at turn down, the values of the equilibrium constants are as given below.

$$\left.\begin{array}{l} \text{For } N_2\text{: } K = 459 \\ \text{For } H_2\text{: } K = 27.2 \end{array}\right\} \text{with } p_{X_2} \text{ in atm}$$

For an average gas bubble pressure of $\overline{P} = 1.5$ atm in the melt, the following rate equations are obtained.

$$\frac{1}{ppm\ N} - \frac{1}{ppm\ N_o} = 0.00395\ \dot{V}\ t \tag{2.2.32}$$

$$\frac{1}{ppm\ H} - \frac{1}{ppm\ H_o} = 0.0804\ \dot{V}\ t \tag{2.2.33}$$

As discussed later in detail, the maximum rates are not observed in steelmaking processes; the rates are limited by mass transfer and or chemical kenetics. Nevertheless equations 2.2.32 and 2.2.33 indicate, even for the limiting case, large quantities of purging gas are required and the processes are normally not feasible.

2.2.3 Chemical Kinetics

The theory of the absolute reaction rates is based on the concept of the formation of an activated complex as an intermediate transition state, which has an infinitesimally short life time of the order of 10^{-15} second. For an indepth study of the theory of reaction kinetics, to which outstanding contributions were made by Eyring and co-workers, reference may be made to the classical text books by Glasstone *et al*.[30] and by Hinshelwood.[31]

As illustrated in Fig. 2.17, there is a change in energy profile accompanying the reaction that involves the formation and decomposition of an activated complex. While the change in free energy accompanying reaction is $\Delta G° < 0$, the activation energy $\Delta G^* > 0$.

In almost all pyrometallurgical processes, we are concerned with heterogeneous reactions
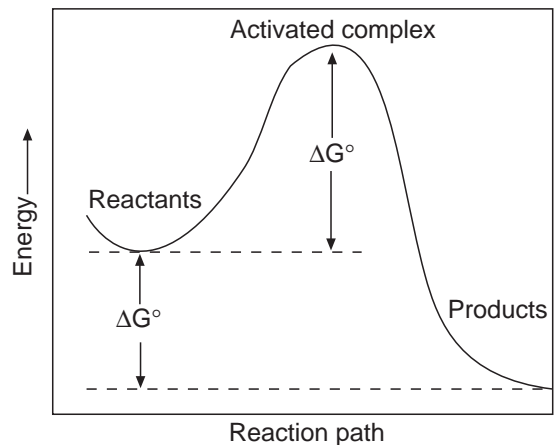
Fig. 2.17 Change in energy profile during the formation and decomposition of the activated complex involved in the reaction.

involving an interface between two reacting phases, e.g. solid-gas, solid-liquid, liquid-gas and two immiscible liquids (slag-liquid metal). For the case of a fast rate of transport of reactants and products to and from the reaction site, the rate is controlled by a chemical reaction occurring in the adsorbed layer at the interface. The reaction between adsorbed species L and M on the surface producing product Q occurs via the formation of an activated complex (LM)*.

$$
\begin{array}{ccccc}
L & + & M & = & (LM)^* & \rightarrow & Q \\
\left\{\begin{array}{c} \text{stage I} \\ \text{reactants} \end{array}\right\} & & & & \left\{\begin{array}{c} \text{activated} \\ \text{complex} \end{array}\right\} & & \left\{\begin{array}{c} \text{stage II} \\ \text{products} \end{array}\right\}
\end{array}
\tag{2.2.34}
$$
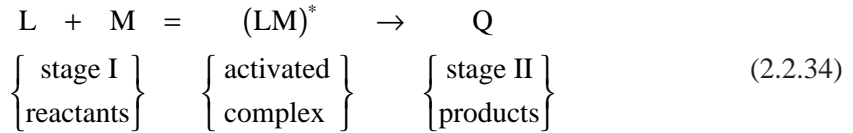
The theory of the absolute rates states that the activated complex is in equilibrium with the reactants for which the equilibrium constant K* for constant temperature is

$$
K^* = \frac{a^*}{a_L \, a_M}
\tag{2.2.35}
$$

where as are the thermodynamic activities.

Next to be considered is the specific rate of decomposition of the activated complex to the overall reaction product Q, represented by

$$
\frac{dn}{dt} = \left(\frac{kT}{h}\right) \Gamma_\circ \, \theta^*
\tag{2.2.36}
$$

where

$$
\begin{array}{rcl}
dn/dt & = & \text{the reaction rate, mol cm}^{-2}\text{s}^{-1}, \\
k & = & \text{the Boltzmann constant, } 1.380 \times 10^{-23} \text{ J K}^{-1}, \\
h & = & \text{the Planck constant, } 6.626 \times 10^{-34} \text{ J s}, \\
T & = & \text{temperature, K}, \\
\Gamma_\circ & = & \text{total number of adsorption sites on the surface, } 10^{15} \text{ mole cm}^{-2}, \\
\theta^* & = & \text{fractional coverage by the activated complex.}
\end{array}
$$

For single site occupancy by the activated complex in the adsorbed layer, the activity of the complex is represented by

$$
a^* = \varphi^* \frac{\theta^*}{1 - \theta}
\tag{2.2.37}
$$

where θ is the total fractional occupancy of the sites by the adsorbed species and φ^* is the activity coefficient of the complex in the chemisorbed layer. Combining equations 2.2.35 - 2.2.37 gives the rate of forward reaction in terms of the absolute reaction rate theory.

$$
R_f = \frac{dn}{dt} = \left(\frac{kT}{h}\right) \Gamma_\circ \left(\frac{K^*}{\varphi^*}\right)(1-\theta)\{a_L \, a_M\}
\tag{2.2.38}
$$

The thermodynamics of the chemisorbed layer at the interface, i.e. value of Γ_o, K* and ,φ are not known, therefore the isothermal rate equation is given in a simplified general form thus

$$
R_f = \Phi_f (1 - \theta)\{a_L \, a_M\}
\tag{2.2.39}
$$

where Φ_f is the isothermal rate constant of the forward reaction.

As the reaction progresses, concentrations of the reactants L and M decrease while the concentration of the product Q increases. Because of these composition changes and the influence of the reverse reaction Q→L + M, the rate decreases with an increasing reaction time. The rate of the reverse reaction is represented by

$$
R_r = - \Phi_r (1 - \theta)\{a_Q\}
\tag{2.2.40}
$$

where Φ_r is the rate constant of the reverse reaction. Therefore, the net overall rate of reaction is

$$\frac{dn}{dt} = \Phi_f(1-\theta)\{a_L a_M\} - \Phi_r(1-\theta)\{a_Q\} \tag{2.2.41}$$

When the rates of forward and reverse reactions are the same, i.e. dn/dt = 0, the reaction is said to be at an equilibrium state. It follows that the ratio of the rate constants Φ_f/Φ_r is the equilibrium constant of the reaction.

$$K = \frac{\Phi_f}{\Phi_r} = \left(\frac{a_Q}{a_L a_M}\right)_{eq} \tag{2.2.42}$$

In terms of a single rate constant, the net reaction rate is formulated as

$$\frac{dn}{dt} = \Phi_f(1-\theta)\left\{a_L a_M - (a_L a_M)_{eq}\right\} \tag{2.2.43}$$

where $(a_L a_M)_{eq}$ is the equilibrium value for the activity a_Q in stage II at any given reaction time.

For a given surface coverage, the temperature dependence of the rate constant is represented by

$$\Phi = \left[\Phi_o \exp\left(\frac{-\Delta H^*}{RT}\right)\right]_\theta \tag{2.2.44}$$

where Φ_o is a pre-exponential constant and ΔH^* is the apparent heat of activation for the reaction at a given site fillage θ.

Since the activation energy ΔG^* is always positive, the enthalpy of activation for the reaction is also positive. As shown in Fig. 2.18 in the plot ln Φ vs 1/T the slope of the line gives ΔH^*. It should be noted that since the thermodynamic quantities for the activated complex (K*/ϕ*) in the chemisorbed layer are not known, the ΔH^* derived from the rate measurements over a sufficiently large temperature range, is the apparent heat of activation.

Another aspect of the kinetics of interfacial reactions is the rate of chemisorption or desorption at the reaction surface as given by the following theoretical equation for an uncontaminated surface.

Fig. 2.18 Effect of temperature on rate constant for reaction involving an activated complex.

$$\Phi_f = (2\pi M_i RT)^{-\frac{1}{2}} \exp\left(\frac{-\Delta H^*}{RT}\right) \tag{2.2.45}$$

where M_i is the molecular mass of the adsorbed species. This equation is transformed to the following form for the maximum rate of vaporization, i.e. free vaporization, from an uncontaminated surface at low pressures

$$Rate_{max} = \frac{p_i}{\sqrt{2\pi M_i RT}} \tag{2.2.46}$$

where p_i is the vapor pressure in atm, for which the equation is reduced to the following form.

$$Rate_{max} \text{ (g-mol cm}^{-2}\text{ s}^{-1}) = 44.3 \, p_i \, (MT)^{-\frac{1}{2}} \tag{2.2.47}$$

2.2.3.1 Examples of Experiments on Rates of Interfacial Reactions

2.2.3.1.1 Nitrogen Transfer Across Iron Surface   The rate of reaction of gaseous nitrogen with liquid and solid iron, in the presence of surface active alloying elements, has been studied by many investigators since the late 1950s. It was in the late 1960s[32–34] that the rate controlling reaction mechanism was resolved, which was further confirmed in the subsequent experimental work done by Fruehan and Martonik[35], Byrne and Belton[36], and Glaws and Fruehan[37].

In particular the latter investigators used an isotope exchange technique which measured the rate of dissociation of the N_2 molecule. They demonstrated the rate of dissociation was the same as the rate of absorption of nitrogen, providing strong evidence that the absorption rate is controlled by dissociation.

When the rate of reaction is not hindered by slow nitrogen transport to and from the gas-metal interface, the rate of nitrogenation

$$N_2 (g) = N_2^* \rightarrow 2[N] \tag{2.2.48}$$

is controlled either by the rate of chemisorption or dissociation of N_2 molecules on the metal surface. The rate of reverse reaction, i.e denitrogenation, is of course a second order type with respect to nitrogen dissolved in the metal. The equation below represents the rate of nitrogen transfer from gas to liquid iron

$$\frac{d[\%N]}{dt} = \frac{100\,A}{\rho\,V}\,\Phi_f\,(1-\theta)\left\{P_{N_2} - \left(P_{N_2}\right)_{eq}\right\} \tag{2.2.49}$$

where ρ is the density of liquid iron, A the surface area of the melt on which the nitrogen stream is impinging and V the volume of the melt. The rate constant Φ_f, in units of g N cm^{-2}min^{-1}atm^{-1}N$_2$, is for the forward reaction 2.2.48. The equilibrium partial pressure $(p_{N_2})_{eq}$ corresponding to the nitrogen content of the melt at the reaction time t, is that given by the equilibrium constant K for nitrogen solubility.

$$\left(p_{N_2}\right)_{eq} = \frac{[\%N]^2}{K} \tag{2.2.50}$$

With this substitution the isothermal rate equation is

$$\frac{d[\%N]}{dt} = \frac{100\,A}{\rho\,V}\,\Phi_f\,(1-\theta)\left\{P_{N_2} - \frac{[\%N]^2}{K}\right\} \tag{2.2.51}$$

For constant N_2 pressure and temperature, the integration of equation 2.2.51 gives for %N = 0 at t = 0,

$$\ln\frac{K\,p_{N_2} + [\%N]}{K\,p_{N_2} - [\%N]} = 2\,p_{N_2}\,\frac{100\,A}{\rho\,V}\,\Phi_f\,(1-\theta)\,t \tag{2.2.52}$$

Byrne and Belton made an accurate determination of the rate constant Φ_f for reaction of N_2 with high purity iron and Fe-C alloys at 1550–1700°C, by measuring the rate of $^{15}N \rightarrow ^{14}N$ isotope exchange that occurs on the iron surface, as represented by

$$\log \Phi_f = \frac{-6340 \pm (710)}{T} + 1.85(\pm 0.38) \tag{2.2.53}$$

where the rate constant Φ_f is in units of g N cm^{-2}min^{-1}atm^{-1}. The apparent heat of activation = 121.4 kJ mol^{-1} is much lower than the value expected for the rate of dissociation of N_2. As pointed out by Byrne and Belton, the rate of chemisorption of N_2 is presumably controlling the reaction mechanism.

The surface active elements dissolved in iron, e.g. O, S, Se, Te, are known to lower the rate of nitrogen transfer across the iron surface. On the basis of the experimental rate data with liquid iron containing O and S, as given in various publications (Refs. 33–38) and the surface tension data, the effects of O and S on the fraction of vacant sites, $1-\theta$, in the chemisorbed layer may be represented by

$$1-\theta = \frac{1}{1+260\left(\%O+\dfrac{\%S}{2}\right)} \tag{2.2.54}$$

which is a slightly simplified form of the equation that was derived by Byrne and Belton.

For the chemical reaction-controlled nitrogen removal from liquid iron (or steel) in reduced pressures or in an inert gas stream with very low N_2 pressure

$$2[N] \rightarrow N_2\,(g) \tag{2.2.55}$$

the integrated form of the rate equation is

$$\frac{1}{\%N}-\frac{1}{\%N_\circ}=\frac{100\,A}{\rho\,V}\,\Phi_r\,(1-\theta)\,t \tag{2.2.56}$$

where $\%N_o$ is the initial nitrogen content and Φ_r the rate constant $= \Phi_f/K$.

The solubility of N_2 in liquid iron or low alloy steel is given by

$$\log K = \frac{[\%N]^2}{p_{N_2}\,(\text{atm})}=-\frac{376}{T}-2.48 \tag{2.2.57}$$

Combining this with equation 2.2.53 gives for the rate constant Φ_r in gN cm^{-2}min^{-1}%N^{-1}

$$\log \Phi_r = \frac{-5964}{T}+4.33 \tag{2.2.58}$$

Now let us consider the chemical-reaction controlled rate of denitrogenation. It will be assumed that the rate is controlled by only chemical kinetics. In actuality it is controlled by mass transfer and chemical kinetics in series which is discussed later in detail. From equation 2.2.58 the rate for 1600°C $\Phi_r = 0.233$ g N cm^{-2}s^{-1}%N^{-1}. For liquid steel containing 600 ppm O and 120 ppm S, $(1 - \theta) = 0.055$ from equation 2.2.54. For the gas flow rate $\dot{V}_T = 34$ m^{3}s^{-1}, $\varepsilon = 0.6$ and the bubble surface area is $S_m = 1.11$ cm^{2}g^{-1} liquid steel. Inserting these numbers in equation 2.2.56 for the limiting case of $\%N_e \approx 0$, gives

$$\frac{1}{\%N}-\frac{1}{\%N_O}=100\times1.11\times0.233\times0.055\,t=1.42\,t \tag{2.2.59}$$

In 60 seconds time of purging, 0.0030% N_o will be reduced only to 0.0024% N. In actual fact, the argon bubbles traversing the melt will contain some N_2; for example, if the nitrogen partial pressure in gas bubbles were 0.001 atm N_2, the equilibrium content in the melt would be 0.0015% N_e. Therefore, with $\%N_e > 0$, the nitrogen removal will be much less than that calculated above for the chemical-reaction controlled rate for the hypothetical limiting case of $\%N_e \approx 0$.

The foregoing predication from the rate equation is in complete accord with the practical experience that even at high rates of argon purging of the melt, as in OBM(Q-BOP), there is no perceptible nitrogen removal primarily because of the presence of surface active solutes, oxygen and sulfur, in the steel bath.

2.2.3.1.2 CO_2 and H_2O Reaction with Fe–C Melts
Another example of chemical kinetics controlling reaction rates is the decarburization of Fe–C melts.

$$\underline{C} + CO_2 = 2CO \tag{2.2.60}$$
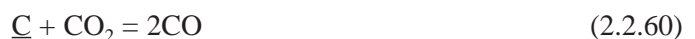
Sain and Belton[39] and later Mannion and Fruehan[40] showed that the rate was affected by surface active elements and was consistent with CO_2 dissociation on the surface controlling the rate.

Nagasaka and Fruehan[41] measured the rate of decarburization by H_2O.

$$H_2O + \underline{C} = CO + H_2 \qquad (2.2.61)$$

They also found that the rate was controlled by chemical kinetics and most likely dissociation of H_2O on the surface. For both the CO_2 and H_2O reaction, the rate constant could be expressed by the relationship

$$k_C = \frac{k_p}{1 + K_S[\%S]} + k_r \qquad (2.2.62)$$

where k_C, k_p and k_r are the rate constants, k_p is the rate constant for pure iron and k_r is the residual rate at high sulfur contents respectively and K_s is the absorption coefficient for sulfur on liquid iron. The first term is based on the analysis by Belton[42] and the residual rate which is relatively small is discussed by Nagasaka *et al* in detail.[41] The overall rate constants are given as a function of sulfur content in Fig. 2.19.
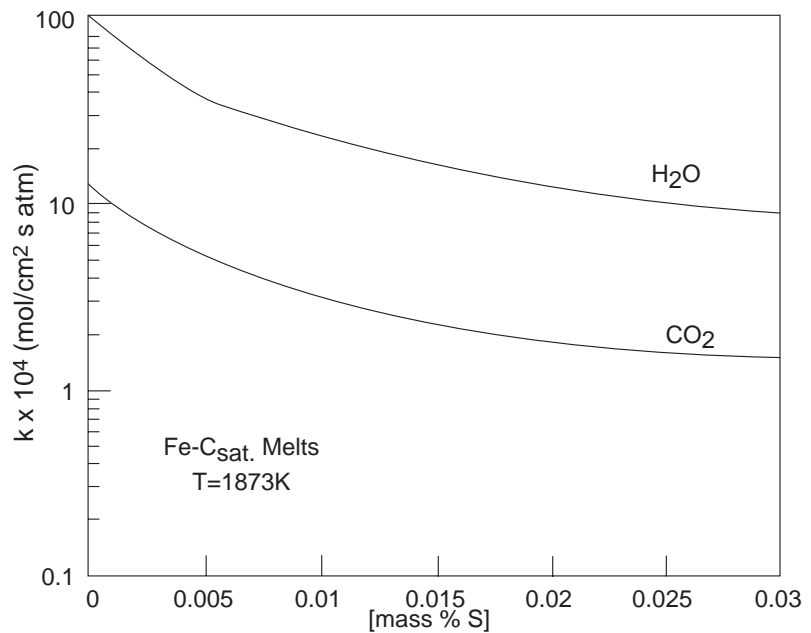
Fig. 2.19 Rates of dissociation of CO_2 and H_2O on iron as a function of sulfur content. *From Ref. 41.*

2.2.3.1.3 Chemical Kinetics of Carbon Oxidation in CO_2–CO Mixtures   Examples of the experimental data on the initial rate of internal oxidation of granular (0.5 mm dia.) electrode graphite and metallurgical coke are given in Figs. 2.20 and 2.21, reproduced from a previous publication.[16]

In a subsequent publication, Turkdogan[27] re-assessed the interpretation of the rate data on the assumption that both CO and CO_2 are chemisorbed on the pore walls of the carbon and the rate of oxidation is due to the rate of dissociation of chemisorbed CO_2. For the limiting case of complete internal burning, the rate equation will be in the following form

$$\text{Rate} = \frac{\Phi' \, p_{CO_2}}{1 + k_1 p_{CO} + k_2 p_{CO_2}} t \qquad (2.2.63)$$
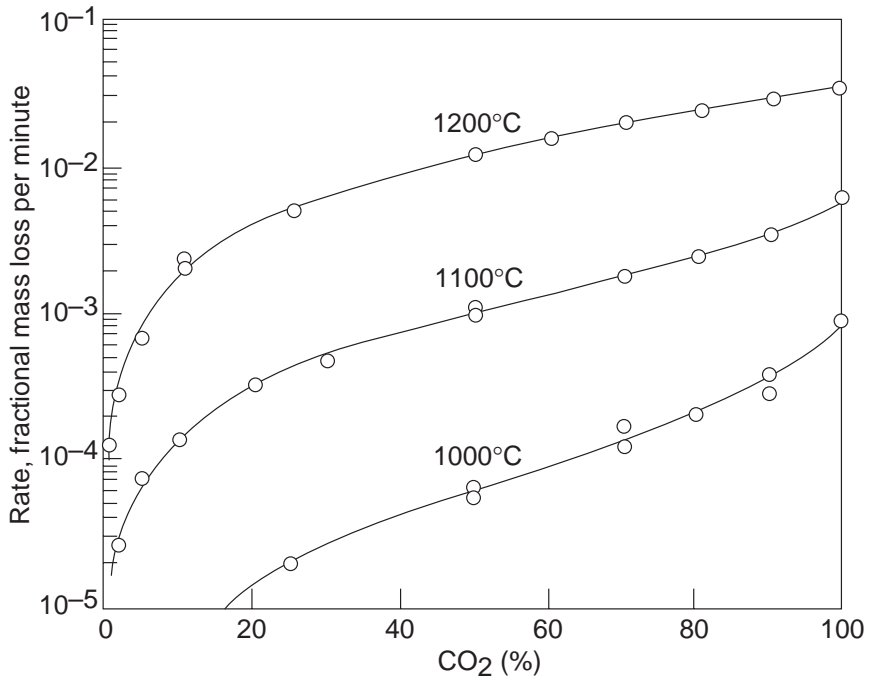
Fig. 2.20 Effects of temperature and gas composition on the rate of oxidation of electrode graphite granules (~0.5 mm dia.) in CO_2–CO mixtures at 0.96 atm total pressure. *From Ref. 16.*
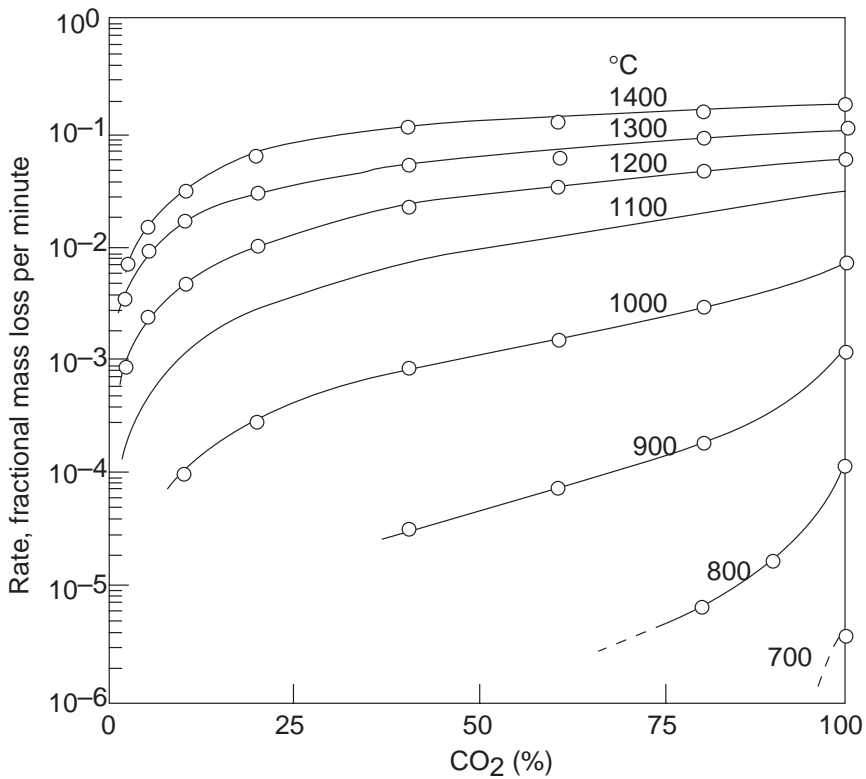
Fig. 2.21 Effect of temperature and gas composition on the rate of oxidation of granular metallurgical coke (~0.5 mm dia.) in CO_2–CO mixtures at 0.96 atm total pressure. *From Ref. 16.*

where Φ' is the rate constant ($min^{-1}atm^{-1}CO_2$) for a given temperature and a particular type of carbon; the constants k_1 and k_2 are associated with the chemisorption of CO and CO_2. It should be noted that in compliance with the notation in equation 2.2.64 for the ideal monolayer, the constants k_1 and k_2 are reciprocals of the respective activity coefficients of the absorbed species, i.e. $k_1 = 1/\varphi_{CO}$ and $k_2 = 1/\varphi_{CO_2}$; the fraction of vacant sites being $(1 - \theta) = (1 - \theta_{CO} - \theta_{CO_2})$.

The fraction of surface sites θ_i covered by the adsorbed species is related to the solute activity as given in the following Langmuir adsorption isotherm.

$$a_i = \varphi_i \frac{\theta_i}{1-\theta_i} \tag{2.2.64}$$

From the cited experimental data for the oxidation of graphite and coke the following equations are obtained for the temperature dependence of Φ', $\varphi_{CO} = 1/k_1$ and $\varphi_{CO_2} = 1/k_2$.

For electrode graphite:

$$\log \Phi' \left(min^{-1} atm^{-1} CO_2\right) = -\frac{16,540}{T} + 10.75 \tag{2.2.65}$$

$$\log \varphi_{CO} (atm) = -\frac{8719}{T} + 4.84 \tag{2.2.66}$$

$$\log \varphi_{CO_2} (atm) = -\frac{590}{T} - 0.072 \tag{2.2.67}$$

For metallurgical coke:

$$\log \Phi' \left(min^{-1} atm^{-1} CO_2\right) = -\frac{16,540}{T} + 11.37 \tag{2.2.68}$$

$$\log \varphi_{CO} (atm) = -\frac{2117}{T} + 0.27 \tag{2.2.69}$$

$$\log \varphi_{CO_2} (atm) = \frac{3840}{T} - 3.45 \tag{2.2.70}$$

It should be noted that these equations fit the measured initial rates of oxidation within a factor of about 1.5 for temperatures 800 to 1200°C and for CO_2 pressures 0.03 to 3 atm. For easy comparison of the reactivities of electrode graphite and metallurgical coke, the numerical values are given below from the above equations for 900 and 1200°C.

Temperature °C	Electrode graphite			Metallurgical coke		
	Φ'	φ_{CO}	φ_{CO_2}	Φ'	φ_{CO}	φ_{CO_2}
900	4.5×10^{-4}	0.0025	0.27	1.9×10^{-3}	0.029	0.67
1200	3.3×10^{-1}	0.083	0.34	1.4×10^{0}	0.068	0.14

After about 3 to 5 percent of initial oxidation, the pore surface area of the coke samples were found to be four to five times greater than the graphite samples; this is consistent with the Φ' values for coke being greater than for graphite by a similar factor. The extent of CO adsorption on the pore walls of electrode graphite or coke is greater than the CO_2 adsorption.

There are variations in the reported values of the apparent heat of activation for oxidation of the electrode (or reactor grade) graphite in CO_2. For example, Gulbransen *et al.*[43] found $\Delta H^* = 368$ kJ mol^{-1} while according to Blackwood's work [44] $\Delta H^* = 260$ kJ mol^{-1}; in the present case $\Delta H^* = 317$ kJ mol^{-1}. Reference should be made also to the papers of Ergun,[45] Hedden and Lowe,[46] and by Grabke[47] for various other interpretations of the kinetics of oxidation of carbons.

Aderibigbe and Szekely[48] also investigated the oxidation of metallurgical coke in CO_2–CO mixtures at 850 to 1000°C. Their rate constants K_1 ($\equiv \Phi'$) are similar to those given by equation 2.2.68 their estimate of the apparent heat of activation being $\Delta H^* = 249 \pm 47$ kJ mol^{-1}.

Recently Story and Fruehan[49] examined the oxidation of carbons in CO–CO_2 gas mixtures at high temperatures (>1300°C) under conditions of high external mass transfer. The gas mixture was jetted at high velocities, reducing the resistance to mass transfer at the surface. They were in limiting case of external oxidation and determined the parameter ($\phi \rho S \, D_e$) from the data, and then using published values of S and computed values of D_e, computed the rate constant. The results are compared to the rates measured at lower temperatures in Fig. 2.22.
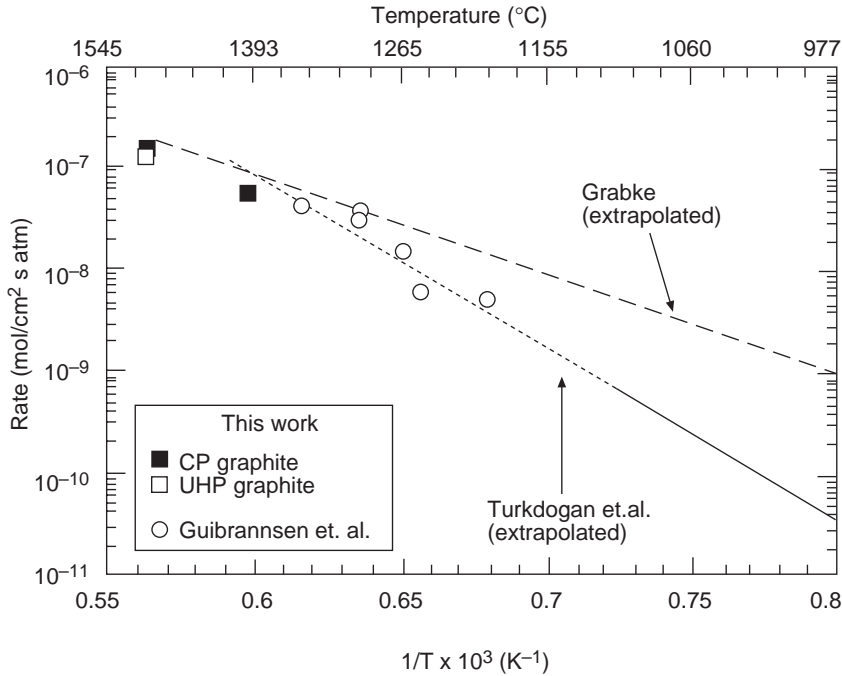
Fig. 2.22 Arrhenius plot of graphite–CO_2 data.

2.2.4 Mixed Control

In many metallurgical operations the rate is not controlled by a single reaction step such as mass transfer or chemical kinetics but rather two steps in series such as mass transfer followed by chemical kinetics. By equating the fluxes for each of the reaction steps it is possible to obtain expressions for the overall rate, or a series of expressions, which can be solved numerically.

2.2.4.1 Mixed Control for Gas Phase Mass Transfer and Chemical Kinetics

In general the temperature dependence of chemical kinetics is greater than for gas phase mass transfer. Consequently at low temperatures chemical kinetics is predominantly controlling the rate while at high temperatures mass transfer dominates. However for many reactions over a large range of conditions including temperature, fluid flow conditions and the concentration of surface active elements which effect the chemical rate, the rate is controlled by both processes in series.

For example, the rate of dissociation of CO_2 and H_2O on liquid iron is controlled by both gas phase mass transfer and chemical kinetics in series over a large range of temperature and fluid flow conditions. In this case the pressure of the reacting gas at the surface is not the bulk composition. The flux of the reacting gas and the rate of the reaction are given by 2.2.71 and 2.2.72 respectively,

$$J = \frac{m_i}{R \, T} \left(p_i^B - p_i^s \right) \tag{2.2.71}$$

$$R = k \left(p_i^s - p_i^e \right) \tag{2.2.72}$$

where

m_i = the gas phase mass transfer coefficient for i,

p_i^B = the pressure of i in the bulk phase,

p_i^s = the pressure of i at the surface,

p_i^e = the equilibrium pressure of i,

k = the chemical rate constant.

Equations 2.2.71 and 2.2.72 assume that the chemical rate is first order and the reaction is equilmolar in terms of the moles of reactant and product gases or the pressure of the reaction gas is low. As it is not possible to accumulate component i at the surface, the processes are assumed to be at steady state and the flux and chemical rate are equated. It is then possible to calculate the pressure at the surface and the rate in terms of the bulk composition. Further simplification gives

$$R = \frac{1}{\dfrac{1}{k} + \dfrac{RT}{m_i}}\left(p_i^B - p_i^e\right) \tag{2.2.73}$$

Equation 2.2.73 is analogous to an electrical current with two resistances in series where k and m_i/RT are analogous to conductivities. The first term in equation 2.2.73 is often referred to as the observed or overall rate constant.

For example Nagasaka and Fruehan[41] measured the rate of dissociation of H_2O on liquid Fe-C-S alloys from 1673 to 1873°K for varying sulfur contents. At 1873K and 0.1% S the measured overall rate constant was 2.5×10^{-4} mole/cm^2 s atm for conditions where the mass transfer coefficient was 100 cm/s. For this case the chemical rate was computed to be 3.9×10^{-4} mole/cm^2 s atm.

Similarly the nitrogen and carbon dioxide reactions can be controlled by gas phase mass transfer and chemical kinetics and equations 2.2.71 – 2.2.73 can be applied.

2.2.4.2 Mixed Control for Chemical Kinetics and Liquid Phase Mass Transfer

For many conditions in steelmaking and refining the rate of pick up or removal of nitrogen from liquid iron is controlled by chemical kinetics and liquid phase mass transfer in series. Fruehan, Lally and Glaws[50] developed a mixed control model and applied it to several metallurgical processes. For nitrogen gas reacting with iron the flux of nitrogen for mass transfer and the chemical reaction are given by 2.2.74 and 2.2.75.

$$J_N = \frac{m\rho}{100}\left[\%N^s - \%N\right] \tag{2.2.74}$$

$$J_N = k\left(p_{N_2} - \frac{\left[\%N^s\right]^2}{K}\right) \tag{2.2.75}$$

where

J_N = flux of nitrogen (g/cm^2 s),

m = mass transfer coefficient for nitrogen (cm/s),

k = chemical rate constant (g/cm^2 s atm),

$\%N^s$ = nitrogen content at the surface,

K = equilibrium constant for nitrogen reaction with liquid iron,

ρ = density of iron (g/cm^3).

Since no nitrogen can be accumulated at the surface it is possible to equate the two flux equations, 2.2.74 and 2.2.75, and solve for the nitrogen content at the surface. The equation is a quadratic and is solved numerically for small time increments for specific conditions.. The surface nitrogen content is then used to compute the rate of nitrogen absorption or removal. This technique was applied to nitrogen absorption into liquid iron when bubbling nitrogen in the ladle and typical results are shown in Fig. 2.23. The rate of nitrogen pick up for low sulfur steel is considerably faster than for high sulfur steel, as sulfur decreases the chemical rate. Below 0.005% S the rate does not increase further as liquid phase mass transfer then dominates and it is not affected by sulfur content.
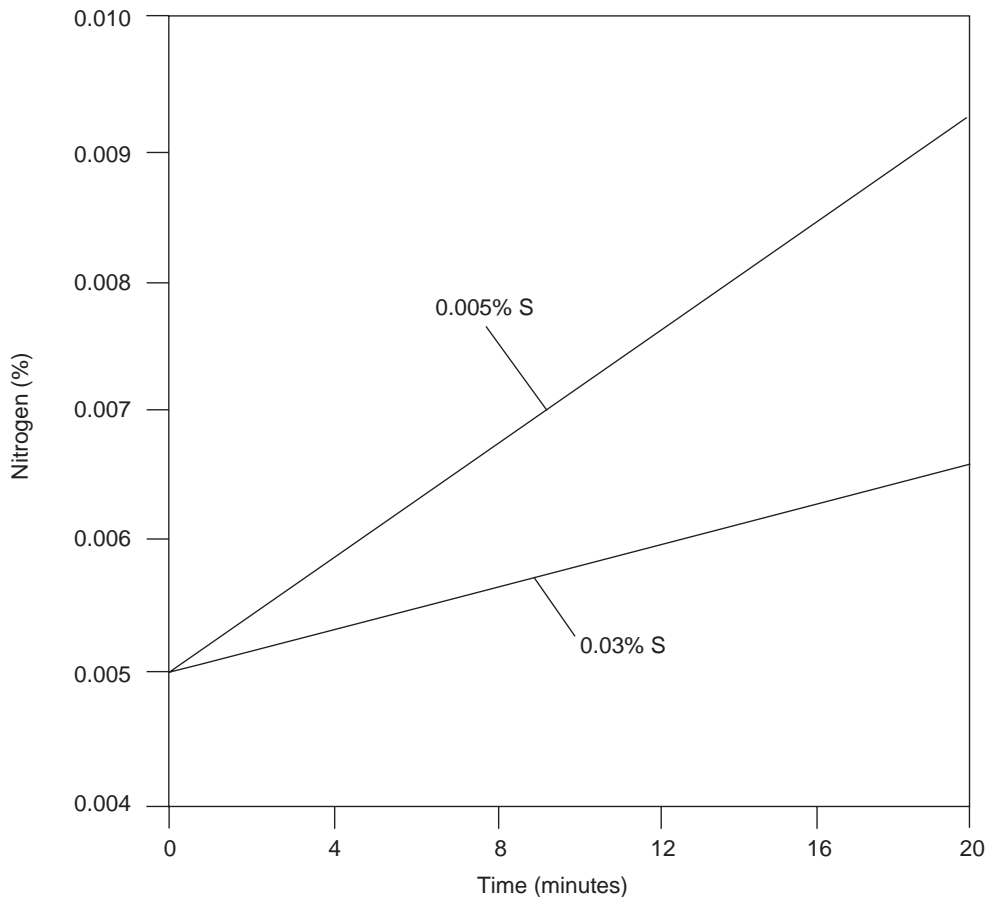
Fig 2.23 Rate of nitrogen pick-up in 200 metric tons of steel containing 0.005 and 0.030% S, using 10 scfm of N_2. *From Ref. 50.*

2.3 Properties of Gases

Of importance to the iron and steelmaking and related pyrometallurgical processes, the selected thermochemical and transport properties of gases are presented in this section.

2.3.1 Thermochemical Properties

2.3.1.1 Heat Content

The molar heat contents of simple selected gases of interest to pyrometallurgical processes are plotted in Fig. 2.24 over the temperature range 300–1900K.
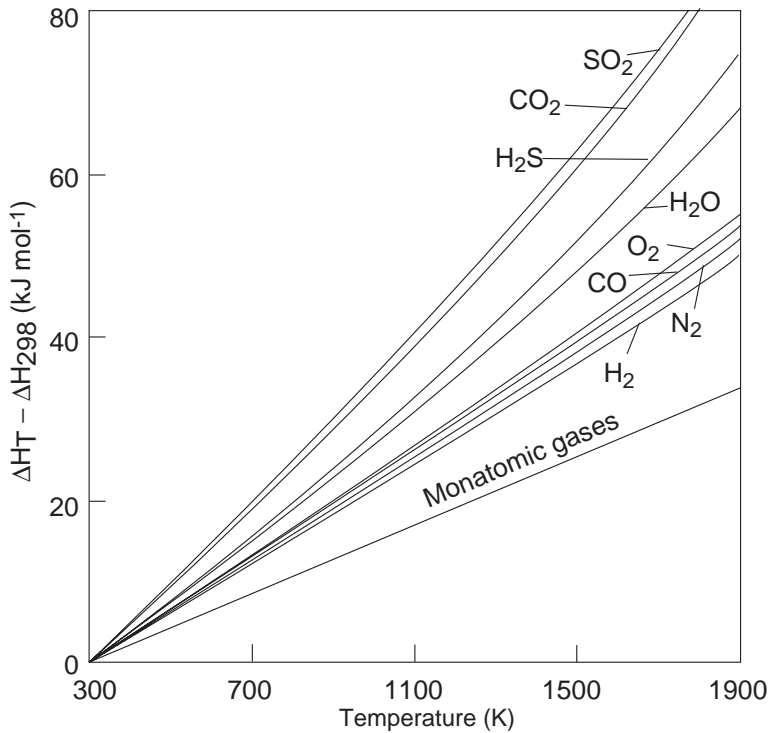
Fig. 2.24 Heat contents of simple gases.

2.3.1.2 Equilibrium States in Gas Mixtures

When assessing the state of reactions involving gas mixtures, the partial pressures of the gaseous species should be evaluated from the reaction equilibrium data for all the pertinent gas reactions. The principle of the computation is demonstrated by the following example for the gas mixture $CO–CO_2–H_2O–CH_4$.

This example is in relation to reheating a reformed gas in the direct iron ore reduction processes. If there is complete gas equilibrium at the reheating temperature and pressure, the activity of carbon in the equilibrated gas mixture must satisfy the following three basic reaction equilibria:

$$2CO = C + CO_2 \tag{2.3.1}$$

$$K_1 = \frac{a_C \, p_{CO_2}}{p_{CO}^2} \tag{2.3.2}$$

$$H_2 + CO = C + H_2O \tag{2.3.3}$$

$$K_2 = \frac{a_C \, p_{H_2O}}{p_{H_2} \, p_{CO}} \tag{2.3.4}$$

$$CH_4 = C + 2H_2 \tag{2.3.5}$$

$$K_3 = \frac{a_C \, p_{H_2}^2}{p_{CH_4}} \tag{2.3.6}$$

For the predominant gaseous species the following equalities are derived from the mass balance for (ΣC), (ΣO) and (ΣH).

$$\frac{\Sigma C}{\Sigma O} = \left(\frac{p_{CO_2} + p_{CO} + p_{CH_4}}{2p_{CO_2} + p_{CO} + p_{H_2O}}\right)_i = \left(\frac{p_{CO_2} + p_{CO} + p_{CH_4}}{2p_{CO_2} + p_{CO} + p_{H_2O}}\right)_e \qquad (2.3.7)$$

$$\frac{\Sigma C}{\Sigma H} = \left(\frac{p_{CO_2} + p_{CO} + p_{CH_4}}{2p_{H_2O} + 2p_{H_2} + 4p_{CH_4}}\right)_i = \left(\frac{p_{CO_2} + p_{CO} + p_{CH_4}}{2p_{H_2O} + 2p_{H_2} + 4p_{CH_4}}\right)_e \qquad (2.3.8)$$

where i and e indicate partial pressures in the ingoing and equilibrated gas mixtures, respectively. The equation below gives the total pressure P of the equilibrated gas mixture.

$$(p_{CO} + p_{CO_2} + p_{H_2} + p_{H_2O} + p_{CH_4})_e = P \qquad (2.3.9)$$

The partial pressures of gaseous species and the activity of carbon in the equilibrated gas mixture are computed by simultaneous solution of equations 2.3.1 to 2.3.9 with known values of the equilibrium constants K_1, K_2, and K_3.

Examples are given in Fig. 2.25 showing the calculated carbon activities for 4 atm total pressure and for an initial gas mixture containing 73% H_2, 18% CO, 8% CO_2, 1% CH_4 to which 0.2% to 6.0% H_2O has been added. The carbon deposition is imminent when its activity in the equilibrated gas exceeds unity, with respect to graphite. With the addition of 0.2% H_2O to this gas mixture, there should be no carbon deposition in the equilibrated gas mixture at temperatures below 512°C and above 720°C. In an earlier study of the reduction of iron oxides in a similar gas mixture, carbon deposition was observed at all temperatures below 1000°C (see Ref. 51), indicating lack of complete gas equilibrium even at 1000°C. These experimental findings suggest that carbon deposition may occur during reheating of reformed natural gas in industrial operations, even when the calculated carbon activity is less than unity in the gas mixture under equilibrium conditions.
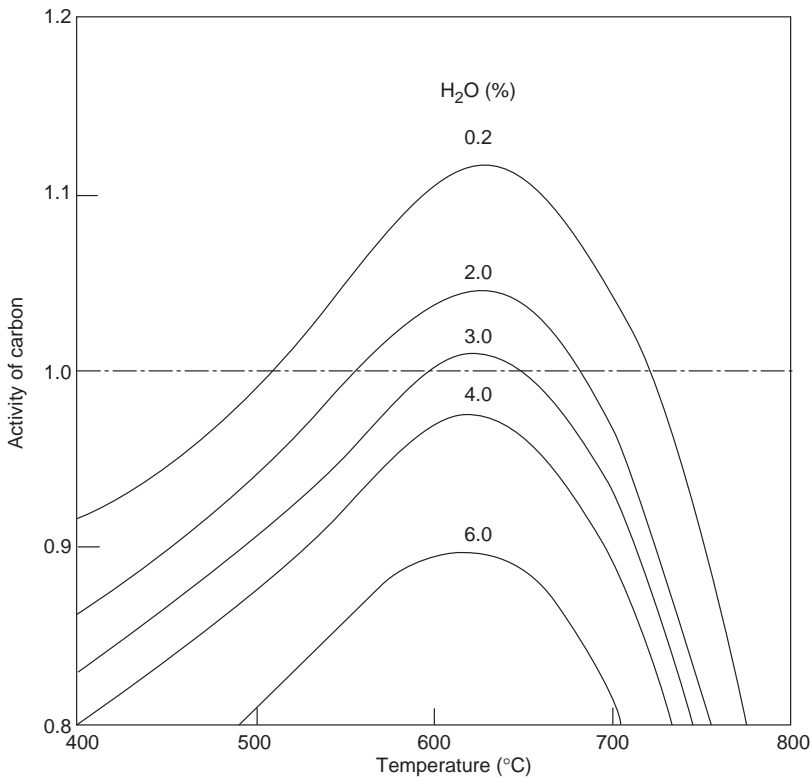
Fig. 2.25 Calculated activity of carbon for complete gas equilibrium at 4 atm and indicated temperatures for reformed natural gas containing 73% H_2, 18% CO, 8% CO_2 and 1% CH_4 to which an indicated amount of H_2O is added. *From Ref. 52.*

The activity of carbon cannot be calculated for a nonequilibrated gas mixture. However, for the purpose of identifying the reactions that may be responsible for carbon deposition, we may calculate carbon activities for individual reactions on the assumption that there is no change in the composition of the inlet gas upon heating. As is seen from the example given in Fig. 2.26 the carbon activities for individual reactions differ considerably from those calculated for complete gas equilibrium. For complete gas equilibrium, the carbon activity is below unity at temperatures below 540 and above 700°C, while for the individual reactions the carbon activity is below unity only within the temperature range 880–1060°C. Therefore, in the nonequilibrated gas, there can be no carbon deposition only within the temperature range 880–1060°C. The temperature at which carbon deposition may start depends on the relative rates of reactions 2.3.1 and 2.3.3: below 730°C if reaction 2.3.1 is fast, and below 880°C if reaction 2.3.3 is fast.

On the basis of the foregoing reasoning, we may compute a diagram of % H_2O in the inlet

Fig 2.26 Calculated activity of carbon for complete gas equilibrium at 4 atm. compared with the activity of carbon for individual reactions in a reformed inlet gas containing 2% H_2O. *From Ref. 52.*

reformed gas versus temperature, as in Fig. 2.27, to delineate the regions where (I) carbon will not deposit, (II) carbon may deposit, and (III) carbon will deposit. With increasing pressure, regions II and III move to higher temperatures and I to higher concentrations of H_2O, and chances of carbon deposition become greater. From the equilibrium constant for reaction 2.3.3, we can also compute the critical p_{H_2O}/p_{CO} ratio for possible carbon deposition at any temperature and partial pressure of H_2 in the inlet gas. The possibility of carbon deposition in region II depends much on the catalytic behavior of the inner surface of the reheater tubes.

Fig. 2.27 Regions of carbon deposition at reheating temperatures of reformed natural gas at 1 atm containing indicated amounts of H_2O. *From Ref. 52.*
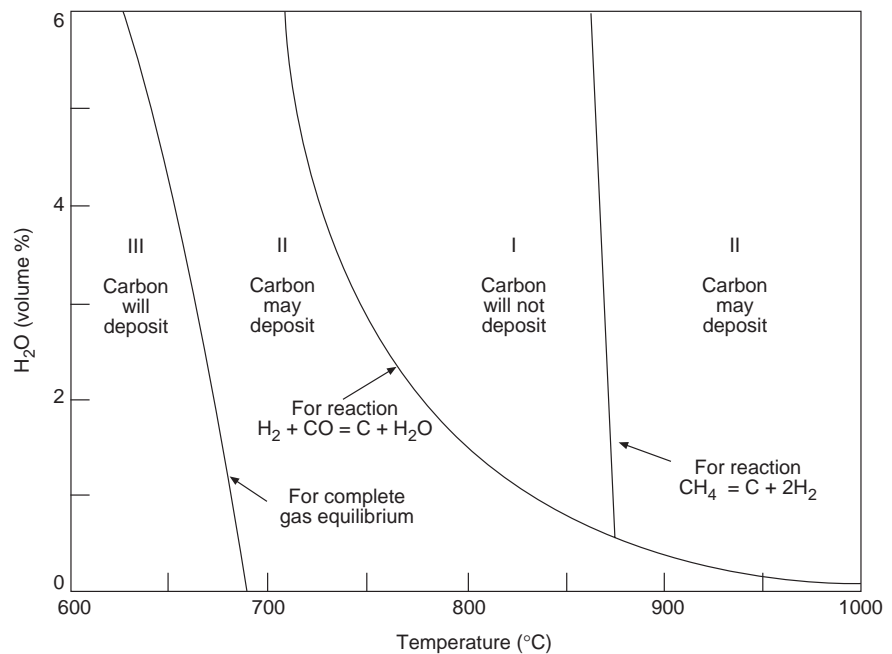
2.3.1.3 Catalytic Decomposition of Carbon Monoxide

The catalytic decomposition of carbon monoxide has been the subject of much study, because of the occurrence of carbon deposition in many processes, e.g., blast furnaces, the Stelling process, the Fischer-Tropsch process, nuclear reactors, and so on. References to early work on this subject are listed in an annotate bibliography by Donald[53]. The consensus is that iron, cobalt, and nickel are the most effective catalysts for the decomposition of carbon monoxide. Kehrer and Leidheiser[54] reported virtually no catalytic effect of copper, silver, chromium, molybdenum, palladium, and rhenium.

In a comprehensive study of carbon deposition in CO–H_2 mixtures at temperatures of 450–700°C, Walker *et al.*[55] observed that the C/H atom ratio in the deposit increased from 10 to 50 with increasing reaction temperature and increasing CO/H_2 ratio in the gas. They also found that the properties of carbon deposit were affected by the amount accumulated on the catalyst, e.g., with increasing thickness of the carbon layer, the crystallinity became poorer, the surface area increased, the electrical conductivity decreased, and the C/H_2 ratio increased. Another important finding was that carbon deposition ultimately ceased when most of the iron was converted to cementite. Upon hydrogen treatment, cementite decomposed to iron and graphite, but the regenerated iron lost most of its reactivity as a catalyst. Similar observations were made by Turkdogan and Vinters[51] in subsequent studies of the catalytic decomposition of carbon monoxide in the presence of porous iron.

It is generally agreed that iron, not cementite, catalyzes the decomposition of carbon monoxide. The chemisorption of H_2 and CO on the surface of iron is believed to approach equilibrium rapidly. The carbon formed by reactions 2.3.1 and 2.3.3 migrates across the surface to a nucleating center where cementite and free carbon are deposited. Based on x-ray diffraction and electron microscopic studies, Ruston *et al.*[56] suggested that although the decomposition of carbon monoxide was catalyzed by iron, an iron carbide Fe_7C_3 formed as an intermediate step in the decomposition of the activated reaction product to graphite.
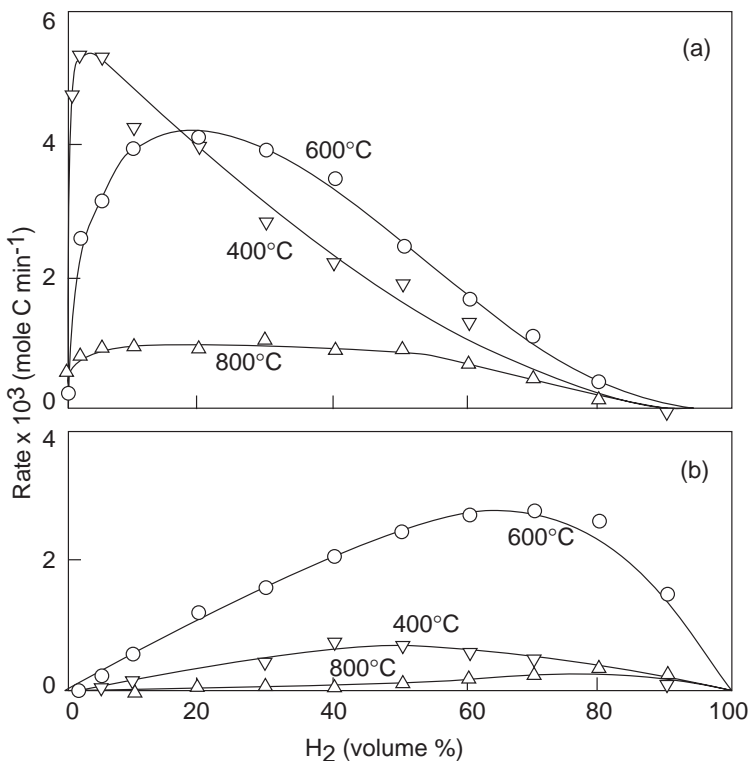
Fig. 2.28 Effect of gas composition (H_2–CO) on rate of carbon deposition on 660-mg porous iron granules at 1 atm(a) by reaction $2CO \rightarrow C + CO_2$ and (b) by reaction $CO + H_2 \rightarrow C + H_2O$. *From Ref. 57.*

As is seen from the experimental results of Olsson and Turkdogan[57] in Fig. 2.28, the rate of carbon deposition on an iron catalyst in CO–H$_2$ mixtures is a complex function of temperature and gas composition. From the measured rate of carbon deposition and the measured CO$_2$/H$_2$O in the exhaust gas, the rates of reactions 2.3.1 and 2.3.3 were determined. These measured rates are shown in Fig. 2.29 as a function of gas composition at 400, 600 and 800°C. The hydrogen appears to have a dual role: at low concentrations the hydrogen catalyzes reaction 2.3.1, and at high concentrations of hydrogen reaction 2.3.3 contributes directly to carbon deposition.
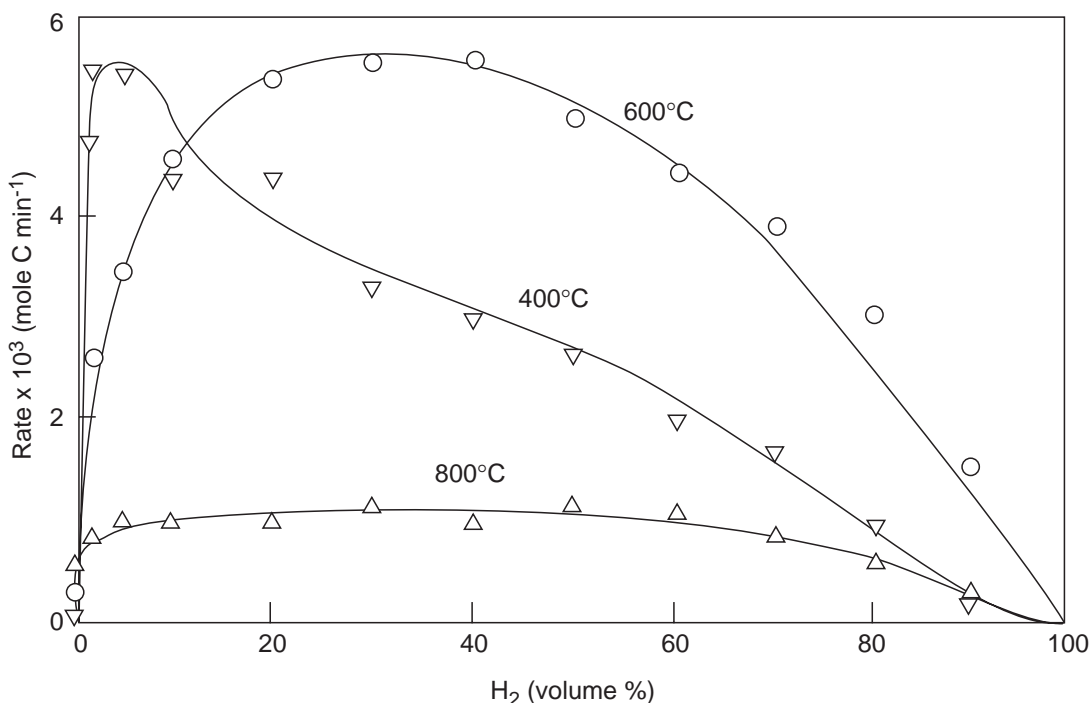
Fig. 2.29 Effect of gas composition (H$_2$–CO) on rate of carbon deposition on 660–mg porous iron granules at atmospheric pressure and indicated temperatures. *From Ref. 57.*

Although H$_2$O is expected to retard or inhibit carbon deposition by virtue of reverse reaction 2.3.4, it has been found[57] that an addition of 0.5%–2% H$_2$O to CO–CO$_2$ mixtures enhances the rate of carbon deposition at 400–600°C. A similar catalytic effect of H$_2$O has been observed for carbon deposition from methane in the presence of nickel[58]. We might mention in passing that the rate of carbon formation by the disproportionation of carbon monoxide is much faster than the pyrolysis of methane under similar conditions.[59] Ever since the first observations made by Byrom[60] and soon after by Carpenter and Smith[61], it has become generally recognized that sulfur in the gas retards or inhibits the catalytic action of iron in the decomposition of carbon monoxide. This is due to the coating of iron surface with cementite, which does not decompose readily in the presence of sulfur. In fact, in the Stelling process[62] the iron ore is reduced to cementite in a CO–CO$_2$ atmosphere without the formation of free carbon, probably because of the presence of sulfur in the system.

The nitrogen-bearing gaseous species such as NH$_3$ and (CN)$_2$ are also known to retard the decomposition of carbon monoxide.[62–63] Again, this may be attributed to extended metastability of cementite in the presence of nitrogen. The retarding effect of sulfur and nitrogen on carbon deposition is similar to sluggish graphitization of steel (by decomposition of cementite) in the presence of sulfur and nitrogen in solution in steel.

The carburization of iron in gas mixtures containing H_2 and CO following reactions similar to 2.3.1 and 2.3.3 occurs on iron surfaces. These reactions are relevant to the early stages of metal dusting and were studied by Fruehan and Martonik.[64] They also found that the rate of reaction 2.3.3 is faster than 2.3.1 and contributes significantly to the carburization of iron[64] as shown in Fig.2.30. When CO is replaced by H_2 the rate increases significantly. The H_2–CO reaction rate constant is approximately tenfold greater than that for CO for carburization.

2.3.2 Transport Properties

The molecular transfer of mass, momentum and energy are interrelated transport processes of diffusion under a concentration gradient, viscous flow in a velocity gradient and heat conduction in a thermal gradient.

The derivation of the transport properties from the rigorous kinetic theory of gases, described in depth by Chapman and Cowling[65] and Hirschfelder *et al*.[66] is based on the evaluation of the intermolecular energy of attraction, the collision diameter and the collision integral involving the dynamics of a molecular encounter, hence the intermolecular force law.

For a brief description of the theoretical equations for the calculation of the transport properties of gases, reference may be made to a previous publication.[52] For the present purpose, it is sufficient to give selected numerical data on the transport properties of a few gases, relevant to ironmaking and steelmaking processes.
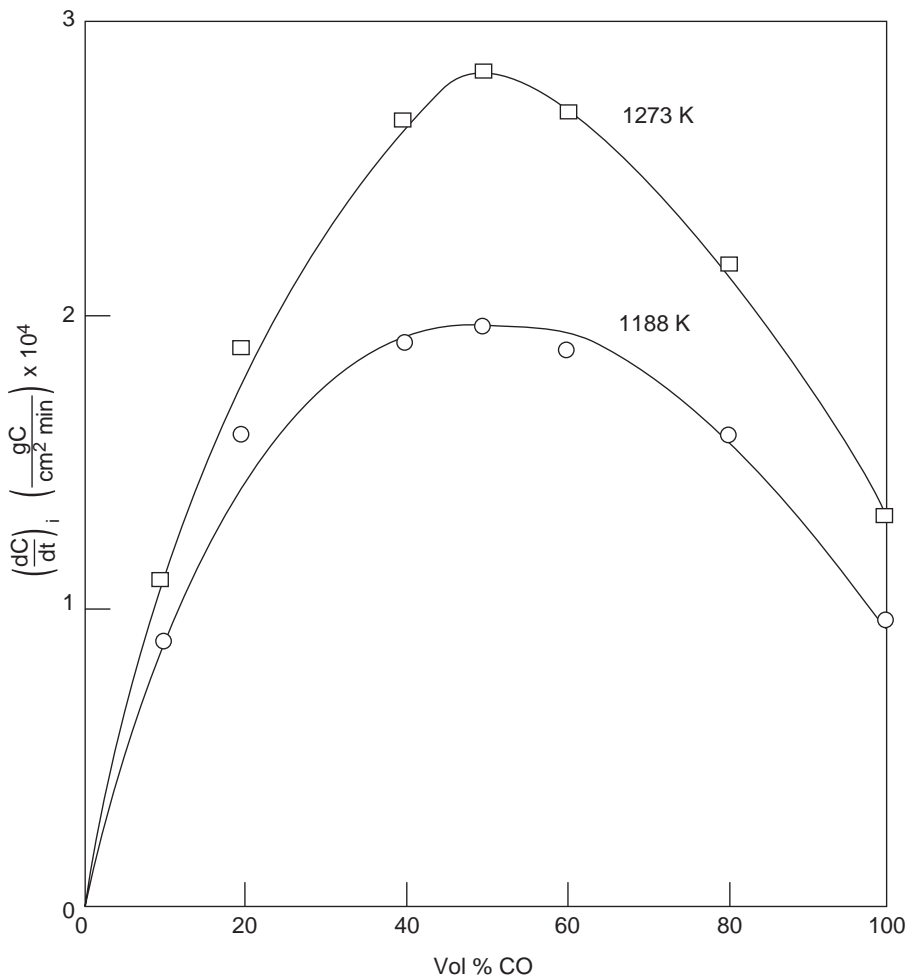
Fig. 2.30 Initial rates of carburization or iron in H_2–CO mixtures (p_T = 0.965 atm). *From Ref. 64.*

Table 2.2   Diffusivity *D* at 1 atm Pressure: cm²s⁻¹ ≡ 10⁻⁴m²s⁻¹

Gas	Temperature, K			
	300	1000	1500	2000
H_2	1.46	10.82	21.07	33.90
Ar	0.18	1.46	2.88	4.56
N_2	0.20	1.59	3.05	4.98
O_2	0.22	1.67	3.27	5.30
CO	0.20	1.63	3.20	5.19
CO_2	0.11	0.93	1.87	3.00
H_2O	0.28	2.83	5.79	9.57

Table 2.3   Viscosity η (poise) ≡ g cm⁻¹ s⁻¹ ≡ 0.1N s m⁻² ≡ 0.1J m⁻³s

Gas	Temperature, K			
	300	1000	1500	2000
H_2	0.89	1.95	2.53	3.06
Ar	2.50	5.34	6.98	8.27
N_2	1.77	4.07	5.11	6.30
O_2	2.07	4.82	6.20	7.64
CO	1.79	4.15	5.34	6.53
CO_2	1.49	3.85	5.01	6.05
H_2O	1.57	4.77	6.44	7.84

Table 2.4   Thermal Conductivity κ × 10⁴, J cm⁻¹s⁻¹K⁻¹ ≡ × 10², kg m s⁻³K⁻¹ ≡ × 10², Wm⁻¹K⁻¹

Gas	Temperature, K			
	300	1000	1500	2000
H_2	17.45	39.96	53.87	67.64
Ar	1.97	4.18	5.44	6.44
N_2	2.50	6.18	8.15	10.53
O_2	2.57	6.68	9.02	11.62
CO	2.53	6.35	8.57	10.96
CO_2	1.62	5.49	7.71	9.95
H_2O	3.84	13.55	20.20	26.93

2.3.2.1 Interrelations Between Transport Properties

2.3.2.1.1 Viscosity/Thermal Conductivity

For monatomic gases,

$$\kappa = \frac{15\,R}{4\,M}\,\eta \qquad\qquad (2.3.10)$$

where

R = 8.314 J mol⁻¹K⁻¹ (molar gas constant),
M = molecular mass, kg mol⁻¹,
η = viscosity, Nsm⁻² ≡ Jm⁻³s.

For polyatomic gases,

$$\kappa = \frac{15\,R}{4\,M}\,\eta\left\{\frac{4}{15}\,\frac{C_V}{R} + \frac{3}{5}\right\} \tag{2.3.11}$$

where C_V is the molar heat capacity at constant volume and

$$\left\{\frac{4}{15}\,\frac{C_V}{R} + \frac{3}{5}\right\}$$

is the Eucken[67] correction factor for thermal conductivity of polyatomic gases.

For monatomic gases $C_V = 3R/2$; with this substitution, equation 2.3.11 is reduced to equation 2.3.10. In terms of the molar heat capacity at constant pressure, $C_V = C_p - R$, equation 2.3.11 is transformed to the following form.

$$\kappa = \left(C_P + \frac{5\,R}{4}\right)\frac{\eta}{M} \tag{2.3.12}$$

2.3.2.1.2 Thermal Diffusivity/Thermal Conductivity   The thermal diffusivity, D^T, is analogous to mass diffusivity and is given by the ratio

$$D^T = \frac{\kappa}{\rho\,C_P} \tag{2.3.13}$$

where ρ is the molar density of the gas.

2.3.2.1.3 Temperature and Pressure Effects: The diffusivity, viscosity and thermal conductivity increase with an increasing temperature, thus

$$D \propto T^{3/2} \tag{2.3.14}$$
$$\eta \propto T^{1/2} \tag{2.3.15}$$
$$\kappa \propto T^{1/2} \tag{2.3.16}$$

The viscosity and thermal conductivity are independent of pressure; however, the diffusivity is inversely proportional to pressure.

2.3.2.1.4 Molecular Mass Effect

$$D \propto M^{-1/2} \tag{2.3.17}$$
$$\eta \propto M^{1/2} \tag{2.3.18}$$
$$\kappa \propto M^{-1} \tag{2.3.19}$$

2.3.3 Pore Diffusion

When the pores are small enough such that the mean free path of the molecules is comparable to the dimensions of the pore, diffusion occurs via the collision of molecules with the pore walls. Knudsen[68] showed that the flux involving collision of molecules with reflection from the surface of the capillary wall is represented by the equation

$$J = -\frac{2}{3}\,\overline{v}r\,\frac{dC}{dx} \tag{2.3.20}$$

where $\overline{v}$ is the mean thermal molecular velocity $= (8kT/\pi m)^{1/2}$, r the radius of capillary tube and dC/dx the concentration gradient along the capillary. For r in cm and the Knudsen diffusivity D_K in cm^2s^{-1}

$$D_K = 9.7 \times 10^3\,r\left(\frac{T}{M}\right)^{1/2} \tag{2.3.21}$$

The Knudsen diffusivity being independent of pressure but molecular diffusivity inversely proportional to pressure, it follows that in any porous medium, the Knudsen diffusion predominates at low pressures where the mean free path is larger than the dimensions of the pore.

For the mixed region of molecular and Knudsen diffusion in capillaries, Bosanquet[69] derived the following expression based on the random walk model in which the successive movements of molecules are terminated by collision with the capillary wall or with other molecules:

$$\frac{1}{D} = \frac{1}{D_{Ki}} - \frac{1}{D_{ii}}$$ (2.3.22)

where D_{ii} is the molecular self-diffusivity. For a porous medium of uniform pore structure with pores of equal size, the Bosanquet interpretation formula gives for the effective diffusivity of component i

$$D_{ei} = \frac{\varepsilon}{\tau} \frac{D_{12} D_{Ki}}{D_{12} + D_{Ki}}$$ (2.3.23)

where ε is the volume fraction of connected pores, τ the tortuosity factor, D_{12} the molecular diffusivity for a binary mixture 1–2 and D_{ki} the Knudsen diffusivity of component i for a given uniform pore radius r.

2.3.3.1 Examples of Experimental Data

The experimental data are shown in Fig. 2.31 for effective diffusivity He–CO_2 at 20°C. As discussed in Section 2.2.2.3 the pore structure of iron becomes finer at a lower reduction temperature. It is for this reason that the Knudsen diffusion effect at lower pressures becomes more pronounced for porous iron reduced at 800°C as compared to that reduced at 1000°C. More detailed information is given in the previous publications on the subject of gas diffusion in porous media.[51, 70]
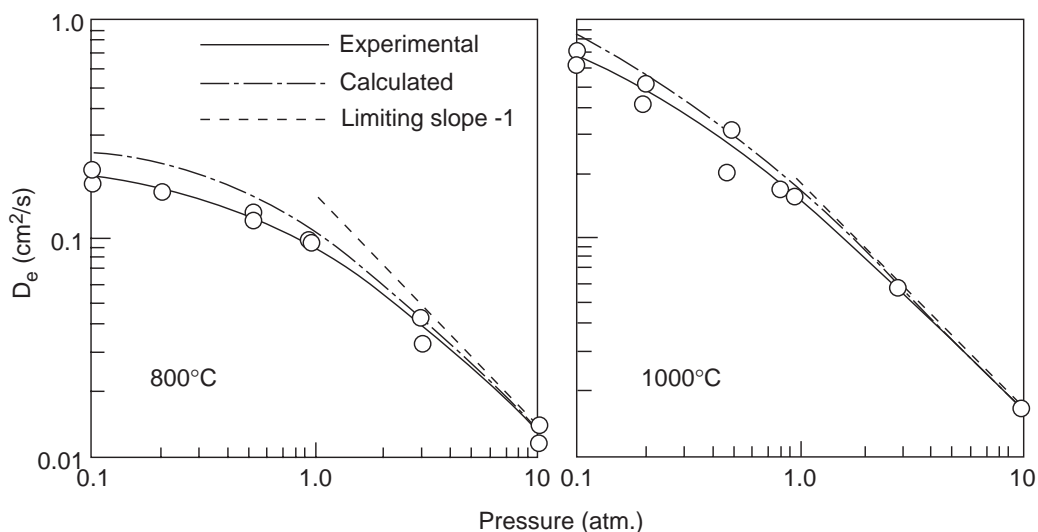
Fig. 2.31 Pressure dependence of effective diffusivity He–CO_2 at 20°C in iron reduced from hematite ore in hydrogen at indicated temperature. *From Ref. 70.*

It is seen from the data in Fig. 2.32 that the effective diffusivities for H_2–H_2O measured directly or calculated from the pore structure considerations, agree well with those derived from the rate measurements within the regime of pore-diffusion control, i.e. from the slopes of the lines in Fig. 2.11. The temperature has a small effect on gas diffusivities. A marked effect of temperature on the effective diffusivity seen in Fig. 2.32 is due mainly to the coarseness of the pore structure of iron when the oxide is reduced at higher temperatures.
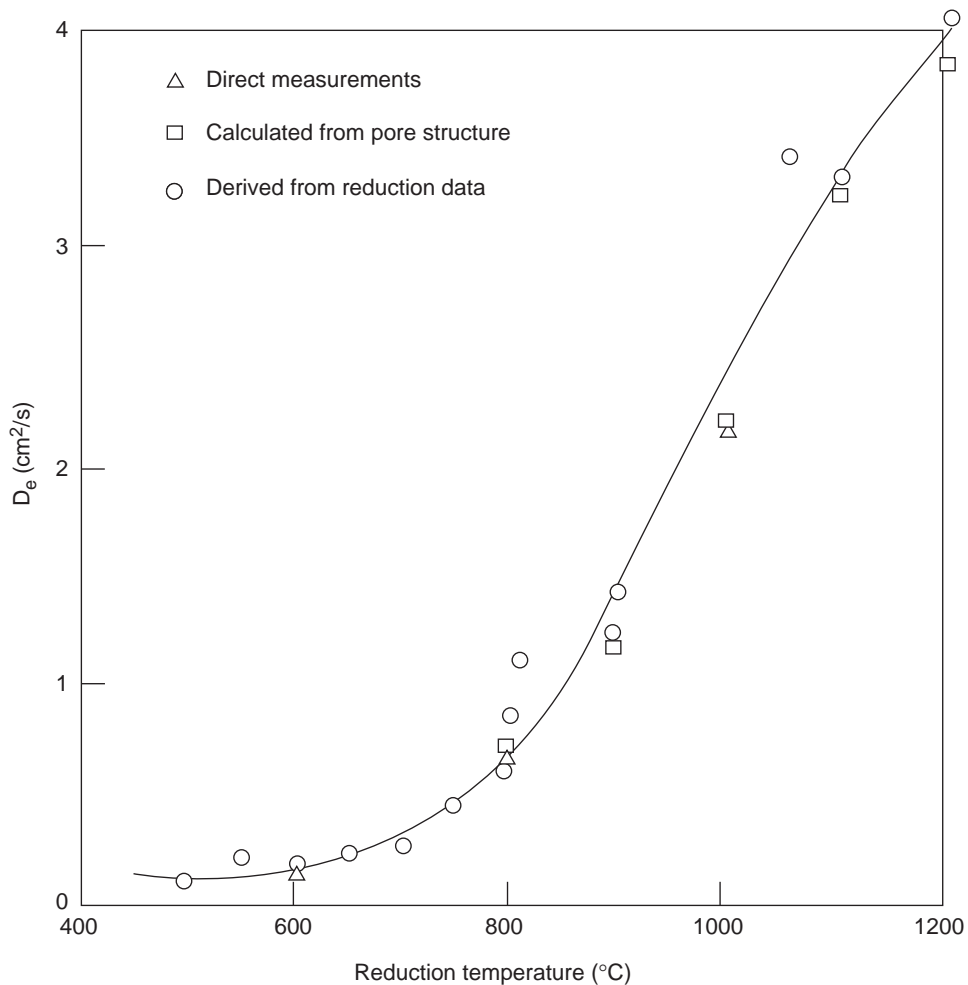
Fig. 2.32 H_2–H_2O effective diffusivity derived from data for rate of reduction of hematite to iron is compared with that obtained by direct measurements and calculated from pore structure. *From Ref. 70.*

In the case of internal burning of carbon, the pore structure becomes coarser as the gasification progresses, resulting in an increase in the effective gas diffusivity. A few examples of the measured CO–CO_2 effective diffusivities for electrode graphite are given in Table 2.5, reproduced from Ref. 17.

Table 2.5   Measured CO–CO_2 Effective Diffusivities for Electrode Graphite

Temperature	% oxidized	D_e(CO–CO_2), $cm^2 s^{-1}$
500	0	0.006
500	3.8	0.016
500	7.8	0.020
500	14.6	0.045
700	0	0.009
700	3.8	0.023
700	7.8	0.029
700	14.6	0.067
800	0	0.012
900	0	0.014

Recently Story and Fruehan[49] demonstrated the effect of Knudsen diffusion in the oxidation of carbon in CO_2–Ar and CO_2–He gas mixtures. Normally one would expect the rate to be significantly faster in CO_2–He and CO_2–Ar due to their higher molecular diffusivities. In general the diffusivity is given by 2.3.22. Knudsen diffusion is important when the pore diameter is smaller than the mean free path of the molecules, where the molecules strike the pore walls and diffusivity does not depend on the molecule size. For ultra pure graphite the overall rate constant for external oxidation, (SDe) as discussed in Section 2.2.2.2, was the same for CO_2–He and CO_2–Ar gas mixtures. For this particular material the pore size was small and Knudsen diffusion predominates. On the other hand for coke with large pores the rate is significantly faster with He as the dilution gas as the pores are large and molecular diffusion dominates.

2.4 Properties of Molten Steel

2.4.1 Selected Thermodynamic Data

The thermodynamic properties of liquid iron alloys have been studied extensively, both experimentally and theoretically. Most of these studies were made over a period from 1950 through 1970. For the present purpose, only a selected set of activity data need to be considered, in relation to the study and understanding of the chemistry of iron and steelmaking reactions.

2.4.1.1 Solute Activity Coefficients

For low solute contents, as in low-alloy steels, the activity is defined with respect to Henry's law and mass percent of the solute

$$a_i = f_i x[\%i] \tag{2.4.1}$$

such that $f_i \rightarrow 1.0$ as $[\%i] \rightarrow 0$.

Up to several percent of the solute content, $\log f_i$ increases or decreases linearly with an increasing solute concentration.

$$\log f_i = e_i[\%i] \tag{2.4.2}$$

The proportionality factor e_i is known as the interaction coefficient.

The binary interaction coefficients e_i^i for dilute solutions in liquid iron are listed in Table 2.6, taken from the data compiled by Sigworth and Elliott.[71]

Table 2.6   Values of e_i^i for Dilute Solutions in Liquid Iron at 1600°C. *From Ref. 71*

Element i	e_i^i	Element i	e_i^i
Al	0.045	O	–0.10
C	0.18	P	0.062
Cu	0.023	S	–0.028
Cr	0.0	Si	0.11
Mn	0.0	Ti	0.013
Ni	0.0	V	0.015

In multicomponent melts, as in alloy steels, the activity coefficient of solute i is affected by the alloying elements for which the formulation is

$$\log f_i = e_i^i[\%i] + \sum e_i^j[\%j] \tag{2.4.3}$$

where e_i^j is the interaction coefficient of i as affected by the alloying element j.

$$e_i^j = \frac{d \log f_i}{d[\%j]} \tag{2.4.4}$$

Selected interaction coefficients in dilute solutions of ternary iron base alloys for C, H, N, O and S at 1600°C are given in Table 2.7.

Table 2.7   Selected Interaction Coefficients in Dilute Solutions of Ternary Iron Base Alloys for C, H, N, O and S at 1600°C. *From Ref. 71.*

Element j	e_C^j	e_H^j	e_N^j	e_O^j	e_S^j
Al	0.043	0.013	−0.028	−3.9	0.035
C	0.14	0.06	0.13	−0.13	0.11
Cr	−0.024	−0.002	−0.047	−0.04	−0.011
Mn	−0.012	−0.001	−0.02	−0.021	−0.026
N	0.13	0	0	0.057	0.007
O	−0.34	−0.19	0.05	−0.20	−0.27
P	0.051	0.011	0.045	0.07	0.029
S	0.046	0.008	0.007	−0.133	−0.028
Si	0.08	0.027	0.047	−0.131	0.063

For the mass concentrations of carbon and silicon above 1%, as in the blast furnace and foundry irons, the following values of f_S^j should be used.

Mass % C or Si:

	2.0	2.5	3.0	3.5	4.0	4.5	5.0
f_S^C:	1.79	2.14	2.53	3.05	3.74	4.56	5.75
f_S^{Si}:	1.37	1.50	1.64	1.78	1.95	2.10	2.32

2.4.1.2 Free Energies of Solution in Liquid Iron

For the solution of element X_i in liquid iron at mass % X_i,

$$X_i \, (\text{pure}) = [X_i] \, (1 \text{ mass \%})$$

the free energy of solution is

$$\Delta G_S = RT \ln\left(\frac{0.5585}{M_i} \gamma_i^\circ \right) \tag{2.4.5}$$

where M_i is the atomic mass (g-atom) and γ_i° the activity coefficient (with respect to pure element) at infinite dilution ($\%X_i \rightarrow 0$).

For ΔG_S in J mol^{-1} and substituting log for ln,

$$\Delta G_S = 19.144 \, T \log\left(\frac{0.5585}{M_i} \gamma_i^\circ \right) \tag{2.4.6}$$

The free energies of solution of various elements in liquid iron are listed in Table 2.8.

2.4.2 Solubility of Gases in Liquid Iron

Diatomic gases such as O_2, S_2, N_2 and H_2 dissolve in liquid and solid metals in the atomic form

$$\tfrac{1}{2} X_2(g) = [X] \tag{2.4.7}$$

for which the isothermal equilibrium constant is

$$K = \frac{[\%X]}{\left(p_{X_2} \right)^{1/2}} \tag{2.4.8}$$

For ideal solutions, the concentration of X is directly proportional to the square root of the equilibrium gas partial pressure; this is known as the Sievert's law.

Table 2.8 Free Energies of Solution in Liquid Iron for 1 mass %: (g) gas, (l) liquid, (s) solid. *From Ref. 71.*

Element i	γ^o_i	ΔG_s, Jmol^{-1}		
Al(l)	0.029	−63,178	−	27.91T
C(gr)	0.57	22,594	−	42.26T
Co(l)	1.07	1,004	−	38.74T
Cr(s)	1.14	19,246	−	46.86T
Cu(l)	8.60	33,472	−	39.37T
$\frac{1}{2}H_2$(g)	–	36,377	+	30.19T
Mg(g)	–	−78,690	+	70.80T
Mn(l)	1.30	4,084	−	38.16T
$\frac{1}{2}N_2$(g)	–	3,599	+	23.74T
Ni(l)	0.66	−20,920	−	31.05T
$\frac{1}{2}O_2$(g)	–	−115,750	−	4.63T
$\frac{1}{2}P_2$(g)	–	−122,173	−	19.25T
$\frac{1}{2}S_2$(g)	–	−135,060	+	23.43T
Si(l)	0.0013	−131,500	−	17.24T
Ti(s)	0.038	−31,129	−	44.98T
V(s)	0.10	−20,710	−	45.61T
W(s)	1.20	31,380	−	63.60T
Zr(s)	0.043	−34,727	−	50.00T

2.4.2.1 Solubilities of H_2, N_2 and O_2

For the solute content in ppm (by mass) and the gas pressure in atm., the temperature dependence of the equilibrium constants for H_2, N_2 and O_2 solubilities are given in Table 2.9 from the compiled data cited in Ref. 27.

Table 2.9 Equilibrium Constants of Solubilities of H_2, N_2 and O_2 in Liquid Iron.

$$\log \frac{[\text{ppm H}]}{\left(p_{H_2}\right)^{\frac{1}{2}}} = -\frac{1900}{T} + 2.423 \qquad (2.4.9)$$

$$\log \frac{[\text{ppm N}]}{\left(p_{N_2}\right)^{\frac{1}{2}}} = -\frac{188}{T} + 2.760 \qquad (2.4.10)$$

$$\log \frac{[\text{ppm O}]}{\left(p_{O_2}\right)^{\frac{1}{2}}} = \frac{6046}{T} + 4.242 \qquad (2.4.11)$$

2.4.2.2 Solubility of Gaseous Oxides

2.4.2.2.1 Solubility of CO   Carbon monoxide dissolves in liquid iron (steel) by dissociating into atomic carbon and oxygen

$$CO(g) = [C] + [O] \qquad (2.4.12)$$

for which the equilibrium constant (which is not too sensitive to temperature) is given by the following equation for low alloy steels containing less than 1% C.

$$K = \frac{[\%C][\text{ppm O}]}{p_{CO}(\text{atm})} = 20 \tag{2.4.13}$$

At higher carbon contents, a correction should be made to K regarding the activity coefficients f_O^C (log $f_O^C = -0.13[\%C]$) and f_C^C(log $f_C^C = 0.18[\%C]$).

For the reaction

$$CO_2 \text{ (g)} = CO(g) + [O] \tag{2.4.14}$$

$$K = \frac{p_{CO}}{p_{CO_2}}[\text{ppm O}] = 1.1 \times 10^4 \text{ at } 1600°C \tag{2.4.15}$$

For 800 ppm O in low carbon steel at tap, the equilibrium ratio p_{CO}/p_{CO_2} is 13.75. For this state of equilibrium, the gas mixture contains 6.8% CO_2 and 93.2% CO.

2.4.2.2.2 Solubility of H₂O From the free energy of formation of water vapor and the solubilitites of hydrogen and oxygen in liquid iron, the following equilibrium constant is obtained for the reaction of water vapor with liquid iron for 1600°C.

$$H_2O(g) = 2[H] + [O] \tag{2.4.16}$$

$$K = \frac{[\text{ppm H}]^2[\text{ppm O}]}{p_{H_2O}(\text{atm})} = 1.77 \times 10^6 \text{ at } 1600°C \tag{2.4.17}$$

The hydrogen and oxygen contents of low alloy liquid steel in equilibrium with H_2–H_2O mixtures at 1 atm pressure and 1600°C are shown in Fig. 2.33.
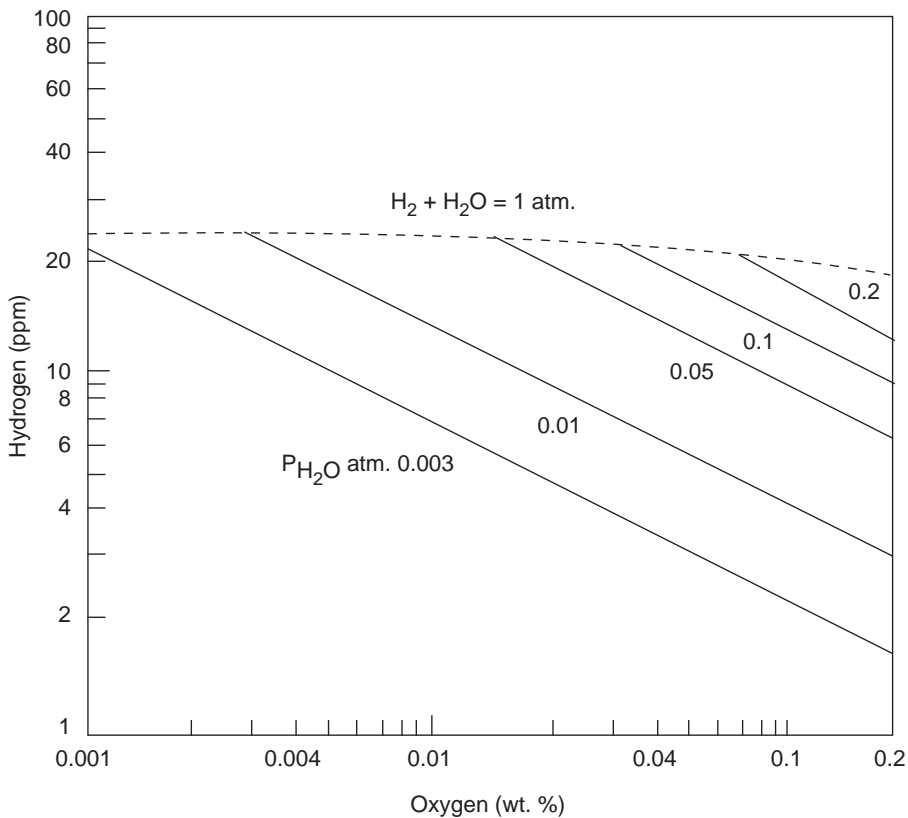
Fig. 2.33 Concentrations of hydrogen and oxygen in liquid iron at 1600°C in equilibrium with indicated compositions of H_2–H_2O mixtures.

2.4.2.2.3 Solubility of SO$_2$ From the free energy of formation of SO$_2$ and the solubilities of gaseous sulfur and oxygen in liquid iron, the following equilibrium constant is obtained for the reaction of SO$_2$ with liquid iron at 1600°C.

$$SO_2(g) = [S] + 2[O] \tag{2.4.18}$$

$$K = \frac{[\%S][\%O]^2}{p_{SO_2}\,(\text{atm})} = 1558 \text{ at } 1600°C \tag{2.4.19}$$

For the concentrations of sulfur and oxygen present in liquid steel, it is seen that the corresponding equilibrium pressure of SO$_2$ is infinitesimally small. It is for this reason that no sulfur can be oxidized to SO$_2$ during steelmaking with oxygen blowing.

2.4.3 Iron-Carbon Alloys

2.4.3.1 Fe-C Phase Equilibrium Diagram

Since carbon is one of the most important ingredients of steel, the study of the iron-carbon phase equilibrium diagram has received much attention during the past several decades. The phase diagram is given in Fig. 2.34.
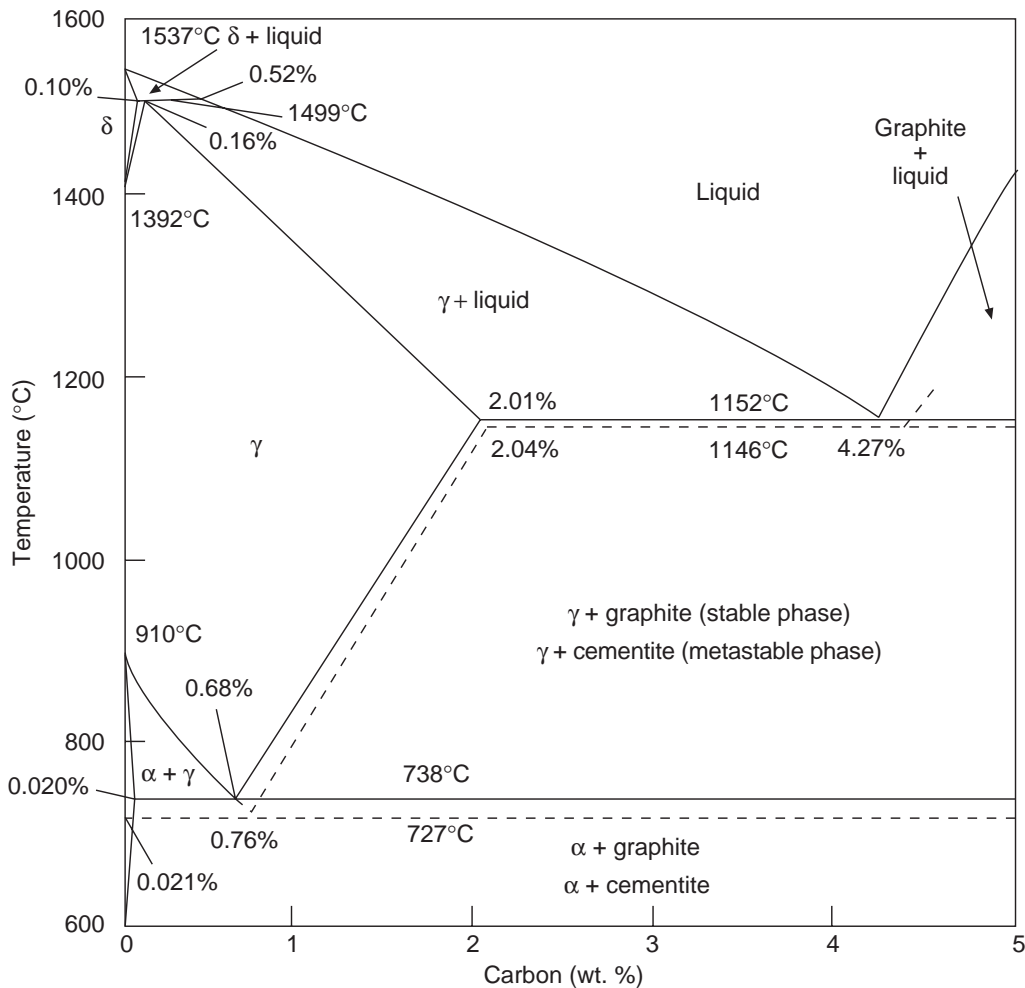
Fig. 2.34 Iron-carbon phase equilibrium diagram. Dashed lines represent phase boundary for metastable equilibrium with cementite.

There are three invariants in this system; peritectic at 1499°C, eutectic at 1152°C and eutectoid at 738°C. The phase boundaries shown by broken lines are for the metastable equilibrium of cementite, Fe_3C, with austenite. During heat treatment of steel if sufficient time is allowed, iron-carbon alloys containing austenite and cementite decompose to austenite and graphite. The solubilitites of graphite and of cementite in α-iron below the eutectoid temperature are given by the following equations

$$\log \%C\,(graphite) = -\frac{5250}{T} + 3.53 \qquad (2.4.20)$$

$$\log \%C\,(cementite) = -\frac{3200}{T} + 1.50 \qquad (2.4.21)$$

The solubility of graphite in pure liquid iron is well established through many independent studies; the experimental data are summarized by the equation

$$[\%C] = 1.30 + 2.57 \text{ x } 10^{-3}T(°C) \qquad (2.4.22)$$

If atom fraction N_C is used, the same set of data can be represented by the following equation in terms of $\log N_C$ and the reciprocal of the absolute temperature.

$$\log N_C = -\frac{560}{T} - 0.375 \qquad (2.4.23)$$

The effect of silicon, phosphorus, sulfur, manganese, cobalt and nickel on the solubility of graphite in molten iron was determined by Turkdogan *et al.*[72, 73] and graphite solubility in iron-silicon and iron-manganese melts by Chipman et at.[74, 75] Similar measurements with iron-chromium melts were made by Griffing and co-workers.[76] The experimental data are given graphically in Fig. 2.35 for 1500°C; the solubility at other temperatures can be estimated from this plot by using the temperature coefficient given in equation 2.4.22 for binary iron-carbon melts. In the iron-sulfur-carbon system there is a large miscibility gap. For example, at 1500°C the melt separates into two liquids containing phase (I) 1.8% S and 4.24% C and phase (II) 26.5% S and 0.90% C.

2.4.3.2 Activity Coefficient of Carbon

The activity of carbon in liquid iron was measured in many independent studies. The data compiled and re-assessed by Elliott *et al.*[77] are given in Figs. 2.36 and 2.37 as activity coefficients γ_C and f_C for two different standard states.

2.4.3.3 Peritectic Reaction

The peritectic reaction occurring in the early stages of solidification of low carbon steels is of particular importance in the continuous casting of steel. The peritectic region of the Fe–C system is shown on a larger scale in Fig. 2.38. As the temperature decreases within the two phase region, δ+liquid, the carbon contents of δ-iron and residual liquid iron increase. At the peritectic temperature 1499°C, δ-iron containing 0.10% C reacts with liquid iron containing 0.52% C to form γ-iron with 0.16% C.
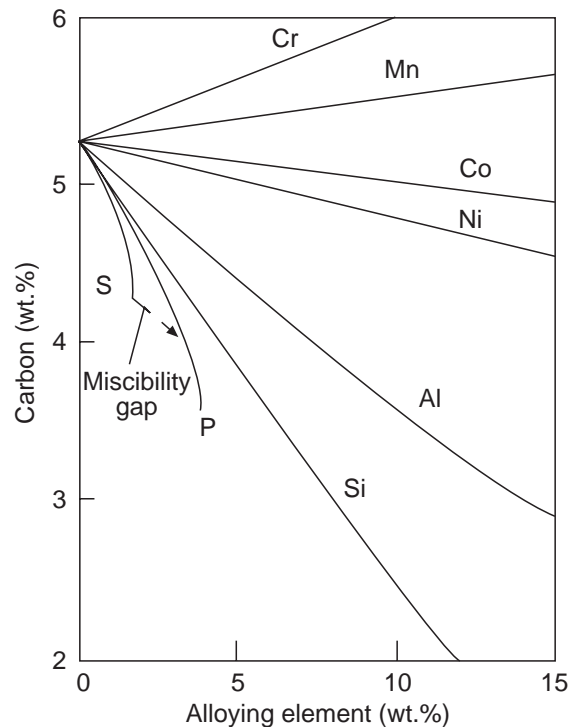
Fig. 2.35 Solubility of graphite in alloyed iron melts at 1500°C.
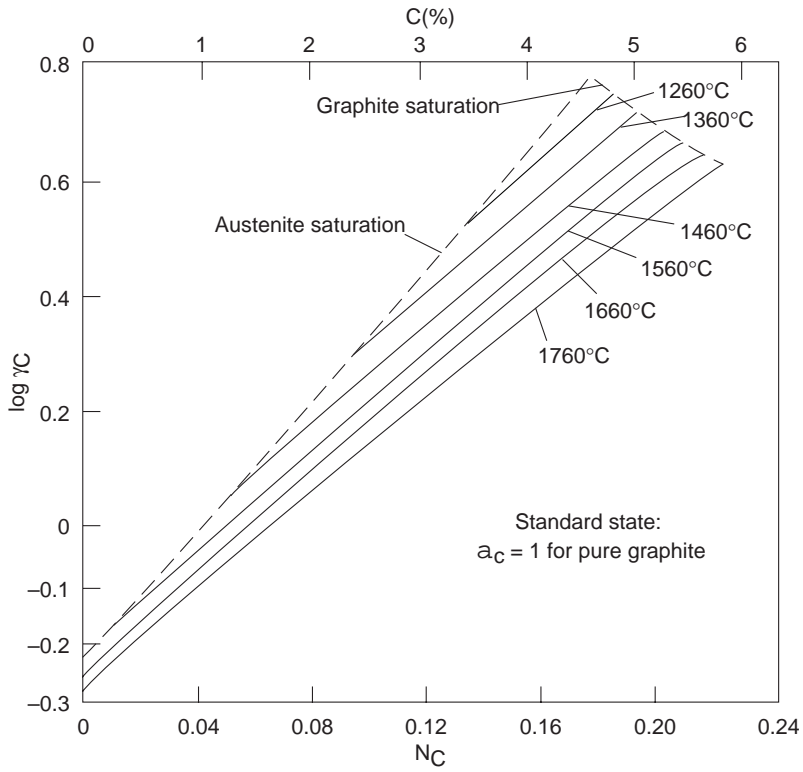
Fig. 2.36 Activity coefficient (γ_C) of carbon in liquid iron.
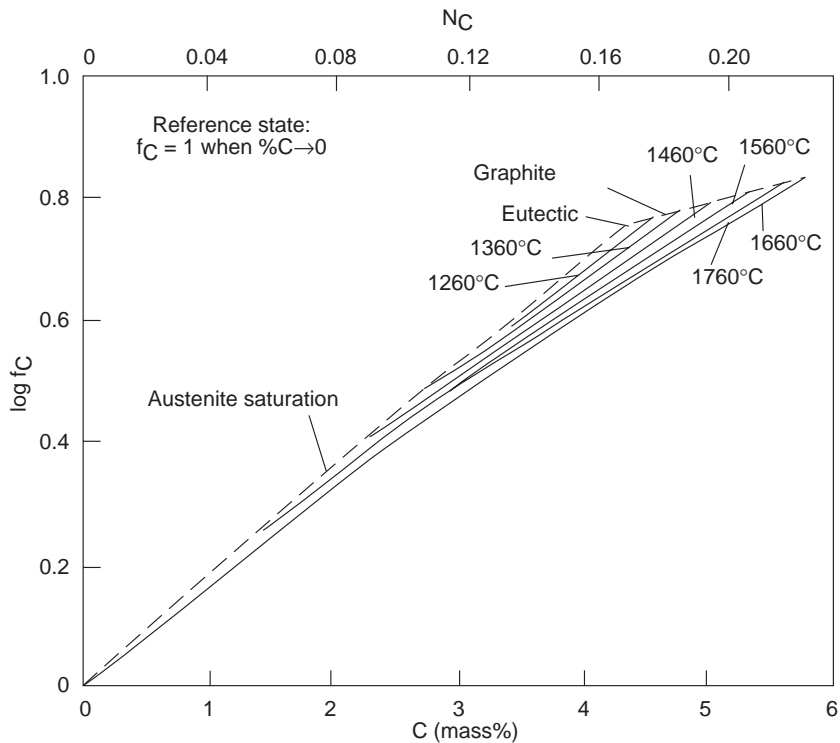
Fig. 2.37 Activity coefficient (f_C) of carbon in liquid iron.
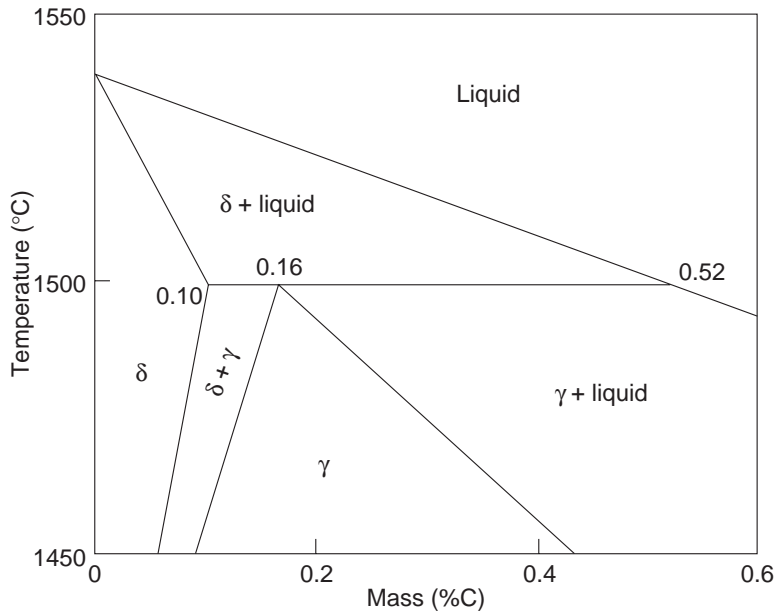
Fig. 2.38 Peritectic region of binary iron-carbon system.

The X-ray diffraction data give for the densities of iron-carbon alloys: 7.89 g cm^{-3} for δ–Fe with 0.10% C and 8.26 g cm^{-3} for γ–Fe with 0.16% C. Hence, the δ to γ phase transformation is accompanied by 4.7% volume shrinkage. Because of this shrinkage, the thin solidified shell in the mould of the caster will contract, producing a gap between the shell surface and mould wall. This situation leads to an uneven surface which is in partial contact with the mould wall, hence resulting in reduced heat flux at contracted areas. A reduced solidification growth rate and a nonuniform shell with thin spots, lowers the resistance of the steel to cracking which may cause a breakout in the mould. This phenomenon was well demonstrated experimentally by Singh and Blazek[78] using a bench scale caster; this subject is discussed further in a paper by Wolf and Kurz.[79]

In low alloy steels containing 0.10 to 0.16% C, the solid/liquid ratio at the peritectic invariant is higher than for steels containing more than 0.16% C. Therefore, due to the peritectic reaction, low alloy steels with 0.10 to 0.16% C are more susceptible to the development of surface cracks in continuous casting than steels with higher carbon contents.

2.4.3.3.1 Effect of Alloying Elements on Peritectic Invariant As shown schematically in Fig. 2.39 for the ternary Fe–C–X, or multicomponent alloy steels, the peritectic reaction occurs over a temperature and composition range. From the experimental data on the liquidus and solidus temperatures of alloy steels, the carbon and temperature equivalents of alloying elements have been evaluated in three independent investigations.[80–82]
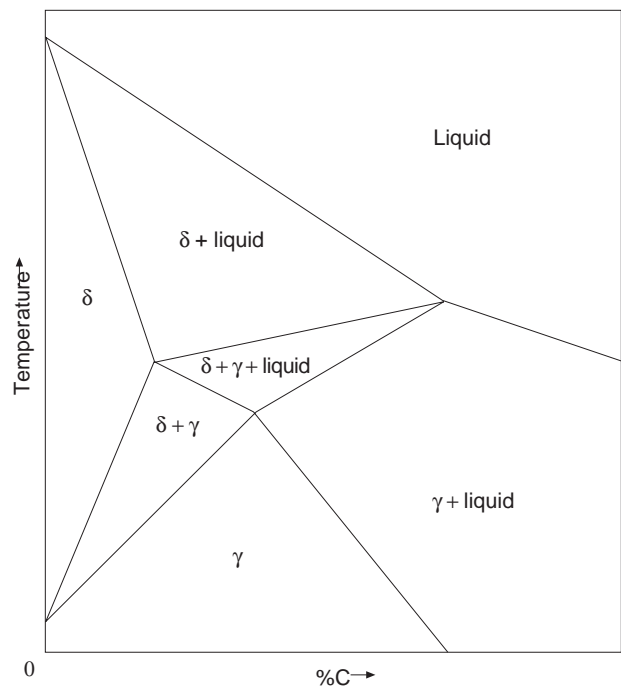
Fig. 2.39 Schematic representation of phase boundaries in low alloy steels as pseudo binary Fe–C system.

The carbon equivalents of the alloying elements for the peritectic reaction

$$C(\delta - Fe) + C\ (l - Fe) = C\ (\gamma - Fe) \tag{2.4.24}$$
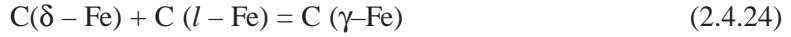
are usually formulated as follows

$$\text{Liquid phase:}\ \ \Delta\%C = 0.52 + \sum \Delta C_{P\ell}^{X}[\%X] \tag{2.4.25}$$

$$\text{Delta phase:}\ \ \Delta\%C = 0.10 + \sum \Delta C_{P\delta}^{X}[\%X] \tag{2.4.26}$$

The changes in peritectic temperatures are formulated as

$$\text{Liquid phase:}\ \ \Delta T = 1499°C + \sum \Delta T_{P\ell}^{X}[\%X] \tag{2.4.27}$$

$$\text{Delta phase:}\ \ \Delta T = 1499°C + \sum \Delta T_{P\delta}^{X}[\%X] \tag{2.4.28}$$

The coefficients ΔC_{P}^{X} and ΔT_{P}^{X} can be positive or negative, depending on the alloying element X. The peritectic temperature and carbon coefficients determined by Yamada *et al.*[81] are listed in Table 2.10 with minor numerical adjustments to some of the parameters in accord with the empirical correlations given in Fig. 2.40, reproduced from Ref. 27.
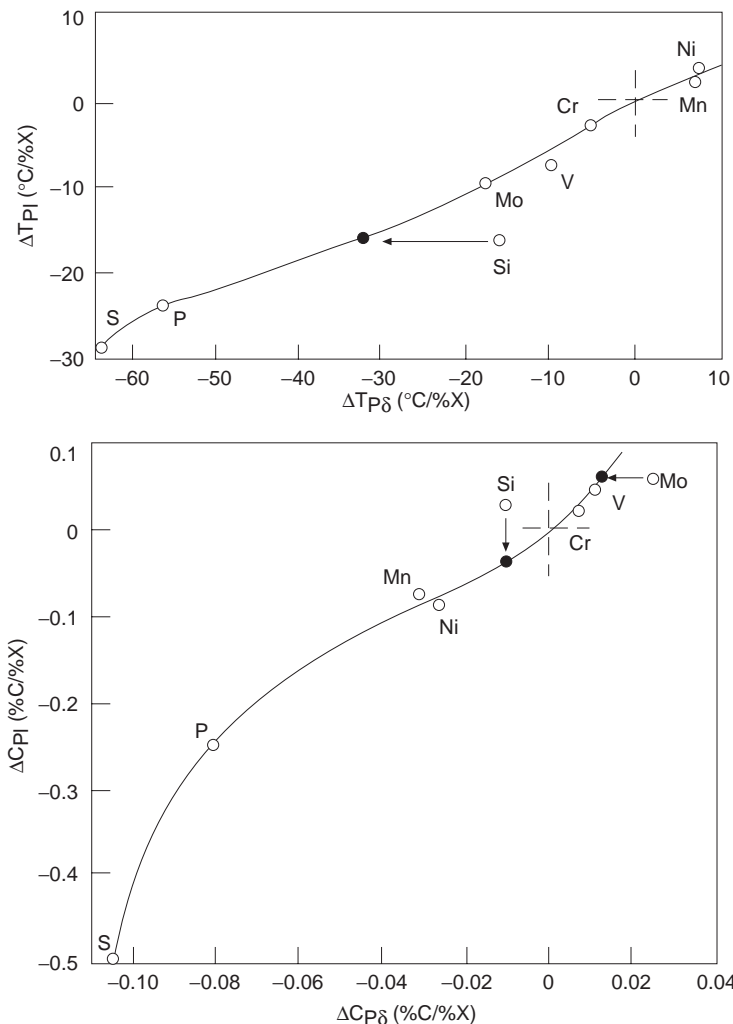
Fig. 2.40 Interrelations between peritectic temperature and composition changes. *From Ref. 27.*

Table 2.10 Peritectic Temperature and Composition Parameters in Accord with the Curves in Fig. 2.40.

Alloying Element	Composition range, wt.%	Δ°C/%X		Δ%C/%X	
		$\Delta T_{P\gamma}$	$\Delta T_{P\delta}$	$\Delta C_{P\gamma}$	$\Delta C_{P\delta}$
Cr	<1.5	–3	–5	+0.022	+0.006
Mn	<1.5	+3	+7	–0.085	–0.029
Mo	<1.5	–10	–18	+0.055	+0.012
Ni	<3.5	+4	+9	–0.082	–0.027
P	<0.05	–24	–56	–0.250	–0.080
S	<0.03	–28	–64	–0.500	–0.105
Si	<0.6	–16	–32	–0.035	–0.010
V	<1.0	–6	–11	+0.045	+0.010

The phase boundaries in the peritectic region of the Fe–C–X alloys, projected on the Fe–C–X composition diagram, are shown schematically in Fig. 2.41 for alloys where X is: (a) ferrite stabiliser and (b) austenite stabiliser. In the Fe–C–Mn (or Ni) system, the peritectic reaction occurs at all compositons between the peritectic regions of the binaries Fe–C and Fe–Mn (Ni) systems. In the Fe–C alloys with ferrite stabilisers, the peritectic reaction will not occur beyond a certain concentration of the alloying element X as shown in Fig. 2.41. This limiting case applies only to high alloy steels.

2.4.4 Liquidus Temperatures of Low Alloy Steels

The liquidus temperatures of low alloy steels are derived from the binary Fe–X systems on the assumption that the coefficients $\alpha = \Delta T/\%X$ are additive in their effects on the melting point of iron.

Below 0.5% C, where the solidification begins with the formation of delta (δ) iron, the following equation would apply

$$\text{Liquidus T (°C)} = 1537 - 73.1[\%C] + \Sigma\alpha[\%X] \qquad (2.4.29)$$

For the carbon contents within the range 0.5 to 1.0% C, where the solidification begins with the formation of gamma (γ) iron, the following equation is recommended.

$$\text{Liquidus T (°C)} = 1531 - 61.5[\%C] + \Sigma\alpha[\%X] \qquad (2.4.30)$$

The same coefficients α are used in both equations.

Alloying element X	Coefficient α, °C/%X
Al	–2.5
Cr	–1.5
Mn	–4.0
Mo	–5.0
Ni	–3.5
P	–30.0
Si	–14.0
S	–45.0
V	–4.0

2.4.5 Solubility of Iron Oxide in Liquid Iron

Subsequent to earlier studies by various investigators, Taylor and Chipman[83] made the most reliable measurement of the oxygen solubility in liquid iron in equilibrium with essentially pure liquid iron oxide at temperatures of 1530–1700°C. In a later study, Distin *et al.*[84] extended the solubility measurements up to 1960°C. The solubility data are represented by the equation

$$\log[\%O]_{sat.} = -\frac{6380}{T} + 2.765 \qquad (2.4.31)$$

The oxygen content of liquid iron oxide in equilibrium with liquid iron decreases with an increasing temperature as given below and reaches the stoichiometric composition (22.27%) at about 2000°C.

Temperature °C	%O in iron	%O in liquid iron oxide
1527 (eutectic)	0.16	22.60
1785	0.46	22.40
1880	0.63	22.37
1960	0.81	22.32

2.4.6 Elements of Low Solubility in Liquid Iron

A few elements of low solubility in liquid iron play some role in the steelmaking technology; a brief comment on the chemistry of such elements in liquid iron is considered desirable.

2.4.6.1 Lead

The break out of the furnace lining is often blamed on the presence of lead in the melt. Small amounts of metal trapped in the crevices of the lining are likely to get oxidized subsequent to tapping. The lead oxide together with iron oxide will readily flux the furnace lining, hence widening the cracks which ultimately leads to failure of the lining. The solubility of lead in liquid iron is sufficiently high that in normal steelmaking practice there should be no accumulation of lead at the bottom of the melt, except perhaps in the early stages of the melting of lead-containing scrap.

At steelmaking temperatures the vapor pressure of lead is about 0.5 atm and the solubility[85] in liquid iron is about 0.24% Pb at 1500°C increasing to about 0.4% Pb at 1700°C. The free-machining leaded steels contain 0.15 to 0.35% Pb. Evidently lead added to such steels is in solution in the metal prior to casting and precipitates as small lead spheroids during the early stages of freezing.

2.4.6.2 Calcium

The boiling point of calcium is 1500°C and its solubility in liquid iron is very low. Sponseller and Flinn[86] measured the solubility of calcium in iron at 1607°C for which the calcium vapor pressure is 1.69 atm. Under these conditions at 1607°C, 0.032% Ca is in solution. That is, the solubility at 1 atm pressure is 189 ppm Ca. They also investigated the effect of some alloying elements on the solubility; as seen from the data in Fig. 2.42, C, Si, Ni and Al increase markedly the calcium solubility in liquid iron. In melts saturated with CaC_2 the solubility of calcium of course decreases with an increasing carbon content.
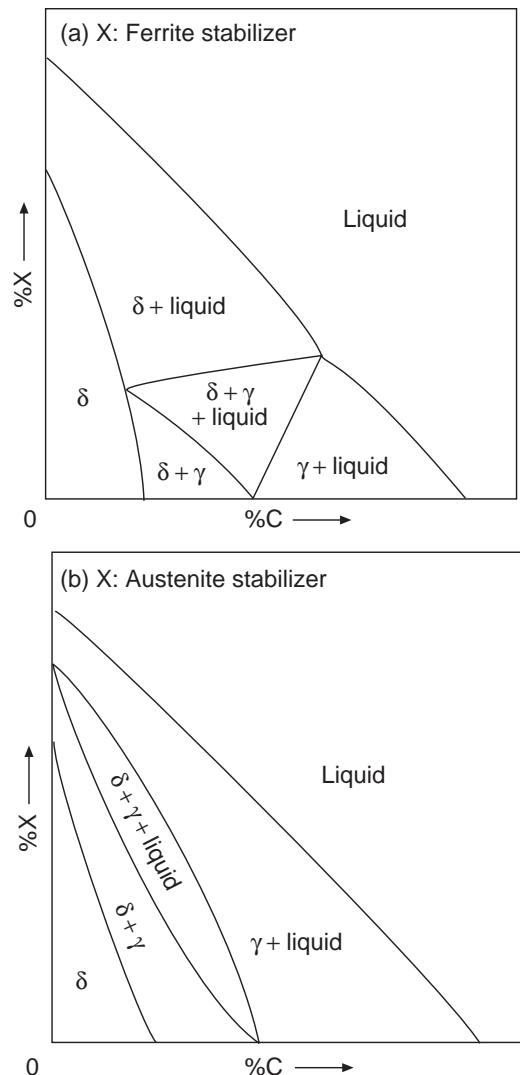
Fig. 2.41 Phase boundaries in the peritectic region of the Fe-C-X alloys projected on the composition diagram.

2.4.6.3 Magnesium

The solubility of magnesium in iron-carbon alloys determined by Trojan and Flinn[87], is shown is Fig. 2.43 as functions of temperature and carbon content. Subsequently, Guichelaar et al.[88], made similar measurements with liquid Fe-Si-Mg alloys. Their data have been used in numerous studies to derive the equilibrium relations for the solubility of magnesium in liquid iron. However, there are some variations in the interpretation of the above mentioned experimental data. A reassessment of these experimental data is considered desirable.

The equilibrium relation for the solubility of Mg (in units of mass % atm^{-1}) is represented by

$$Mg(g) = [Mg]$$

$$K_{Mg} = \frac{[\%Mg]f_{Mg}}{P_{Mg}} \qquad (2.4.32)$$

where f_{Mg} is the activity coefficient affected by the alloying elements. In the experiments with the Fe–C–Mg melts coexistent with liquid Mg, the latter contained less than 2 percent Fe, therefore, the Mg vapor pressure prevailing in the reactor would be essentially the same as that for pure Mg for which the following is obtained from the data of Guichelaar, *et al*.

$$\log P_{Mg}^o (atm) = -\frac{6730}{T} + 4.94 \qquad (2.4.33)$$
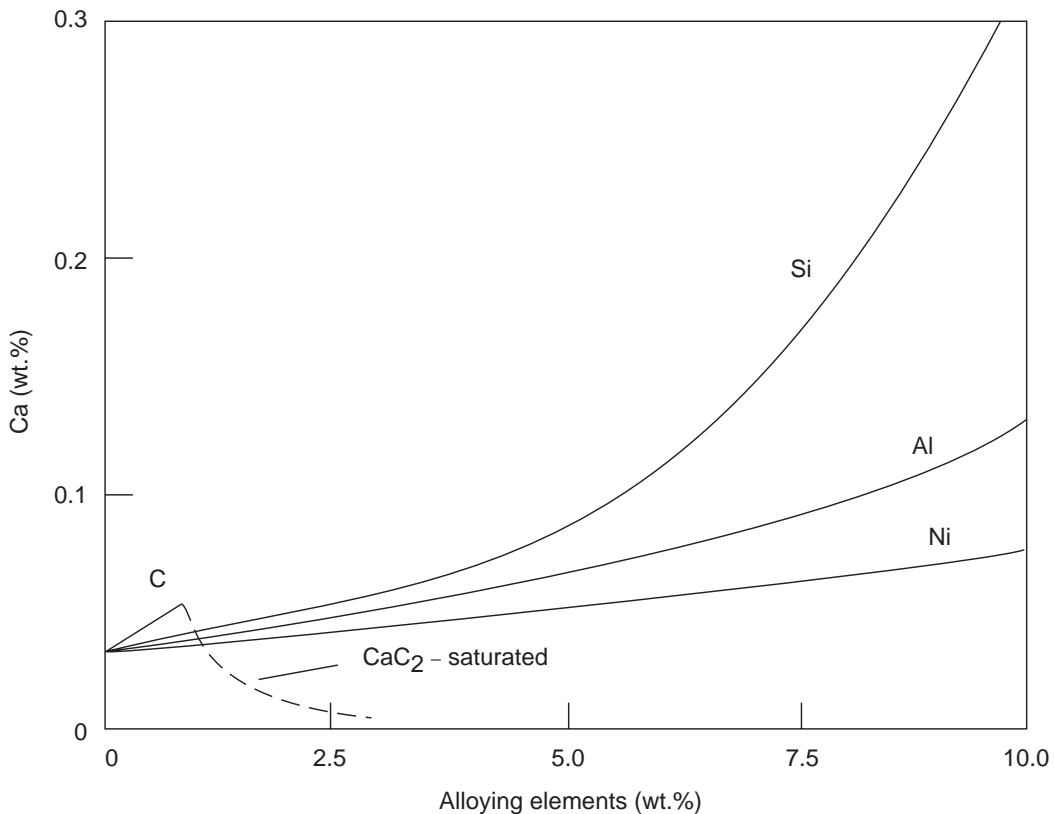
Fig. 2.42 Effect of alloying elements on the solubility of liquid calcium in liquid iron at 1607°C, corresponding to 1.69 atm pressure of calcium vapor. *From Ref. 87.*
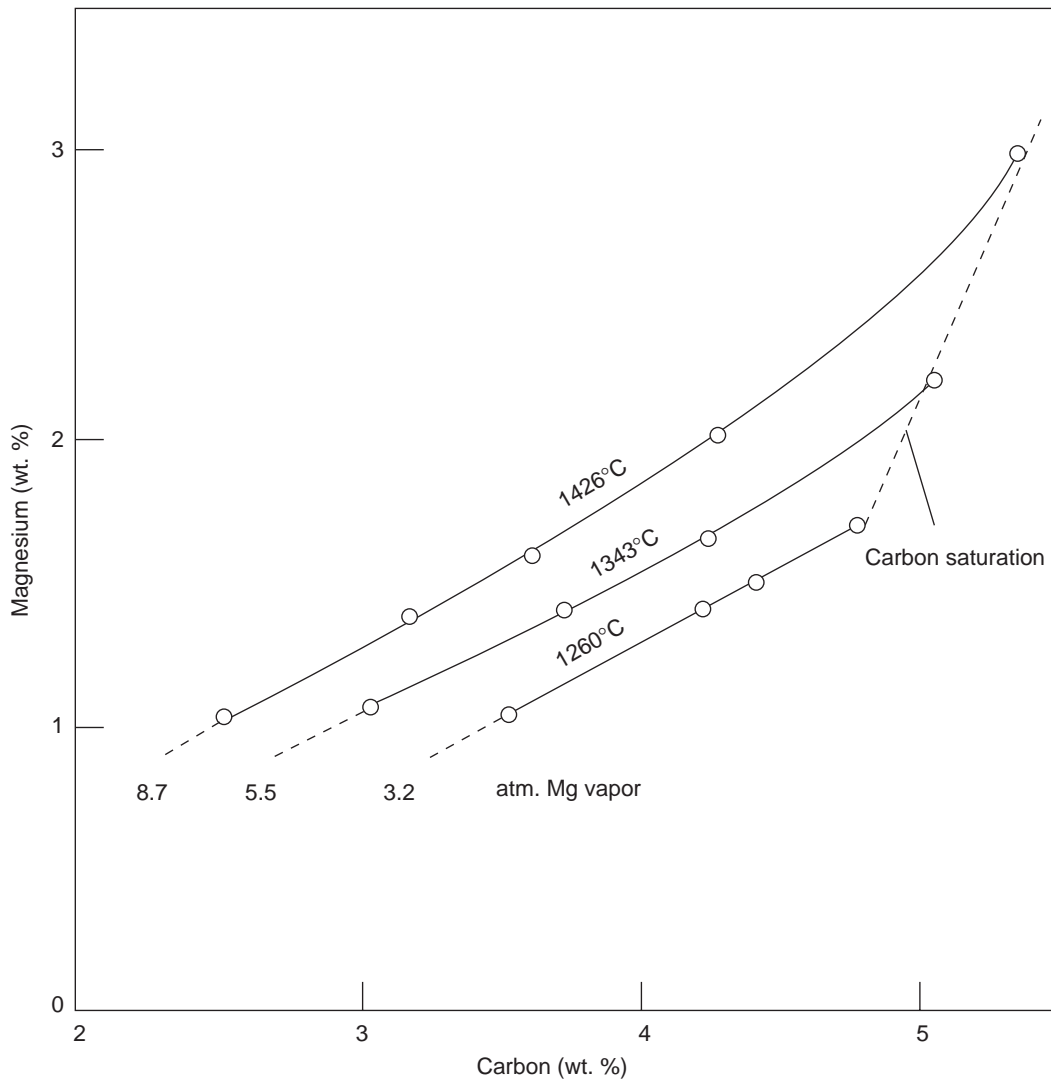
Fig. 2.43 Solubility of magnesium in liquid iron–carbon alloys at indicated temperatures and pressures of magnesium vapor. *From Ref. 88.*

2.4.7 Surface Tension

The experimental data for the surface tension of liquid iron and its binary alloys have been compiled recently by Keene.[89] For purified liquid iron, the average value of the surface tension at temperature T(°C) is represented by

$$\sigma_{Fe} = (2367 \pm 500) - 0.34(°C), \text{ mNm}^{-1} \qquad (2.4.34)$$

Keene derived the following weighted average limiting values of (mNm⁻¹) for dilute solutions of X in Fe-X binary alloys.

Fe–C:	Virtually no effect of C on σ_{Fe}
Fe–Ce:	$\sigma = \sigma_{Fe} - 700[\%Ce]$
Fe–Mn:	$\sigma = \sigma_{Fe} - 51[\%Mn]; \partial\sigma/\partial T = -0.22$
Fe–N:	$\sigma = \sigma_{Fe} - 5585[\%N]$
Fe–P:	$\sigma = \sigma_{Fe} - 25[\%P]$
Fe–S:	(Discussed later)
Fe–Si:	$\sigma = \sigma_{Fe} - 30[\%Si]; \partial\sigma/\partial T = -0.25$

Gibbs' exact treatment of surface thermodynamics gives, for fixed unit surface area and constant temperature and pressure,

$$d\sigma = -RT\sum_{i}^{k}\Gamma_i d\left(\ln a_i\right) \qquad (2.4.35)$$

where Γ_i is the surface excess concentration of the ith component and a_i its activity. For a ternary system, equation 2.4.35 is reduced to

$$d\sigma = -RT(\Gamma_2 d(\ln a_2) + \Gamma_3 d(\ln a_3)) \qquad (2.4.36)$$

Since carbon dissolved in iron has virtually no effect on the surface tension of liquid iron, for the ternary system Fe–C–S, equation 2.4.36 is simplified to

$$d\sigma = -RT\Gamma_s d(\ln a_s) \qquad (2.4.37)$$

As is seen from the compiled data in Fig. 2.44, the experimental results of various investigators for the Fe–S melts are in close agreement. References to these data are given in an earlier publication.[90]
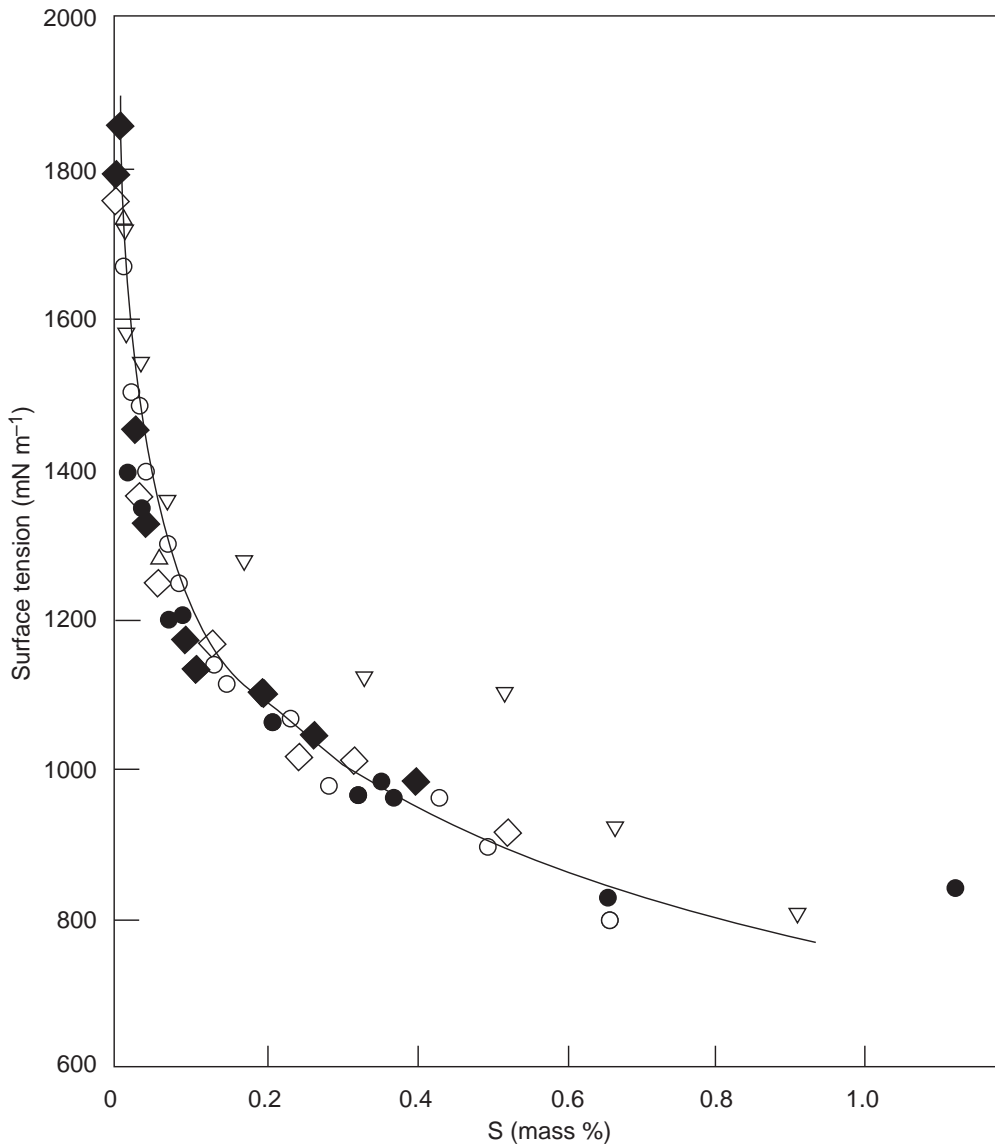
Fig. 2.44 Surface tension of Fe–S alloys at 1550-1600°C. *From Ref. 90.*

The classical work of Kozakevitch[91] on the surface tension of Fe–C–S melts at 1450°C are reproduced in Fig. 2.45

The points read off from the curves in Figs. 2.44 and 2.45 are plotted in Fig. 2.46 as σ versus log a_S. It is seen that for a_S (%S x f_S) > 0.01, σ is a linear function of log a_S, a limiting case for almost complete surface coverage with chemisorbed S. The shaded area represents the data of Selcuk and Kirkwood[92] for 1200°C.
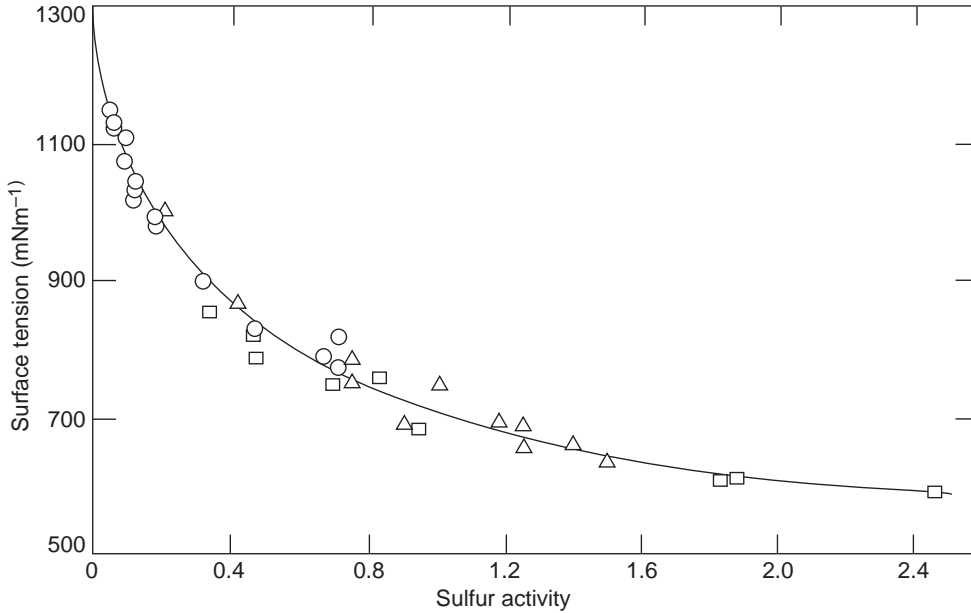
Fig. 2.45 Surface tension of liquid Fe–C–S alloys at 1450°C. *From Ref. 91.*

Fig. 2.46 Surface tension of Fe–S, Fe–C–S and Fe–C–Si–S alloys related to sulfur activity; $a_S \rightarrow$ %S when %C and %Si$\rightarrow$0. *From Ref. 90.*
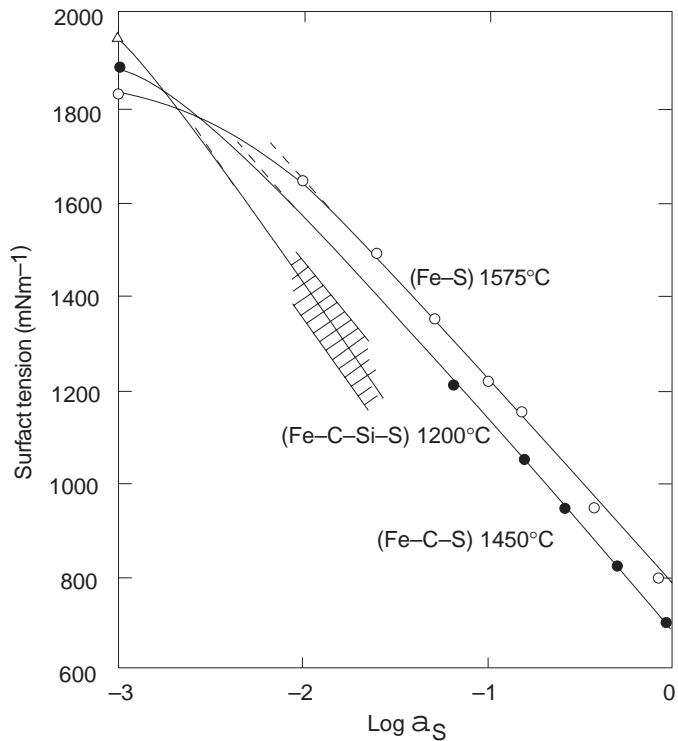
Numerous studies have been made of the surface tension of the Fe–O melts. The more recent experimental data[93,94] are reproduced in Fig. 2.47. At oxygen activities a_O (%O x f_O) > 0.1, there is essentially complete surface coverage with the chemisorbed oxygen.
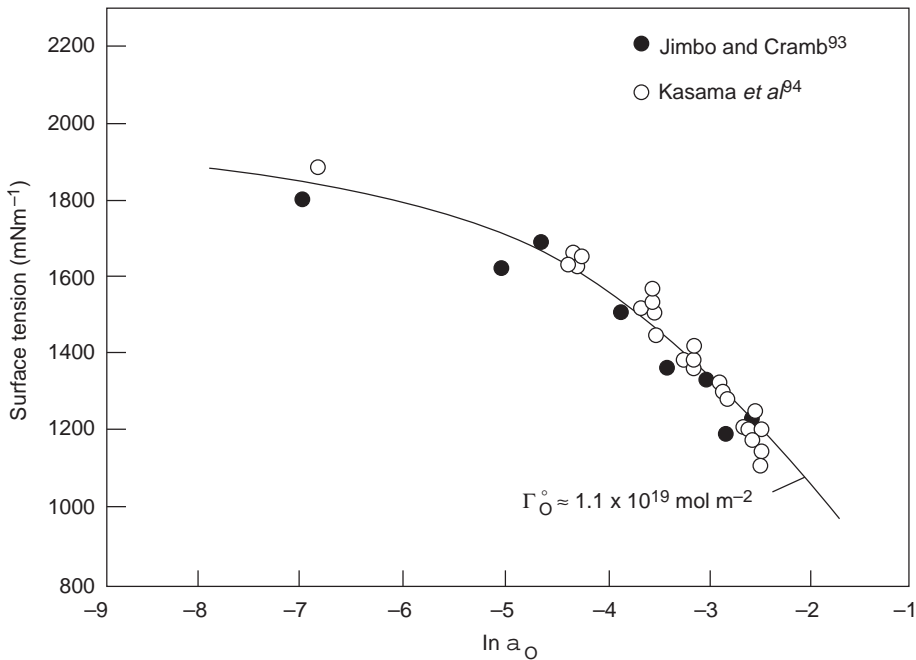
Fig. 2.47 Effect of oxygen on surface tension of liquid iron at 1550°C.

2.4.8 Density

The temperature dependence of the densities of liquid iron, nickel, cobalt, copper, chromium, manganese, vanadium and titanium are given by the following equations as a linear function of temperature in °C in g cm^{-3}:

Iron:	$8.30 - 8.36 \times 10^{-4}T$
Nickel:	$9.60 - 12.00 \times 10^{-4}T$
Cobalt:	$9.57 - 10.17 \times 10^{-4}T$
Copper:	$9.11 - 9.44 \times 10^{-4}T$
Chromium:	$7.83 - 7.23 \times 10^{-4}T$
Manganese:	$7.17 - 9.30 \times 10^{-4}T$
Vanadium:	$6.06 - 3.20 \times 10^{-4}T$
Titanium:	$4.58 - 2.26 \times 10^{-4}T$

The specific volume and density of liquid iron-carbon alloys are given in Fig. 2.48 for various temperatures. It should be noted that the density of the liquid in equilibrium with austenite does not change much over the entire liquidus range.

2.4.9 Viscosity

The viscosity is a measure of resistance of the fluid to flow when subjected to an external force. As conceived by Newton, the shear stress ε, i.e. force per unit area, causing a relative motion of two adjacent layers in a fluid is proportional to the velocity gradient du/dz, normal to the direction of the applied force

$$\varepsilon = \eta \frac{du}{dz} \qquad (2.4.38)$$

where the proportionality factor η is viscosity of the fluid (liquid or gas).

Fig. 2.48 Density of iron-carbon alloys. *From Ref. 95.*
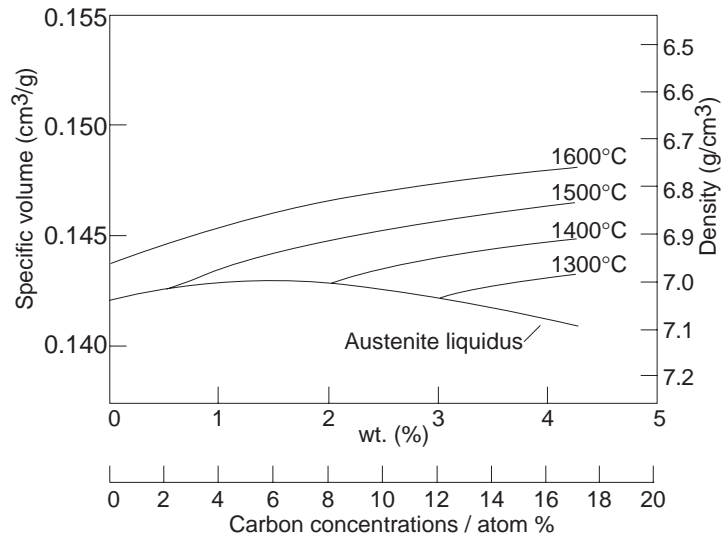
Viscosity unit: poise (g cm^{-1}s^{-1}) ≡ 0.1N s m^{-2}.

The viscosities of Fe–C alloys determined by Barfield and Kitchener[96] are given in Fig. 2.49. In the iron-carbon melts the coefficient of viscosity is essentially independent of composition within the range 0.8 to 2.5% C; above 2.5% C, the viscosity decreases continously with an increasing carbon content.

2.4.10 Diffusivity, Electrical and Thermal Conductivity, and Thermal Diffusivity

The diffusivity is an exponential function of temperature,

$$D = D_{\circ} \exp\left(-\frac{E}{RT}\right) \tag{2.4.39}$$

where D_o is a constant for a given solute and E the activation energy (enthalpy) for the diffusion process.
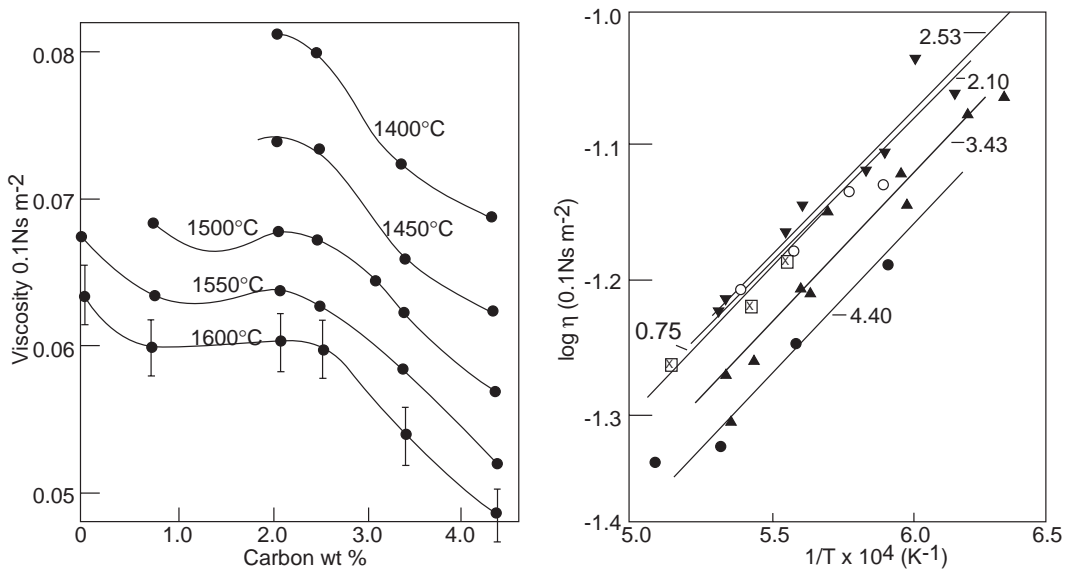
Fig. 2.49 Composition and temperature dependence of the viscosity coefficient of iron-carbon melts. *From Ref. 96.*

The general trend in the temperature dependence of solute diffusivity in solid iron is shown in Fig. 2.50. The interstitial elements, e.g. O, N, C, B, H have diffusivities much greater than the substitutional elements. Because of larger interatomic spacing, the diffusivities of interstitials in bcc-iron are greater and the heats of activations (~ 85 kJ) are smaller than those in the fcc-iron with E ~ 170 kJ. With the substitutional elements, the heat of activation is within 210 to 250 kJ for bcc-iron and within 250 to 290 kJ for fcc-iron.

In liquid iron alloys, diffusivities of elements are within 10^{-5} to 10^{-4} cm²s^{-1} with E within 15 to 50 kJ.

Some solute diffusivity data for liquid iron and iron-carbon alloys are given in Table 2.11.

Table 2.11   Selected Solute Diffusivities in Liquid Fe-C Alloys

Diffusing element	Concentration mass %	Medium	Temp. range °C	D cm²sec^{-1}	D$_o$ cm²sec^{-1}	E kJ
C	0.03	Fe	1550	7.9×10^{-5}	–	–
C	2.1	Fe	1550	7.8×10^{-5}	–	–
C	3.5	Fe	1550	6.7×10^{-5}	–	–
Co	Dilute sol.	Fe	1568	4.7×10^{-5}	–	–
Co	Dilute sol.	Fe	1638	5.3×10^{-5}	–	–
Fe	–	Fe–4.6%C	1240–1360	–	4.3×10^{-3}	51
Fe		Fe–2.5%C	1340–1400	–	1.0×10^{-2}	66
H	Dilute sol.	Fe	1565–1679	–	3.2×10^{-3}	14
Mn	2.5	gr.satu.Fe	1300–1600	–	1.93×10^{-4}	24
N	Dilute sol.	Fe	1600	1.1×10^{-4}	–	–
N	Dilute sol.	Fe–0.15%C	1600	5.6×10^{-5}	–	–
O	Dilute sol.	Fe	1600	5.0×10^{-5}	–	–
P	Dilute sol.	Fe	1550	4.7×10^{-5}	–	–
S	<0.64	gr.satu.Fe	1390–1560	–	2.8×10^{-4}	31
S	~1	Fe	1560–1670	–	4.9×10^{-4}	36
Si	<2.5	Fe	1480	2.4×10^{-5}	–	–
Si	<1.3	Fe	1540	3.8×10^{-5}	–	–
Si	1.5	gr.satu.Fe	1400–1600	–	2.4×10^{-4}	34

The electrical conductivity λ in the units of Ω^{-1}cm^{-1} is the reciprocal of the electrical resistivity. The electrical conductivity of liquid low alloy steel is about $\lambda = 7140\ \Omega^{-1}$cm^{-1} at steelmaking temperatures.

From Fick's law, the thermal conductivity is defined by

$$\kappa = -\frac{Q}{\partial T/\partial x} \tag{2.4.40}$$

where Q is heat flux, energy per unit per unit time, $\partial T/\partial x$ the temperature gradient normal to the direction of heat flow and κ the thermal conductivity.

Units of κ: J cm^{-1}s^{-1}K$^{-1} \equiv 10^{-2}$ kg m s^{-3}K$^{-1} \equiv 10^{-2}$ Wm^{-1}K^{-1}

The effect of temperature on the thermal conductivities of iron, carbon steels and high alloy steels are shown in Fig. 2.51.

Analogous to mass diffusivity, the thermal diffusivity is defined as

$$\alpha = \frac{\kappa}{\rho C_p}\ \mathrm{cm}^2\mathrm{s}^{-1} \tag{2.4.41}$$

where ρ is density and C_p molar heat capacity. In metals, the electrons migrate at much faster rates than the atoms; therefore the thermal diffusivity is much greater than the mass diffusivity.

For low–alloy steels at 1000°C:

$$\alpha \approx 0.04\ \mathrm{cm}^2\mathrm{s}^{-1}$$
$$D \approx 3 \times 10^{-12}\ \mathrm{cm}^2\mathrm{s}^{-1}\ \text{(substitutional)}$$
$$D \approx 3 \times 10^{-7}\ \mathrm{cm}^2\mathrm{s}^{-1}\ \text{(interstitial)}$$
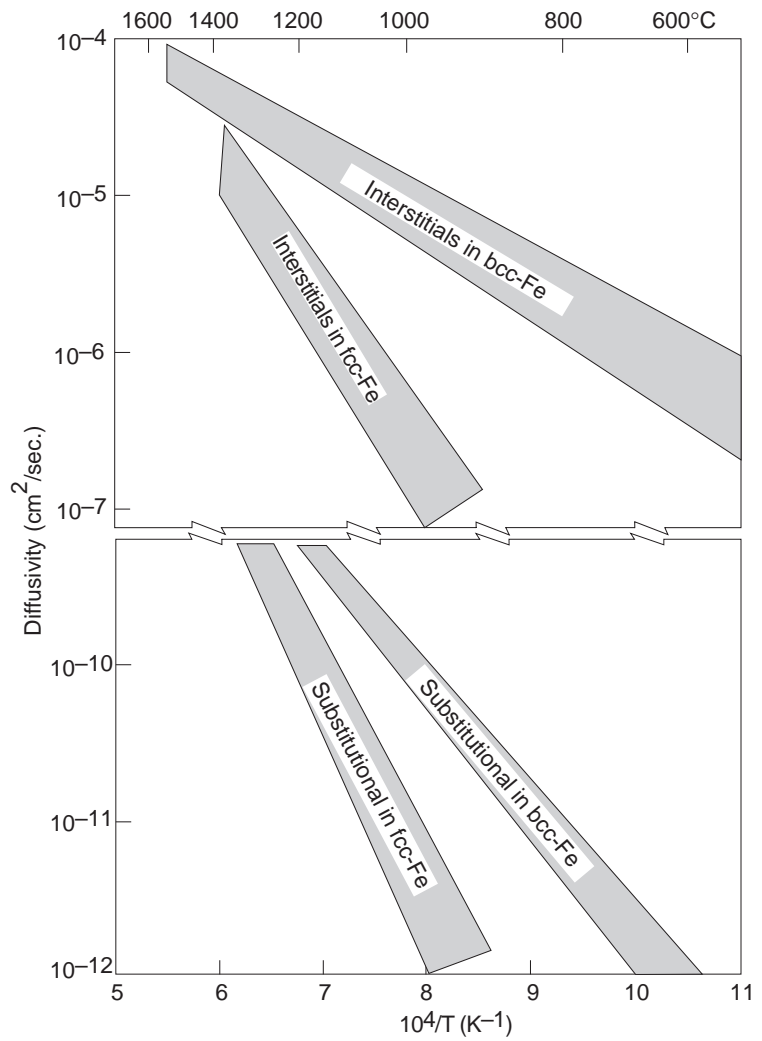
Fig. 2.50 Range of diffusivities of interstitial and substitutional elements in bcc and fcc iron.
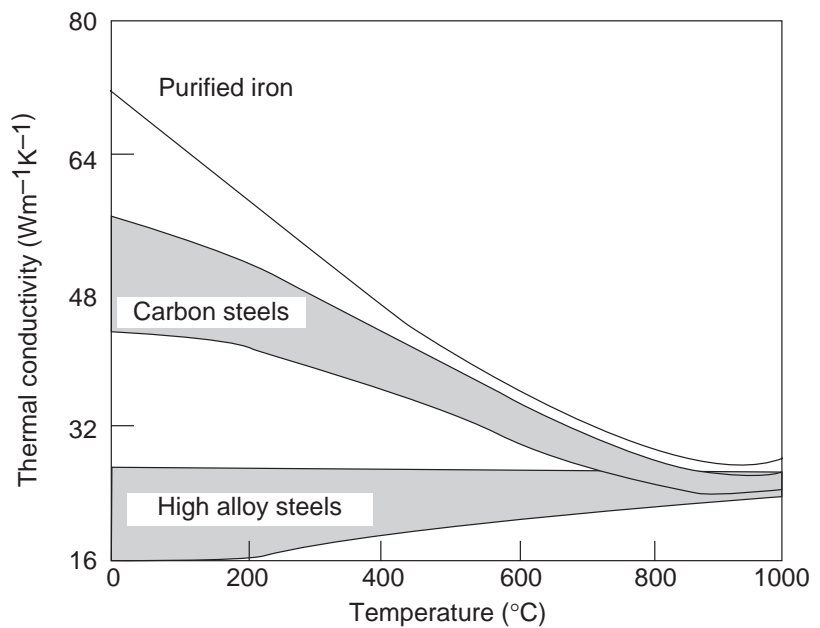
Fig. 2.51 Temperature dependence of thermal conductivity of purified iron and iron alloys.

2.5 Properties of Molten Slags

2.5.1 Structural Aspects

Molten slags are ionic in nature consisting of positively charged ions known as cations, and negatively charged complex silicate, aluminate and phosphate ions known as anions.

The fundamental building unit in solid silica and molten silicates is the silicate tetrahedron SiO_4^{4-}. Each silicon atom is tetrahedrally surrounded by four oxygen atoms and each oxygen atom is bonded to two silicon atoms. The valency of silicon is +4 and that of oxygen is –2, therefore the silicate tetrahedron has 4 negative charges.

The addition of metal oxides such as FeO, CaO, MgO, . . . to molten silica brings about a breakdown of the silicate network, represented in a general form by the reaction

$$\left(-\overset{|}{\underset{|}{Si}}-O-\overset{|}{\underset{|}{Si}}-\right) + MO \rightarrow 2\left(-\overset{|}{\underset{|}{Si}}-O\right)^{-} + M^{2+} \tag{2.5.1}$$
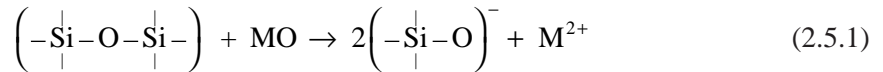
The cations are dispersed within the broken silicate network. In MO–SiO_2 melts the atom ratio $O/Si > 2$, therefore part of the oxygen atoms are bonded between two silicon atoms and part to only one silicon atom. Partial depolymerization of the silicate network with the addition of a metal oxide MO is illustrated in Fig. 2.52.
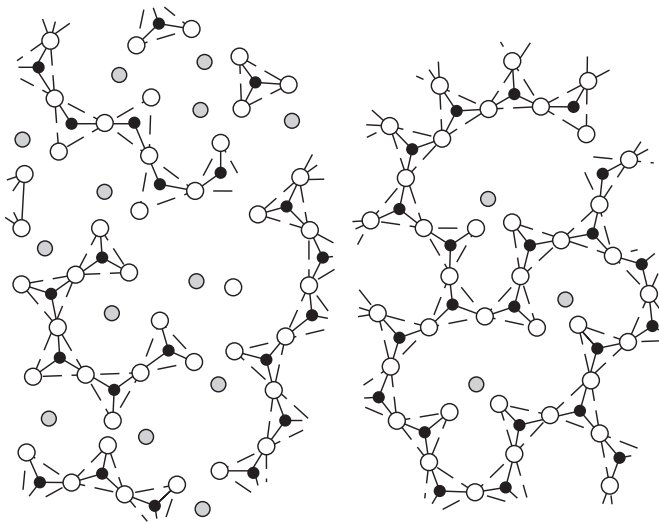
Fig. 2.52 Schematic representation of depolymerization of the silicate network with the dissolution of metal oxides in silicate melts.

In highly basic slags with molar ratio $MO/SiO_2 > 2$, the silicate network completely breaks down to individual SiO_4 tetrahedra intermixed with cations M^{2+} and some oxygen ions O^{2-}.

At low concentrations, Al_2O_3 behaves like a network-modifying oxide and forms aluminum cations Al^{3+}. At high concentrations, the aluminum enters the tetrahedral structure isomorphous with silicon.

This process may be schematically represented by the reaction

$$\left(-\overset{|}{\underset{|}{Si}}-O-\overset{|}{\underset{|}{Si}}-\right) + MAlO_2 \rightarrow \left(-\overset{|}{\underset{|}{Si}}-O-\overset{|}{\underset{|}{Al}}-O-\overset{|}{\underset{|}{Si}}- \atop \quad\quad O \right)^{-} + M^{+} \tag{2.5.2}$$
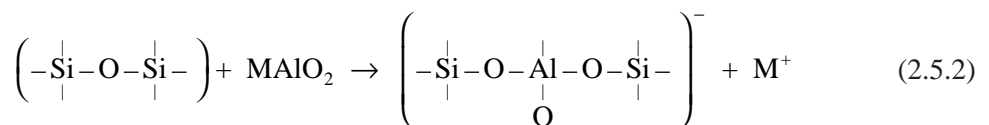
The cation M^{+} is located in the vicinity of Al–O bonding to preserve the local charge balance. At low concentrations of phosphorus in steelmaking slags, the phosphate ions PO_4^{3-} are incorporated in the silicate network. In steelmaking slags, the sulfur exists as a sulfide ion S^{2-}. The sulfate ions SO_4^{2-} exist in slags only under highly oxidizing conditions and in the absence of iron or any other oxidizable metal.

Although molten slags are ionized, the slag composition can be represented in terms of the constituent oxides, e.g. CaO, FeO, SiO_2, P_2O_5. The thermodynamic activity of an ion in the slag cannot be determined. However, the activity of an oxide dissolved in molten slag, forming M^{2+} and O^{2-} ions, can be determined experimentally and the following equality can be written

$$MO \rightarrow M^{2+} + O^{2-} \tag{2.5.3}$$

$$\frac{a_{MO}}{(a_{MO})^{\circ}} = \frac{\left(a_{M^{2+}}\, a_{O^{2-}}\right)}{\left(a_{M^{2+}}\, a_{O^{2-}}\right)^{\circ}} \tag{2.5.4}$$

where the superscript $^{\circ}$ refers to the standard state which is usually pure solid or liquid oxide.

2.5.2 Slag Basicity

For steelmaking slags of low phosphorus content, the slag basicity has traditionally been represented by the mass concentration ratio

$$V = \frac{\%CaO}{\%SiO_2} \tag{2.5.5}$$

For slags containing high concentrations of MgO and P_2O_5, as in some laboratory experiments, the basicity may be defined by the following mass concentration ratio, with the assumption that on a molar basis the concentrations of CaO and MgO are equivalent. Similarly, on a molar basis 1/2 P_2O_5, i.e. $PO_{2.5}$, is equivalent to SiO_2.

$$B = \frac{\%CaO + 1.4 \times \%MgO}{\%SiO_2 + 0.84 \times \%P_2O_5} \tag{2.5.6}$$

For slags containing MgO < 8% and P_2O_5 < 5%, the basicity B is essentially directly proportional to V.

$$B = 1.17V \tag{2.5.7}$$

Another measure of slag basicity is the difference between the sum of the concentrations of basic oxides and acidic oxides.

$$(\%CaO + \%MgO + \%MnO) - (\%SiO_2 + P_2O_5 + TiO_2) \tag{2.5.8}$$

This formulation of slag basicity is not used very often.

For the calcium aluminate type of slags used in steel refining in the ladle furnace, the slag basicity used in some German and Japanese publications, is defined by the ratio

$$\frac{\%CaO}{\%SiO_2 \times \%Al_2O_3} \tag{2.5.9}$$

However, such a ratio becomes meaningless at low concentrations of either SiO_2 or Al_2O_3. For the ladle furnace slag the basicity may be defined by the following mass concentration ratio, on the assumption that on a molar basis Al_2O_3 is equivalent to SiO_2.

$$B_{LF} = \frac{\%CaO + 1.4 \times \%MgO}{\%SiO_2 + 0.6 \times \%Al_2O_3} \tag{2.5.10}$$

The slag basicities as defined above are for the compositions of molten slags. In practice, the steelmaking slags often contain undissolved CaO and MgO. The chemical analyses of such slag samples without correction for undissolved CaO and MgO, will give unrealistic basicities which are much higher than those in the molten part of the slag.

There has been a trend in recent years to relate some physiochemical properties of slags, such as sulfide capacity, phosphate capacity, carbide capacity, etc., to optical slag basicity. The optical basicity is discussed briefly in Section 2.5.12.

2.5.3 Iron Oxide in Slags

Iron oxide dissolves in slags in two valency states: divalent iron cations Fe^{2+} and trivalent iron cations Fe^{3+}. The ratio Fe^{3+}/Fe^{2+} depends on temperature, oxygen potential and slag composition; this is discussed later in this section. In the formulation of the equilibrium constants of slag-metal reactions and the thermodynamic activities of oxides in slags, the total iron dissolved in the slag as oxides is usually converted to the stoichiometric formula FeO and denoted by Fe_tO, thus

$$\%Fe_tO = \%FeO \text{ (analyzed)} + 0.9 \text{ x } \%Fe_2O_3 \text{ (analyzed)} \tag{2.5.11}$$

or

$$\%Fe_tO = 1.286 \text{ x } \%Fe \text{ (total as oxides)} \tag{2.5.12}$$

For the ease of understanding, the subscript t will be omitted in all the subsequent equations and diagrams.

2.5.4 Selected Ternary and Quaternary Oxide Systems

Most steelmaking slags consist primarily of CaO, MgO, SiO_2 and FeO. In low-phosphorus steelmaking practices, the total concentration of these oxides in liquid slags is in the range 88 to 92%. Therefore, the simplest type of steelmaking slag to be considered is the quaternary system CaO–MgO–SiO_2–FeO.

First let us consider the ternary system CaO·SiO_2–FeO; the liquidus isotherms of this system is shown in Fig. 2.53. The isothermal section of the composition diagram in Fig. 2.54 shows the phase equilibria at 1600°C.
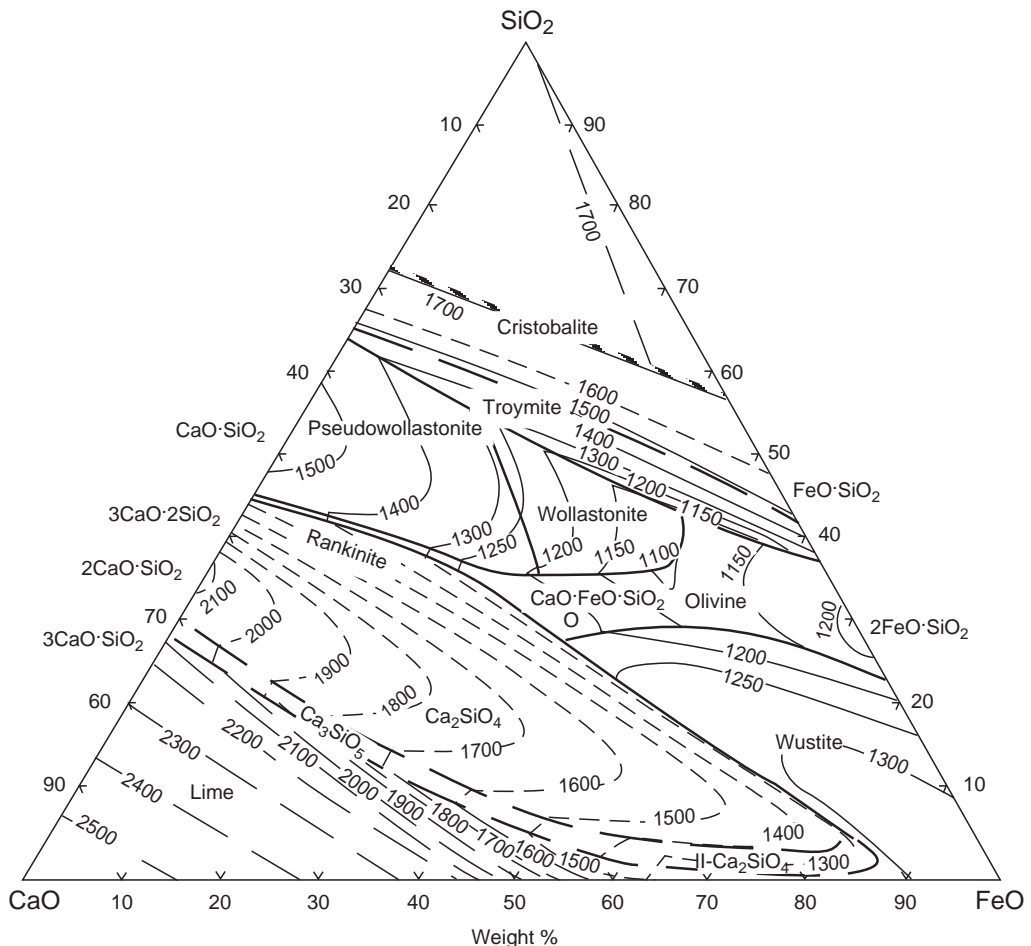
Fig. 2.53 Liquidus isotherms of CaO–SiO_2–FeO system.

Fig. 2.54 Phase equilibrium in the system CaO–SiO$_2$–FeO in equilibrium with liquid iron at 1600°C.
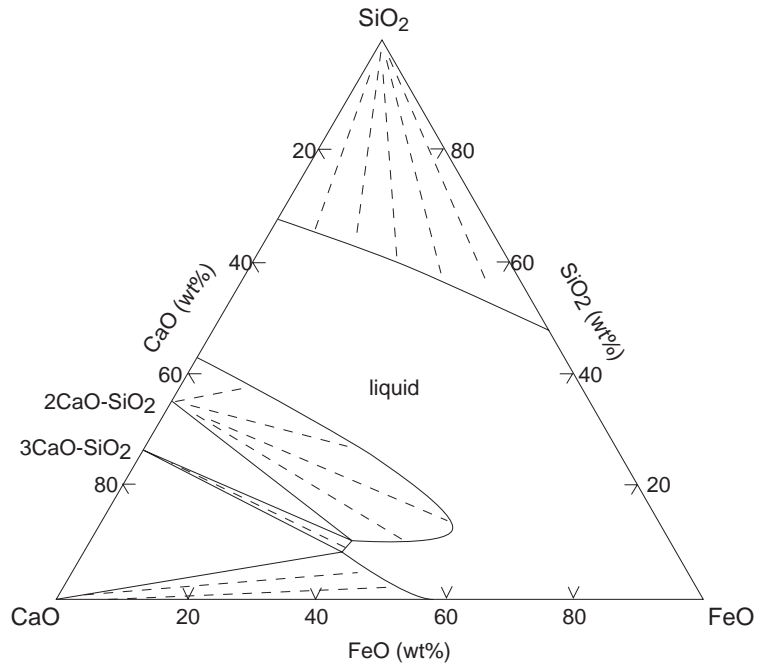
There are four two-phase regions where, as depicted by dotted lines, the melt is saturated with SiO$_2$, 2CaO·SiO$_2$, 3CaO·SiO$_2$ or CaO; two three-phase regions (2CaO·SiO$_2$ + 3CaO·SiO$_2$ + liquid) and (3CaO·SiO$_2$ + CaO + liquid); and one liquid phase region.

Magnesia is another important ingredient of steelmaking slags, which are invariably saturated with MgO to minimize slag attack on the magnesia refractory lining of the furnace.

The effect of MgO on the solubility of calcium silicates and calcium oxide is shown in Fig 2.55 for the system (CaO + MgO)–SiO$_2$–FeO, in equilibrium with liquid iron at 1600°C.

Fig. 2.55 Effect of MgO (wt.%) on the solubility isotherms at 1600°C in the system (CaO + MgO)–SiO$_2$–FeO in equilibrium with liquid iron.
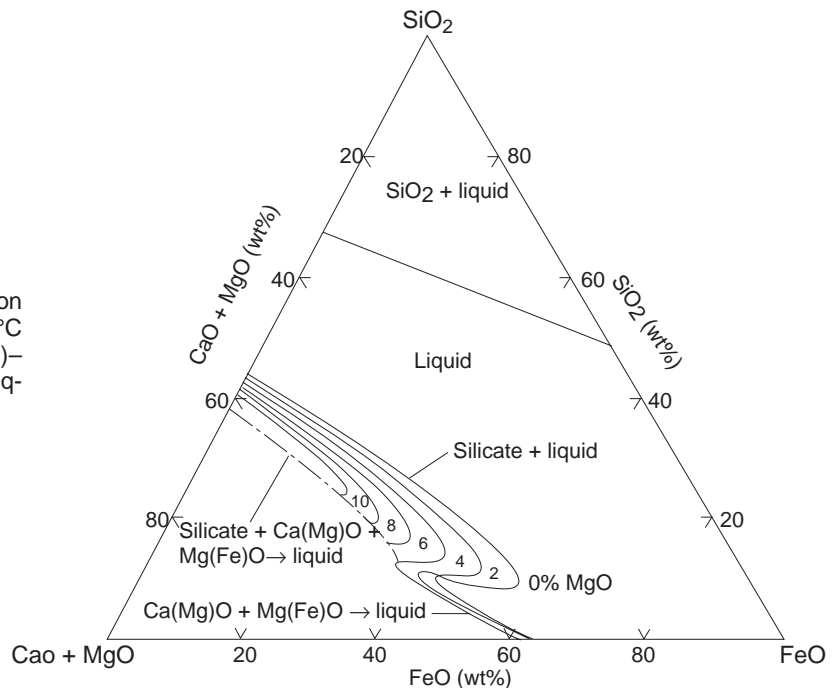
The broken-line curve delineates the region of saturation of molten slag with solid calcium (magnesium) silicates and solid magnesio-wustite (MgO–FeO solid solution). Effects of the concentrations of MgO and FeO on the solubility of CaO in $2CaO \cdot SiO_2$-saturated slags are shown in Fig. 2.56.

Tromel *et al.*[97] have made a detailed study of the solubility of MgO in iron–calcium silicate melts in equilibrium with liquid iron at 1600°C. Below the dotted curve BACD in Fig. 2.57 for double saturations, the curves for 10 to 60% FeO are the MgO solubilities in the slag.
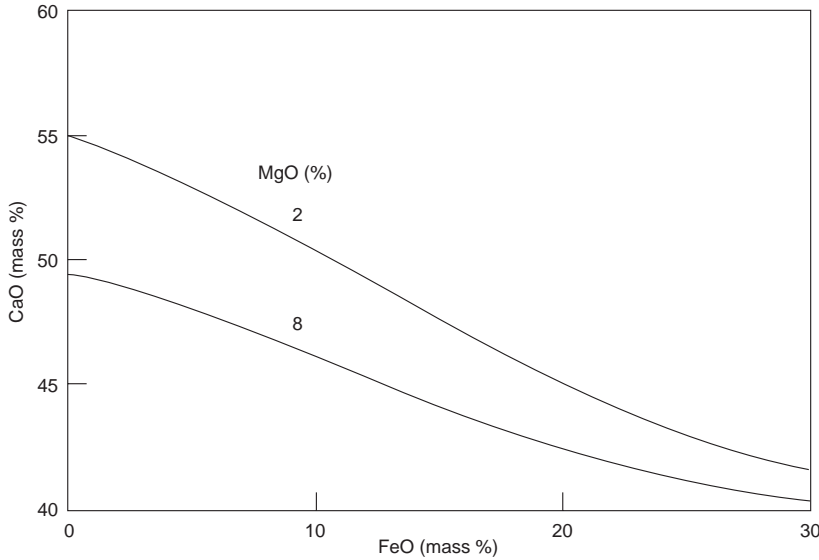
Fig. 2.56 Solubility of CaO in (CaO–MgO–SiO$_2$–FeO) slags saturated with $2CaO \cdot SiO_2$ at 1600°C.
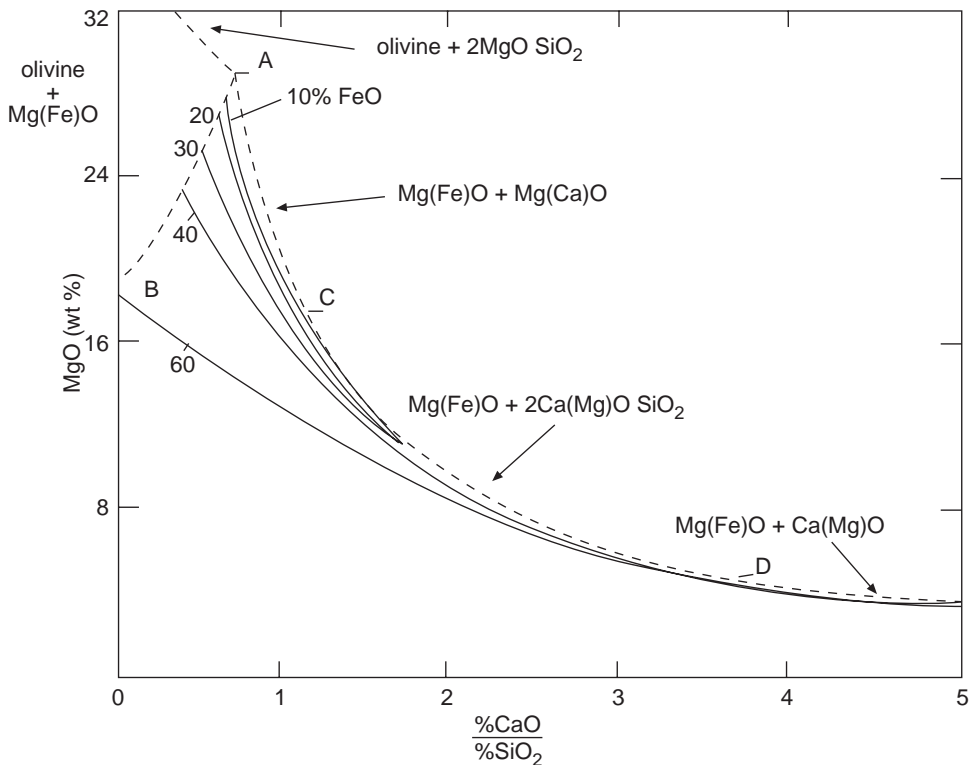
Fig. 2.57 Solubility of MgO, as magnesio–wustite, in the system CaO–MgO–SiO$_2$–FeO at 1600°C as a function of slag basicity and FeO concentration. *From Ref. 97.*
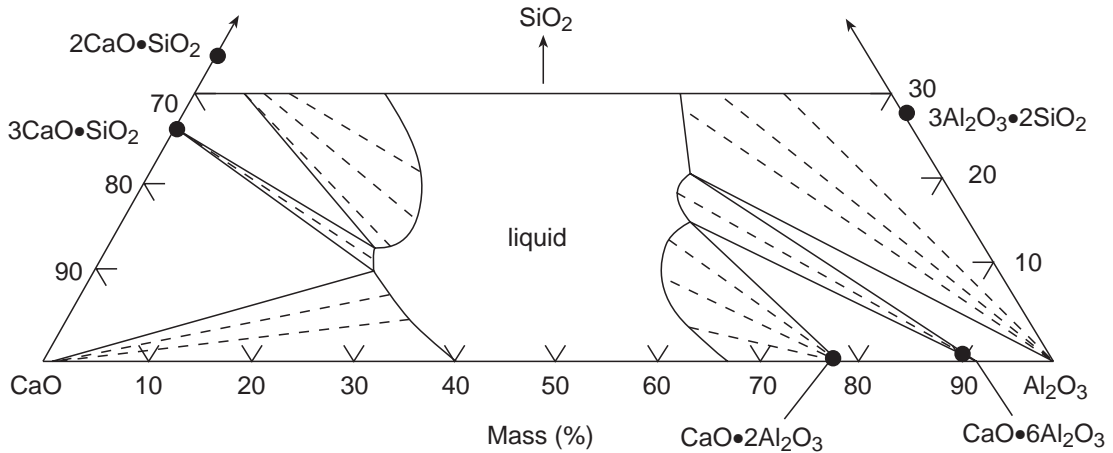
Fig. 2.58 Phase equilibria in the system CaO–Al$_2$O$_3$–SiO$_2$ at 1600°C.

Pertinent to the compositions of neutral ladle slags, the phase equilibria in part of the system CaO–Al$_2$O$_3$–SiO$_2$ at 1600°C is shown in Fig. 2.58.

2.5.5 Oxide Activities in Slags

In this section the activity data are given for a few ternary and multicomponent systems which are closely related to the iron and steelmaking slags.

2.5.5.1 Activities in CaO – FeO–SiO$_2$ System

The oxide activities in the CaO–FeO–SiO$_2$ melts relevant to oxygen steelmaking in equilibrium with liquid iron at about 1550°C are given in Fig. 2.59. The iso-activity curves in the left diagram represent the experimentally determined activities of iron oxide with respect to liquid FeO.[98–99] The activities of CaO and SiO$_2$ with respect to solid oxides were calculated from the FeO activities by Gibbs-Duhem integration.[99]
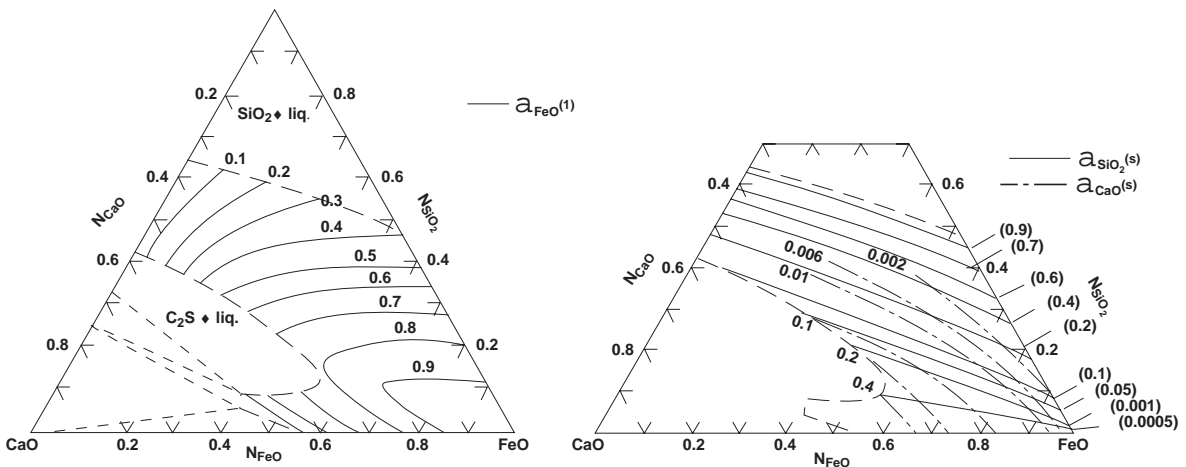
Fig. 2.59 Activities of FeO(l) (experimental), CaO(s) and SiO$_2$(s) (by Gibbs-Duhem integration) in CaO–FeO–SiO$_2$ melts in equilibrium with liquid iron at 1550°C. From Refs. 98, 99.

Recently new iron smelting processes have been developed and are briefly discussed here. The slags are CaO–SiO$_2$–FeO–Al$_2$O$_3$–MgO (saturated) with low FeO contents (<5%). Knowledge of the activity of FeO in these slags is critical and has been recently measured by Liu *et al*.[100] The activity coefficient of FeO in these slags is given in Fig. 2.60 and is approximately 3.5. It increases slightly with basicity as shown in Fig. 2.61 but is nearly constant with a value of 3.5.
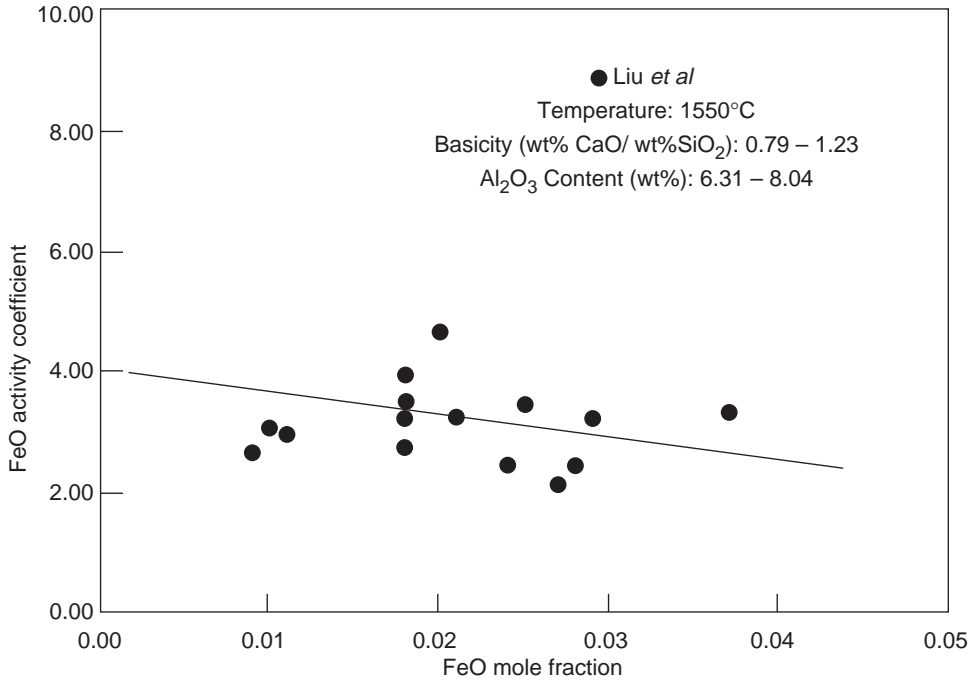
Fig. 2.60 The activity of FeO in CaO–SiO$_2$–Al$_2$O$_3$–FeO–MgO (saturated) slags relevant to iron smelting. *From Ref. 100.*
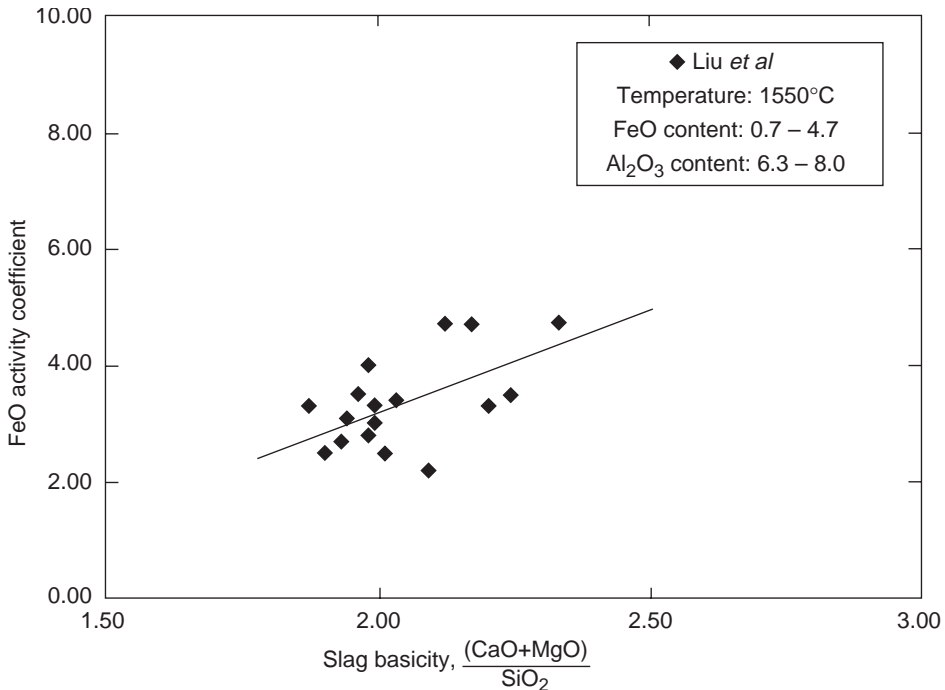
Fig. 2.61 The effect of slag basicity on the activity coefficient of FeO in CaO–SiO$_2$–Al$_2$O$_3$–FeO–MgO (saturated) slags relevant to iron smelting. *From Ref. 100.*

2.5.5.2   Activities in CaO–Al$_2$O$_3$–SiO$_2$ System

Rein and Chipman[101] measured the activity of silica in the CaO–Al$_2$O$_3$–SiO$_2$ system; from these experimental data they calculated the activities of CaO and Al$_2$O$_3$ by Gibbs-Duhem integration. The salient features of these oxide activities at 1600°C, with respect to solid oxides, are shown in Fig. 2.62 for the mass ratios of CaO/Al$_2$O$_3$ = 2/3 and 3/2; the compositions of ladle slags are well within the range given in Fig. 2.62.

Rein and Chipman also measured the activity of silica in the quaternary melts CaO–MgO–Al$_2$O$_3$–SiO$_2$. The activity coefficients of SiO$_2$ derived from these data are given in Fig. 2.63 for melts containing 10% MgO and 0, 10 or 20% Al$_2$O$_3$.

Fig. 2.62 Silica and alumina activities, with respect to solid oxides, in CaO–Al$_2$O$_3$–SiO$_2$ melts at 1600°C, derived from experimental data of Rein and Chipman.[101]
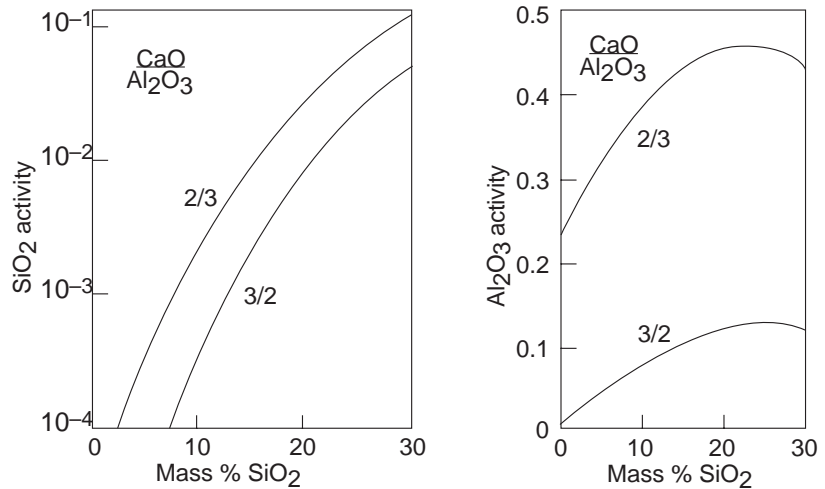
Fig. 2.63 Activity coefficient of SiO$_2$ with respect to pure solid oxide, in CaO–MgO–Al$_2$O$_3$–SiO$_2$ melts at 1600°C, containing 10% MgO and 0, 10 or 20% Al$_2$O$_3$, derived from experimental data of Rein and Chipman[101].
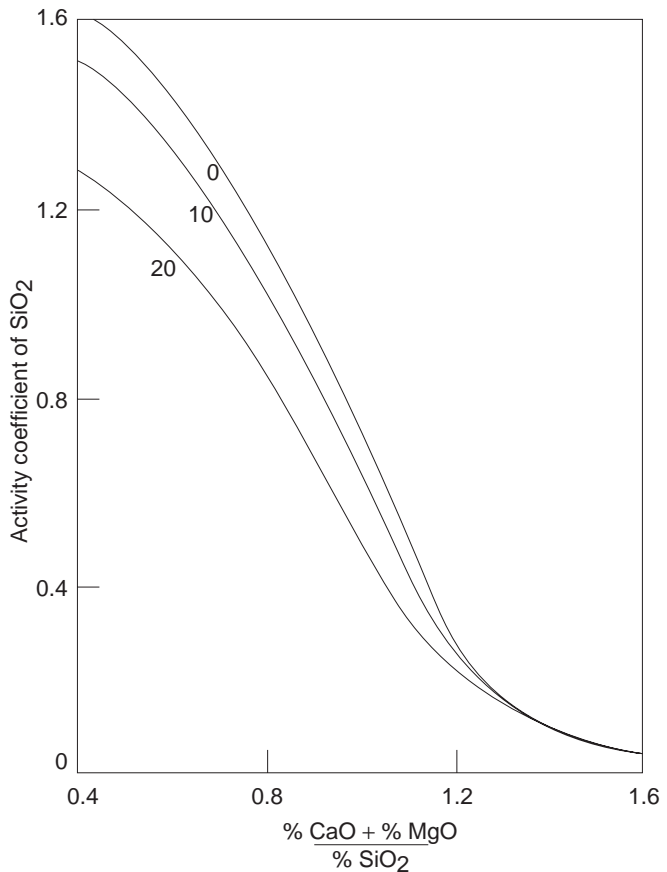
The ratio of the activities $(a_{Al_2O_3})^{1/3}/a_{CaO}$ within the entire liquid composition range up to 30% SiO_2 is shown in Fig. 2.64 reproduced from Ref. 27.

2.5.5.3 Activities in MnO–Al$_2$O$_3$–SiO$_2$ System

In the deoxidation of steel with the ladle addition of silicomanganese and aluminum together, the deoxidation product is molten manganese aluminosilicate with the mass ratio MnO/SiO_2 at about 1:1 and containing 10 to 45% Al_2O_3. The activities of oxides in the MnO–Al_2O_3–SiO_2 melts at 1550 and 1650°C were computed by Fujisawa and Sakao[102] from the available thermochemical data on the system. They also determined experimentally the activities of MnO and SiO_2 by the selected slag-metal equilibrium measurements and found a close agreement with the computed data.

The activities of Al_2O_3 and SiO_2, with respect to solid oxides, are plotted in Fig. 2.65 for melts with mass ratio of $MnO/SiO_2 = 1$. For melts containing up to 30% Al_2O_3 the activity of MnO remains essentially unchanged at about 0.1 then decreases to about 0.05 at 40% Al_2O_3.

2.5.5.4 Activity Coefficient of FeO in Slags

With hypothetical pure liquid FeO as the standard state, the activity of iron oxide is derived from the concentration of dissolved oxygen in liquid iron that is in equilibrium with the slag. For the reaction equilibrium

$$FeO(l) = Fe + [O] \qquad (2.5.13)$$

$$K_O = \frac{[a_O]}{a_{FeO}} \qquad (2.5.14)$$

where $a_O = [\%O]f_O$, using $\log f_O = -0.1 \times [\%O]$. The temperature dependence of the equilibrium constant K_O is given below.

$$\log K_O = -\frac{5370}{T} + 2.397 \qquad (2.5.15)$$
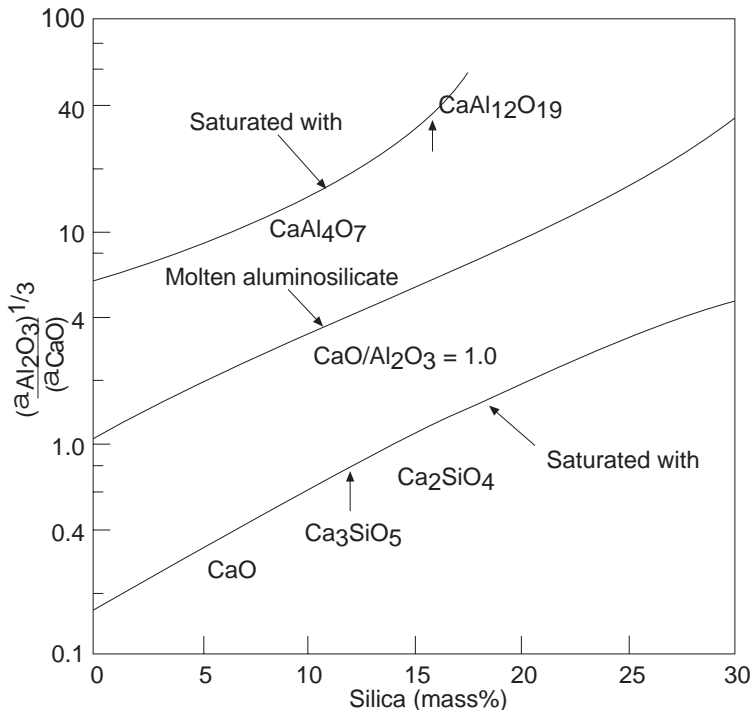
Fig. 2.64 Effect of slag composition on the activity ratio $(a_{Al_2O_3})^{1/3}/a_{CaO}$ for the system CaO–Al$_2$O$_3$–SiO$_2$ at 1600°C. *From Ref. 27.*
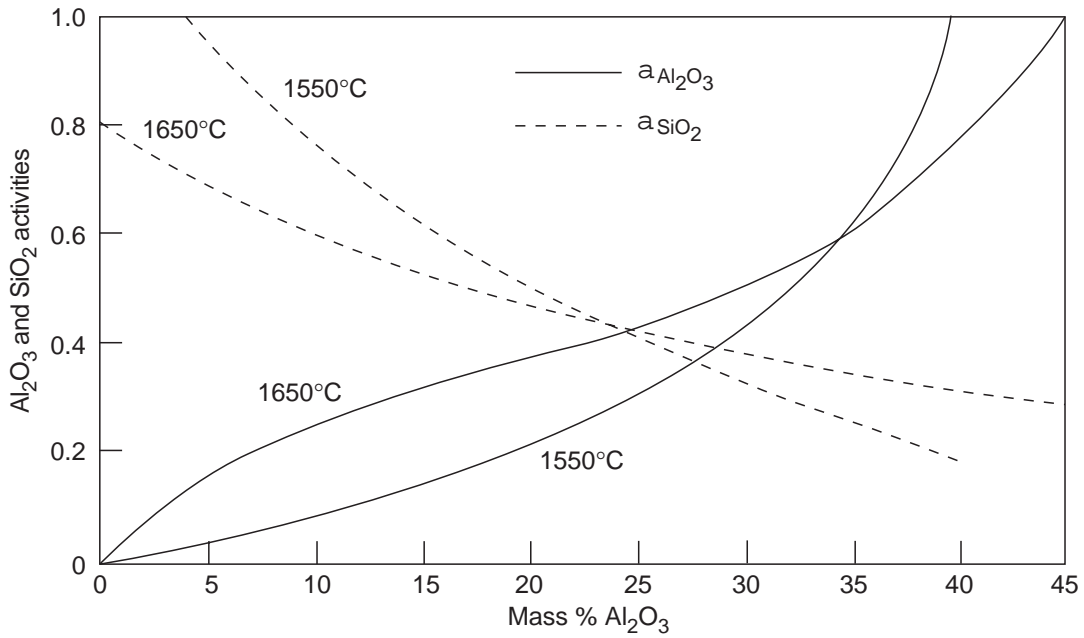
Fig. 2.65 Al_2O_3 and SiO_2 activities in $MnO-Al_2O_3-SiO_2$ system for mass ratio $MnO/SiO_2 = 1$, derived from data compiled by Fujisawa & Sakao[102].

In the past a wide variety of formulations were generated to represent the composition dependence of the iron oxide activity or activity coefficient in complex slag. On a recent reassessment of this property of the slag, Turkdogan[103] came to the conclusion that, within the limits of uncertainty of the experimental data on slag-metal reaction equilibrium, there is a decisive correlation between the activity coefficient of FeO and the slag basicity as shown in Fig. 2.66. The γ_{FeO} reaches a peak at a basicity of about B = 1.8. It should be pointed out once again that the concentration of iron oxide is for total iron as oxides in the slag represented by the stoichiometric formula FeO.

As discussed in Ref. 103, the experimental data used in deriving the relation in Fig. 2.66 are for simple and complex slags which differ considerably in their compositions thus: in mass percent, CaO 0–60, MgO 0–20, SiO_2 0–35, P_2O_5 0–20, FeO 5–40, MnO 0–15.

2.5.5.5 Activity of MnO in Slags

The activity coefficient ratio $\gamma_{FeO}/\gamma_{MnO}$, derived from the slag-metal equilibrium data cited in Ref. 103, varies with slag basicity as shown in Fig. 2.67. There is a sharp decrease in the ratio of the activity coefficients as the basicity B increases from 1.5 to 2.0. At basicities above 2.5, the ratio $\gamma_{FeO}/\gamma_{MnO}$ is essentially constant at about 0.63. The curve for γ_{MnO} in Fig. 2.66 is that derived from combination of the curve for γ_{FeO} with the ratio in Fig. 2.67.
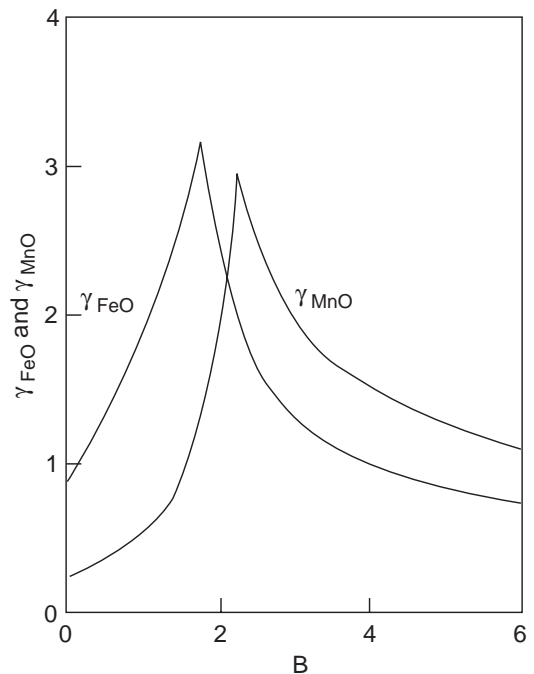
Fig. 2.66 Effect of slag basicity B on the activity coefficients of FeO and MnO, with respect to pure liquid oxides, in simple and complex slags at temperatures of 1550 to 1700°C. *From compiled data in Ref. 103.*

2.5.6 Gas Solubility in Slags

2.5.6.1 Solubility of H₂O

In acidic melts, H_2O vapor reacts with double bonded oxygen and depolymerizes the melt, thus

$$\left(-\overset{|}{\underset{|}{Si}}-O-\overset{|}{\underset{|}{Si}}-\right)+H_2O = 2\left(-\overset{|}{\underset{|}{Si}}-OH\right)$$
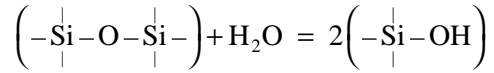
In basic melts, H_2O reacts with free oxygen ions

$$(O^{2-}) + H_2O = 2(OH)^- \qquad (2.5.16)$$

Both for acidic and basic melts the overall reaction is represented by

$$(O^*) + H_2O = 2(OH^*) \qquad (2.5.17)$$

where O* represents double or single bonded oxygen, or O^{2-}, and OH* is single bonded to silicon or as a free ion. The equilibrium constant for a given melt composition is

$$C_{OH} = \frac{(\text{ppm } H_2O)}{\left(p_{H_2O}\right)^{1/2}} \qquad (2.5.18)$$

where P_{H_2O} is the vapor partial pressure.

The solubilities of H_2O (in units of mass ppm H_2O) at 1 atm pressure of H_2O vapor in CaO–FeO–SiO₂ at 1550°C, measured by Iguchi *et al.*[104] are given in Fig. 2.68.

Fig. 2.67 Variation of activity coefficient ratio with basicity. *From Ref. 103.*
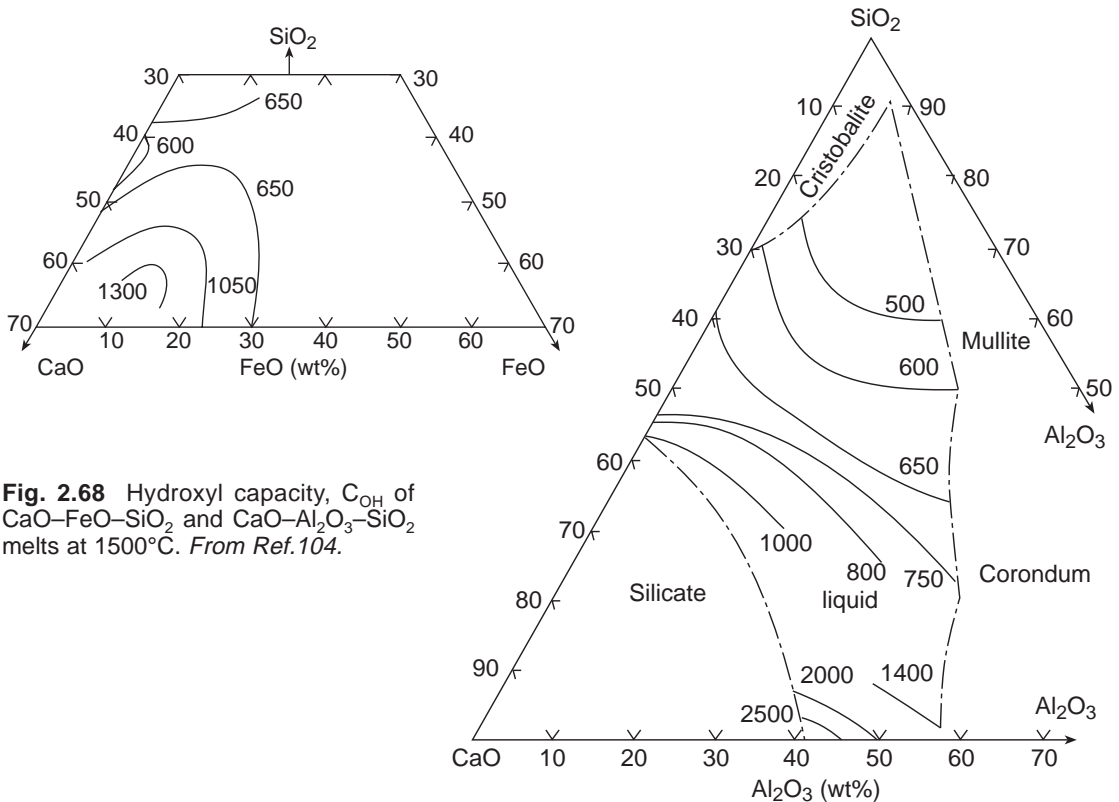
Fig. 2.68 Hydroxyl capacity, C_{OH} of CaO–FeO–SiO₂ and CaO–Al₂O₃–SiO₂ melts at 1500°C. *From Ref.104.*

2.5.6.2 Solubility of N_2

Nitrogen dissolves in molten slags as a nitride ion N^{3-} only under reducing conditions

$$\tfrac{1}{2}N_2(g) + \tfrac{3}{2}(O^{2-}) = (N^{3-}) + \tfrac{3}{4}O_2(g) \tag{2.5.19}$$
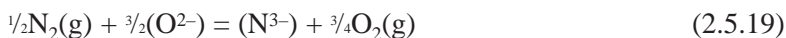
for which the equilibrium constant (known as nitride capacity) is

$$C_N = (\%N)\frac{p_{O_2}^{\frac{3}{4}}}{p_{N_2}^{\frac{1}{2}}} \tag{2.5.20}$$

Many studies have been made of the solubility of nitrogen in $CaO–Al_2O_3$ and $CaO–Al_2O_3–SiO_2$ melts in the 1970s. These were reviewed in a previous publication[3]. Reference should be made also to a subsequent work done by Ito and Fruehan[105] on the nitrogen solubility in the $CaO–Al_2O_3–SiO_2$ melts. They showed that the nitride capacity of the aluminosilicate melts increases with a decreasing activity of CaO.

2.5.6.2.1 Nitrogen Dissolution into Slags

The nitride capacity in certain slag systems increases and in others decreases with basicity. According to equation 2.5.19 one would expect it to increase with increasing slag basicity, i.e. increasing concentration of free oxygen ion O^{2-}. The reason for this apparent contradiction is that nitrogen can enter the slag by replacing single bonded oxygen ions in the SiO_2 network. This phenomena is explained in detail by Ito and Fruehan.[105]

Briefly, spectroscopic research indicates that the nitrogen is combined with the network former in silicate melts which can be represented by

$$(2O^-) + \tfrac{1}{2}N_2 = (N^-) + \tfrac{1}{2}(O^{2-}) + \tfrac{3}{4}O_2 \tag{2.5.21}$$
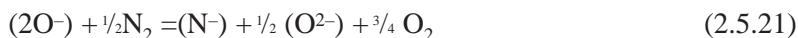
where O^- is a nonbridging system in the network. If SiO_2 is the network former equation 2.5.21 corresponds to

$$\left(O^- - \overset{|}{\underset{|}{Si}} - O^-\right) + \tfrac{1}{2}N_2 = \left(\overset{|}{\underset{|}{Si}} = N^-\right) + \tfrac{1}{2}\left(O^{2-}\right) + \tfrac{3}{4}O_2 \tag{2.5.22}$$
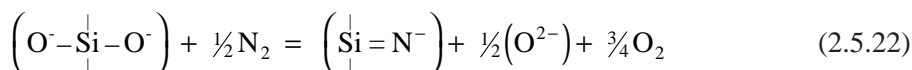
In this case the nitride capacity is given by

$$C_{N^{3-}} = \frac{\left(\%N^{3-}\right)\left(p_{O_2}\right)^{\frac{3}{4}}}{\left(p_{N_2}\right)^{\frac{1}{2}}} = K\frac{a_{O^-}}{f_{N^-}\left(a_{O^{2-}}\right)^{\frac{1}{2}}} \tag{2.5.23}$$

where K is an equilibrium constant for reaction 2.5.21, f_i is an activity coefficient for species i. In this case N^{3-} does not mean a free nitride ion but the nitrogen analyzed as a nitride which is associated with the network former. Similar reactions can be written for bridging oxygen, but then reactions are less likely. In either case the nitride capacity decreases with oxygen ion activity, i.e. increasing slag basicity.

For the $CaO–SiO_2$, $CaO–Al_2O_3$, and $CaO–SiO_2–Al_2O_3$ systems CaO is the basic component. Therefore the equations predict that a plot of the logarithm of nitride capacity versus the logarithm of the activity of CaO should yield a straight line with a slope of $-\tfrac{1}{2}$ as shown in Fig. 2.69.
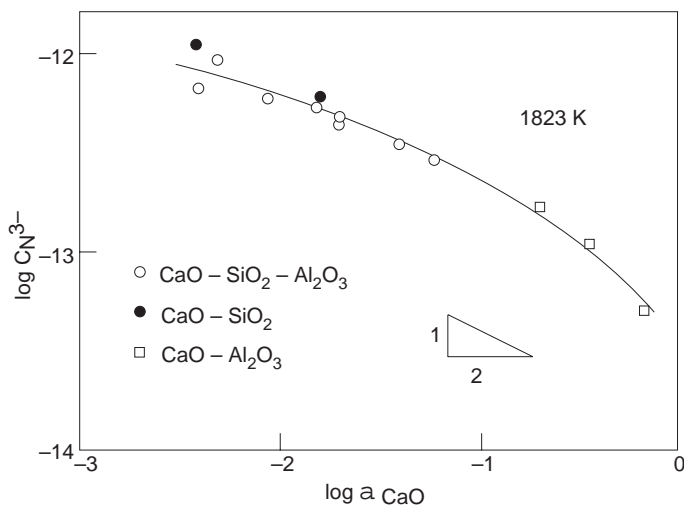
Fig. 2.69 The relation between the nitride capacity and the activity of lime for $CaO–SiO_2–Al_2O_3$ slag at 1823 K. Ref. 105.

For highly basic oxide systems the nitrogen enters as a free nitride ion and the simple relationship given by 2.5.19 is valid. In this case the free nitride concentration and the nitride capacity is proportional to the oxygen ion activity to the 3/2 power ($a_{O^{2-}}$)$^{3/2}$. Min and Fruehan[106] have shown that the nitride capacity does increase with basicity for highly basic slags, particularly when there is no strong network former such as SiO_2 present. In theory the nitride capacity should decrease with basicity when the nitrogen is primarily in the network and increase when it is a free nitride. This was observed for the $BaO–B_2O_3$ and $CaO–B_2O_3$ system as shown in Fig. 2.70.
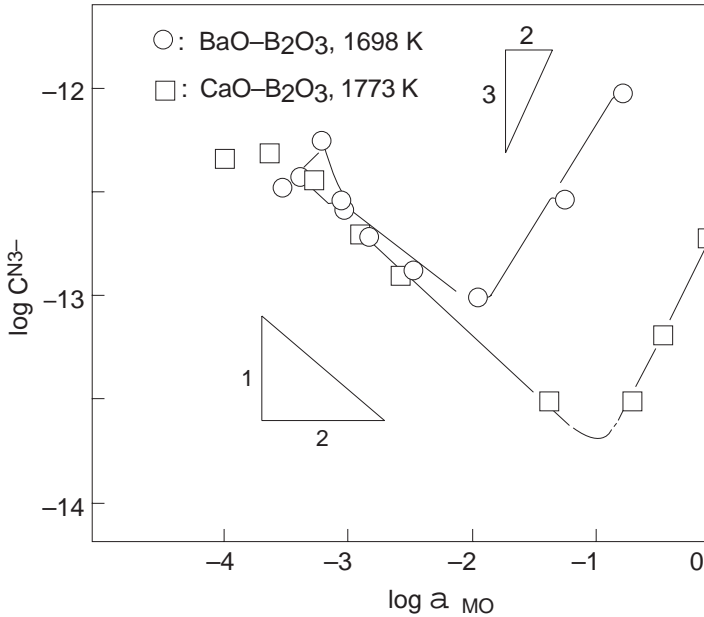
Fig. 2.70 Nitride capacity of the slags as a function of the activity of CaO or BaO. *From Ref. 106.*

2.5.6.2.2 Nitrogen Removal by Slags   For Al-killed steels the corresponding equilibrium partial pressure of oxygen is

$$p_{O_2} \text{ (atm)} = \frac{1.22 \times 10^{-16}}{[\%Al]^{4/3}} \text{ at } 1600°C \qquad (2.5.24)$$

From the solubility data for nitrogen we have

$$\left(p_{N_2}\right)^{1/2} \text{ (atm)}^{1/2} = 21.9[\%N] \text{ at } 1600°C \qquad (2.5.25)$$

Substituting these in the equation for C_N gives

$$C_N = \frac{(\%N)}{[\%N][\%Al]} \times 5.3 \times 10^{-14}$$

In lime-rich aluminate ladle slags of low SiO_2 content, the lime activity is $a_{CaO} = 0.5$ for which $C_N = 10^{-13}$. These give the following equilibrium relation

$$\frac{(\%N)}{[\%N]} = 1.9 \times [\%Al]$$

Dissolved [%Al]	(%N) / [%N]
0.005	0.0095
0.02	0.038
0.06	0.114
0.10	0.190

The equilibrium nitrogen distribution ratio between slag and steel is very low even at high aluminum contents, well above the practical range. The slag/steel mass ratio in the ladle is also low, about 1/100. For these reasons, liquid steel in the ladle cannot be de-nitrogenized by the slag that is usable in industry in steel refining.

As noted from the recent experimental studies of Fruehan and co-workers,[106–108] that even with fluxes of high nitride capacities (as with alkaline earth borates) it is not practically possible to remove nitrogen from the aluminum-killed steel in the ladle. The highest nitride capacity was for a slag containing about 22% CaO – 27% BaO – 48% Al_2O_3 – 3% TiO_2 and was about 5×10^{-12}. For this case for a steel containing 0.06% Al the nitrogen distribution ratio is about 5.5 which is still not high enough for effective nitrogen removal.

2.5.6.3 Solubility of S_2

Sulfur-bearing gases dissolve in molten slags as sulfide ions (S^{2-}) under reducing conditions, and as sulfate ions (SO_4^{2-}) under highly oxidizing conditions. In steelmaking the oxygen potential is not high enough for the solution of sulfur as sulfate ions, therefore we need to consider only the sulfide reaction.

Whether the sulfur-bearing species is primarily H_2S or SO_2, there is a corresponding equilibrium value of p_{S_2} depending on the temperature and gas composition. It is convenient to consider the reaction in a general form as

$$\tfrac{1}{2}S_2(g) + (O^{2-}) = (S^{2-}) + \tfrac{1}{2}O_2(g) \tag{2.5.26}$$
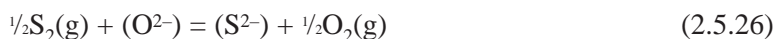
For a given slag composition the equilibrium relation is represented by

$$C_S = (\%S)\left(\frac{p_{O_2}}{p_{S_2}}\right)^{\tfrac{1}{2}} \tag{2.5.27}$$

where p's are equilibrium gas partial pressures. The equilibrium constant C_S is known as the sulfide capacity of the slag. The value of C_S depends on slag composition and temperature.

Experimentally determined sulfide capacities of binary oxide melts are shown in Fig. 2.71. References to experimental data are given in Ref. 3.

For the slag-metal system, the sulfur reaction is formulated in terms of the activities

($\cong$ concentrations) of sulfur and oxygen dissolved in the steel.

$$[S] + (O^{2-}) = (S^{2-}) + [O] \tag{2.5.28}$$

For low-alloy steels

$$k_S = \frac{(\%S)}{[\%S]}[\%O] \tag{2.5.29}$$

where the equilibrium constant k_S depends on slag composition and temperature.

2.5.6.3.1 Conversion of p_{O_2}/p_{S_2} to [%O]/[%S] The free energies of solution of O_2 and S_2 in liquid low alloy steel are given below; see Table 2.1 in section 2.1.2.4.2.

$$\tfrac{1}{2}S_2 = [S]; \quad \Delta G_s = -135,060 + 23.43T J \tag{2.5.30}$$

$$\tfrac{1}{2}O_2 = [O]; \quad \Delta G_o = -115,750 - 4.63T J \tag{2.5.31}$$

For the reaction equilibrium

$$\tfrac{1}{2}S_2 = [O] = \tfrac{1}{2}O_2 + [S]$$
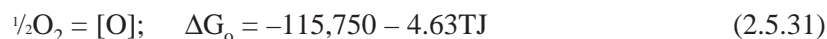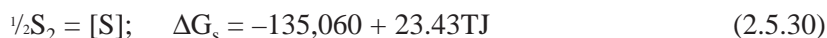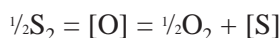
the standard free energy change is

$$\Delta G° = \Delta G_s - \Delta G_o = -19,310 + 28.06T J \tag{2.5.32}$$

$$\log\left(\frac{p_{O_2}}{p_{S_2}}\right)^{1/2}\frac{[\%S]}{[\%O]}=\frac{1009}{T}-1.466 \tag{2.5.33}$$

For steelmaking temperatures an average value of K is 0.133; with this conversion factor the following is obtained.

$$\left(\frac{p_{O_2}}{p_{S_2}}\right)^{1/2}=0.133\frac{[\%O]}{[\%S]} \tag{2.5.34}$$

With this substitution the values of C_S are converted to k_S.

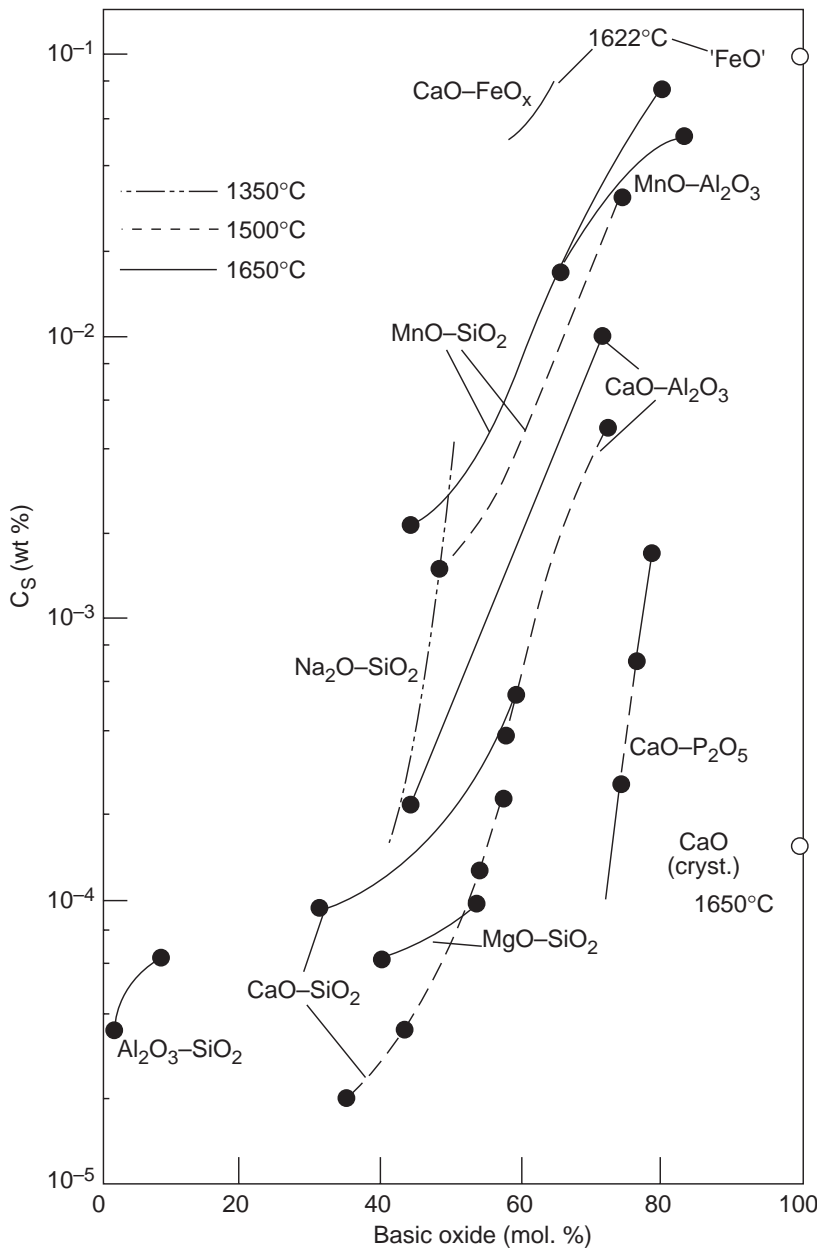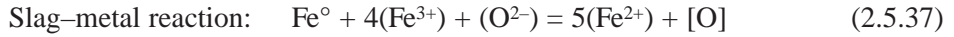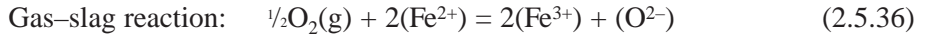$$7.5\times C_S = k_S = \frac{(\%S)}{[\%S]}[\%O] \tag{2.5.35}$$

Fig. 2.71 Sulfide capacities of binary oxide melts. *From Ref. 3.*

A slag of high k_S value and steel deoxidation to low levels of [O] are necessary conditions for steel desulfurization. The subject is discussed in more detail later.

2.5.6.4 Solubility of O_2

Oxygen dissolves in molten slags by oxidizing the divalent iron ions to the trivalent state.

$$\text{Gas–slag reaction:} \quad \tfrac{1}{2}O_2(g) + 2(Fe^{2+}) = 2(Fe^{3+}) + (O^{2-}) \qquad (2.5.36)$$

$$\text{Slag–metal reaction:} \quad Fe° + 4(Fe^{3+}) + (O^{2-}) = 5(Fe^{2+}) + [O] \qquad (2.5.37)$$

These reactions provide the mechanism for oxygen transfer from gas to metal through the over-laying slag layer. Partly for this reason, the steel reoxidation will be minimized by maintaining a low concentration of iron oxide in the ladle slag, tundish and mold fluxes.

Examples are given in Fig. 2.72 of variations of the ratio Fe^{3+}/Fe^{2+} with slag composition of melts co-existing with liquid iron, reproduced from a paper by Ban-ya and Shim[109].
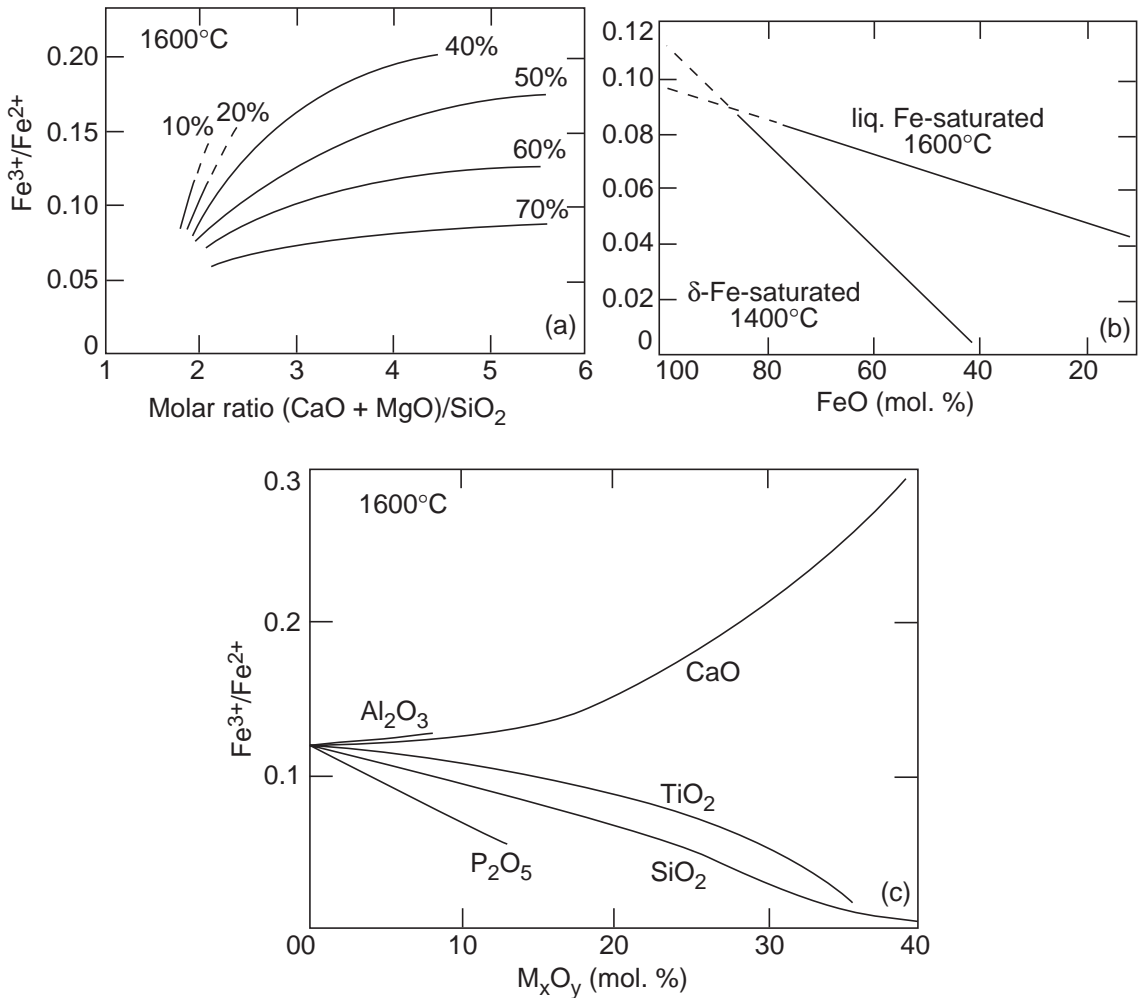
Fig. 2.72 Effect of slag composition on the ratio Fe^{3+}/Fe^{2+} in melts saturated with metallic iron at 1600°C: (a) CaO–MgO–SiO$_2$–FeO melts at indicated molar concentrations of total iron oxide FeO; (b) MgO–SiO$_2$–FeO melts; (c) pseudobinary FeO–M$_x$O$_y$ melts. *From Ref. 109.*

2.5.7 Surface Tension

Surface tensions measured by Kozakevitch[110] are given in Fig. 2.73 for binary melts with iron oxide, and in Fig. 2.74 for FeO–MnO–SiO$_2$ and FeO–CaO–SiO$_2$ melts at 1400°C. For additional data on surface tension of a wide variety of slags and mold fluxes, reference may be made to a review paper by Mills and Keene[111].
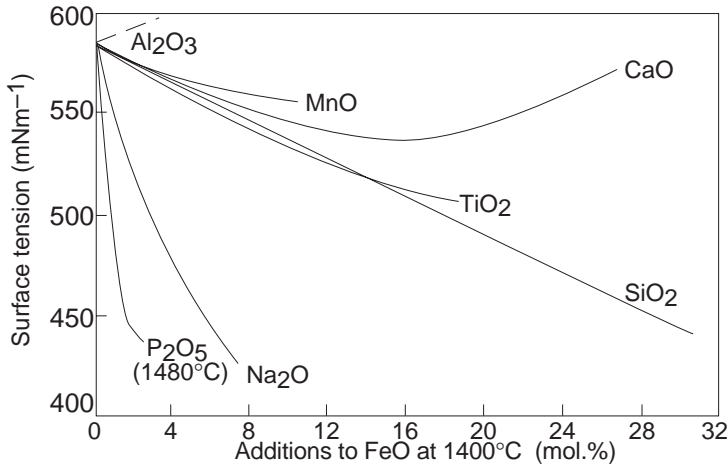
Fig. 2.73 Surface tensions of binary iron oxide melts at 1400°C. *From Ref. 110.*
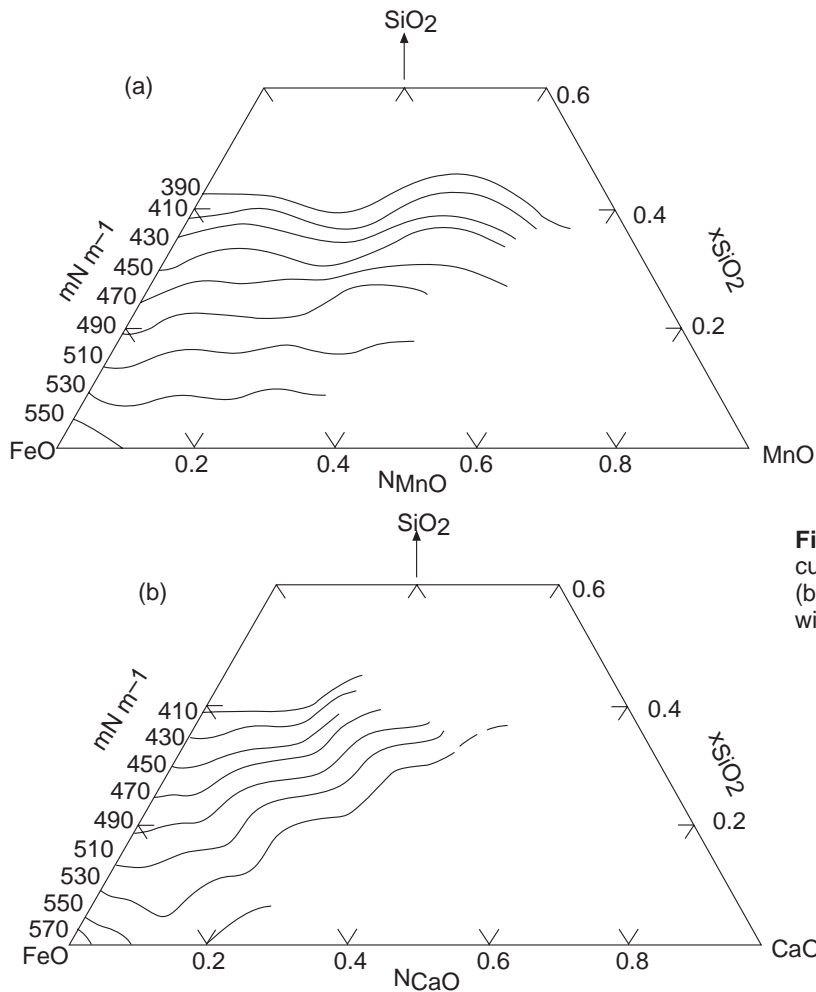
Fig. 2.74 Isosurface tension curves in (a) FeO-MnO-SiO$_2$ and (b) FeO-CaO-SiO$_2$ melts saturated with iron at 1400°C. *From Ref. 110.*

2.5.7.1 Interfacial Tension

The slag-metal interfacial tensions have values between those for the gas-slag and gas-metal surface tensions. Consequently, the addition of surface active elements to liquid iron lowers the slag-metal interfacial tension.

Effects of sulfur and oxygen dissolved in iron on the interfacial tension between liquid iron and CaO–Al_2O_3–SiO_2 melts at 1600°C, determined by Gaye *et al.*[112], are shown in Figs. 2.75 and 2.76; compared to the surface tensions of Fe–S and Fe–O melts. The effect of oxygen on the interfacial tension is greater than sulfur, e.g. $\sigma_i = 600$ mN m^{-1} with $a_O = 0.05$ (0.05%) while at $a_S = 0.05$ (0.05%), $\sigma_i = 1000$ mN m^{-1}.

Fig. 2.75 Effect of oxygen in iron on the interfacial tension between liquid iron and CaO–Al_2O_3–SiO_2 melts, determined by Gaye et al.[112] is compared to the surface tension of Fe–O melt at 1600°C.
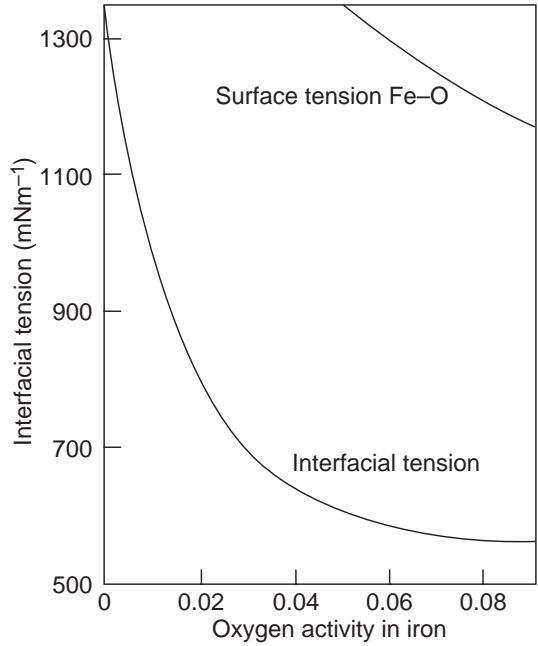
Fig. 2.76 Effect of sulfur in iron on the interfacial tension between liquid iron and CaO–Al_2O_3–SiO_2 melts, determined by Gaye et al.[112] is compared to the surface tension of Fe–S melts at 1600°C.
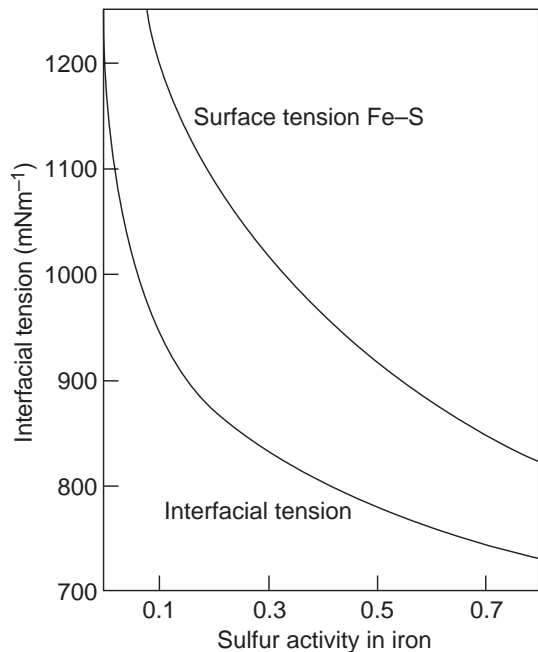
As shown by Ogino *et al.*[113] Fig. 2.77, a single curve describes adequately the effect of oxygen in iron on the interfacial tension between liquid iron and a wide variety of simple and complex slags, including those containing Na_2O and CaF_2. In the case of slags containing iron oxide, a decrease in interfacial tension with an increasing iron oxide content is due entirely to the corresponding increase in the oxygen content of the iron.

Recently Jimbo and Cramb[114] accurately measured the interfacial tension between liquid iron and $CaO–Al_2O_2–SiO_2$ slags. As shown in Fig. 2.78 their results are slightly higher than those of Gaye *et al.*
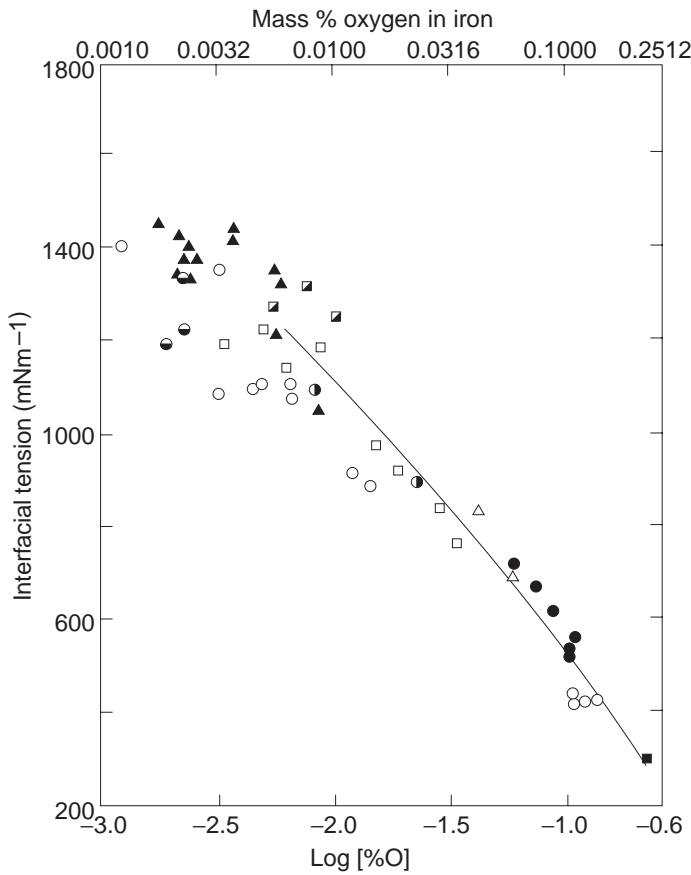
Fig. 2.77 General relation between the oxygen content of iron and the interfacial tension between the metal and various slag systems at 1580°C. *From Ref. 113.*
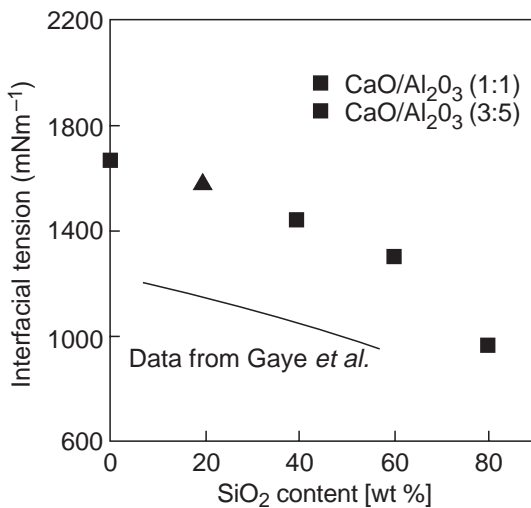
Fig. 2.78 Interfacial tension between $CaO–Al_2O_3–SiO_2$ and Fe at 1600°C. *From Ref. 114.*

2.5.8 Density

Many repetitive measurements of slag densities have been made. Only selected references are given on the density data cited here for steelmaking type of slags. Since the density of silica (2.15 g cm^{-3} at 1700°C) is much lower than the densities of other metal oxide components of slags, densities of slags will decrease with an increasing silica content.

The density data for binary silicates are given in Fig. 2.79. The data in Fig. 2.80 are for CaO–MgO–Al$_2$O$_3$–SiO$_2$ melts, relevant to neutral slags for steel refining in the ladle.

Fig. 2.79 Densities of binary silicate melt. *From Refs. 115–119.*
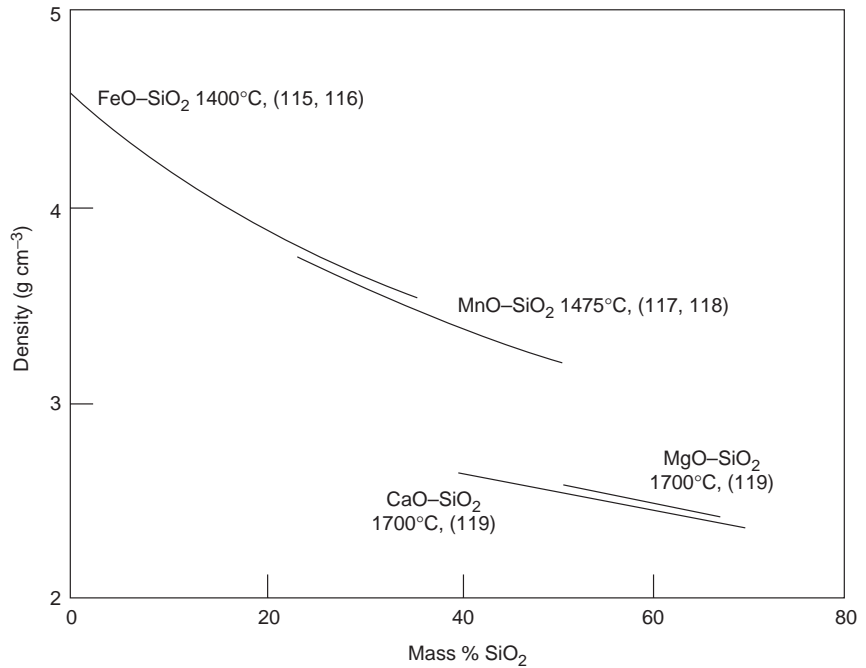
Fig. 2.80 Densities of CaO–MgO–Al$_2$O$_3$–SiO$_2$ melt at 1550°C, using data in Refs; 120–122. (a) 0% MgO, CaO/Al$_2$O$_3$ = 1; (b) 0% MgO, 5% Al$_2$O$_3$; (c) 5% MgO, 5%Al$_2$O$_3$.
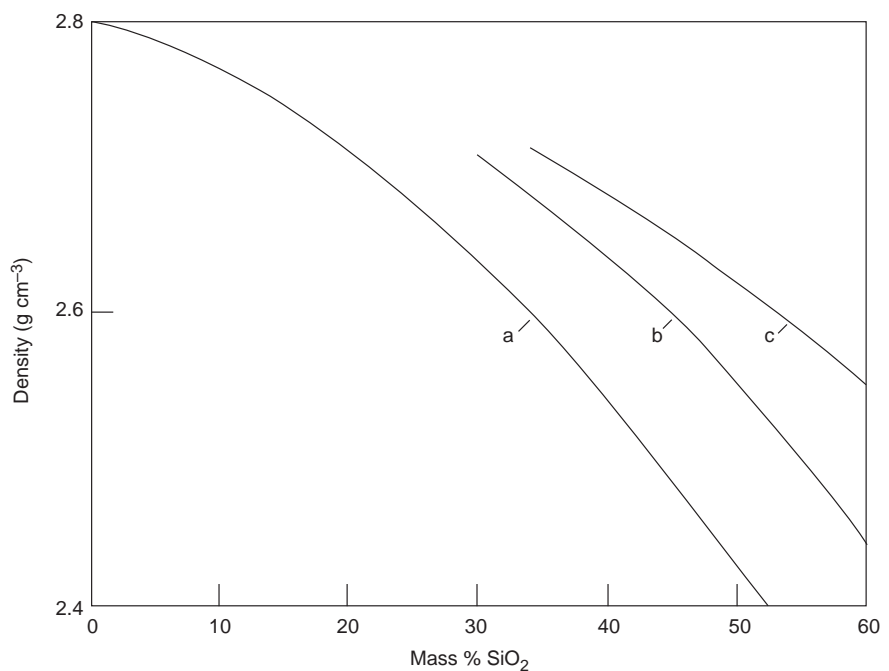
The density data in Fig. 2.81 compiled by Mills and Keene[111] are for simple and complex slags containing FeO, CaO, MgO, SiO$_2$ and P$_2$O$_5$. Since the densities of FeO–SiO$_2$ and MnO–SiO$_2$ are essentially the same, the average of the data in Fig. 2.81 is represented by the following equation in terms of (%FeO + %MnO).

$$\rho, gcm^{-3} = 2.46 + 0.018 \text{ x } (\%FeO + \%MnO) \tag{2.5.38}$$
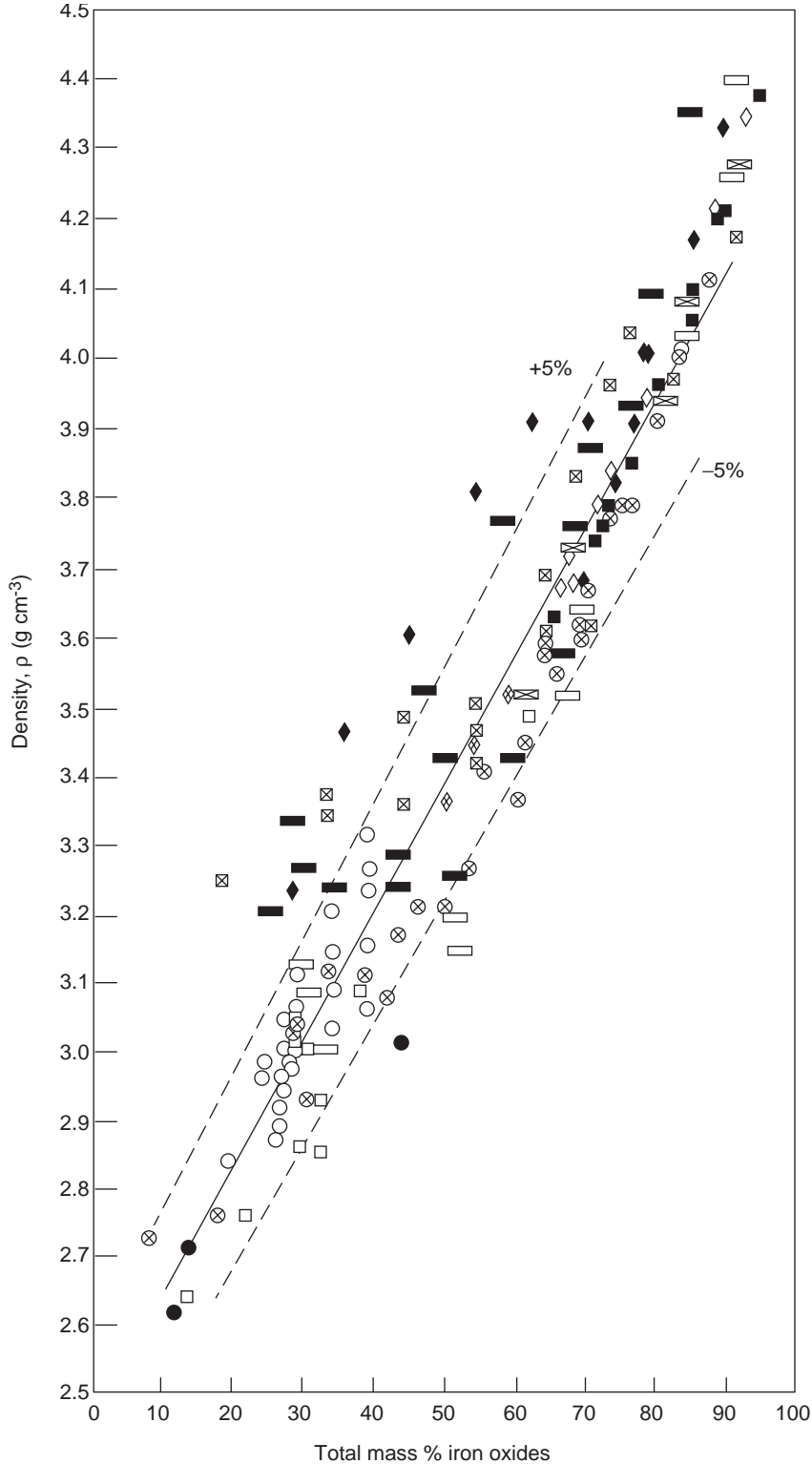
Fig. 2.81 Densities of simple and complex slags containing iron oxide at about 1400°C. *From Ref. 111.*

2.5.9 Viscosity

The size of the silicate and aluminosilicate network in molten slags becomes larger with increasing SiO_2 and Al_2O_3 contents, hence their mobility decreases resulting in a higher viscosity. The addition of metal oxides or an increase in temperature leads to the breakdown of the $Si(Al)O_4$ network, resulting in lower melt viscosity.

Machin and Yee[123] made an extensive study of the viscosity of $CaO–MgO–Al_2O_3–SiO_2$ melts at temperatures of 1350 to 1500°C. The data in Fig. 2.82 are for the ternary system at 1500°C. The isokoms are approximately parallel to the binary side $Al_2O_3–SiO_2$, indicating that $Al_2O_3–SiO_2$ are isomorphous in their effect on the slag viscosity. The isokoms in Fig. 2.83 are for the quaternary system with 35% and 50% SiO_2. In this case, the isokoms are approximately parallel to the binary side $CaO–MgO$, indicating that Ca^{2+} and Mg^{2+} cations have similar effects on the breakdown of the aluminosilicate network.

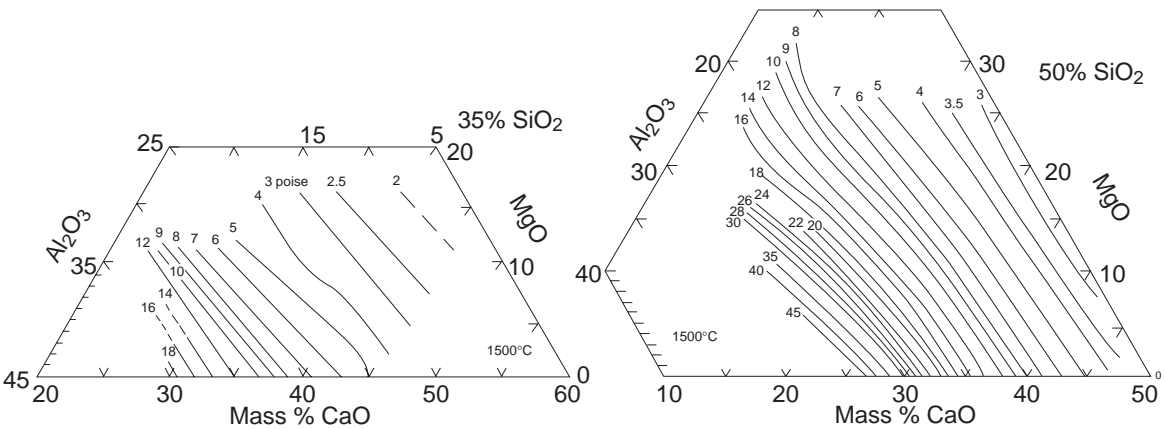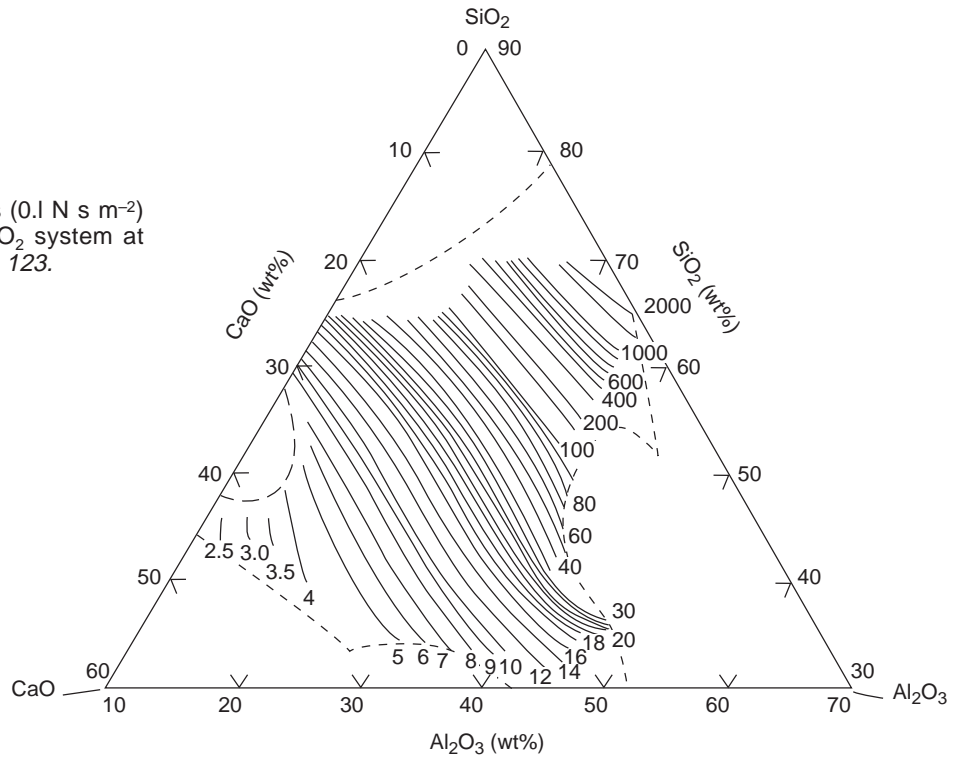**Fig. 2.82** Isokoms (0.l N s m⁻²) for $CaO–Al_2O_3–SiO_2$ system at 1500°C. *From Ref. 123.*

Fig. 2.83 Isokoms (0.l N s m⁻²) for $CaO–MgO–Al_2O_3–SiO_2$ system at 1500°C for melts containing 35% and 50% SiO_2. *From Ref. 123.*
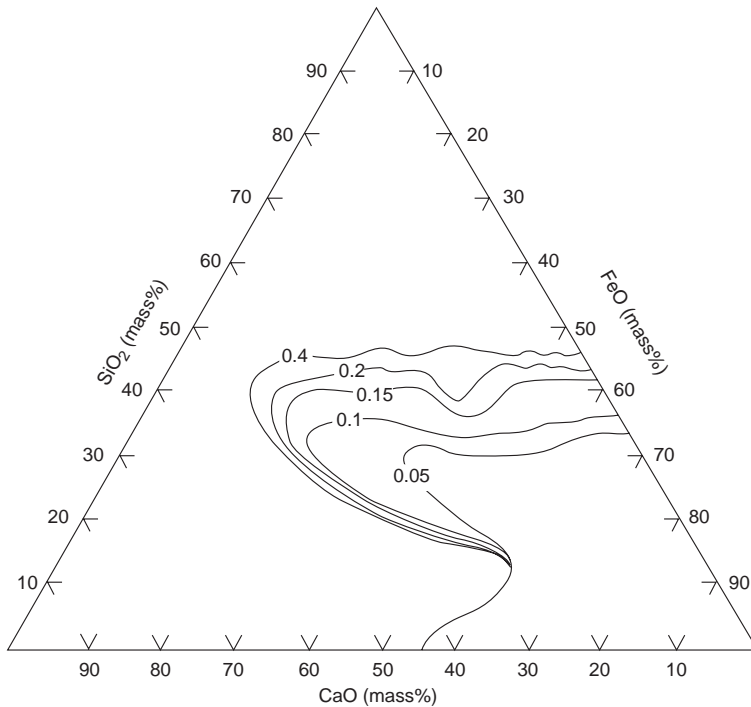
Fig. 2.84 Viscosity (N s m^{-2}) of CaO–FeO–SiO$_2$ melts in 1400°C. *From Ref. 110.*

Viscosities of steelmaking slags are well represented by the experimental data of Kozakevitch[110] given in Fig. 2.84

In the study of viscosities of mold fluxes for continuous casting, the experimental results have been represented as a function of temperature using the relation.

$$\eta = AT \exp (B/T) \qquad (2.5.39)$$

where A and B are functions of slag composition. For the composition range (wt %) 33–56% SiO_2, 12–45% CaO, 0–11% Al_2O_3, 0–20% Na_2O and 0–20% CaF_2, an interpolation formula has been derived for the parameters A and B as a function of the mole fractions of the constituents as given below.

$$\ln A = -17.51 - 35.76(Al_2O_3) + 1.73(CaO) + 5.82(CaF_2) + 7.02(Na_2O) \qquad (2.5.40)$$

$$B = 31,1140 - 68,833(Al_2O_3) - 23,896(CaO) - 46,351(CaF_2) - 39,519(Na_2O) \qquad (2.5.41)$$

where A is in units of 0.1 N s m^{-2} K^{-1} (poise/deg.) and B in degrees Kelvin.

2.5.10 Mass Diffusivity, Electrical Conductivity and Thermal Conductivity

2.5.10.1 Mass Diffusivity

Because of the ionic nature of molten slags, the diffusive mass transfer is by ions. The ionic diffusivities are measured using the radioactive tracer elements dissolved in an oxidized form in the melt. Typical examples of ionic diffusivities in slags at 1600°C are given below.

Ion	D_i^*, cm^2/s
Si^{4+}, O^{2-}	$4 \times 10^{-7} - 1 \times 10^{-6}$
Al^{3+}	$\approx 1 \times 10^{-6}$
Ca^{2+}, Mg^{2+}, Fe^{2+}	$6 \times 10^{-6} - 1 \times 10^{-5}$
S^{2-}	$\approx 4 \times 10^{-6}$

Since the electroneutrality has to be maintained, diffusion of a cation is accompanied by diffusion of the oxygen ion. The diffusion that occurs in the dissolution of a solid oxide in the slag is controlled by the mobility of the O^{2-} ion which is smaller than the divalent cations.

2.5.10.2 Electrical Conductivity

The electrical current in molten slags is carried by the cations. However, in slags containing high concentrations of FeO or MnO (> 70%) the electronic conduction becomes the dominant mechanism.

The ionic conductivity λ_i is theoretically related to the self diffusivity of the ionic species i by the Nernst-Einstein equation

$$D_i^* = \frac{RT}{F^2 Z_i^2 C_i} \lambda_i \tag{2.5.42}$$

where

$\quad$ F $\quad=\quad$ Faraday constant; 96,489 C mol^{-1},
$\quad$ Z_i $\quad=\quad$ valency of ion i,
$\quad$ C_i $\quad=\quad$ concentration of ion i, mol cm^{-3},
$\quad$ λ_i $\quad=\quad$ specific conductivity, Ω^{-1}cm^{-1}.
$\qquad\qquad\qquad$ For steelmaking slags: $\lambda = 0.5$–1.5 Ω^{-1}cm^{-1}.
$\qquad\qquad\qquad$ For ladle slags: $\lambda = 0.4$–0.7 Ω^{-1}cm^{-1}.

The electrical conductivity increases with an increasing slag basicity and increasing temperature.

2.5.10.3 Thermal Conductivity

Because of the presence of iron oxide, the metallurgical slags are opaque to infrared radiation, therefore the heat conduction is primarily thermal.

Thermal conductivity of slags and mold fluxes are in the range 0.5 to 1.2 Wm^{-1}K^{-1}. From experimental data the following approximate empirical relation has been found

$$\kappa(\text{Wm}^{-1}\,\text{K}^{-1}) = 1.8 \times 10^{-5}\,\text{V}^{-1} \tag{2.5.43}$$

where V is the molar volume = M/ρ, m^{3}mol^{-1}.

2.5.11 Slag Foaming

Slag foaming plays an important role in many steelmaking processes. In oxygen steelmaking excessive foaming can lead to slopping. On the other hand controlled foaming in the electric arc furnace is desirable to protect the refractories from the electrical arc radiation. In the direct ironmaking processes such as DIOS and AISI Direct Steelmaking, excessive foaming can cause operational problems. However some foam is desirable to help capture the energy from post combustion. Slag foaming should not be confused with simple gas bubbling or hold up. Whenever gas passes through a liquid, the liquid expands due to the presence of the gas. However in some liquids a stable foam develops which consists of foam bubbles on the top of an unfoamed liquid.

Early work on foaming was limited to a qualitative understanding of this complex phenomenon. Due to the added importance of foaming in the EAF and iron bath systems Ito and Fruehan[124,125] and other researchers developed a quantitative measure of foaming and measured the foaming characteristics of many important slag systems. The foam index (Σ) was defined by

$$\Sigma = \frac{\Delta h}{V_g^s} \tag{2.5.44}$$

$$V_g^s = \frac{Q}{A} \tag{2.5.45}$$

where

$\quad$ Δ $\quad=\quad$ the increase in the height of the slag,
$\quad$ V_g^s $\quad=\quad$ the superficial gas velocity,
$\quad$ Q $\quad=\quad$ the gas flow rate,
$\quad$ A $\quad=\quad$ the area of the vessel.

It follows that the volume of foam is approximately given by

$$Vf = Q\Sigma \tag{2.5.46}$$

The foam index has the units of time and represents the average traveling time of the gas through the foam.

The foam can also be characterized by the time for the foam to decay. The average foam life (τ) is defined by the first order decay

$$\ln \frac{h}{h_\circ} = -\frac{t}{\tau} \qquad (2.5.47)$$

where h and $h_\circ$ are the foam height and the foam height when the gas flow stops, respectively. It can be shown that for an ideal foam, in which the gas fraction of the foam is constant, that the foam index (Σ) and foam life (τ) are equal.

The foam index for CaO–SiO$_2$–FeO–Al$_2$O$_3$ system is shown in Fig. 2.85. The foam index decreases initially with increasing basicity because the viscosity is decreasing. However when the solubility limit is reached the foam index increases with basicity because the second phase particles increase the bulk viscosity of the slag.

Zhang and Fruehan[126] later demonstrated that the foam index on stability increased with decreasing bubble size and developed a general correlation demonstrated in Fig. 2.86 from which the foam index for many complex systems would be desired.

$$\Sigma = \frac{\eta^{1.2}}{\sigma^{0.2} \rho D_B^{0.9}} \qquad (2.5.48)$$

where

$$\begin{aligned}
\eta &= \text{slag viscosity,} \\
\sigma &= \text{surface tension,} \\
\rho &= \text{slag density,} \\
D_B &= \text{foam bubble diameter.}
\end{aligned}$$

Takumetsu et al[127] showed that in bath smelting processes char could reduce foaming significantly. Zhang and Fruehan[128] examined the fundamentals of slag control by carbonaceous materials. Due to surface tension phenomenon the slag foam bubbles collapse and form longer bubbles resulting in a less stable foam. Carbonaceous materials will cause the foam to collapse while others such as alumina particles or iron oxide pellets do not due to the different wetting characteristics with the slag.

The fundamentals of slag foaming have been applied to a variety of processes such as oxygen and EAF steelmaking, bath smelting and ladle processing. The fundamental principles allow for reasonable predictions of foaming in these processes.
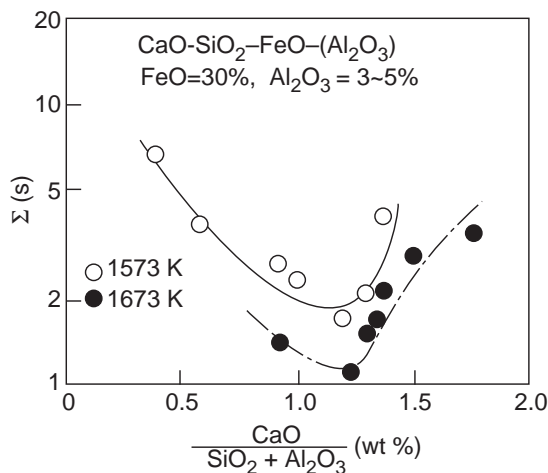

Fig. 2.85 The foam index of CaO–SiO$_2$–FeO–Al$_2$O$_3$ slags illustrating the effect of second phase particles. *From Ref. 126.*
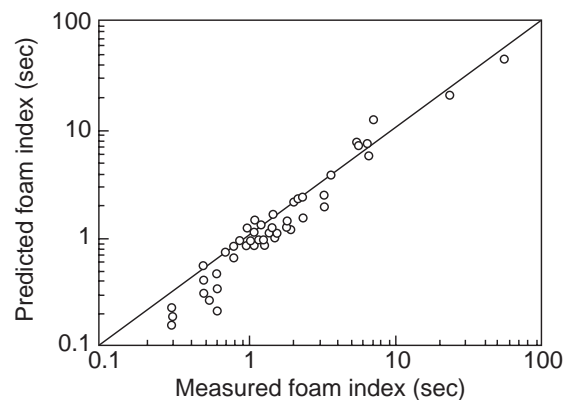
Fig. 2.86 Comparison between the measured foam index and that predicted by the correlation equation 2.5.48. From Ref 126.

2.5.12 Slag Models and Empirical Correlations for Thermodynamic Properties

There have been several attempts to develop models and correlations for slags, from which thermo-dynamic properties such as activities and capacities can be predicted. Simple models such as a regular solution have been used.[129] However because of the ionic nature and structure of slags they are generally inadequate. Recently Gaye and Lehmann reviewed the current status of structural models.[130]

The most successful models have been developed by Gaye and coworkers[131] at IRSID and Blander *et al*.[132] In the IRSID model the slag is represented using an oxygen sublattice and a cationic sublattice. The structure is defined in terms of cells composed of a central oxygen surrounded by two cations. Two parameters are used to calculate the energy of the system; the energies of formation of asymmetric cells and the interaction energies limited to one parameter per couple of cations. These parameters are computed from the known thermodynamics of the binary systems. It is beyond the scope of this chapter to describe the model in greater detail. The model has been used successfully to estimate the phase diagrams and thermodynamic activities in multi-component systems as well as sulfide capacities. Whereas this model is complex and requires binary data, to date it is the best model available for estimating thermodynamic properties of slags.

In recent years various capacities such as the sulfide and phosphate capacities have been correlated to a term called the optical basicity. This concept has been recently reviewed by Summerville *et al*.[133] Briefly each oxide is assigned a value for its optical basicity which is related to the Pauling electronegativity. By definition the optical basicity of CaO is taken as unity. Components such as Na_2O have optical basicities greater than one while acidic oxides such as SiO_2 have values less than one. The optical basicity of a slag is then computed from a weighted average of the components in the slag. The optical basicity has been used to correlate a large number of studies on sulfide and other capacities.[133, 134] Whereas the optical basicity is an interesting concept, the correlations are not sufficiently accurate to predict capacities for industrial purposes. For example the deviations between the correlation and actual data is 25–50% in some cases. This is not accurate enough for computing sulfur equilibrium in industrial applications. However the optical basicity correlation maybe useful for making crude estimates of capacities for which no data exists or to predict trends when changing slag compositions slightly.

2.6 Fundamentals of Ironmaking Reactions

Reference may be made to a book entitled "The Iron Blast Furnace", authored by Peacey and Davenport.[135] In this book, the theoretical, experimental and operational data have been put together about the blast furnace with particular emphasis on the interrelations between countercurrent heat and mass transfer between gases and solids in the blast furnace stack. Reference may also be made to the earlier studies of Rist and co-workers[136–140] on the heat and mass transfer and reduction reactions in the stack.

In this section, the following aspects of the blast furnace reactions are considered: oxygen potential diagram, role of vapor species in blast furnace reactions, slag-metal equilibrium, reaction mechanisms and operational slag-metal data.

2.6.1 Oxygen Potential Diagram

The reducibility of a metal oxide relative to other oxides, or the oxidisability of a metal relative to other metals, can readily be assessed from the free energy data.

For the oxidation reaction involving pure metals and metal oxides in their standard states, i.e. $a_M = 1$, $a_{MO} = 1$

$$2M + O_2 = 2MO \qquad (2.6.1)$$

the isothermal equilibrium constant is

$$K = \frac{1}{p_{O_2}} \qquad (2.6.2)$$

where p_{O_2} is the equilibrium oxygen partial pressure for which the standard state is 1 atm at the temperature under consideration. The standard free energy change is

$$\Delta G^\circ = -RT \ln K = RT \, 1n \, p_{O_2} \tag{2.6.3}$$

which is also called the oxygen potential.

In an earlier study, Richardson and Jeffes[141] compiled the free energy data on metal oxides which were then available, and presented the data, Fig. 2.87, as an oxygen potential diagram.

The oxides for which the oxygen potential lines are above that of CO may be reduced by carbon. As the affinity of the metals for oxygen increases, i.e. ΔG° decreases, the temperature of reduction of the oxides by carbon increases.

For easy conversion of oxygen potentials to the corresponding values of p_{O_2} or to the equilibrium ratios of H_2/ H_2O and CO/CO_2, appropriate scales are included in the enclosed oxygen potential diagram for various oxides of metallurgical interest.

Scale for p_{O_2}:

>Lines drawn from the point O on the ordinate for the absolute zero temperature through the points marked on the right hand side of the diagram give the isobars. For example, for the Fe–FeO equilibrium the oxygen potential is –82 kcal (–343 kJ) at 1200°C. By drawing a line passing through this point and the point O, the oxygen partial pressure of about 7×10^{-13} atm is read off the log p_{O_2} scale.

Scale for CO/CO_2:

>Draw the line from point C to a point on the oxygen potential; the extension of this line gives the corresponding equilibrium log CO/CO_2 ratio.

Scale for H_2/H_2O:

>Same as above by using point H.

These diagrams can be used to predict CO/CO_2 or H_2/H_2O ratios as well as the pressure of oxygen in equilibrium with numerous metals and their oxides. They are particularly useful for predicting the CO/CO_2 ratio in a blast furnace or the H_2/H_2O ratio in direct reduction with natural gas. It also gives an indication of the relative reduceability of the oxides. It should be remembered that the diagrams are for unit activity of the metal. If the metal is in solution, it is easier to reduce. For example, if the activity of Si is 10^{-3} relative to pure Si in liquid iron, the equilibrium oxygen pressure is 10^3 times higher. Similarly, if the activity of SiO_2 is lowered in a slag it is more difficult to reduce.

2.6.2 Role of Vapor Species in Blast Furnace Reactions

Because of the high temperatures involved, vaporization plays a significant role in pyrometallurgical reactions. In a reactor such as a blast furnace, the formation and condensation of various vapor species is responsible for the recycle of some of the elements between the high and low temperature regions of the furnace.

The countercurrent flow in the blast furnace of solids from low- to high-temperature zones and of gases from high- to low-temperature zones brings about a cyclic process of vaporization and condensation which has a decisive influence on the overall operation of the furnace.

2.6.2.1 Vapor Species SiO, SiS and CS

It is now well established that the silicon and sulfur in the coke are transferred to the slag and iron in the blast furnace via the vapor species SiO, SiS, CS, and other minor sulfur-bearing species. The earlier and recent studies of quenched blast furnaces have revealed that while the sulfur content of the slag increases with the descent of the burden in the bosh, the sulfur and silicon contents of the metal droplets reach maxima and then decrease as they pass through the slag layer. This phenomenon of vapor-phase mass transfer has been substantiated by the experimental work of Tsuchiya *et*

al,[142] Turkdogan *et al* [143] and Ozturk and Fruehan[144] under conditions partly simulating the bosh region of the blast furnace.

In the presence of carbon and depending on temperature and activity of silica in the slag or coke, the SiO vapor is generated by one of the following reactions
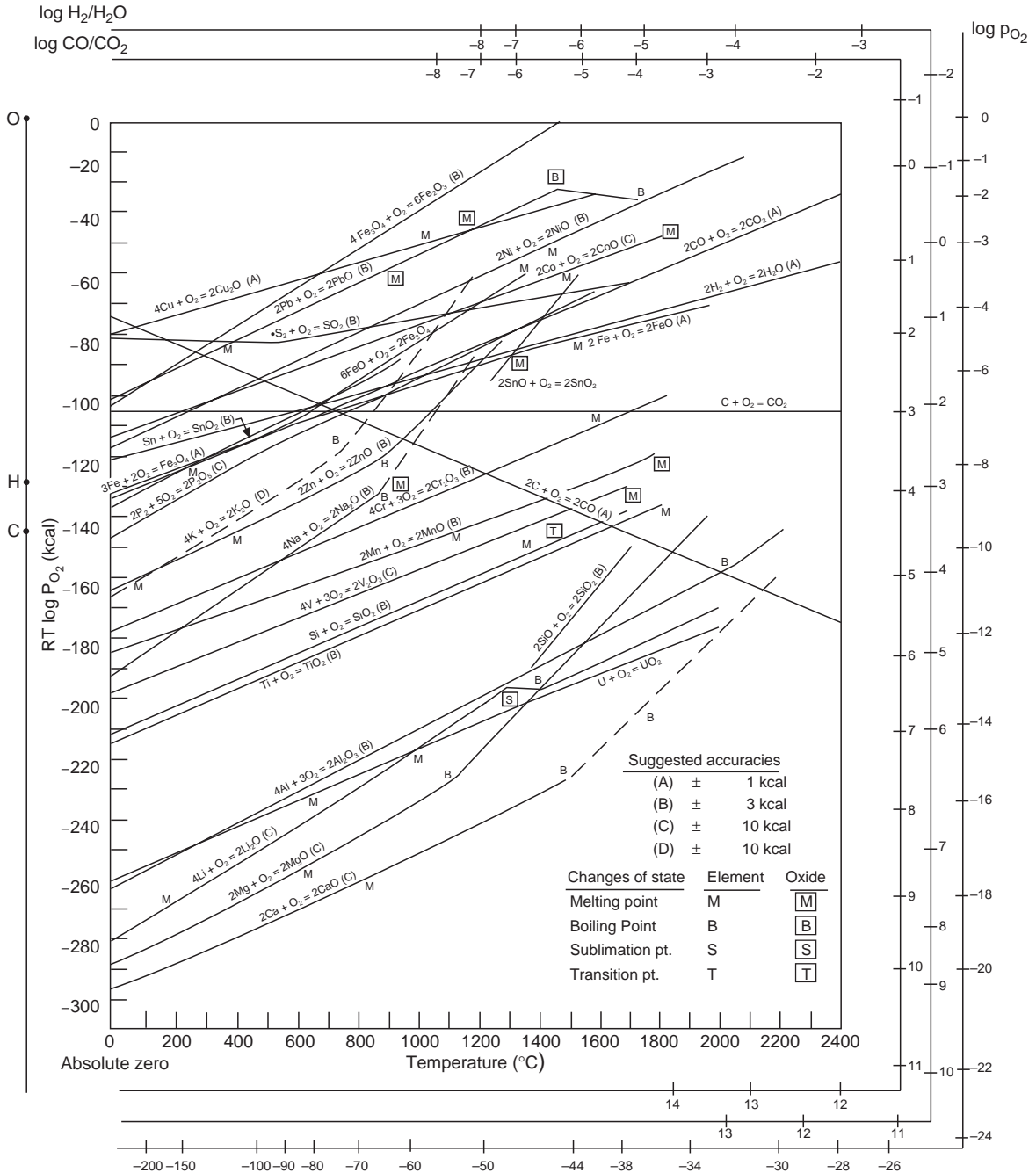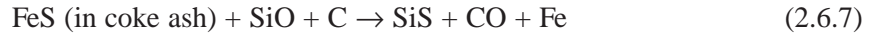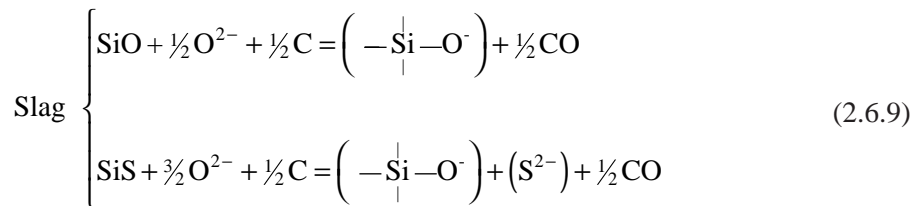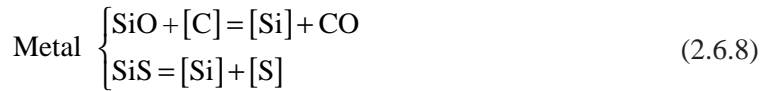
$$SiO_2 \text{ (in coke ash or slag)} + C \rightarrow SiO + CO \qquad (2.6.4)$$

$$SiC + CO \rightarrow SiO + 2C \qquad (2.6.5)$$

Fig. 2.87 Oxygen potential diagram. *From Ref. 141.*

At 1 bar pressure of CO, $a_{SiO_2} = 1$ and above about 1500°C, SiO_2 is converted to SiC and SiO is generated by reaction 2.6.5; for $a_{SiO_2} = 0.1$, reaction 2.6.5 applies only at temperatures above about 1610°C. In the experiments cited,[143] the SiO generated by passage of CO through a coke bed at temperatures of 1600 to 1900°C, were found to be close to the equilibrium values for reaction 2.6.5. Volatile SiS is generated by reactions of the type with the coke ash:

$$CaS \text{ (in coke ash)} + SiO \rightarrow SiS + CaO \tag{2.6.6}$$

$$FeS \text{ (in coke ash)} + SiO + C \rightarrow SiS + CO + Fe \tag{2.6.7}$$

The reaction of these vapor species with metal and slag may be represented by the equations:

$$\text{Metal} \begin{cases} SiO + [C] = [Si] + CO \\ SiS = [Si] + [S] \end{cases} \tag{2.6.8}$$

$$\text{Slag} \begin{cases} SiO + \frac{1}{2}O^{2-} + \frac{1}{2}C = \left(-\overset{|}{\underset{|}{Si}} - O^- \right) + \frac{1}{2}CO \\ \\ SiS + \frac{3}{2}O^{2-} + \frac{1}{2}C = \left(-\overset{|}{\underset{|}{Si}} - O^- \right) + \left(S^{2-} \right) + \frac{1}{2}CO \end{cases} \tag{2.6.9}$$

Ozturk and Fruehan,[144] in carefully controlled experiments, demonstrated that the rate of the SiO reactions with metal and slag are controlled by gas phase mass transfer and are rapid.

Coke samples taken from the tuyere zone of the blast furnace usually contain 12 to 16% ash which has a basicity $(CaO + MgO)/SiO_2$ of about 0.6; for a typical blast furnace slag, the basicity is about 1.5. Therefore, the partial pressures of SiO and sulfur-bearing species in the gas near the coke surface are expected to differ from those interacting with the slag. For the purpose of comparison, calculations are made for assumed local equilibrium at 1500°C for the systems gas-slag and gas-coke ash; the results are given in Table 2.12. The amount of ash in the tuyere coke and its composition suggests that, although most of the silica and sulfur in the coke ash are removed from the furnace by the slag and liquid iron, there is significant recycle of silicon and sulfur in the bosh region by the vaporization and condensation of these species on the coke particles.

Table 2.12 Calculated Equilibrium Vapor Pressures in bar for the Systems Gas–Slag and Gas–Coke Ash at 1500°C and 1 bar Pressure of CO.

Vapor	B = 1.5, $a_{SiO_2} = 0.05$ 2%(S), $C_S = 3 \times 10^{-4}$, (wt%) *	B = 0.6, $a_{SiO_2} = 0.3$ 5%(S), $C_S = 10^{-5}$, (wt%)*
SiO	2.6×10^{-4}	1.5×10^{-3}
SiS	3.9×10^{-5}	1.7×10^{-2}
S_2	8.6×10^{-9}	4.9×10^{-5}
CS	5.5×10^{-5}	4.3×10^{-3}
COS	5.5×10^{-6}	1.2×10^{-4}

* C_S(wt%) is the sulfide capacity of the slag.

2.6.2.2 Alkali Recycle and Removal by Slag

The alkalies constitute another dominant vapor species in the bosh and stack regions of the blast furnace. Many studies have been made of the alkali recycle in the blast furnace via the process of vaporization and condensation; the subject is well covered in the references cited.[145–147] General consensus evolved from elementary thermodynamic calculations is that the alkali silicates in the ore

and coke ash decompose at elevated temperatures in the lower part of the bosh and the combustion zone. In part the alkali vapors carried away with the ascending gas react with the slag and can therefore be removed from the furnace; part are converted to alkali cyanides and carbonates and deposited on the burden and the refractory lining of the furnace stack. Some new thoughts are presented in the following discussion on the sequence of reactions and vapor species that may govern the alkali recycle in the blast furnace.

As an example, let us calculate the equilibrium vapor pressure of potassium for the reduction reaction:

$$(K_2O) + C = 2K(g) + CO(g) \tag{2.6.10}$$

The computed equilibrium values in Table 2.13 are for a blast furnace slag containing 0.5% K_2O and having a basicity of B = 1.5: K is the equilibrium constant for reaction 2.6.10 from the thermochemical data and a_{K_2O} is the activity of K_2O in the slag, relative to the hypothetical solid K_2O, from the experimental data of Steiler.[148]

If the potassium input with the blast furnace burden is 4 kg K/t–HM and 80% of it is removed by the slag, about 0.8 kg K/t–HM will be in the vapor phase carried away by the furnace gas. For a typical total gas volume of 2300 nm^3/t–HM, the partial pressure of the total potassium vapor species would be 7.2 x 10^{-4} bar (for a total gas pressure of 3.6 bar in the bosh region). Comparison of this total potassium pressure in the gas with those in Table 2.13 for the gas-slag equilibrium indicates that the slag particles will pick up potassium from the gas only at temperatures below 1200°C. The ash in the coke samples taken from the tuyere zone contains 2 to 4% $(Na_2O + K_2O)$ which is several fold of that in the original coke ash. Because of the low basicity of coke ash, the amount of alkali therein is expected to be 5 to 10 times greater than that found in the slag. In the upper part of the bosh, the slag and coke will pick up alkalies from the gas. As the temperature of the slag and coke increases during descent in the bosh, they will emit alkali vapors to the gas phase. However, the partial pressure of potassium vapor in the gas would probably be below that given in Table 2.13 for the gas-slag equilibrium. Nevertheless, the numerical examples cited suggest that much of the alkalies accumulated in the bosh and hearth zone of the blast furnace, via recycling, are in the gas phase.

Table 2.13   Equilibrium Vapor Pressure of Potassium for Reaction 2.6.10 with Slag having 0.5% K_2O and B = 1.5.

Temperature (°C)	K, bar	a_{K_2O}	p_K, bar
1200	3.10×10^5	2.1×10^{-12}	7.1×10^{-4}
1300	2.69×10^6	5.5×10^{-12}	3.4×10^{-3}
1400	1.81×10^7	1.4×10^{-11}	1.4×10^{-2}
1500	9.78×10^7	3.5×10^{-11}	2.6×10^{-1}

According to a mass spectrometric study of vaporization of potassium cyanide by Simmons et. al,[149] the equilibrium pressures of vapor species are in the order $p_{(KCN)_2} > p_{(KCN)} > p_{(KCN)_3}$. For atmospheric pressure of nitrogen and at graphite saturation, the following are the equilibrium ratios of the vapor species: at the melting point of KCN (635°C), $(KCN)_2$: KCN : K = 2 : 1 : 0.76 and at the boiling point (1132°C), $(KCN)_2$: KCN : K = 4.6: 1 : 0.19. It is all too clear that $(KCN)_2$ is the dominant alkali-bearing species in the blast furnace. The sodium in the burden undergoes cyclic reactions similarly to potassium; however, the concentration of sodium-bearing species are about one-tenth of the potassium-bearing species.

One method of minimizing the ascent of alkali vapors to the stack, hence reducing the alkali recycle, is by operating the furnace with a slag of low basicity, particularly when the alkali input is high. The slag of low basicity, however, will have an adverse effect on the composition of the hot metal produced; it will result in low manganese, high silicon and high sulfur in the metal. For a given preferred basicity, the slag mass per ton of hot metal may have to be increased when there is an increase in the alkali input to the furnace. An increase in amount of slag will increase the coke rate,

hence will increase the alkali input. Obviously, with a burden of high alkali input, a compromise has to be made in adjusting slag basicity and slag mass so that the alkali recycle would be low.

Even with a low alkali input some alkali buildup will occur. To prevent excessive accumulation of alkalies, which lead to scaffolding, gas channeling, furnace upsets and so on, periodic additions of gravel (silica) or olivine (magnesium silicate) are made to the blast furnace charge. The silica reacts with alkali carbonates and cyanides, thus facilitates the discharge of the accumulated alkalies from the furnace by the slag. Practical experience also shows that periodic addition of calcium chloride to the burden also facilitates the removal of alkalies by the slag.

2.6.2.3 Ammonia and Hydrogen Cyanide in Blast Furnace Stack

The contaminants in the wash water for the iron blast-furnace off-gas are in the ranges 10–300 mg NH_3/l, 1–30 mg CN_t (total)/l, and 0.3–15 mg phenols/l. In terms of ppm by volume in the stack gas, the concentrations are usually in the ranges 3000–4000 ppm NH_3 and 150–250 ppm CN_t. As observed by Pociecha and Biczysko,[150] for example, most of the cyanide in the de-dusted furnace off gas is in the form of hydrogen cyanide. They also found that the blast furnace dust contains only a small amount of solid cyanides (presumably alkali cyanides) in comparison with the amount of hydrogen cyanide present in the de-dusted top gas. The same contaminants in the ferromanganese blast furnace off gas are about an order of magnitude greater than those in the iron blast furnace.

The experimental work of Turkdogan and Josephic,[151] under conditions partly simulating the blast furnace stack, substantiated the validity of this mechanism of generation of ammonia and hydrogen cyanide in the stack, by the following reactions.

$$2K(Na)CN + 3H_2O = (K, Na)_2CO_3 + 2NH_3 + C \tag{2.6.11}$$

$$NH_3 + CO = HCN + H_2O \tag{2.6.12}$$
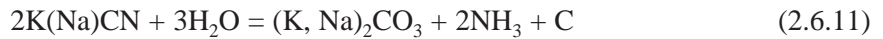
The amounts of ammonia and hydrogen cyanide generated will increase with an increase in the concentration of water vapor in the stack gas. Other reactions will occur with these volatile species generating some amino-nitro phenols, e.g. $NH_2(NO_2)C_6H_3OH$. The equilibrium concentrations of these volatile organic species become greater at lower temperatures.

2.6.3 Slag-Metal Reactions in the Blast Furnace

Slag-metal reactions in the hearth of the blast furnace control the chemistry of the hot metal. In particular, the silicon, sulfur and manganese contents depend upon these reactions. In this section the equilibrium and reaction mechanisms are presented.

2.6.3.1 Slag-Metal Equilibrium for Blast Furnace Reactions

From the thermodynamics of the slag systems and of the various solutes in iron such as sulfur, silicon and manganese, it is possible to predict the equilibrium relationship for blast furnace reactions.

The three-phase reactions to be considered are for graphite-saturated melts at 1 atm pressure of carbon monoxide, which is close to the partial pressure of CO in the blast furnace bosh and hearth zones.

2.6.3.1.1 Silicon Reaction The reaction equilibrium to be considered is

$$(SiO_2) + 2[C] = [Si] + 2CO(g) \tag{2.6.13}$$

$$K_{Si} = \frac{[\%Si]f_{Si}}{(a_{SiO_2})}\left(\frac{p_{CO}}{a_C}\right)^2 \tag{2.6.14}$$

where the SiO_2 and C activities are with respect to pure solid silica and graphite, respectively.

The temperature dependence of the equilibrium constant is from the free energy data

$$\log K_{Si} = -\frac{30,935}{T} + 20.455 \tag{2.6.15}$$

Substituting $a_{SiO_2} = (\%SiO_2)\gamma_{SiO_2}/60 \times 1.65$ and for the activity coefficient $f_{Si} = 15$ in graphite-saturated iron containing $Si < 2\%$, the equilibrium metal/slag silicon distribution ratio is represented by

$$\frac{[\%Si]}{(\%SiO_2)} p_{CO}^2 = 6.73 \times 10^{-4} \, \gamma_{SiO_2} \, K_{Si} \quad (2.6.16)$$

The equilibrium silicon distribution ratios computed previously, using the γ_{SiO_2} values for the blast furnace type slags (CaO, 10% MgO, 10% Al_2O_3, SiO_2), are given in Fig. 2.88. The dotted curves are derived from other data discussed later. For the blast furnace type slags, the basicity is usually defined by the mass ratio $(\%CaO + \%Mg)/\%SiO_2$.

2.6.3.1.2 Manganese Reaction   For the reaction

$$(MnO) + [C] = [Mn] + CO(g) \quad (2.6.17)$$
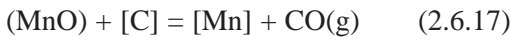
$$K_{Mn} = \frac{[\%Mn] f_{Mn}}{(a_{MnO})} \frac{p_{CO}}{a_C} \quad (2.6.18)$$

$$\log K_{Mn} = -\frac{15,090}{T} + 10.970 \quad (2.6.19)$$

For the graphite-saturated iron, the activity coefficient $f_{Mn} = 0.8$, and inserting $a_{MnO} = (\%MnO) \, \gamma_{MnO}/71 \times 1.65$, the equilibrium manganese distribution ratio is represented by

Fig. 2.88   Silicon distribution ratio for graphite–saturated melts for blast furnace type slags containing about 10% MgO and 10% Al_2O_3. Lines – – – are derived from the data in Fig. 2.90 and equation (2.6.23).

$$\frac{[\%Mn]}{(\%MnO)} p_{CO} = 1.07 \times 10^{-2} \, \gamma_{MnO} \, K_{Mn} \quad (2.6.20)$$

Abraham *et al.*[152] measured the MnO activity in CaO–Al_2O_3–SiO_2– MnO melts containing $Al_2O_3 < 20\%$ and $MnO < 8\%$. The values of γ_{MnO} derived from their data are seen in Fig. 2.89 to increase with an increasing slag basicity. The equilibrium manganese distribution ratio for graphite saturated melts thus evaluated are given in Fig. 2.90.

Fig. 2.89   Activity coefficient of MnO, relative to pure solid oxide, in CaO–Al_2O_3–SiO_2–MnO slags, with $MnO < 8\%$, at 1500 to 1650°C, derived from the data of Abraham, Davies and Richardson[152].
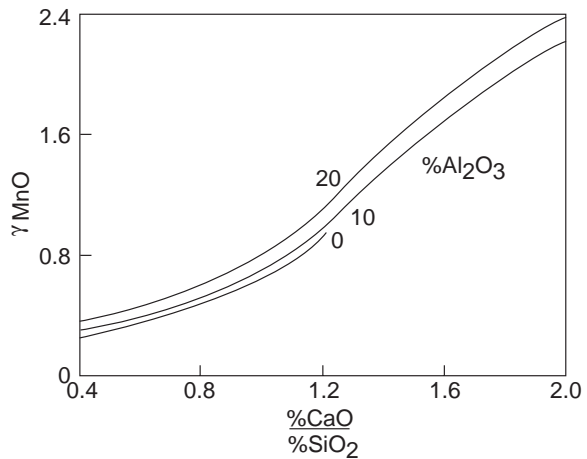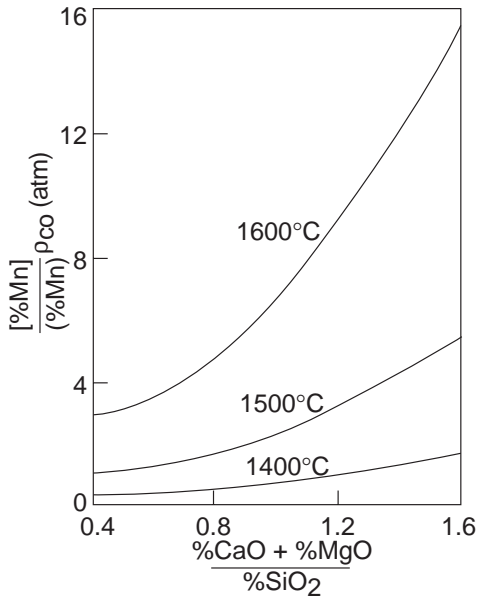
Fig. 2.90 Manganese distribution ratio for graphite-saturated melts derived for blast furnace type slags containing about 10% MgO and 10% Al_2O_3.

2.6.3.1.3 Si–Mn Coupled Reaction

The silicon-manganese coupled reaction

$$2(MnO) + [Si] = (SiO_2) + 2[Mn] \tag{2.6.21}$$

between graphite-saturated iron and blast furnace type slags has been investigated by several experimental studies.[143,153,154]

$$K = \left(\frac{[\%Mn]}{(\%MnO)}\right)^2 \frac{(\%SiO_2)}{[\%Si]} = 0.17 \frac{K_{Mn}^2}{K_{Si}} \frac{\gamma_{MnO}^2}{\gamma_{SiO_2}} \tag{2.6.22}$$

The combination of equations 2.6.16 and 2.6.20 gives the following equilibrium constant for reaction (2.6.21)

The variation of the equilibrium relation K_{MnSi} with slag basicity is shown in Fig. 2.91. The dotted line for 1400 to 1600°C is calculated from the thermochemical data, i.e. from the computed equilibrium data in Figs. 2.88 and 2.90. The difference of the calculated equilibrium dotted line from the average experimental values by a factor of 2.7 ($\equiv$ ~15 kJ) is due to the accumulated uncertainties in the free energy data on MnO and SiO_2 as well as ΔG_s for solutions of Mn and Si in graphite-saturated iron.

The experimental data in Fig. 2.91 for graphite saturated melts at 1400 – 1600°C may be represented by the following equation.

$$\log K_{MnSi} = 2.8\left(\frac{\%CaO + \%MgO}{\%SiO_2}\right) - 1.16 \tag{2.6.23}$$

To be consistent with the experimental data in Fig. 2.91, the dotted curves are derived from the reliable equilibrium data in Fig. 2.90 and the experimental data represented by equation (2.6.23) for the Si–Mn coupled reaction in graphite saturated melts.

In a study of slag-metal equilibria between CaO–MnO–SiO_2 slags and graphite-saturated manganese-base alloys, Turkdogan and Hancock[155] found that the ratios Si/SiO_2 and Mn/MnO varied with slag basicity in a manner similar to that for iron base alloys. Their results for 1400°C are shown in Fig. 2.92; the dot-dash line is for the iron-base alloys, reproduced from Fig. 2.91.
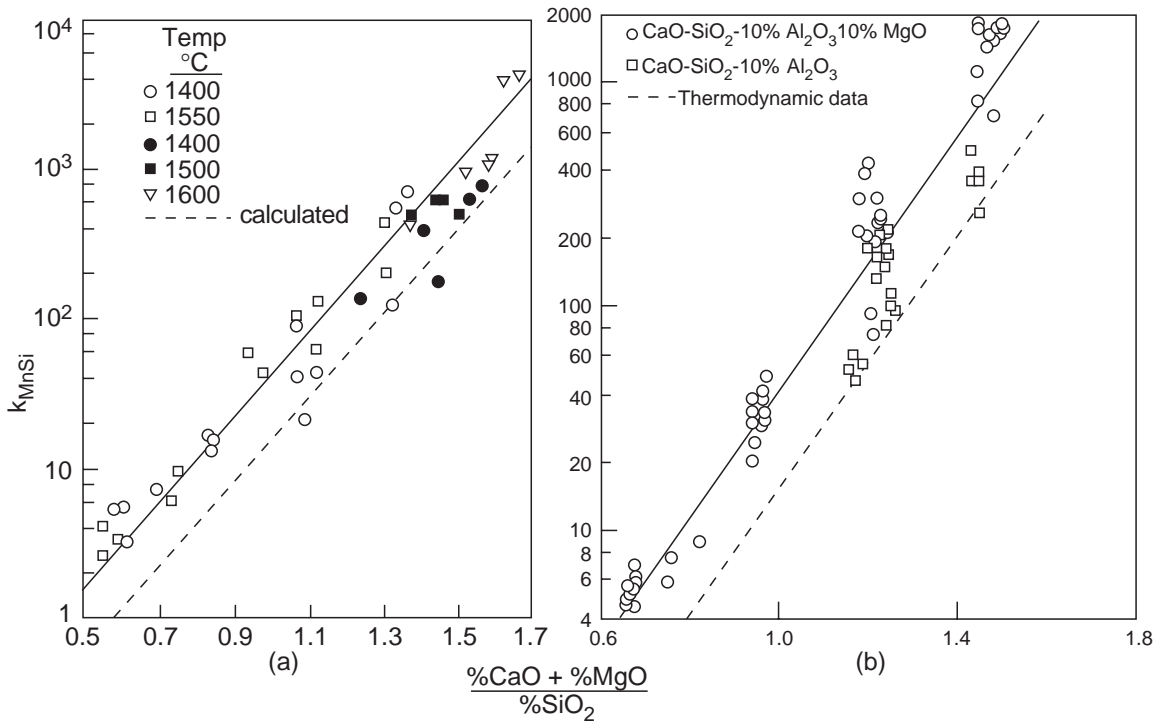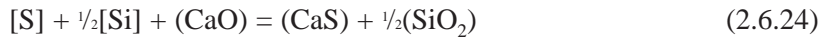
Fig. 2.91 Experimental data showing the equilibrium relation K_{MnSi} with basicity of the blast furnace type slags at graphite saturation: (a) reproduced from Ref. 143 and (b) from Ref. 154; lines---derived from equation 2.6.23 and Fig. 2.90.

2.6.3.1.4 Si–S and Mn–S Coupled Reactions The silicon-sulfur coupled reaction is represented by

$$[S] + \tfrac{1}{2}[Si] + (CaO) = (CaS) + \tfrac{1}{2}(SiO_2) \tag{2.6.24}$$

for which the isothermal equilibrium constant is

$$K_{SiS} = \frac{(\%S)}{[\%S]} \left\{ \frac{(\%SiO_2)}{[\%Si]} \right\}^{\tfrac{1}{2}} \frac{1}{(\%CaO)} \tag{2.6.25}$$

From an analysis of the most available experimental data, Turkdogan *et al.*[143] developed a relation for K_{SiS} shown in Fig. 2.93. For the range 1400 to 1600°C, the temperature dependence of K_{SiS} is represented by the equation

$$\log K_{SiS} = \frac{6327}{T} - 4.43 + 1.4 \left(\frac{\%CaO + \%MgO}{\%SiO_2} \right) \tag{2.6.26}$$

From the experimental data represented by equations 2.6.23 and 2.6.26, the following equation is obtained for the temperature dependence of the equilibrium relation for the manganese-sulfur coupled reaction in graphite-saturated melts.

$$\log K_{MnS} = \log \frac{(\%S)}{[\%S]} \frac{(\%MnO)}{[\%Mn]} \frac{1}{(\%CaO)} = \frac{6327}{T} - 3.85 \tag{2.6.27}$$

The equilibrium sulfur distribution ratio as a function of slag basicity in graphite-saturated melts shown in Fig. 2.94.
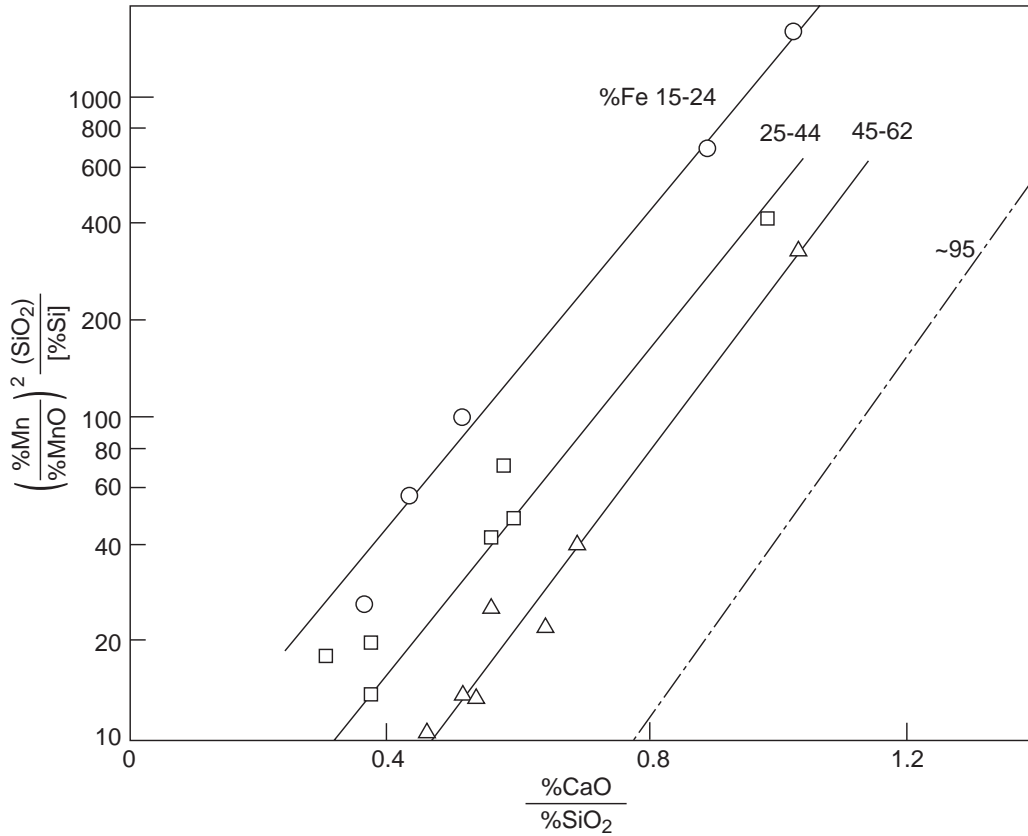
Fig. 2.92 Product of manganese and silicon ratios for graphite–saturated ferromanganese melts, of indicated iron contents, equilibrated with CaO–MnO–SiO$_2$ slags at 1400°C and 1 atm CO, derived from the data of Turk-dogan and Hancock.[155]
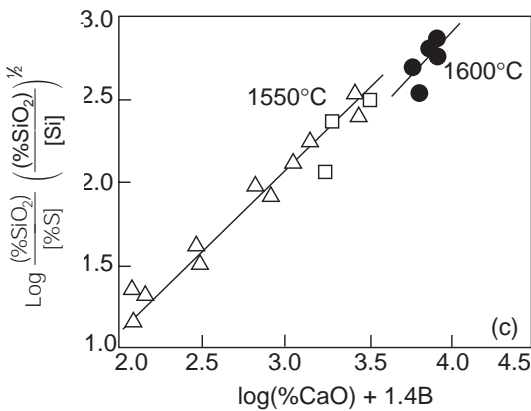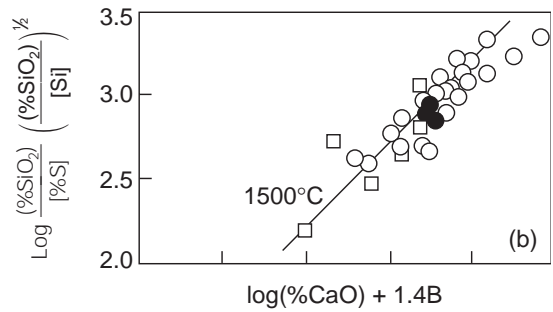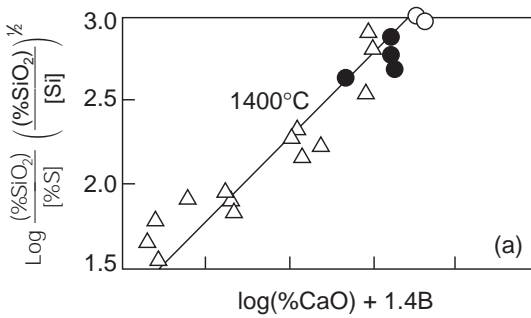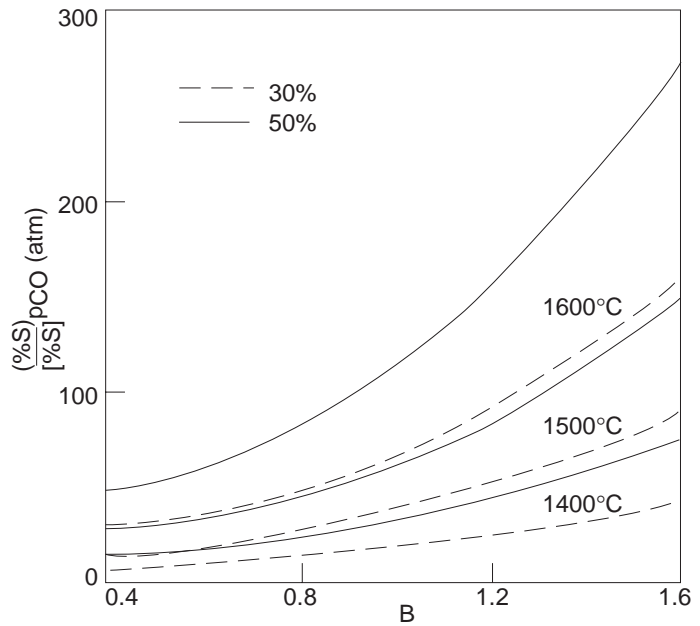

Fig. 2.93 (a) 1400°C; (b) 1500°C; (c) 1550°C and 1600°C. Variation of equilibrium relation for the silicon-sulfur coupled reaction with slag basicity B for unit activity of carbon. Reference cited in Ref. 143.

Fig. 2.94 Sulfur distribution ratio for graphite-saturated melts as a function of slag basicity. *From Ref. 143.*

2.6.3.1.5 Si–Ti Coupled Reaction Delve *et al.*[156] have studied the silicon-titanium coupled reaction in graphite-saturated melts using blast furnace type slags:

$$(TiO_2) + [Si] = (SiO_2) + [Ti] \qquad (2.6.28)$$

Their experimental results, for temperatures of 1500 and 1600°C and basicities of 1 to 2, may be summarized by the following equation.

$$K_{SiTi} = \frac{[\%Ti]}{(\%TiO_2)} \frac{(\%SiO_2)}{[\%Si]} \qquad (2.6.29)$$

$$\log K_{SiTi} = 0.46 \frac{\%CaO}{\%SiO_2} + 0.39 \qquad (2.6.30)$$

2.6.3.2 Mechanisms of Slag-Metal Reactions

2.6.3.2.1 Experimental Work Experiments were made by the authors[143] to simulate the events in the upper part of the blast furnace hearth where metal droplets pass through the slag layer. Solid pieces (4 to 5 mm dia.) of graphite-saturated iron containing Si and S were dropped on the surface of a pool of remelted blast furnace slag (65 g) contained in a graphite tube (20 mm dia.) at 1480°C; an argon atmosphere was maintained over the melt. Twenty pieces of metal (7 g total) were dropped one at a time at 10–20 s intervals, within 7–10 min total time of the experiment. The metal pieces melted rapidly and descended a 10 cm deep column of molten slag as individual metal droplets. After the last piece was dropped the melt was rapidly cooled. The residence time of the droplets in the slag column is estimated to be about 1–2 s, if there is no appreciable buoyancy effect due to gas evolution. The metal droplets collected in a well at the bottom of the slag column; metal and slag were subsequently analyzed for manganese, silicon and sulfur.

With the addition of MnO to the slag, there is silicon transfer from metal to slag. As is seen from the experimental results in Fig. 2.95, the extent of silicon oxidation increases with increasing %MnO in the slag via the Si–Mn coupled reaction
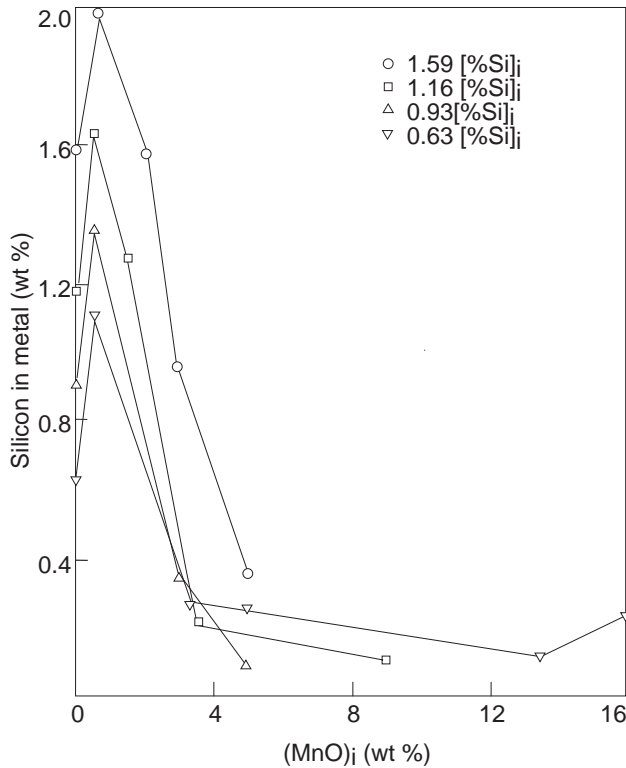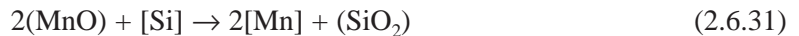
Fig. 2.95 Change in silicon content of metal droplets passing through a 10 cm deep slag column. *From Ref. 143.*

$$2(MnO) + [Si] \rightarrow 2[Mn] + (SiO_2) \qquad (2.6.31)$$

In addition, there is also MnO reduction by carbon in the metal droplets.

$$(MnO) + [C] \rightarrow [Mn] + CO \qquad (2.6.32)$$

With the slags containing MnO > 3%, the metal droplets desiliconized down to 0.1 – 0.3% Si. Within this region, the silicon and manganese distribution ratios are within the ranges $(\%SiO_2)/[\%Si] = 120$ to 350 and $[\%Mn]/(\%MnO) = 0.7$ to 1.8. These ratios give K_{MnSi} values below the equilibrium value of 1096 derived from equation 2.6.23 for the slag basicity of 1.5.

The effect of MnO content of the slag on the extent of desulfurization of metal droplets during descent in the slag column is shown in Fig. 2.96. The shaded area within the range 0.010 to 0.035% S corresponds to the state of slag-metal equilibrium represented by equation 2.6.26, for metal droplets containing 0.1 to 0.3% Si and the slag of basicity 1.5 containing 41% CaO, 35% SiO_2 and 1.5% S.

The extremely fast rates of reactions observed in the foregoing experiments may be attributed to the presence of a thin gas film (consisting of the vapor species CO, SiO, SiS and Mn) around the metal droplets, which provides the reaction path for the transfer of reactants to and from slag and metal via the gas phase.

2.6.3.3 Blast Furnace Tap Chemistry Data

In a previous study[157] an assessment was made of the state of slag-metal reactions in the blast furnace hearth from an analysis of the daily average compositions of metal and slag samples as normally recorded in the plants. The plant data used were those reported by Okabe *et al.*[158] from Chiba Works of Kawasaki Steel and the daily average data for a period of a month from U.S. Steel plants.

In the plant data used, the melt temperatures at tap are mostly in the range $1500 \pm 25°C$. The average slag compositions in mass percent are in the range 38–42% CaO, 8–10% MgO, 34–38% SiO_2, 10–12% Al_2O_3, 0.5–1.0% MnO, 2% S and minor amounts of other oxides. The slag basicity is about
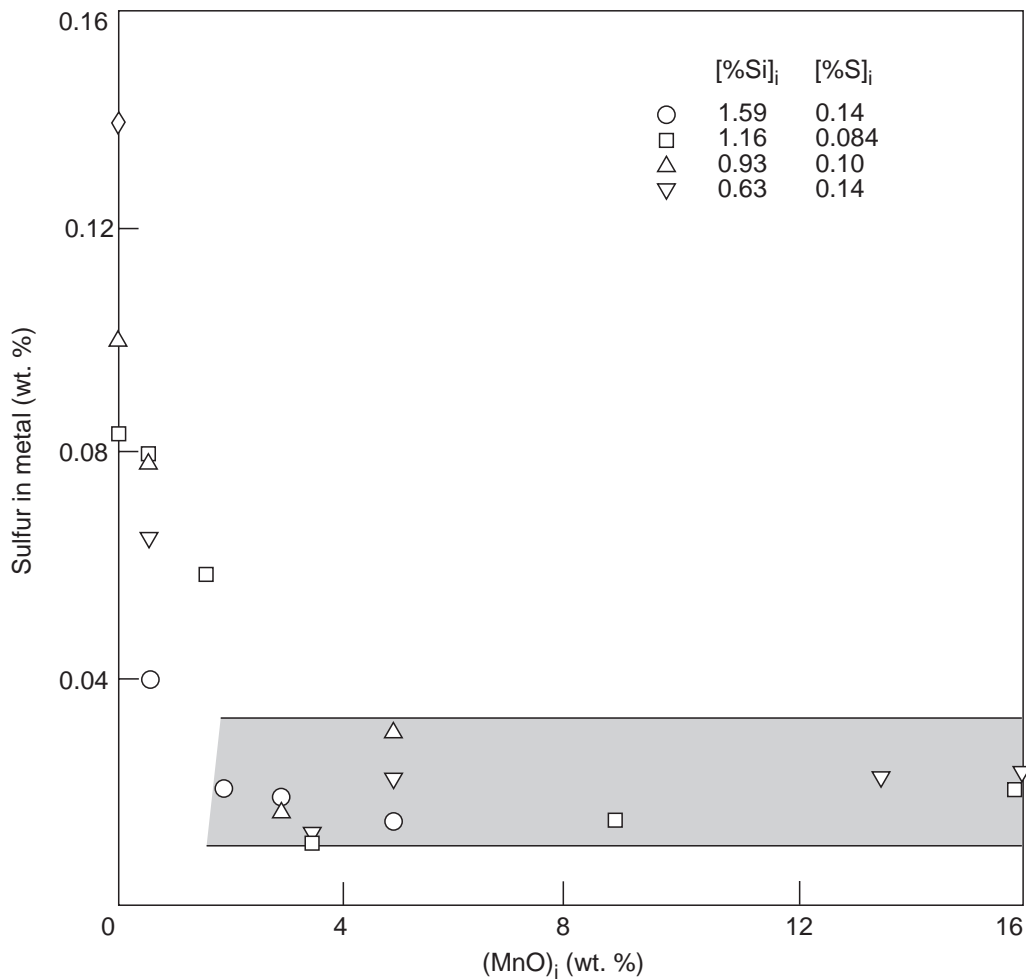
Fig. 2.96 Change in sulfur content of metal droplets passing through a 10 cm deep slag column; shaded region is for slag-metal equilibrium at 1480°C. *From Ref. 143.*

1.4 ± 0.15. The hot metal compositions in the tap stream are in the range: 0.4–0.8% Mn, 0.5–1.5% Si, 0.02–0.05% S, 5% C and other usual impurities.

The silicon, manganese and sulfur distribution ratios from plant data are scattered within the shaded areas in Fig. 2.97. The dotted lines are for the slag-metal equilibria at 1 atm pressure of CO, which is close to the CO partial pressure in the hearth zone of the blast furnace. It should be noted that the equilibrium line for the Si/SiO_2 ratio is based on equation 2.6.16 representing the experimental data and the equilibrium relation in Fig. 2.88, i.e. dotted curves. It is only the silicon distribution ratio that is scattered about the gas-slag-metal equilibrium line for the three-phase reaction

$$(SiO_2) + 2[C] = [Si] + 2CO(g) \qquad (2.6.33)$$

Values of K_{MnSi} scattered within the shaded area in Fig. 2.98 are below the equilibrium line (dotted). It should be pointed out that in the upper part of the slag layer, the iron oxide content will be higher than manganese oxide. Therefore, the silicon in metal droplets will be oxidized more readily by iron oxide in the upper part of the slag layer, resulting in the observed non-equilibrium state for the Si–Mn coupled reaction in equation 2.6.31.

With iron ore of low basicity in the blast furnace burden, the slag basicity will be low and furthermore, the iron oxide content in the upper part of the slag layer is expected to be higher. It is
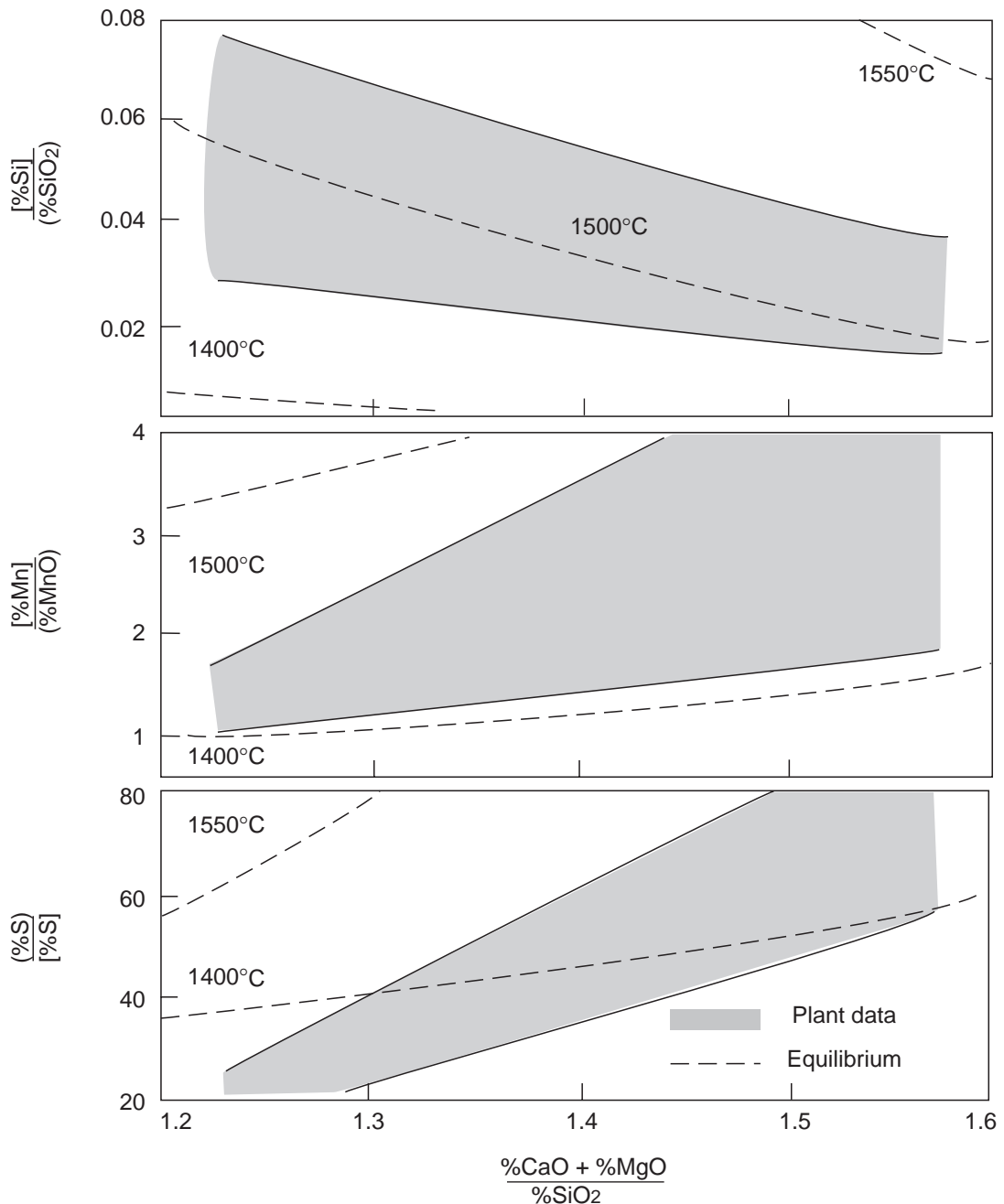
Fig. 2.97 Si, Mn and S distribution ratios are compared with the equilibrium data for graphite-saturated melts at 1 atm CO. *From Ref. 159.*

presumably for this reason that a low slag basicity, the K_{MnSi} values are much lower than the equilibrium values for the Si–Mn couple reaction.

In an earlier study of plant data from a ferromanganese blast furnace in the UK,[160] it was found that there were departures from equilibrium for the Si oxidation by MnO in the slag in a manner similar to that observed for the iron blast furnace.

The plant data in Fig. 2.99 for the sulfur distribution ratio are scattered about the equilibrium line for the Mn–S coupled reaction at 1500°C, represented by equation 2.6.27. However, the ratios

Fig. 2.98 K_{MnSi} values for plant data are compared with the equilibrium values (dotted line). *From Ref. 159.*
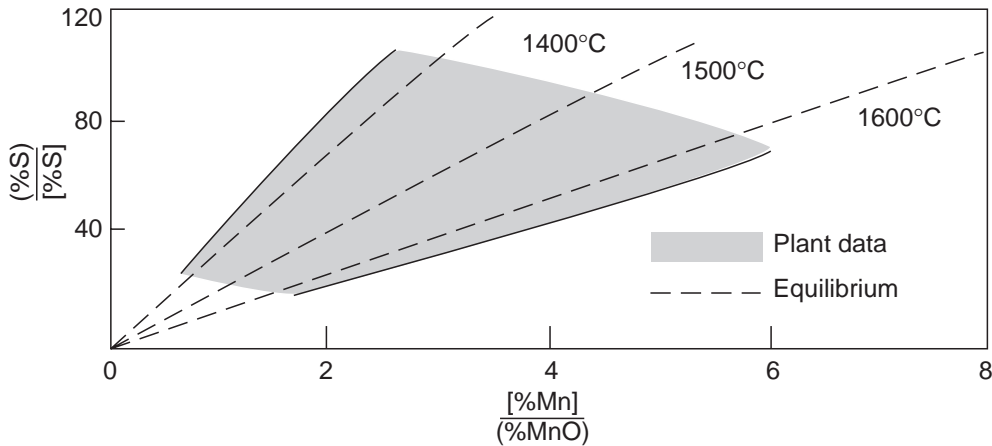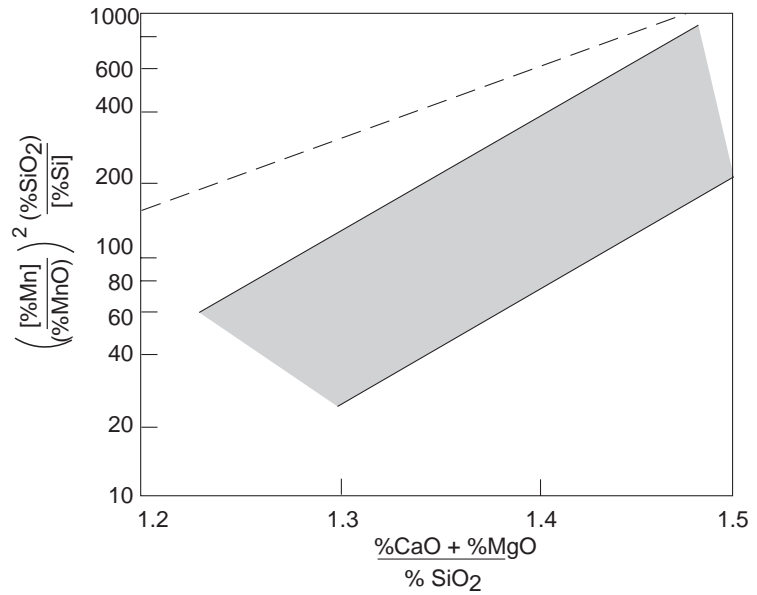

Fig. 2.99 The blast furnace data are compared with the slag–metal equilibrium values for the Mn–S coupled reaction. *From Ref. 159.*

(%S)/[%S] in the plant data are lower than the equilibrium values for the Si–S coupled reaction represented by equation 2.6.26. Nevertheless, despite departures from equilibrium, the silicon and sulfur contents of the blast furnace iron change in a systematic manner, i.e. high silicon/low sulfur and low silicon/high sulfur.

It should be borne in mind that because of fluctuations in the operating conditions in the blast furnace, there will be variations in temperature and the extent of reaction of metal droplets during descent through the slag layer. Consequently, the metal droplets of varying composition collecting in the stagnant hearth will bring about the composition and temperature stratification that is common to all blast furnaces.

2.7 Fundamentals of Steelmaking Reactions

In this section of Chapter 2, the discussion of steelmaking reactions will be confined to an assessment of the reaction mechanisms and the state of slag-metal reactions at the time of furnace tapping.

2.7.1 Slag-Metal Equilibrium in Steelmaking

The reaction equilibria in the liquid steel-slag systems have been extensively studied, both experimentally and theoretically by applying the principles of thermodynamics and physical chemistry. In a recent reassessment of the available experimental data on steel-slag reactions[103], it became evident that the equilibrium constants of slag-metal reactions vary with the slag composition in different ways, depending on the type of reaction. For some reactions the slag basicity is the key parameter to be considered; for another reaction the key parameter could be the mass concentration of either the acidic or basic oxide components of the slag.

2.7.1.1 Oxidation of Iron

In steelmaking slags, the total number of g-mols of oxides per 100 g of slag is within the range 1.65 ± 0.05. Therefore, the analysis of the slag-metal equilibrium data, in terms of the activity and mol fraction of iron oxide, can be transposed to a simple relation between the mass ratio [ppm O]/(%FeO) and the sum of the acidic oxides $\%SiO_2 + 0.84 \times \%P_2O_5$ as depicted in Fig. 2.100(a). The experimental data used in the diagram are those cited in Ref. 103. There is of course a corollary relation between the ratio [ppm O]/(%FeO) and the slag basicity as shown in Fig. 2.100(b).

(a)

(b)

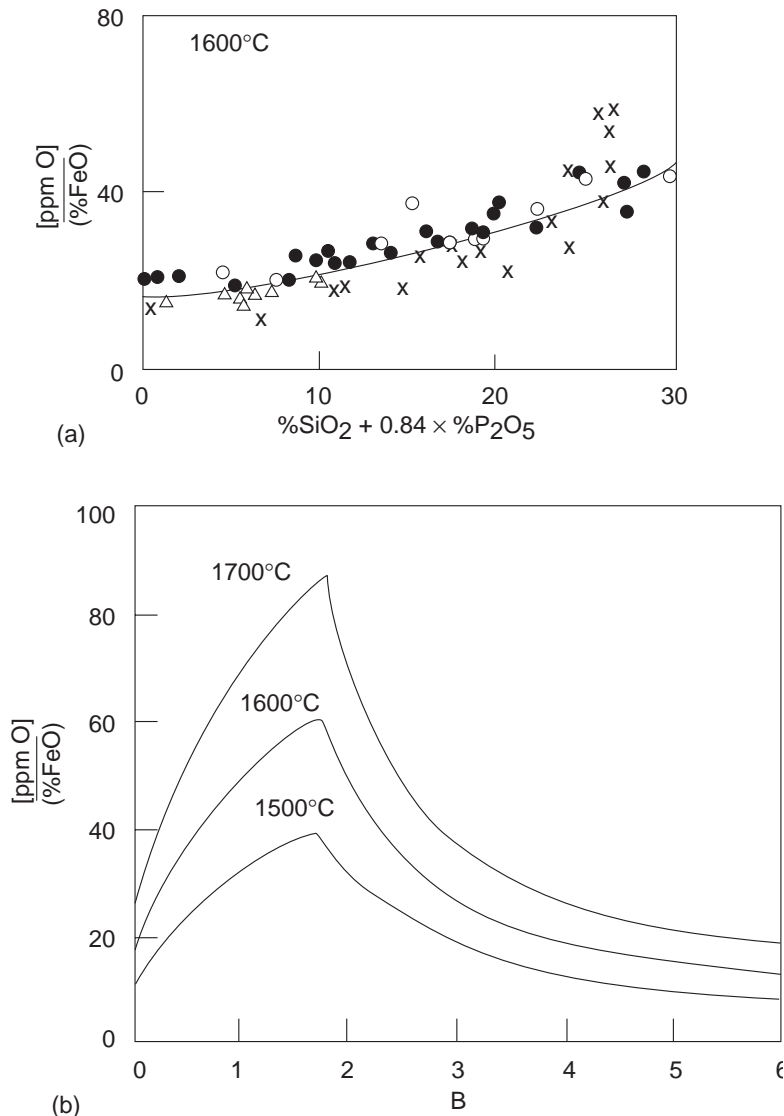**Fig. 2.100** Equilibrium ratio [ppm O]/(%FeO) related to (a) SiO_2 and P_2O_5 contents and (b) slag basicity; experimental data are those cited in Ref. 103.

2.7.1.2 Oxidation of Manganese

For the FeO and MnO exchange reaction involving the oxidation of manganese in steel, formulated below,

$$(FeO) + [Mn] = (MnO) + [Fe] \tag{2.7.1}$$

the equilibrium relation may be described in terms of the mass concentrations of oxides

$$K'_{FeMn} = \frac{(\%MnO)}{(\%FeO)[\%Mn]} \tag{2.7.2}$$

where the equilibrium relation K'_{FeMn} depends on temperature and slag composition.

The values of K'_{FeMn} derived from the equilibrium constant for reaction 2.7.1, given in Ref. 27 and the activity coefficient ratios $\gamma_{FeO}/\gamma_{MnO}$ in Fig. 2.67, are plotted in Fig. 2.101 against the slag basicity. In BOF, OBM(Q-BOP) and EAF steelmaking, the slag basicities are usually in the range 2.5 to 4.0 and the melt temperature in the vessel at the time of furnace tapping in most practices is between 1590 and 1630°C for which the equilibrium K'_{FeMn} is 1.9 ± 0.3. The plant analytical data for tap samples give K'_{FeMn} values that are scattered about the indicated slag-metal equilibrium values.

Morales and Fruehan[161] have recently determined experimentally the equilibrium constant K'_{FeMn} for reaction 2.7.1 using MgO-saturated calcium silicate melts. Their values of K'_{FeMn} are plotted in Fig. 2.102 together with some data from the studies of Chipman *et al.*[162] and Suito *et al.*[163]. The broken line curve is reproduced from Fig. 2.101. Resolution of observed differences in the values of K'_{FeMn} awaits future studies.
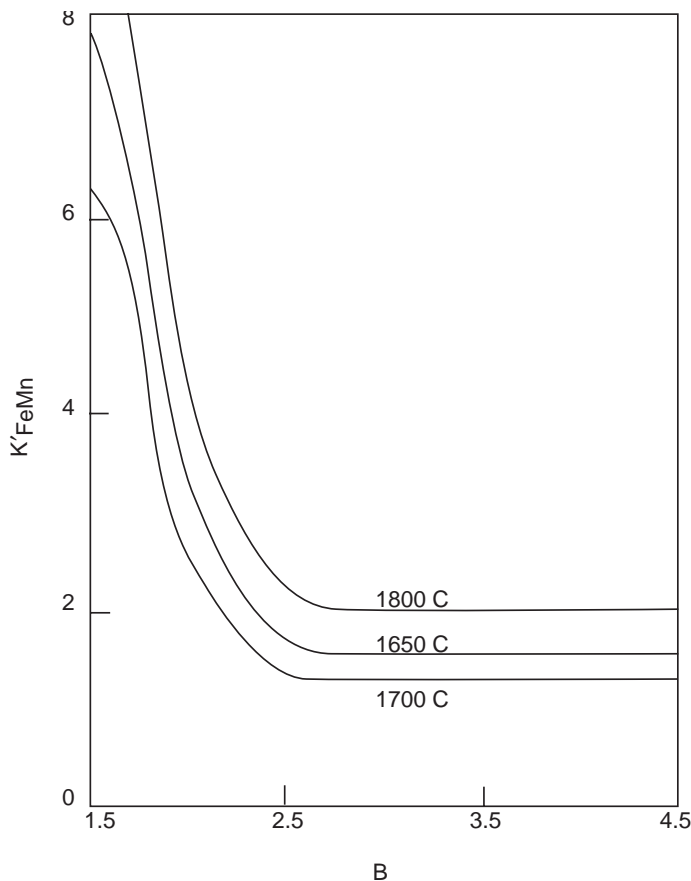

Fig. 2.101 Equilibrium relation in equation 2.7.2 related to slag basicity. *From Ref. 103.*

2.7.1.3 Oxidation of Carbon

With respect to the slag-metal reaction, the equilibrium relation for carbon oxidation would be

$$(FeO) + [C] = CO + [Fe] \tag{2.7.3}$$

$$K_{FC} = \frac{p_{CO}\,(atm)}{[\%C]\,a_{FeO}} \tag{2.7.4}$$
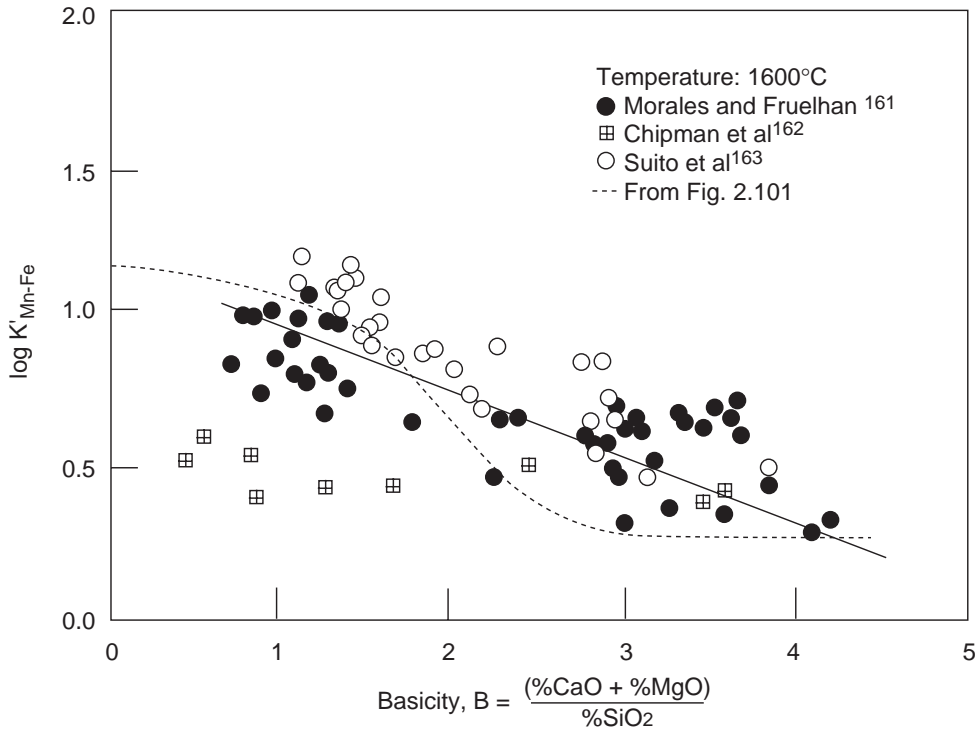
$$\log K_{FC} = -\frac{5730}{T} + 5.096 \tag{2.7.5}$$

Fig. 2.102 Experimental values of K'_{FeMn} measured recently by Morales and Fruehan[161].

For 1600°C, γ_{FeO} = 1.3 at slag basicity of B = 3.2 and p_{CO} = 1.5 atm (average CO pressure in the vessel), we obtain the following equilibrium relation between the carbon content of steel and the iron oxide content of slag.

$$K_{FC} = 108.8$$

$$a_{FeO} = 1.3\,N_{FeO} \approx \frac{1.3}{72 \times 1.65}(\%FeO) = 0.011 \times (\%FeO) \tag{2.7.6}$$

2.7.1.4 Oxidation of Chromium

There are two valencies of chromium (Cr^{2+} and Cr^{3+}) dissolved in the slag. The ratio Cr^{2+}/Cr^{3+} increases with an increasing temperature, decreasing oxygen potential and decreasing slag basicity. Under steelmaking conditions, i.e. in the basic slags and at high oxygen potentials, the trivalent chromium predominates in the slag. The equilibrium distribution of chromium between slag and metal for basic steelmaking slags, determined by various investigators, is shown in Fig. 2.103; slope of the line represents an average of these data.

$$\frac{(\%Cr)}{[\%Cr]} = (0.3 \pm 0.1) \times (\%FeO) \tag{2.7.7}$$

2.7.1.5 Oxidation of Phosphorus

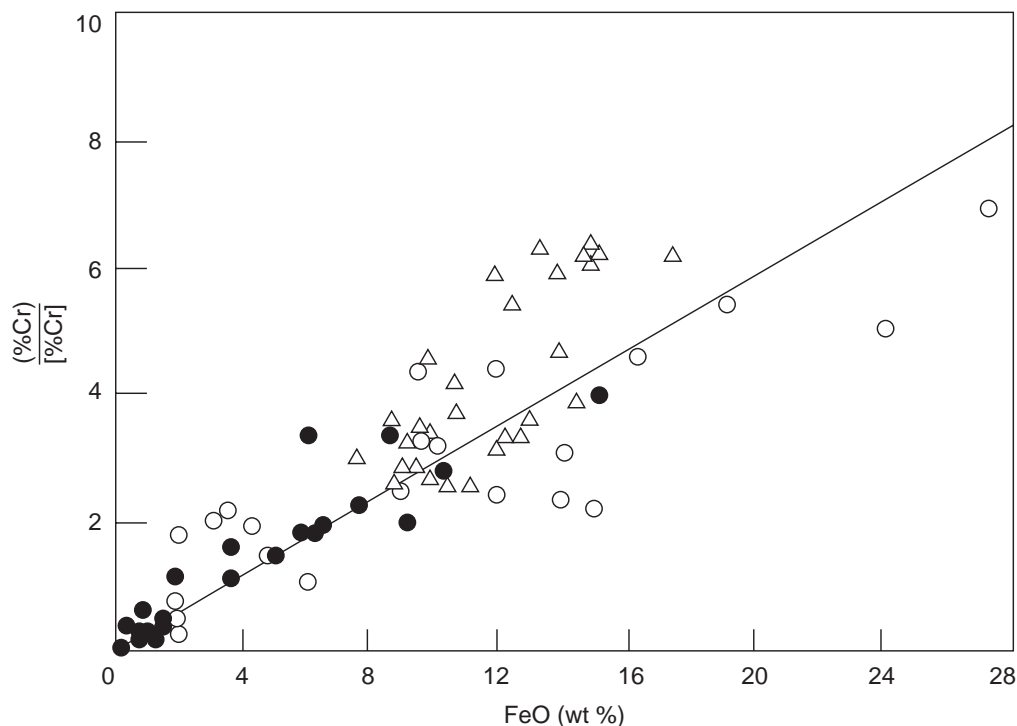It was in the late 1960s that the correct formulation of the phosphorus reaction was at last realized, thus

$$[P] + \tfrac{5}{2}[O] + \tfrac{3}{2}(O^{2-}) = (PO_4^{3-}) \tag{2.7.8}$$

Fig. 2.103 Variation of chromium distribution ratio with the iron oxide content of slag, in the ($\triangle$) open hearth[164] and (o) electric arc furnace[165] at tap is compared with the results of laboratory experiments[166]($\bullet$).

At low concentrations of [P] and [O], as in most of the experimental melts, their activity coefficients are close to unity, therefore mass concentrations can be used in formulating the equilibrium relation K_{PO} for the above reaction.

$$K_{PO} = \frac{(\%P)}{[\%P]} [\%O]^{-5/2} \tag{2.7.9}$$

The equilibrium relation K_{PO}, known as the phosphate capacity of the slag, depends on temperature and slag composition.

From a reassessment of all the available experimental data, discussed in detail in Ref. 103, it was concluded that CaO and MgO components of the slag, had the strongest effect on the phosphate capacity of the slag. Over a wide range of slag composition and for temperatures of 1550 to 1700°C, the steel-slag equilibrium with respect to the phosphorus reaction may be represented by the equation

$$\log K_{PO} = \frac{21,740}{T} - 9.87 + 0.071 \times BO \tag{2.7.10}$$

where $BO = \%CaO + 0.3 \, (\%MgO)$.

2.7.1.6 Reduction of Sulfur

The sulfur transfer from metal to slag is a reduction process as represented by this equation

$$[S] + (O^{2-}) = (S^{2-}) + [O] \tag{2.7.11}$$

for which the state of slag-metal equilibrium is represented by

$$K_{SO} = \frac{(\%S)}{[\%S]} [\%O] \tag{2.7.12}$$

As is seen from the plots in Fig. 2.104, the sulfide capacities of slags, K_{SO}, measured in three independent studies are in general accord. The effect of temperature on K_{SO} is masked by the scatter in the data. The concentration of acidic oxides, e.g. $\%SiO_2 + 0.84 \times \%P_2O_5$, rather than the slag basicity seems to be better representation of the dependence of K_{SO} on the slag composition.

2.7.2 State of Reactions in Steelmaking

There are numerous versions of oxygen steelmaking such as top blowing (BOF, BOP, LD, etc.), bottom blowing (OBM, Q-BOP, etc.) and combined blowing (K-OBM, LBE, etc.). The state of the refining reactions depend to some degree on the process. Bottom blowing in general provides better slag-metal mixing and reactions are closer to equilibrium. In the following section the state of reactions for top blowing (BOF) and bottom blowing (OBM) is given. The state of reactions for combined or mixed blowing processes would be between these two limiting cases. The analytical plant data used in this study were on samples taken from the vessel at first turndown from the BOP and Q-BOP shops of U.S. Steel. These plant data were acquired through the kind collaboration of the USS research personnel at the Technical Center.

2.7.2.1 Decarburization and FeO Formation

The most important reaction in steelmaking is decarburization. It not only determines the process time but also the FeO content of the slag, affecting yield and refining. When oxygen is injected into an oxygen steelmaking furnace a tremendous quantity of gas is evolved, forming a gas-metal-slag emulsion which is three to four times greater in volume than the non-emulsified slag and metal. The chemical reactions take place between the metal droplets, the slag and gas in the emulsion. These reactions have been observed in the laboratory using x-ray techniques indicating in many cases, the gas phase (primarily CO) separates the slag and metal, and that gaseous intermediates play a role in decarburization.
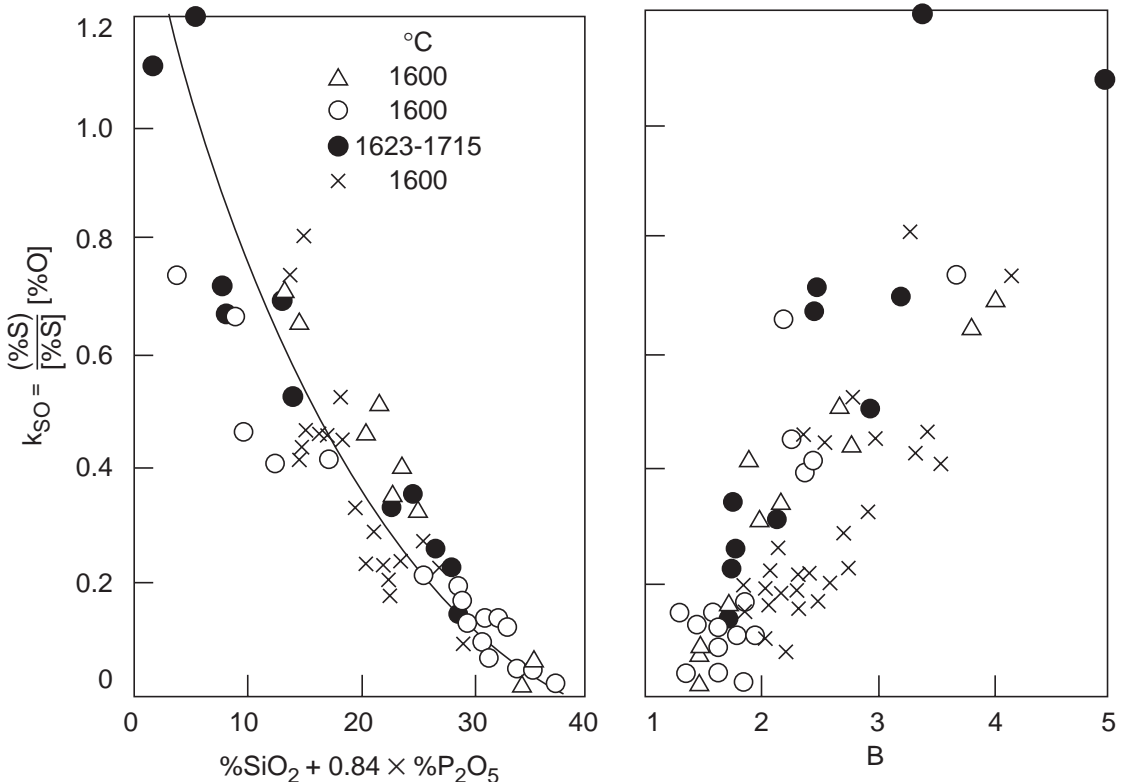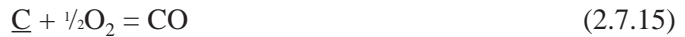

Fig. 2.104 Sulfide capacities of slags. *From Ref. 103.*

When oxygen first contacts a liquid iron-carbon alloy it initially reacts with iron according to reaction 2.7.13, even though thermodynamically it favors its reaction with carbon. This is due to the relative abundance of iron in comparison to carbon. Carbon in the liquid metal then diffuses to the interface reducing the FeO by reaction 2.7.14. The net reaction is the oxidation of carbon, reaction 2.7.15.

$$Fe + \tfrac{1}{2}O_2 = FeO \tag{2.7.13}$$

$$FeO + \underline{C} = CO + Fe \tag{2.7.14}$$

$$\underline{C} + \tfrac{1}{2}O_2 = CO \tag{2.7.15}$$

However, carbon is only oxidized as fast as it can be transferred to the surface.

At high carbon contents the rate of mass transfer is high such that most of the FeO formed is reduced and the rate of decarburization is controlled by the rate of oxygen supply:

$$\frac{d\%C}{dt} = -\frac{\dot{N}_{O_2} M_C 100}{W}(f+1) \tag{2.7.16}$$

where

$\dot{N}_{O_2}$ = the flow rate of oxygen in moles,
M_C = the molecular weight of carbon (12),
W = the weight of steel,
f = the fraction of the product gas which is CO; the remainder is CO_2 and f is close to unity (0.8 to 1).

Below a critical carbon content the rate of mass transfer is insufficient to react with all the injected oxygen. In this case the rate of decarburization is given by[168]:

$$\frac{d\%C}{dt} = -\frac{\rho}{W}\left(\%C - \%C_e\right)\sum_i m_i A_i \tag{2.7.17}$$

where

ρ = density or steel,
$\%C_e$ = the equlibrium carbon with the slag for reaction 2.7.14 and is close to zero,
m_i = the mass transfer coefficient for the specific reaction site,
A_i = the metal-FeO surface area for the specific reaction site.

For top blown processes the reaction takes place between the metal droplets ejected into the emulsion and the FeO in the slag. For bottom blowing there is less of an emulsion and the reaction takes place at the interface of the metal bath and the rising bubbles which have FeO associated with them. The critical carbon is when the rates given by 2.7.16 and 2.7.17 are equal and is typically about 0.3% C.

The actual values of m_i and A_i are not known, consequently an overall decarburization constant (k_C) can be defined and the rate below the critical carbon content is given by 2.7.19 and 2.7.20:

$$k_C = \frac{\rho}{W}\sum_i m_i A_i \tag{2.7.18}$$

$$\frac{d\%C}{dt} = -k_C\left(\%C - \%C_e\right) \tag{2.7.19}$$

or,

$$\ln\frac{\left(\%C - \%C_e\right)}{\left(\%C_C - \%C_e\right)} = -k_C\left(t - t_C\right) \tag{2.7.20}$$

where t_c is the time at which the critical carbon content is obtained. The equilibrium carbon content ($\%C_e$) is close to zero. However in actual steelmaking there is a practical limit of about 0.01 to 0.03 for $\%C_e$.

The value of k_C increases with the blowing rate since the amount of ejected droplets and bubbles increases. Also, k_c decreases with the amount of steel, (W), as indicated by 2.7.19. In actual processes, the blowing rate is proportional to the weight of steel and , therefore, k_C has similar values in most oxygen steelmaking operations. For top blowing, k_C is about 0.015 s^{-1} and for bottom blowing 0.017 s^{-1}. The values of the critical carbon content are also similar ranging from 0.2 to 0.4% C. The rate of decarburization for a typical steelmaking process is shown in Fig. 2.105. At the initial stage when silicon is being oxidized, which will be discussed later, the rate of decarburization is low. The value of k_C is higher for bottowm blowing because mixing is more intensive and the reaction occurs at the interface of the rising bubbles as well as the slag-metal emulsion.

Below the critical carbon content, when the rate of mass transfer of carbon is insufficient to reduce all of the FeO formed and, therefore, the FeO content of the slag increases rapidly. In actual processes, initially, some FeO forms because it has a low activity in the slag resulting in about 5-10 % FeO in the slag. The FeO remains constant until the critical carbon content and then the FeO increases rapidly. The amount of FeO can be computed from a mass balance for oxygen. Specifically the oxgyen not used for carbon, silicon or manganese oxidizes iron to FeO. The moles of FeO in the slag at anytime (N_{FeO}) is given by:

$$N_{FeO} = \int_0^t 2\left[\dot{N}_{O_2} - \frac{d\%C}{dt} \frac{W(1+f)}{M_C\,100} \right] dt - \left(N_{O_2}^{Si} + N_{O_2}^{Mn} \right) \qquad (2.7.21)$$

where $N_{O_2}^{Si}$ and $N_{O_2}^{Mn}$ are the moles of oxygen consumed in oxidizing Si and Mn. Since the rate of decarburizaiton is slightly higher for bottom and mixed blowing these processes have lower FeO contents.

At all levels of turndown carbon, the iron oxide content of BOF slag is about twice that of OBM (Q-BOP) slag (Fig. 2.106). The dotted line depicts the slag-metal equilibrium value of $(\%FeO)[\%C] \approx 1.25$.

As depicted in Fig. 2.107, the square root correlation also applies to the product $(\%FeO)[\%C]$ for low carbon contents, with marked departure form this empirical correlation at higher carbon contents. The slopes of the lines for low carbon contents are given below.
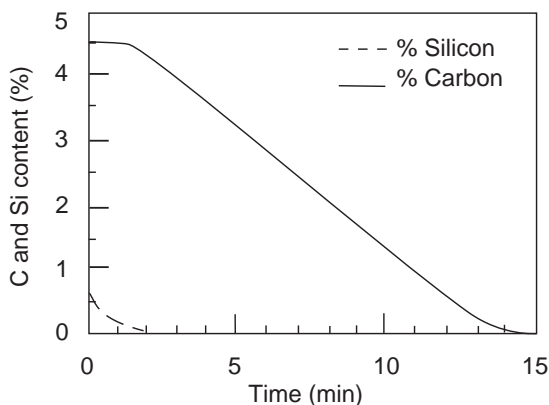

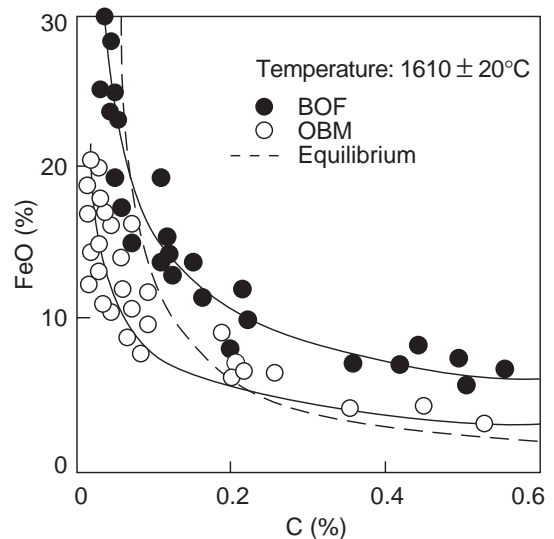**Fig. 2.105** Computed carbon and silicon contents of steel in oxygen steelmaking processes.

Fig. 2.106 Iron oxide-carbon relations in BOF and OBM (Q-BOP) are compared with the average equilibrium relation (-------). *From Ref. 103.*
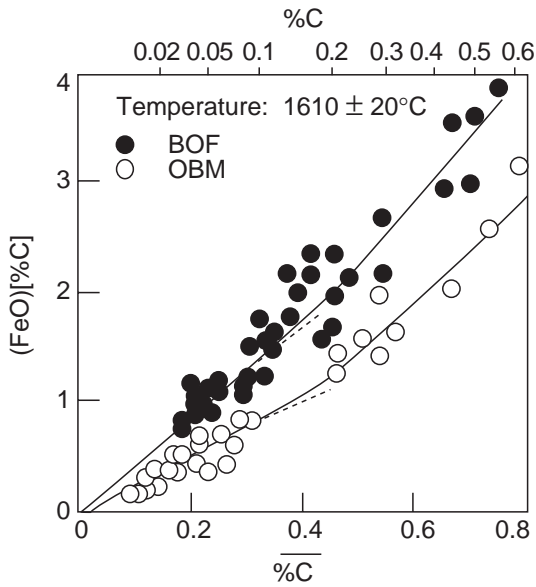
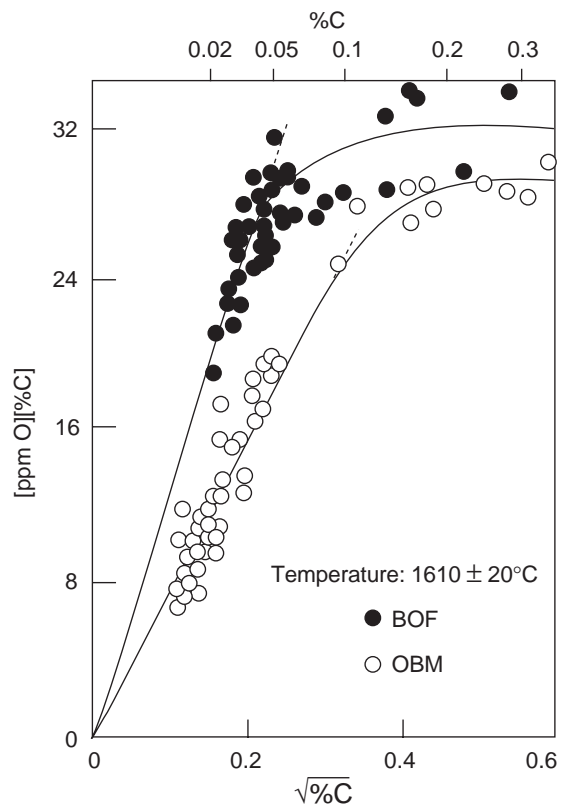**Fig. 2.107** Variation of product (FeO)[%C] with carbon content of steel at first turndown. *From Ref. 103.*

Fig. 2.108 Variation of product [ppm O][%C] with carbon content of steel at first turndown. *From Ref. 103.*

$$BOF \text{ with } C < 0.10\%,$$
$$(\%FeO)\sqrt{\%C} = 4.2 \pm 0.3 \tag{2.7.22}$$

$$OBM (Q\text{-}BOP) \text{ with } C < 0.10\%,$$
$$(\%FeO)\sqrt{\%C} = 2.6 \pm 0.3 \tag{2.7.23}$$

2.7.2.2 Oxygen-Carbon Relation

Noting from the plot in Fig. 2.108, there is an interesting correlation between the product [ppm O] [%C] and the carbon content of the steel. The square root correlation holds up to about 0.05% C in BOF and up to 0.08% C in OBM(Q-BOP) steelmaking. At low carbon contents, the oxygen content of steel in the BOF practice is higher than that in OBM steelmaking. For carbon contents above 0.15% the product [ppm O] [%C] is essentially constant at about 30 ± 2, which is the equilibrium value for an average gas (CO) bubble pressure of about 1.5 atmosphere in the steel bath.

At low carbon levels in the melt near the end of the blow, much of the oxygen is consumed by the oxidation of iron, manganese and phosphorus, resulting in a lower volume of CO generation. With the bottom injection of argon in the BOF combined-blowing practice, and the presence of hydrogen in the gas bubbles in OBM, the partial pressure of CO in the gas bubbles will be lowered in both processes when the rate of CO generation decreases. A decrease in the CO partial pressure at low carbon contents will be greater in OBM than in BOF practices, because the hydrogen content of gas bubbles in OBM is greater than the argon content of gas bubbles in BOF. It is presumably for this reason that the concentration product [O][C] in OBM steelmaking is lower than in the BOF combined-blowing practice, particularly at low carbon levels.

The non-equilibrium states of the carbon-oxygen reaction at low carbon contents in BOF and OBM(Q-BOP) are represented by the following empirical relations.

$$\text{BOF with C} < 0.05\%,$$

$$[\text{ppm O}]\sqrt{\%C} = 135 \pm 5 \tag{2.7.24}$$

$$\text{OBM (Q-BOP) with C} < 0.08\%,$$

$$[\text{ppm O}]\sqrt{\%C} = 80 \pm 5 \tag{2.7.25}$$

2.7.2.3 Desiliconization

Silicon is oxidized out of hot metal early in the process. The oxidation reaction supplies heat and the SiO_2 reacts with the CaO to form the slag.

$$\underline{Si} + \tfrac{1}{2}O_2 = (SiO_2) \tag{2.7.26}$$

The thermodynamics of the reaction indicate virtually all of the Si is oxidized. The rate is controlled by liquid phase mass transfer, represented by the following equation:

$$\frac{d\%Si}{dt} = -\frac{A\rho m_{Si}}{W}\left[\%Si - \%Si_e\right] \tag{2.7.27}$$

where

$$
\begin{aligned}
m_{Si} &= \text{mass transfer coefficient for silicon,} \\
\%Si_e &= \text{the silicon content in the metal in equilibrium with the slag and is} \\
&\quad\text{close to zero.}
\end{aligned}
$$

As with decarburization, an overall rate parameter for Si can be defined, k_{Si}, similar to k_C. Within our ability to estimate k_{Si} it is about equal to k_C since A, W, and are the same and mass transfer coefficients vary only as the diffusivity to the one half power. Therefore 2.7.27 simplifies to:

$$\ln\frac{\%Si}{\%Si°} = -k_{Si}\, t \tag{2.7.28}$$

where $\%Si°$ is the initial silicon and k_{Si} is the overall constant for Si and is approximately equal to k_C. The rate for Si oxidadtion is shown in Fig. 2.105.

2.7.2.4 Manganese Oxide–Carbon Relation

At low carbon contents, the ratio $[\%Mn]/(\%MnO)$ is also found to be proportional to $\sqrt{\%C}$, represented as given below.

$$\text{BOF with C} < 0.10\%,$$

$$\frac{[\%Mn]}{(\%MnO)}\frac{1}{\sqrt{\%C}} = 0.1 \pm 0.02 \tag{2.7.29}$$

$$\text{OBM (Q-BOP) with C} < 0.10\%,$$

$$\frac{[\%Mn]}{(\%MnO)}\frac{1}{\sqrt{\%C}} = 0.2 \pm 0.02 \tag{2.7.30}$$

2.7.2.5 FeO–MnO–Mn–O Relations

From the foregoing empirical correlations for the non-equilibrium states of reactions involving the carbon content of steel, the relations obtained for the reaction of oxygen with iron and manganese are compared in the table below with the equilibrium values for temperatures of $1610 \pm 20°C$ and slag basicities of B = 3.2 ± 0.6.

	BOF C < 0.05%	OBM(Q-BOP) C < 0.08%	Values for slag-metal equilibrium
$\dfrac{[\text{ppm O}]}{(\%\,\text{FeO})}$	32 ± 4	32 ± 5	26 ± 9
$\dfrac{[\%\,\text{Mn}][\text{ppm O}]}{(\%\,\text{MnO})}$	13.6 ± 3.2	16.1 ± 2.6	18 ± 6
$\dfrac{(\text{MnO})}{(\%\,\text{FeO})[\%\,\text{Mn}]}$	2.6 ± 0.5	2.2 ± 0.2	1.9 ± 0.2

It is seen that the concentration ratios of the reactants in low carbon steel describing the states of oxidation of iron and manganese, are scattered about the values for the slag-metal equilibrium. However, as indicated by the plant data in Fig. 2.108, the oxidation of iron and manganese are in the non-equilibrium states for high carbon contents in the steel at turndown. Although the concentration product [O][C] is close to the equilibrium value for an average CO pressure of about 1.5 atm in the steel bath, the concentrations of iron oxide and manganese oxide in the slag are above the equilibrium values for high carbon contents in the melt.

It is concluded from these observations that:

(i) at low carbon contents the equilibrium state of iron and manganese oxidation controls the concentration of dissolved oxygen

(ii) at high carbon contents it is the CO–C–O equilibrium which controls the oxygen content of the steel.
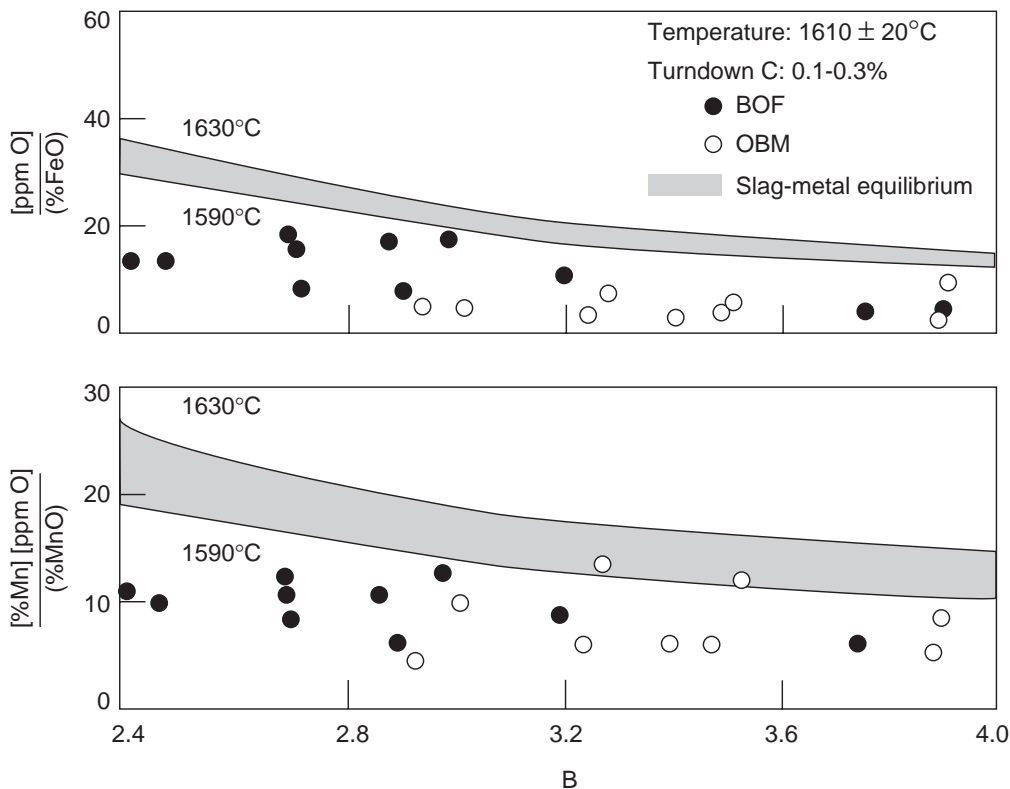

Fig. 2.108 Non-equilibrium states of oxidation of iron and manganese at high carbon contents in steel. *From Ref. 103.*
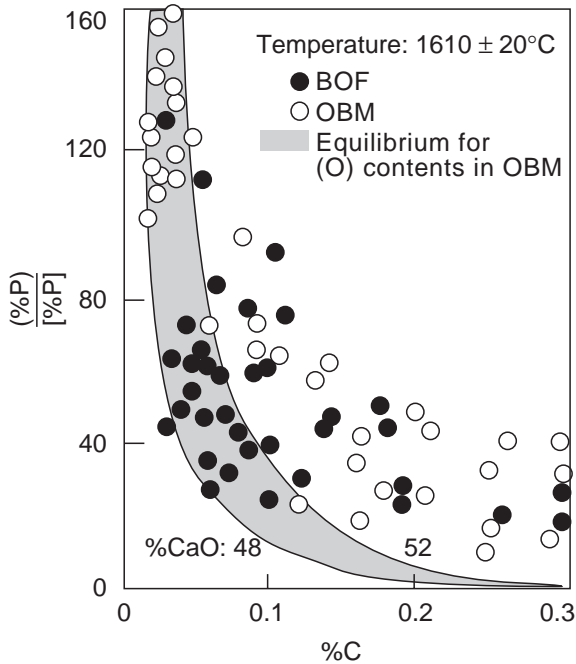
Fig. 2.109 Slag/metal phosphorus distribution ratios at first turndown in BOF and OBM(Q–BOP) practices; slag–metal equilibrium values are within the hatched area for Q–BOP. *From Ref. 103.*

2.7.2.6 State of Phosphorus Reaction

The slag/metal phosophorus distribution ratios at first turndown in BOF and OBM (Q-BOP) steelmaking are plotted in Fig. 2.109 against the carbon content of the steel. The plant data are for the turndown temperatures of $1610 \pm 20°C$ and slags containing $50 \pm 2\%$ CaO and $6 \pm 2\%$ MgO. The shaded area is for the slag-metal equilibrium for the above stated conditions in OBM(Q-BOP), based on the empirical [O][C] relations, i.e. for C < 0.08%, [ppm O] $\sqrt{\%C}$ = 80 and for C > 0.15%, [ppm O][%C] = 30.

Noting that the oxygen contents of the steel at low carbon levels are greater in BOF steelmaking, the equilibrium phosphorus distribution ratios will likewise be greater in BOF than in (OBM) Q-BOP steelmaking. For example, at 0.05% C and about 600 ppm O in BOF at turndown the average equilibrium value of (%P)/[%P] is about 200 at 1610°C, as compared to the average value of 60 in OBM(Q-BOP) at 0.05% C with about 360 ppm O.

Below 0.04% C the phosphorus distribution ratios in OBM(Q-BOP) are in general accord with the values for slag-metal equilibrium. However, at higher carbon contents the ratios (%P)/[%P] are well above the equilibrium values. In the case of BOF steelmaking below 0.1% C at turndown, the ratios (%P)/[%P] are much lower than the equilibrium values. On the other hand, at higher carbon contents the phosphorus distribution ratios are higher than the equilibrium values as in the case of OBM(Q-BOP).

The effect of temperature on the phosphorus distribution ratio in OBM(Q-BOP) is shown in Fig. 2.110 for melts containing 0.014% to 0.022% C with BO = 52 ± 2% in the slag.

2.7.2.7 State of Sulfur Reaction

A highly reducing condition that is required for extensive desulfurization of steel is opposite to the oxidizing condition necessary for steel making. However, some desulfurization is achieved during oxygen blowing for decarburization and dephosphorization. As seen from typical examples of the BOF and OBM(Q-BOP) plant data in Fig. 2.111, the state of steel desulfurization at turndown, described by the expression [%O](%S)/[%S], is related to the SiO_2 and P_2O_5 contents of the slag. Most of the points for OBM(Q-BOP) are within the hatched area for the slag-metal equilibrium reproduced from Fig. 2.104. However, in the case of BOF steelmaking the slag/metal sulfur distribution ratios at turndown are about one-third or
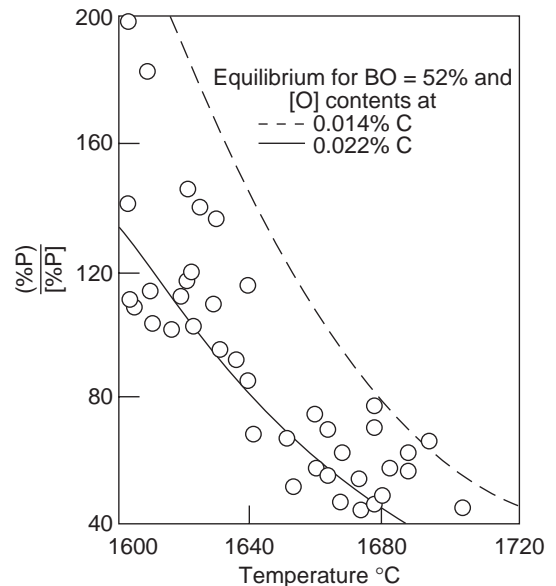

Fig. 2.110 Effect of turndown temperature on the slag/metal phosphorus distribution ratios in OBM (Q-BOP) for turndown carbon contents of 0.014 to 0.022% C; curves are for slag–metal equilibrium. *From Ref. 103.*
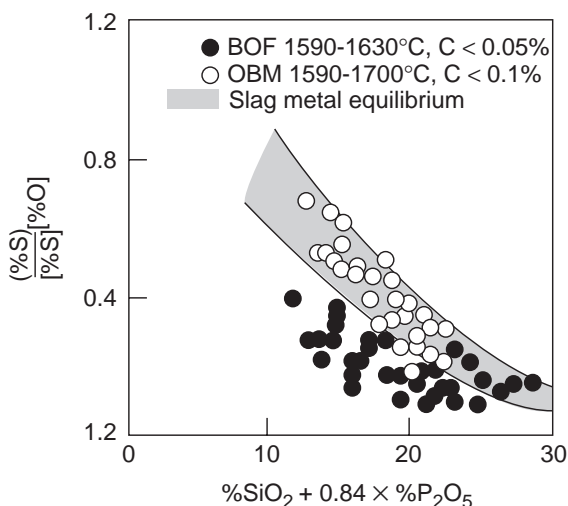
Fig. 2.111 Equilibrium and non–equilibrium states of sulphur reaction in OBM(Q-BOP) and BOF steelmaking. *From Ref. 103.*

one-half of the slag-metal equilibrium values. At higher carbon contents, e.g. C > 0.1%, the sulfur distribution ratios in both processes are below the slag-metal equilibrium values.

2.7.2.8 Hydrogen in BOF and OBM(Q-BOP) Steelmaking

Hydrogen and nitrogen are removed from the steel bath during oxygen blowing by CO carrying off H_2 and N_2.

$$2\underline{H}(in\ steel) \rightarrow H_2(g) \qquad (2.7.31)$$

$$2\underline{N}(in\ steel) \rightarrow N_2(g) \qquad (2.7.32)$$

There is however continuous entry of both hydrogen and nitrogen into the bath by various means. In both BOF and OBM(Q-BOP) there is invariably some leakage of water from the water cooling system of the hood into the vessel. In the case of OBM(Q-BOP), the natural gas (CH_4) used as a tuyere coolant is a major source of hydrogen.

The hydrogen content of steel in the tap ladle, measured by a probe called HYDRIS, is less than 5 ppm in BOF steelmaking and 6 to 10 ppm H in OBM(Q-BOP) steelmaking. Because natural gas (CH_4) is used as a tuyere coolant in the OBM, the hydrogen content of steel made in this vessel is always higher than that in the BOF vessel. In both practices the re-blow will always increase the hydrogen content of the steel. A relatively small volume of CO evolved during the re-blow cannot overcome the hydrogen pickup from various sources.

2.7.2.9 The Nitrogen Reaction

As demonstrated, the decarburization reaction is reasonably well understood as well as the slag-metal re-fining reactions which approach equilibrium. The removal of nitrogen is complex and depends on numerous operating variables. With the advent of the production of high purity interstitial free (IF) steels the control of nitrogen has become of great importance. For years there have been "rules of thumb" for achieving low nitrogen. For example, using more hot metal and less scrap in the charge or with combined blowing processes, switching the stirring gas from nitrogen to argon have resulted in lower nitrogen contents.

The sources of nitrogen in oxygen steelmaking include the hot metal, scrap, impurity nitrogen in the oxygen, and nitrogen in the stirring gas. Nitrogen from the atmosphere is not a major factor unless at first turndown a correction or reblow is required, in which case the furnace fills up with air which is entrained into the metal when the oxygen blow restarts, resulting in a significant nitrogen pickup of 5 to 10 ppm.

Goldstein and Fruehan[169] developed a comprehensive model to predict the nitrogen reaction in steelmaking. Nitrogen is removed by diffusing to the CO bubbles in the emulsion,or to the bubbles in the bath in bottom blowing. The nitrogen atoms combine to form N_2, the rate of which is controlled by chemical kinetics and the nitrogen gas is removed with the CO bubbles. Both mass transfer and chemical kinetics contribute to the overall rate of removal.
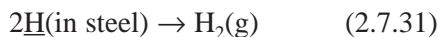
$$\underline{N}(metal) = \underline{N}(surface) \qquad (2.7.33)$$

$$2\underline{N}(surface) = N_2 \qquad (2.7.34)$$

The mixed control model presented previously is the basis for the model. There are, however, several complications. For example, all of the rate parameters are functions of temperature. The sulfur

content of the metal changes with time and the oxygen content at the surface is considerably different from the bulk concentration. Consequently the temperature and surface contents of oxygen and sulfur must be known as functions of time. Also, scrap is melting during the process changing the composition of the metal.

An example of the results of the model calculations are shown in Fig. 2.112 and Fig. 2.113. In Fig. 2.112 the nitrogen contents are shown for two hypothetical cases for a 200 ton oxygen steelmaking converter blowing oxygen at 800 Nm³/min. In one case the charge contains 80% heavy scrap, 16 cm thick containing 50 ppm nitrogen; in the second case there is no scrap but cooling is achieved by the use of a 15% addition of DRI containing 20 ppm nitrogen. For the case of the heavy scrap, it melts late in the process releasing its nitrogen after most of the CO is generated, causing the nitrogen content to increase to 30 ppm at the end of the blow. With no scrap the final nitrogen is significantly lower at 20 ppm. The model also indicates if ore, which has no nitrogen, is used for cooling, levels of 10 ppm nitrogen can be obtained. In comparing the bulk and surface nitrogen contents, it is found that the surface concentration is only slightly less than the bulk, indicating that the nitrogen reaction is primarily controlled by chemical kinetics. In particular, towards the end of the blow the oxygen content at the surface is high, retarding the rate. This model is useful for optimizing the process for nitrogen control. For example, the effect of oxygen purity, the time of switching the stirring gas from N_2 to argon, the metal sulfur content and the amount and size of scrap can be determined. The effect of switching the stirring gas from N_2 to Ar is shown in Fig. 2.113.

2.7.2.10 General Considerations

The analyses of plant data on slag and metal samples taken at first turndown have revealed that there are indeed equilibrium and non-equilibrium states of reactions in oxygen steelmaking. In all the reactions considered, the carbon content of steel is found to have a decisive effect on the state of slag-metal reactions.
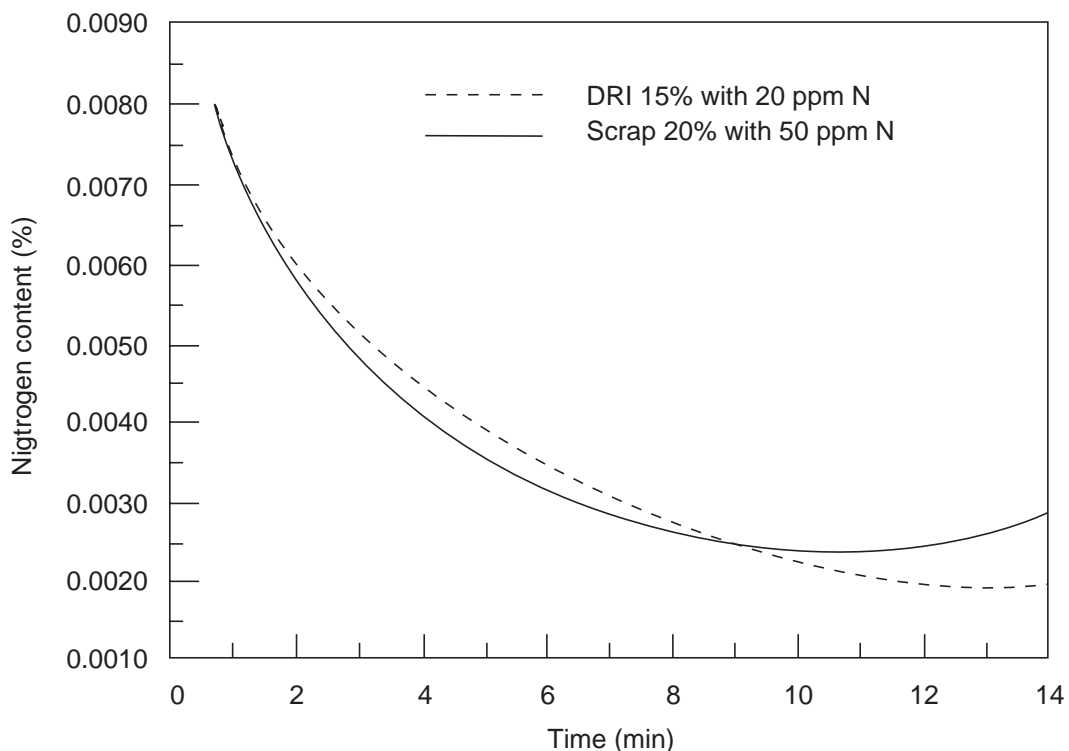

Fig. 2.112 Computed nitrogen content in a 200 ton oxygen steelmaking converter for 20% heavy scrap – 80% light scrap and DRI at a blowing rate of 800 Nm³/min O_2. *From Ref. 167.*
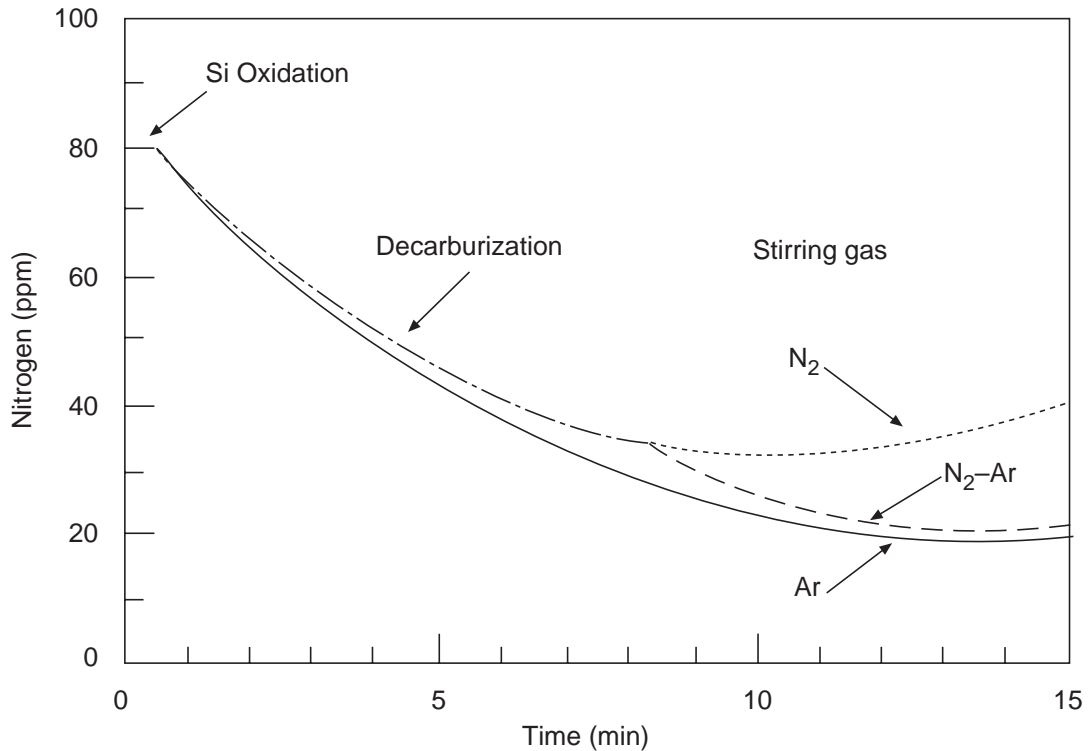
Fig. 2.113 The effect of bottom stirring practice on nitrogen removal in the BOF with N_2 during the entire blow, Ar during the entire blow, and with a switch from N_2 to Ar at 50% through the blow. *From Ref. 167.*

Considering the highly dynamic nature of steelmaking with oxygen blowing and the completion of the process in less than 20 minutes, it is not surprising that the slag-metal reactions are in the non-equilibrium states in heats with high carbon contents at turndown. With regard to low carbon heats all the slag-metal reactions are close to the equilibrium states in bottom blown processes. In the case of BOF steelmaking however, the states of steel dephosphorization and desulfurization are below the expected levels for slag-metal equilibrium. As we all recognize it is of course the bottom injection of lime, together with oxygen, that brings about a closer approach to the slag-metal equilibrium in OBM(Q-BOP) as compared to the BOF practice, particularly in low carbon heats.

References

1. L. Onsager and R. M. Fuoss, *J. Phys. Chem.* 36 (1932): 2687.
2. A. Einstein, *Ann. Phys (Leipzig)* 17 (1905): 54; *Z. Elektrochem* (1908): 14,235.
3. E. T. Turkdogan, "Physicochemical Properties of Molten Slags and Glasses," The Metals Society (now The Institute of Materials), London, 1983.
4. J. Szekely, *Fluid Flow Phenomena in Metals Processing* (New York: Academic Press, 1979).
5. J. Szekely and N. J. Themelis, *Rate Phenomena in Process Metallurgy* (New York: Wiley, 1971).
6. G. H. Geiger and D. R. Poirier, *Transport Phenomena in Metallurgy* (Reading, MA: Addison-Wesley, 1973).
7. J. Szekely, J. W. Evans, and J. K. Brimacombe, *The Mathematical and Physical Modelling of Primary Metals Processing Operations* New York: Wiley, 1988).
8. J. Szekely, G. Carlsson, and L. Helle, *Ladle Metallurgy* (Berlin: Springer, 1989).
9. J. Szekely and O. J. Ilegbusi, *The Physical and Mathematical Modelling of Tundish Operations* (Berlin: Springer, 1989).

10. J. S. Sheasby, W. E. Boggs, and E. T. Turkdogan, *Metal Science* 18 (1984): 127.
11. C. Wagner, *Z. Phys. Chem., Abt B* 21 (1933), 25 (in "Atom Movements," ASM (1950): 153.
12. L. Himmel, R. F. Mehl, and C. E. Birchenall, *Trans. AIME* 197 (1953): 827.
13. P. Hembree and J. B. Wagner, *Trans. AIME* 245, (1969): 1547.
14. P. L. Walker, F. Rusinko, and L. G. Austin, *Advan. Catalysis* 21 (1959): 33.
15. E. T. Turkdogan et al., *Carbon* 6 (1968): 467.
16. E. T. Turkdogan and J. V. Vinters, *Carbon* 7 (1969): 101; 8 (1970): 39.
17. E. T. Turkdogan, R. G. Olsson, and J. V. Vinters, *Carbon* 8 (1970): 545.
18. R. H. Tien and E. T. Turkdogan, *Carbon* 8 (1970): 607.
19. D. A. Aderibigbe and J. Szekely, *Ironmaking and Steelmaking* 9 (1982): 32.
20. W .M. McKewan, *Trans. TMS-AIME* 218 (1960): 2.
21. J. M. Quets, M. E. Wadsworth, and J. R. Lewis, *Trans. TMS-AIME* 218 (1960): 545: 221 (1961): 1186.
22. N. J. Themelis and W. H. Gauvin, *A.E. Ch. E.J.* 8, (1962): 437; *Trans. TMS-AIME* 227 (1963): 290.
23. N. A. Warner, *Trans. TMS-AIME* 230 (1964): 163.
24. R .H. Spitzer, F. S. Manning, and W. O. Philbrook, *Trans. TMS-AIME* 236 (1966): 726.
25. E. T. Turkdogan and J. V. Vinters, *Metall. Trans.* 2 (1971): 3175; 3 (1972): 1561.
26. P. H. Calderbank, *Chem. Eng. (London)* 212 (1967): CE 209.
27. E. T. Turkdogan, "Fundamentals of Steelmaking," The Institute of Materials, London, 1996.
28. I. Leibson et al., *A.I.Ch.E.J.* 2, (1956): 296.
29. V. G. Levich, *Physicochemical Hydrodynamics* (Englewood Cliffs: Prentice-Hall, 1962).
30. S. Glasstone, K. J. Laidler, and H. Eyring, The Theory of Rate Processes (New York: McGraw-Hill, 1941).
31. C. N. Hinshelwood, Kinetics of Chemical Change, (London: Oxford University Press, 1942).
32. T. Fuwa, S. Ban-ya, and T. Shinohara, *Tetsu-to-Hagane* 53 (1967): S328.
33. M. Inouye and T. Choh, *Trans. Iron Steel Inst. Japan* 8 (1968): 134.
34. K. Mori and K. Suzuki, *Trans. Iron Steel Inst. Japan* 10 (1970): 232.
35. R. J. Fruehan and L. J. Martonik, *Metall. Trans. B* 11B (1980): 615.
36. M. Byrne and G. R. Belton, *Metall. Trans. B* 14B (1983): 441.
37. P. Glaws and R. J. Fruehan, *Metall Trans. B* 16B (1985): 551.
38. S. Ban-ya et al., *Tetus-to-Hagane* 60 (1974): 1443.
39. G. Sain and G. R. Belton, *Metall Trans. B* 5B (1974): 1027–32; 7B (1976): 403–7.
40. F. Mannion and R. J Fruehan, *Metall Trans. B,* 20B (1989): 853.
41. T. Nagasaka and R. J. Fruehan, *Metall Trans. B,* 25B (1994): 245.
42. G. R. Belton, *Metall Trans. B,* 7B (1976): 35–42.
43. E. A. Gulbransen, K. F. Andrew, and F. A. Brassort, *Carbon* 2 (1965): 421.
44. J. D. Blackwood, *Aust. J. Appl. Sci.* 13 (1962): 199.
45. S. Ergun, *J. Phys. Chem.* 60 (1956): 480.
46. K. Hedden and A. Lowe, *Carbon* 5 (1967): 339.
47. H. J. Grabke, *Ber. Bunsenges. Physik Chem.* 70 (1966): 664.
48. D. A. Aderibigbe and J. Szekely, *Ironmaking & Steelmaking* 8 (1981): 11.
49. S. Story and R. J. Fruehan, To be submitted to Metall Trans., 1997
50. R. J. Fruehan, B. Lally, and P. C. Glaws, *Trans. ISS, I&SM,* (April 1987), 31.
51. E. T. Turkdogan and J. V. Vinters, *Metall. Trans.* 5 (1974): 11.
52. E. T. Turkdogan, *Physical Chemistry of High Temperature Technology* (New York: Academic Press, 1980).
53. H. J. Donald, "An Annotated Bibliography," Mellon Inst. Ind. Res. Pittsburgh, PA. 1956.
54. J. V. Kehrer and H. Leidheiser, *J. Phys. Chem.* 58, (1954): 550.
55. W .R. Walker, J. F. Rakszawski, and G. R. Imperial, *J. Phys. Chem.* 63 (1959): 133, 140.
56. W. R. Ruston et al., *Carbon* 7 (1969): 47.
57. R. G. Olsson and E. T. Turkdogan, *Metall. Trans.* 5 (1974): 21.
58. J. Macak, P. Knizek, and J. Malecha, *Carbon* 16 (1978): 111.
59. E. R. Gilliland and P. Harriott, *Ind. Eng. Chem.* 46 (1954): 2195.
60. T. H. Byrom, *J. Iron Steel Inst.* 92 (1915): 106.

61. H. C. H. Carpenter and C. C. Smith, *J. Iron Steel Inst.* 96 (1918): 139.
62. O. Stelling, *J. Met.* 10 (1958): 290.
63. H. Schenck and W. Maachlanka, *Arch. Eisenhuttenwes.*31 (1960): 271.
64. R. J. Fruehan and L. J. Martonik, *Metall Trans*. 4 (1973): 2129.
65. S. Chapman and T. G. Cowling, *The Mathematical Theory of Non-uniform Gases,* 3rd ed. (London: Cambridge University Press, 1970).
66. J. O. Hirschfelder, C. F. Curtiss, and R. B. Bird, *Molecular Theory of Gases and Liquids,* (New York: Wiley, 1954).
67. A. Eucken, *Physik.Z.* 14 (1913): 324.
68. M. Knudsen, *Ann. Phys. (Leipzig)* 28 (1909): 75.
69. C. H. Bosanquet, Br. TA Rep. BR–507, September 1944.
70. E. T. Turkdogan, R. G. Olsson, and J. V. Vinters, *Metall. Trans.* 2 (1971): 3189.
71. G. K. Sigworth and J. F. Elliott, *Met. Sci.* 8 (1974): 298.
72. E. T. Turkdogan and L. E. Leake, *J. Iron and Steel Inst.* 179 (1955): 39.
73. E. T. Turkdogan and R. A. Hancock, 179 (1955): 155; 183 (1956): 69.
74. J. Chipman et al., *Trans. ASM.* 44 (1952): 1215.
75. J. Chipman and T. P. Floridis, *Acta Met* 3 (1955): 456.
76. N. R. Griffing, W. D. Forgeng, and G. W. Healy, *Trans. AIME* 224 (1962): 148.
77. J. F. Elliott, M. Gleiser, and V. Ramakrishna, *Thermochemistry for Steelmaking,* vol. II (Reading, MA: Addison-Wesley, 1963).
78. S. N. Singh and K. E. Blazek, *J. Metals (AIME)* 26(10) (1974): 17.
79. M. M. Wolf and W. Kurz, *Metall.Transaction B* 12B (1981) 85.
80. A. A. Howe, *Applied Scientific Research* 44 (1987): 51.
81. H. Yamada, T. Sakurai, and T. Takenouchi, *Tetsu-to-Hagane* 76 (1990): 438.
82. M. M. Wolf, in "1st European Conference on Continuous Casting", p. 2.489. Florence, Italy, Sept. 23–25, 1991.
83. C. R. Taylor and J. Chipman, *Trans. AIME* 154 (1943): 228.
84. P .A. Distin, S. G. Whiteway, and C. R. Masson, *Can. Metall. Q.* 10 (1971): 13.
85. A. E. Lord and N. A. Parlee, *Trans. Met. Soc. AIME* 218 (1960): 644.
86. D. L. Sponseller and R. A. Flinn, *Trans. Met. Soc. AIME* 230 (1964): 876.
87. P. K. Trojan and R. A. Flinn, *Trans. ASM 54* (1961): 549.
88. P. J. Guichelaar et al., *Metall. Trans.* 2 (1971): 3305.
89. B. J. Keene, A survey of extant data for the surface tension of iron and its binary alloys, NPL Rep. DMA(A) 67, June 1983.
90. E. T. Turkdogan, in *Foundry Processes—Their Chemistry and Physics*, ed. S. Katz and C. F. Landefeld (New York: Plenum Press, 1988), 53.
91. P. Kozakevitch, in *Surface Phenomena of Metal* (London: Chem. Ind., 1968), 223.
92. E. Selcuk and D. H. Kirkwood, *J. Iron and Steel Inst.* 211 (1973): 134.
93. I. Jimbo and A. W. Cramb, *Iron Steel Inst. Japan International* 32 (1992): 26.
94. A. Kasama et al., *Can. Met. Quart.* 22 (1983): 9.
95. L. D. Lucas, *Compt. Rend.* 248 (1959): 2336.
96. R. N. Barfield and J. A. Kitchener, *J. Iron and Steel Inst.* 180 (1955): 324.
97. G. Tromel et al., *Arch. Eisenhuttenwes.* 40 (1969): 969.
98. C. R. Taylor and J. Chipman, *Trans. AIME* 159 (1943): 228.
99. M. Timucin and A. E. Morris, *Metall. Trans* 1 (1970): 3193.
100. S. H. Liu, A. Morales, and R. J. Fruehan, To be submitted to Metall Trans. B, 1997.
101. R. H. Rein and J. Chipman, *Trans. Met. Soc. AIME* 233 (1965): 415.
102. T. Fujisawa and H. Sakao, *Tetsu-to-Hagane* 63 (1977): 1494, 1504.
103. "Ethem T. Turkdogan Symposium", pp. 253–269. The Iron and Steel Society of AIME, May 15–17, 1994.
104. Y. Iguchi, S. Ban-ya and T. Fuwa, *Trans. Iron and Steel Inst. Japan* 9 (1969): 189.
105. K. Ito and R. J. Fruehan, *Metall. Trans. B* 19B (1988): 419.
106. D. J. Min and R. J. Fruehan, *Metall Trans. B* 21B (1990): 1025.
107. H. Suito and R. Inoue, *Tetsu-to-Hagane* 73 (1987): S246.
108. K. Nomura, B. Ozturk, and R. J. Fruehan, *Metall Trans. B* 22B (1991): 783.

109. S. Ban-ya and J. D. Shim, *Can. Metall. Q.* 21 (1982): 319.
110. P. Kozakevitch, *Rev. Metall.* 46 (1949): 505, 572.
111. K. C. Mills and B. J. Keene, *Inter. Met. Rev.* 26 (1981): 21.
112. H. Gaye et al., *Can. Metall. Q.* 23 (1984): 179.
113. K. Ogino et al., *Trans. Iron and Steel Inst. Japan* 24 (1984): 522.
114. I. Jimbo and A. W. Cranb, The Sixth International Iron and Steel Congress, Naguya, ISIJ, 1990, 499.
115. D. R. Gaskell, A. McLean, and R. G. Ward, *Trans. Faraday Soc.* 65 (1969): 1498.
116. Y. Skiraishi et al., *Trans. Japan Inst. Met.* 19 (1978): 264.
117. Yu M. et al., *Soob A Gruz. SSR* 32(1) (1963): 117.
118. L. Segers, A. Fontana, and R. Winand, *Electrochem. Acta.* 23 (1978): 1275.
119. J. W. Tomlinson, M. S. R. Heynes, and J. O'M. Bockris, *Trans. Faraday Soc.* 54 (1958): 1822.
120. L. R. Barrett and A. G. Thomas, *J. Glas Technol.* (1959): 179s.
121. H. Winterhager, L. Greiner, and R. Kammel, *Forschungsberichte des Landes* (Nordrhein-Westfalen, Nr. 1630: Westdeutscher Verlag, 1966).
122. E. V. Krinochkin, K. T. Kurochin, and P. V. Umrikhin, *Fiz. Khim. Poverkh*. (Kiev: Naukova Dumba, Yavlenii Rasp., 1971) ,179–83.
123. J. S. Machin and T. B. Yee, *J. Am. Cerm. Soc.* 32 (1948): 200; 37 (1954) 177.
124. K. Ito and R. J. Fruehan, *Metall Trans. B* 20B (1989): 509.
125. K. Ito and R.J. Fruehan, *Metall Trans. B* 20B (1989): 515.
126. Y. Zhang and R. J. Fruehan, *Metall Trans. B* 26B (1995): 811.
127. T. Tokumetsu et al., Process Technology Conference Proceedings, Toronto, ISS, 1989.
128. Y. Zhang and R. J. Fruehan, *Metall Trans. B*. 26B (1995): 803.
129. S. Ban-ya, *ISIJ International* 33 (1993): 2–11.
130. H. Gaye and J. Lehmann, *Molten Slags, Fluxes, and Salts Conference,* Sydney, 1997, IS Warrendale, PA, 27–34.
131. H. Gaye and J. Welfinger, *Proc. Second International Symposium on Slags and Fluxes*, 1984, TMS Warrendale, PA 357–375.
132. M. Blander, A Pelton and G. Erikssen, *4th Internation Conference on Slags and Fluxes*, 1992, ISIJ, 56–60.
133. I. D. Sommerville, A. McLean and Y. D. Yang, Molten Slags, Fluxes, and Salts Conference, Sydney, 1997, ISS Warrendale PA, 375–383.
134. D. J. Sosinsky and I. D. Sommerville, *Metall Trans. B*. 17B (1986): 331–7.
135. J. G. Peacey and W. G. Davenport, *The Iron Blast Furnace* (Oxford: Pergamon Press, 1979).
136. A. Rist and G. Bonnivard, *Rev. Met.* 60 (1963): 23.
137. A. Rist and N. Meysson, *Rev. Met.* 61 (1964): 121.
138. N. Meysson, J. Weber, and A. Rist, *Rev. Met.* 61 (1964): 623
139. A. Rist and N. Meysson, *Rev. Met.* 62 (1965): 995.
140. N. Meysson, A. Maaref, and A. Rist, *Rev. Met.* 62 (1965): 1161.
141. F. D. Richardson and J. H. E. Jeffes, *J. Iron and Steel Inst.* 160 (1948): 261.
142. N. Tsuchiya, M. Tokuda, and M. Ohtani, *Metall. Trans* B7 (1976): 315.
143. E. T. Turkdogan, G. J. W. Kor, and R. J. Fruehan, *Ironmaking and Steelmaking* 7 (1980): 268.
144. B. Ozturk and R. J. Fruehan, *Metall Trans. B* 16B (1985): 121.
145. N. Standish and W.-K. Lu, eds., *Alkalies in Blast Furnaces* (Ontario: McMaster University Press, 1973).
146. K. P. Abraham and L. J. Staffansson, *Scand. J. Metall.* 4 (1975): 193.
147. J. Davies, J. T. Moon and F. B. Traice, *Ironmaking and Steelmaking* 5 (1978): 151.
148. J. M. Steiler, "Etude Thermodynamique des Laitiers Liquides des Systems K_2O–SiO_2 et K_2O–CaO–SiO_2–Al_2O_3," IRSID, PCM–RE 646, July 1979.
149. L. L. Simmons, L. R. Lowden and T. C. Ehlert, *J. Phys. Chem.* 81 (1977): 709.
150. Z. Pociecha and J. Biczysko, in Seminar on Problems of Air and Water Pollution Arising in the Iron and Steel Industry, Leningrad, Aug. 1971, CI.
151. E. T. Turkdogan and P .H. Josephic, *Ironmaking and Steelmaking* 11 (1984): 192.
152. K. L. Abraham, M. W. Davies, and F. D. Richardson, *J. Iron and Steel Inst.* 19 (1960): 82.
153. E. W. Filer and L. S. Darken, *Trans. AIME* 194 (1952): 253.
154. W. Oelsen, *Arch. Eisenhuttenwes* 35 (1964): 699, 713, 1039, 1115.

155. E. T. Turkdogan and R. A. Hancock, *Trans. Inst. Min. Metall.* 67 (1957–58): 573.
156. F. D. Delve, H. W. Meyer, and H. N. Lander, in *Phys. Chem. Proc. Metallurgy,* ed. G. R. St. Pierre (New York: Interscience, 1961).
157. E. T. Turkdogan, *Metall. Trans. B* 9B (1978): 163.
158. K. Okabe et al., Kawasaki Steel Tech. Res. Lab. Rept, pp. 1–43, May 4, 1974 (English Translation BISI 13657); pp. 1–11 November 27, 1974 (English Translation 13658).
159. E. T. Turkdogan, *Trans. Iron and Steel Inst. Japan* 24 (1984): 591.
160. E. T. Turkdogan, *J. Iron and Steel Inst.* 182 (1956): 74.
161. A. Morales and R. J. Fruehan, *Metall Trans. B,* To be published 1997.
162. J. Chipman et al., *Trans. AIME* 188 (1950): 341.
163. H. Suito and R. Inoue, *Trans. ISIJ* 24 (1984): 301.
164. P. Bremer, *Stahl u. Eisen* 71 (1951): 575.
165. E. Aukrust, P. J. Koros, and H. W. Meyer, *J. Met.* 18 (1966): 433.
166. R. V. Pathy and R. G. Ward, *J. Iron and Steel Inst.* 202 (1964): 995.
167. R. J. Fruehan, in *Advanced Physical Chemistry for Process Metallurgy,* ed. N. Sano, wKLW and P. Ribaud (London: Academic Press, 1977).
168. R. J. Fruehan, *Ironmaking and Steelmaking* 1 (1976): 33.
169. D. Goldstien and R. J. Fruehan, Submitted to *Metall Trans. B*, 1997.